

# Low Dimensional Ion-Conducting Nanomaterials for Fuel Cell Membrane Applications

バイヤー, トーマス

<https://doi.org/10.15017/1654880>

---

出版情報：九州大学, 2015, 博士（工学）, 課程博士  
バージョン：  
権利関係：全文ファイル公表済

# Low Dimensional Ion-Conducting Nanomaterials for Fuel Cell Membrane Applications

A dissertation submitted to the  
Kyushu University  
in partial fulfilment of the requirements for the degree of  
Doctor of Engineering

By

**Thomas Bayer**

Department of Hydrogen Energy Systems  
Graduate School of Engineering  
Kyushu University



**九州大学**  
KYUSHU UNIVERSITY

Approved by:

Prof. Dr. Kazunari Sasaki (examiner/supervisor)

*Department of Hydrogen Energy Systems, Graduate School of Engineering, Kyushu University*

Prof. Dr. Akari Hayashi (co-examiner)

*Department of Hydrogen Energy Systems, Graduate School of Engineering, Kyushu University*

Prof. Dr. Naotoshi Nakashima (co-examiner)

*Department of Chemical Systems and Engineering, Graduate School of Engineering, Kyushu University*

Associate Prof. Dr. Stephen M. Lyth (co-examiner/co-supervisor)

*International Institute for Carbon-Neutral Energy Research, Kyushu University*

Fukuoka, Japan

2016



## Abstract

Fuel cells are the key technology in the move towards a “hydrogen society” in Japan. Polymer electrolyte membrane fuel cells (PEMFCs) are to date the most commercially successful type of fuel cell. They are currently being utilized to a limited extent in fuel cell vehicles (e.g. FCV MIRAI, *Toyota*), and micro-combined heat and power plants (e.g. ENE-Farm). Their limited commercialization in broader fields is largely due to their high cost, stemming from the materials used, e.g. the platinum electrocatalyst and the Nafion<sup>®</sup> proton exchange membrane (PEM). Decreasing the cost of fuel cells can be directly achieved by using cheaper materials, or indirectly by improving device performance and lifetime. Here we attempt this by finding novel membrane materials.

Any new fuel cell membrane material must satisfy three major conditions. First, it must be possible to reproducibly manufacture sufficiently mechanically stable membranes in a scalable manner. Second, such membranes must fulfill the basic requirements for fuel cell operation, namely: water uptake, ionic conductivity, electronic insulation, and sufficient gas barrier properties. Third, it should be possible to incorporate the materials into membrane electrode assemblies (MEAs), where they can be evaluated for their fuel cell performance. Here, two novel low dimensional ionic conductors are investigated as new membrane materials for PEMFCs and alkaline anion exchange membrane fuel cells (AAEMFCs); i.e., graphene oxide (GO) and nanocellulose.

In Chapter 1 a detailed introduction about fuel cells is given, including the history and operating principles of fuel cells. The background of graphene oxide and nanocellulose is discussed. The experimental methods used in this work are explained in Chapter 2.

GO is explored in detail as a membrane material in Chapter 3. First, membranes are prepared by vacuum-filtration, and their morphology, chemical composition, and mechanical properties are investigated. Next, the suitability of GO membranes for fuel cell applications is determined by measuring the water uptake, conductivity, and hydrogen gas barrier properties, compared with Nafion. In particular the conductivity (and permittivity) is systematically investigated over a wide temperature and humidity range by impedance spectroscopy and blocking measurements, giving insight into the conduction mechanisms. Finally, GO membranes are incorporated into MEAs and their fuel cell performance is measured. The dependence of fuel cell performance on membrane

thickness is investigated, and very thin, electrode-supported membranes are investigated using novel spray-based fuel cell fabrication techniques.

In Chapter 4 the application of GO membranes in AAEMFCs is investigated. First, GO in dispersion is reacted with potassium hydroxide in order to introduce mobile OH<sup>-</sup> ions, then vacuum filtered to make membranes. The morphology, chemical composition, thermal stability, water uptake and mechanical properties of alkaline treated GO (GO<sub>KOH</sub>) are investigated. Next, the suitability of GO<sub>KOH</sub> membranes for alkaline fuel cell applications is determined by measuring the water uptake, ion exchange capacity, conductivity, and hydrogen gas barrier properties, compared with the original GO, and commercially available anion exchange membrane. In particular the conductivity is systematically investigated over a wide temperature and humidity range by impedance spectroscopy, giving insight into the conduction mechanisms. The dominant charge carrier is confirmed using blocking measurements. Finally MEAs are fabricated and investigated for their performance in an alkaline fuel cell.

Chapter 5 deals with the application of nanocellulose as a fuel cell membrane material. Two varieties of nanocellulose are studied, namely: cellulose nanofibers (CNF), and cellulose nanocrystals (CNCs). First, nanocellulose papers are prepared by vacuum-filtration of nanocellulose water dispersions, and their morphology, chemical composition and mechanical properties are investigated. Next, the suitability of nanocellulose paper for fuel cell membrane applications is investigated by hydrogen gas barrier measurements, water uptake, and conductivity measurements, and the results are compared with Nafion. In particular, the conductivity is systematically investigated over a wide temperature and humidity range by the aid of impedance spectroscopy, and the conduction mechanism is elucidated via activation energy determination. Finally MEAs are fabricated with nanocellulose membranes and their fuel cell performance is investigated.

In Chapter 6, the main empirical results are summarized, the conclusions of this work are outlined, and the prospects for application of these novel materials are discussed. Finally, the planned future directions of this work are considered.

## Acknowledgement

At first, I would like to express my deepest gratitude to my professor and supervisor, *Professor Kazunari Sasaki*, for teaching and advising me in fuel cell technology and in writing this PhD thesis, as well as his continuous and extraordinary support in developing academic skills. I am glad and proud that I could enter his research group for doing my doctoral research.

Beside my professor, I would like to thank the members of the dissertation committee, *Professor Naotoshi Nakashima*, *Professor Akari Hayashi* and Associate Professor *Stephen M. Lyth* for their kind acceptance to act as co-examiner for my dissertation.

I am deepest grateful to *Associate Professor Stephen M. Lyth*, for guiding my research in the three years of study and teaching me how to conduct systematic and precise scientific work as well as scientific writing. Without his precious and persistent support my academic achievements and this thesis would not have been possible.

I am very grateful to *Professor Akari Hayashi* for her insightful comments and suggestions during the PEFC Seminars. Her constructive comments helped me to improve my scientific illustration and presentation skills. Additionally I am very thankful for her kind support on fuel cell-related questions.

I would like to thank *Dr. Masamichi Nishihara* for all his help and support during my study, especially for his guidance and help in chemical issues. His help in many administrative, device- or chemical-related issues at I<sup>2</sup>CNER disburdened the work of all foreign researchers in the fuel cell group there.

I would like to thank *Dr. Sean R. Bishop* and *Dr. Nicola H. Perry* for their extraordinary support and their insightful comments and suggestions on impedance spectroscopic issues. I have greatly benefited from collaborative work with them.

I thank my colleagues and friends in the Hydrogen Utilization Processes Laboratory and the International Institute for Carbon-Neutral Energy Research (I<sup>2</sup>CNER) for their assistance during my studies. Especially I want to thank *Dr. Jianfeng Liu* for her kind help and elaborate introduction into X-ray photoelectron spectroscopy, membrane electrode assembly preparation and fuel cell evaluation. Also special thanks to *Dr. Zhiyun Noda* for her kind advice and support on my experiments throughout my studies, and to

*Mr. Yoshinori Nagai* and *Mr. Takeshi Daio* for their kind help and instructions on scanning electron microscopy.

I would like to thank *Dr. Benjamin V. Cunning* for his kind support and explanations on Raman spectroscopy and material preparation, as well as *Associate Professor Shigenori Fujikawa* and *Dr. Roman Selyanchyn* for their extraordinary support and expertise on gas barrier measurements.

Special thanks to *Mrs. Ayumi Zaitso* for her continuing help in administrative duties.

I would like to thank the *International Institute for Carbon-Neutral Energy Research (I<sup>2</sup>CNER)* for employing me as super research assistant during my study, without I could not have afforded the doctoral course.

I would like to thank all the members of the *Kyushu University Rugby Football Club* for all the good and tough practice, celebrations and all the fun we had together; it helped me to relax from study and kept my mind open for new ideas.

Finally I want thank *my family* for their love and support. Especially I want to thank *my brother Markus*, who's taking care of my parents during my stay abroad.

Fukuoka, January 2016

Thomas Bayer

## Publications

1. Spray Deposition of Nafion Membranes for Fabrication of Electrode-Supported Polymer Electrolyte Membrane Fuel Cells; T. Bayer, K. Sasaki, S.M. Lyth; in preparation.
2. Tunable Mixed Ionic / Electronic Conductivity and Permittivity of Graphene Oxide Paper; T. Bayer, S. R. Bishop, N. H. Perry, K. Sasaki, S. M. Lyth; submitted.
3. High Temperature Proton Conduction in Nanocellulose Membranes: Paper Fuel Cells ; T. Bayer, R. Selyanchyn, B. V. Cunning, M. Nishihara, S. Fujikawa, K. Sasaki, S. M. Lyth; submitted.
4. Alkaline Anion Exchange Membranes based on KOH-treated Multilayer Graphene Oxide; T. Bayer, R. Selyanchyn, B. V. Cunning, T. Daio, M. Nishihara, S. Fujikawa, K. Sasaki, S. M. Lyth; Journal of membrane Science, in revision.
5. In-Situ ESEM and EELS Observation of Water Uptake and Ice Formation in Multilayer Graphene Oxide; T. Daio, T. Bayer, T. Ikuta, T. Nishiyama, K. Takahashi, Y. Takata, K. Sasaki, and S. M. Lyth; Scientific Reports, 5, 11807, 2015.
6. Graphene Oxide Membrane Fuel Cells: Utilizing of a New Class of Ionic Conductor; T. Bayer, S. R. Bishop, M. Nishihara, K. Sasaki and S. M. Lyth; ECS Transactions, Volume 64, Issue 3, p. 441-448, 2014.
7. Characterization of a graphene oxide membrane fuel cell; T. Bayer, S. R. Bishop, M. Nishihara, K. Sasaki and S. M. Lyth; Journal of Power Sources, Volume 272, p. 239-247, 2014.

## **Presentations**

1. ECS Fall Meeting 2015; Phoenix, USA (Lecture)
2. 2<sup>nd</sup> M.I.T.-Kyushu Workshop on Electrochemical Energy 2015; Fukuoka, Japan (Lecture)
3. ECS Conference on Electrochemical Energy Conversion & Storage with SOFC-XIV, 2015; Glasgow, Scotland (Lecture)
4. I<sup>2</sup>CNER Annual Symposium 2015; Fukuoka, Japan (Poster)
5. 1<sup>st</sup> M.I.T.-Kyushu Workshop on Electrochemical Energy 2014; Boston, USA (Lecture)
6. 55<sup>th</sup> Battery Symposium; Kyoto, Japan (Lecture)
7. ECS Fall Meeting 2014; Cancun, Mexico (Lecture)
8. 15<sup>th</sup> IUMRS-International Conference in Asia; Fukuoka, Japan (Lecture)
9. 第 51 回化学関連支部合同九州大会, 北九州市小倉 (Poster)
10. I<sup>2</sup>CNER Annual Symposium 2014; Fukuoka, Japan (Poster)
11. 49<sup>th</sup> I<sup>2</sup>CNER Institute Interest Seminar Series; Fukuoka, Japan (Lecture)
12. 第 50 回化学関連支部合同九州大会, 北九州市小倉 (Poster)

## **Patents**

1. Fuel Cell and Nanocellulose Membrane for use as Electrolyte Membrane;  
PCT/JP2015/140285 Japan Patent Office; Filed 14th July 2015.
2. Anion Exchange Membrane and Method for Manufacturing the Same;  
PCT/JP2015/001683 Japan Patent Office; Filed 24th March 2015.

# Contents

|   |       |
|---|-------|
| Abstract .....  | i     |
| Acknowledgement.....  | iii   |
| Publications .....  | v     |
| Presentations.....  | vi    |
| Patents .....   | vii   |
| Contents.....   | viii  |
| List of Figures .....   | xii   |
| List of Tables.....   | xviii |
| 1 Introduction.....   | 1     |
| 1.1 The Hydrogen Society .....                                    | 1     |
| 1.2 Fuel Cell - Definition and History .....                      | 2     |
| 1.3 Fuel Cell - Theory.....                                       | 5     |
| 1.4 Overview of Different Fuel Cell Types and Applications.....   | 9     |
| 1.5 Proton Exchange Membrane Fuel Cells .....                     | 11    |
| 1.5.1 Characteristics of Proton Exchange Membrane Fuel Cells..... | 11    |
| 1.5.2 Membrane Electrode Assembly .....                           | 12    |
| 1.5.2.1 Proton Exchange Membranes .....                           | 13    |
| 1.5.2.2 Electrocatalyst Layer .....                               | 16    |
| 1.5.2.3 Gas Diffusion Layer .....                                 | 17    |
| 1.5.3 Hardware for Fuel Cell Assembly.....                        | 18    |
| 1.5.3.1 Flow Field Plates .....                                   | 19    |
| 1.5.3.2 End Plates .....  | 20    |
| 1.6 Alkaline Fuel Cells .....                                     | 21    |
| 1.6.1 Characteristics of Alkaline Fuel Cells.....                 | 21    |
| 1.6.2 Components of Alkaline Fuel Cells .....                     | 23    |
| 1.6.2.1 Alkaline Anion Exchange Membranes.....                    | 23    |
| 1.6.2.2 Other Components of Alkaline Fuel Cells .....             | 24    |
| 1.7 Low Dimensional Proton Conductors .....                       | 25    |
| 1.7.1 Zeolites .....  | 28    |
| 1.7.2 Zirconium Phosphate Hydrate.....                            | 29    |
| 1.7.3 Clays.....  | 30    |
| 1.7.4 Beta-Alumina .....  | 30    |
| 1.8 Graphene Oxide.....   | 32    |

|        |   |    |
|--------|---|----|
| 1.8.1  | Introduction.....   | 32 |
| 1.8.2  | Graphene Oxide in Fuel Cells.....                                 | 36 |
| 1.9    | Nanocellulose.....  | 40 |
| 1.9.1  | Introduction.....   | 40 |
| 1.9.2  | Nanocellulose in Fuel Cells.....                                  | 43 |
| 1.10   | Objectives of this Study.....                                     | 45 |
|        | References.....   | 46 |
| 2      | Experimental.....   | 64 |
| 2.1    | Sample Preparation.....   | 64 |
| 2.1.1  | Graphene Oxide Membranes.....                                     | 64 |
| 2.1.2  | Nanocellulose Membranes.....                                      | 65 |
| 2.2    | Experimental Techniques for Material Characterization.....        | 66 |
| 2.2.1  | Scanning Electron Microscopy.....                                 | 66 |
| 2.2.2  | Laser Scanning Microscopy.....                                    | 67 |
| 2.2.3  | X-Ray Photoelectron Spectroscopy.....                             | 68 |
| 2.2.4  | X-Ray Diffraction.....  | 70 |
| 2.2.5  | Raman Spectroscopy.....   | 71 |
| 2.2.6  | Atomic Force Microscopy.....                                      | 72 |
| 2.2.7  | Thermogravimetric Analysis.....                                   | 73 |
| 2.2.8  | Ion Exchange Capacity Measurements.....                           | 75 |
| 2.2.9  | Water Uptake and Swelling Measurements.....                       | 75 |
| 2.2.10 | Gas Barrier Measurements.....                                     | 76 |
| 2.2.11 | Tensile Strength Testing.....                                     | 79 |
| 2.2.12 | Impedance Spectroscopy.....                                       | 80 |
| 2.3    | Membrane Electrode Assembly Fabrication and Characterization..... | 83 |
| 2.3.1  | Membrane Electrode Assembly Fabrication.....                      | 83 |
| 2.3.2  | Membrane Electrode Assembly Characterization.....                 | 84 |
|        | References.....   | 87 |
| 3      | Graphene Oxide Membrane Fuel Cells.....                           | 90 |
| 3.1    | Introduction and Motivation.....                                  | 90 |
| 3.2    | Sample Preparation and Nomenclature.....                          | 90 |
| 3.3    | General Material Characterization.....                            | 91 |
| 3.3.1  | Scanning Electron Microscopy.....                                 | 91 |
| 3.3.2  | Laser Microscopy and Surface Roughness.....                       | 93 |
| 3.3.3  | X-Ray Photoelectron Spectroscopy.....                             | 95 |

|       |  |     |
|-------|--|-----|
| 3.3.4 | Raman Spectroscopy .....   | 97  |
| 3.3.5 | X-Ray Diffraction .....  | 98  |
| 3.3.6 | Water Uptake and Swelling.....                                       | 99  |
| 3.3.7 | Tensile Strength Measurements .....                                  | 101 |
| 3.3.8 | Gas Barrier Properties .....   | 103 |
| 3.4   | Impedance Spectroscopy .....   | 105 |
| 3.4.1 | Electrical Conductivity.....   | 105 |
| 3.4.2 | Electron Blocking Measurements .....                                 | 110 |
| 3.4.3 | In-plane Proton Conductivity .....                                   | 114 |
| 3.4.4 | Capacitive Contributions.....  | 116 |
| 3.4.5 | Water Content Measurements .....                                     | 118 |
| 3.4.6 | Discussion: Electronic and Capacitive Behaviour of Graphene Oxide... | 120 |
| 3.5   | Membrane Electrode Assembly Characterization .....                   | 122 |
| 3.6   | Electrode-supported Fuel Cells: Sprayed Membranes .....              | 127 |
| 3.6.1 | Introduction .....   | 127 |
| 3.6.2 | Fabrication Method .....   | 128 |
| 3.6.3 | Characterization of Electrode-Supported GOMFC.....                   | 130 |
| 3.7   | Conclusions .....  | 134 |
|       | References .....   | 137 |
| 4     | Anion Exchange Graphene Oxide Membrane Fuel Cells.....               | 144 |
| 4.1   | Introduction and Motivation.....                                     | 144 |
| 4.2   | Sample Preparation and Nomenclature .....                            | 144 |
| 4.3   | General Material Characterization.....                               | 145 |
| 4.3.1 | Scanning Electron Microscopy .....                                   | 145 |
| 4.3.2 | X-Ray Photoelectron Microscopy.....                                  | 146 |
| 4.3.3 | X-Ray Diffraction .....  | 149 |
| 4.3.4 | Ion Exchange Capacity.....   | 149 |
| 4.3.5 | Water Uptake and Swelling.....                                       | 150 |
| 4.3.6 | Tensile Strength Measurements .....                                  | 151 |
| 4.3.7 | Thermogravimetric Analysis.....                                      | 152 |
| 4.3.8 | Gas Barrier Properties .....   | 154 |
| 4.4   | Impedance Spectroscopy .....   | 155 |
| 4.4.1 | Conductivity of GO <sub>KOH</sub> Membranes .....                    | 155 |
| 4.4.2 | Determination of Dominant Ionic Species .....                        | 158 |
| 4.5   | Membrane Electrode Assembly Characterization .....                   | 160 |

|       |   |     |
|-------|---|-----|
| 4.6   | Conclusions .....                                 | 163 |
|       | References .....                                  | 165 |
| 5     | Nanocellulose Fuel Cells .....                    | 168 |
| 5.1   | Introduction and Motivation .....                 | 168 |
| 5.2   | Sample Preparation and Nomenclature .....         | 168 |
| 5.3   | General Material Characterization.....            | 170 |
| 5.3.1 | Atomic Force Microscopy .....                     | 170 |
| 5.3.2 | X-Ray Photoelectron Spectroscopy .....            | 171 |
| 5.3.3 | Water Uptake and Swelling .....                   | 172 |
| 5.3.4 | Tensile Strength Measurements.....                | 174 |
| 5.3.5 | Gas Barrier Properties.....                       | 175 |
| 5.3.6 | Impedance Spectroscopy .....                      | 179 |
| 5.4   | Membrane Electrode Assembly Characterization..... | 182 |
| 5.5   | Conclusions .....                                 | 187 |
|       | References .....                                  | 190 |
| 6     | Conclusions and Future Work .....                 | 192 |
| 6.1   | Conclusions .....                                 | 192 |
| 6.2   | Future Work .....                                 | 198 |

## List of Figures

|   |    |
|---|----|
| Figure 1.1. Fuel cell history from the very first fuel cell (1842) to the stack of Toyota's fuel cell car FCHV (2004). a) Schematic of Grove's gas voltaic battery. <sup>16</sup> b) Bacon's alkaline fuel cell (5 kW) from the 1960. <sup>26</sup> c) Fuel Cell system of the Space Shuttle (12 kW). <sup>27</sup> d) Fuel cell stack of Toyota's FCHV (90 kW). .....  | 4  |
| Figure 1.2. Generations of fuel cell vehicles. a) The world's first fuel cell powered vehicle, an Allis-Chalmers tractor with a 15 kW AFC stack, in 1959. <sup>26</sup> b) General Motor's "Electrovan" with a 150 kW AFC stack, the world's first fuel cell powered passenger car in 1967. <sup>28</sup> c) Toyota FCV MIRAI with 114 kW PEMFC stack, first commercial fuel cell vehicle in the world, in 2014. .... | 5  |
| Figure 1.3. Schematic of the working principle of a hydrogen operated fuel cell with electrode reactions; the change in Gibbs free energy; and the resulting theoretical cell voltage. ....   | 6  |
| Figure 1.4. Representative polarization curve of a fuel cell, showing regions of different loss mechanisms. ....  | 8  |
| Figure 1.5. Schematic of a fuel cell stack. ....  | 9  |
| Figure 1.6. Schematic of different fuel cell technologies showing the differences in used fuel and ion flow direction. ....   | 10 |
| Figure 1.7. Schematic of the working principle of a polymer electrolyte membrane fuel cell (PEMFC) with electrode reactions, change in Gibbs free energy and the resulting theoretical cell voltage. ....   | 11 |
| Figure 1.8. Schematic of a membrane electrode assembly (MEA) of a PEMFC. ....   | 12 |
| Figure 1.9. Schematic representation of the Grotthuss mechanism and the vehicle mechanism for proton transport in PEMs. ....  | 16 |
| Figure 1.10. a) SEM image of carbon black. b) TEM image of Pt/CB. <sup>78</sup> .....   | 17 |
| Figure 1.11. Laser microscope (left, GDL surface) and SEM images (right, GDL cross-section) of two different gas diffusion layers: a-b) carbon paper made up of randomly orientated carbon fibers; and c-d) carbon paper coated with a microporous layer. ....  | 18 |
| Figure 1.12. a) Schematic of a single cell fuel cell structure. b-c) NEDO single cell holder. ....  | 19 |
| Figure 1.13. Flow field plate (graphite) with a PTFE gasket. ....   | 20 |
| Figure 1.14. End plate (stainless steel) with an additional current collector (brass). ....   | 21 |
| Figure 1.15. Schematic of the working principle of an alkaline fuel cell (AFC) with electrode reactions and the resulting theoretical cell voltage. ....  | 22 |
| Figure 1.16. a) Schematic of the regular, porous structure of a zeolite crystal (ZSM-5). <sup>145</sup> b) SEM image of ZSM-5 zeolite crystals. <sup>146</sup> .....  | 28 |

|   |    |
|---|----|
| Figure 1.17. a) Structure of $\alpha$ -zirconium phosphate. <sup>148</sup> b) SEM image of $\alpha$ -zirconium phosphate. <sup>149</sup> .....  | 29 |
| Figure 1.18. a) Structure of the clay material montmorillonite. <sup>148</sup> b) SEM image of montmorillonite clay. <sup>152</sup> .....   | 30 |
| Figure 1.19. a-b) Stacking structure with corresponding conduction planes of $\beta'$ -alumina (a) and $\beta''$ -alumina (b). <sup>155</sup> c) SEM image of polycrystalline $\beta''$ -alumina. <sup>156</sup> .....  | 31 |
| Figure 1.20. Structures of graphene (a) and graphene oxide (b). <sup>192</sup> TEM images of graphene oxide (c,d). .....  | 34 |
| Figure 1.21. Cellulose, the major constituent of the cell walls of plants.....  | 41 |
| Figure 1.22. Chemical structure of cellulose: a) naturally occurring cellulose; b) with carboxylic acid functional groups formed during the pulping process; c) with sulfate ester groups formed during acid hydrolysis. <sup>192</sup> .....   | 42 |
| Figure 2.1. a) Vacuum-filtration of graphene oxide (GO) dispersion. b-c) Free-standing and flexible GO membranes. ....  | 65 |
| Figure 2.2. a) CNF slurry (3.0 wt% solids). b) CNC slurry (11.8 wt% solids). c) Appearance of prepared CNF and CNC papers in comparison to regular printer paper (all similar thickness, $\sim 90 \mu\text{m}$ ).....   | 66 |
| Figure 2.3. a-b) Principle of scanning electron microscopy. c) Hitachi SEM S-5200. ..   | 67 |
| Figure 2.4. a) Principle of laser scanning microscopy. <sup>9</sup> b) Olympus LEXT 3d OLS 4000. ....   | 68 |
| Figure 2.5. a) Principle of X-ray photoelectron microscopy (XPS). <sup>17</sup> b) KRATOS Analytical ESCA-3400 c) PHI 5000 Versa Probe II. ....   | 69 |
| Figure 2.6. a) Principle of X-ray diffraction (XRD). b) Rigaku Smartlab X-ray Diffractometer.....   | 70 |
| Figure 2.7. a) Principle of Raman spectroscopy. b) RENISHAW inVia Raman Microscope.....   | 72 |
| Figure 2.8. a) Principle of atomic force microscopy. b) Microscope image of an SN-AF01 cantilever (SiN, $100\mu\text{m}$ height). c) Seiko Instruments scanning probe microscope unit SPA300HV with SPI 3800 N probe station. d) SPI 3800 N probe station with laser attachment and camera unit. .... | 73 |
| Figure 2.9. a) Schematic of a TGA Device. b) Rigaku Thermo plus EVO2 TG8121; c) internal balance beams with holders. ....   | 74 |
| Figure 2.10. Mettler Toledo analytic balance. b) Mitutoyo micrometer. ....  | 76 |
| Figure 2.11. Gas permeation measurement system: a) Schematic of the permeation cell; b) Schematic of the GTR-11A/31A gas permeation measurement system; c) Graphene   |    |

|   |     |
|---|-----|
| oxide membrane mounted in the system; d) Permeation cells of the gas permeability analyzer; e) Schematic of gas permeability analyzer GTR-11A/31A.....  | 78  |
| Figure 2.12. a) Hydraulic Testing Machine SHIMPO FGO-C-TV with 5 N force gauge. b) Dumbbell shape specimen cutter. ....   | 80  |
| Figure 2.13. a) Membrane test system MTS 740 (right) with Solartron impedance analyzer (left). b) Electrode setup of the MTS 740 for through-plane conductivity measurements with Pt-blocking electrodes. c) Electrode setup of the MTS 740 for in-plane conductivity measurements. d) Representative impedance spectra of GO membrane at 30°C and 100% RH showing measurement data and fitting curve with equivalent circuit. e) Schematic of the MTS 740 electrode setup for through-plane conductivity measurement with corresponding electrode/membrane interfaces and representative equivalent circuits. .... | 82  |
| Figure 2.14. a) General fabrication process of a membrane electrode assembly. b) Nordson K.K. Spraying Device. c) Sinto Digital Press CYPT-10.....  | 84  |
| Figure 2.15. a) Cell holder used in our laboratory. b) Potentiostat VersaSTAT 4 (Amtek). ....   | 86  |
| Figure 3.1. SEM images of a GO membrane. a-c) Upper side surface at different magnifications. d) Surface of the underside. e-f) Cross-section of a GO membrane at different magnifications showing the layered structure. ....  | 92  |
| Figure 3.2. Laser microscopy images of the GO membrane surface: a) 5x magnification; b) 100x magnification; c) 3D projection; and d) Colored 3D projection with height profile. ....  | 94  |
| Figure 3.3. a) XPS wide scan spectra of GO. b) Component analysis of the C 1s peak of GO. c) Component analysis of the O 1s peak of GO. ....  | 96  |
| Figure 3.4. Wide scan Raman spectra of GO and G <sub>G4</sub> . ....  | 98  |
| Figure 3.5. XRD patterns graphene (Grade 4), graphite and graphene oxide.....   | 99  |
| Figure 3.6. Water uptake (a) and swelling (b) of graphene oxide and Nafion.....   | 100 |
| Figure 3.7. Stress-strain curve of GO (a) and Nafion (b) membranes. The insets show an enlarged plot of low strain regions for both samples. ....   | 102 |
| Figure 3.8. Tensile strength (a) and strain until rupture (b) of GO and Nafion. ....  | 103 |
| Figure 3.9. Dependence of the hydrogen permeability on temperature for graphene oxide and Nafion. Dashed lines are linear fits of the measurement data. ....  | 104 |
| Figure 3.10. a) Impedance spectra for 29, 42 and 64 μm thick GO paper at 30°C and 100% RH. The diameter of the high frequency arc increases with increasing membrane thickness, confirming that it corresponds to conduction within the GO paper. b) Electrode setup of the membrane test system MTS 740 with corresponding electrode/membrane interfaces and representative equivalent circuits.....   | 107 |

|  |     |
|--|-----|
| Figure 3.11. a) GO membrane paper conductivity dependence on humidity at different temperatures. Measurements were performed using isothermal steps of high to low humidity with increasing temperature. b) Arrhenius plot of conductivity for 100 to 0% RH (with steps of 10% RH). Dashed lines are linear fits from which the slope yields the activation energy. c) Activation energy of conductivity and capacitance extracted from Arrhenius plots..... | 109 |
| Figure 3.12. a) Upper graph shows conductivity dependence on humidity at 120°C. The chamber was pressurized at 230 kPa total pressure. The inset image shows the membrane before and after measurement. The lower graph shows an Arrhenius plot obtained during a cool down process at 0% RH (120 to 30°C). b) Impedance spectra of GO at 120°C. Disappeared low frequency semi-circle indicates dominating electronic conductivity. ....                    | 110 |
| Figure 3.13. Equivalent circuits for (a) the non-blocking case, and (b) with the addition of Nafion “blocking” electrodes. These appear to be blocking by virtue of the large interfacial impedance for electronic incorporation into GO ( $Z_{int,i2}$ ) via water redox reactions. c-d) Impedance spectra of GO without (c) and with Nafion blocking layer (d) at 60°C and 50% RH.....   | 112 |
| Figure 3.14. a) Conductivity of GO with and without Nafion blocking layers, showing the prevalence of electronic conductivity at low humidity. b) Arrhenius plot of the GO membrane covered with Nafion blocking layers and activation energy. c) Electronic contribution to overall conductivity and ionic transference number in dependence on humidity. ....  | 113 |
| Figure 3.15. Conductivity and Arrhenius plot of the in-plane and through-plane conductivity of Nafion and graphene oxide at 100% RH. Dashed lines are linear fits from which the slope yields the activation energy. ....  | 115 |
| Figure 3.16. Proton transport in GO. Proton conduction modes in the interlayer water (bulk water) and transport along the oxygen groups on the surface. <sup>59</sup> .....  | 115 |
| Figure 3.17. a) Dependence of permittivity of GO on temperature and humidity. b) Arrhenius plot of permittivity for 100 to 10% RH (with steps of 10% RH). Activation energy for permittivity values is shown in Figure 3.11c. ....   | 117 |
| Figure 3.18. a) Water uptake of GO at different relative humidity reported in mass of water per mass of GO (left axis) and number of water molecules per GO unit cell ( $\lambda$ , right axis). b) Permittivity dependence on the number of water molecules per GO unit cell ( $\lambda$ ). ....  | 119 |
| Figure 3.19. a) Graphene oxide membrane fuel cell (GOMFC). b) Cross-section of the GOMFC shown in Image (a). c-d) Cross-section of a GOMFC showing the layered structure of the GO membrane.....   | 124 |
| Figure 3.20. Polarization curves and power density of the GOMFC at different temperatures: a) 30 to 50°C; and b) 60 to 80°C.....   | 125 |
| Figure 3.21. Polarization curves and power density for 16 and 50 $\mu\text{m}$ thick GOMFCs, and a 50.1 $\mu\text{m}$ thick Nafion-based PEMFC at 30°C. b) Durability measurement of a 50 $\mu\text{m}$ thick GOMFC with 2 mA load current at 30°C.....  | 126 |

|   |     |
|---|-----|
| Figure 3.22. Discoloration of the GO membrane after fuel cell operation. ....   | 126 |
| Figure 3.23. a-b) Fabrication process of electrolyte-supported (a) and electrode-supported (b) GOMFCs. c) Structure of the electrode-supported GOMFC. ....  | 129 |
| Figure 3.24. a) Schematic of the spray deposition of GO electrolyte onto the cathode-containing carbon paper (electrode), showing the increasing electrolyte thickness with several spraying steps. b) Fabrication of electrode-supported GOMFC. From left to right: After cathode preparation, after GO electrolyte deposition and after anode preparation. .... | 130 |
| Figure 3.25. a) Polarization curves and power density of electrolyte- and electrode supported GOMFCs in comparison to Nafion-based PEMFCs. b) Durability measurement of the electrode-supported GOMFC at 100 mA constant load current. c) Power density in dependence on electrolyte thickness showing the strong performance of electrode-supported GOMFCs. .... | 132 |
| Figure 3.26. SEM image of the cross-section (post-operation) showing the ultrathin GO electrolyte in comparison to the electrocatalyst layer. ....  | 133 |
| Figure 4.1. SEM images of multilayer (a,b) GO, and (c,d) GO <sub>KOH</sub> membranes.....   | 146 |
| Figure 4.2. XPS of multilayer GO and GO <sub>KOH</sub> membranes. a) Wide scan spectra; b) C 1s spectra with component analysis.....  | 147 |
| Figure 4.3. XPS of multilayer GO and GO <sub>KOH</sub> membranes. a) O 1s spectra with component analysis. b) K 2p spectra of the multilayer GO <sub>KOH</sub> membrane.....  | 148 |
| Figure 4.4. XRD spectra of GO and GO <sub>KOH</sub> . Increased interlayer spacing for GO <sub>KOH</sub> . ....   | 149 |
| Figure 4.5. Water uptake of GO and GO <sub>KOH</sub> .....  | 150 |
| Figure 4.6. Tensile strength (a) and strain until rupture (b) of GO and GO <sub>KOH</sub> .....   | 151 |
| Figure 4.7. a) TGA curves of GO (red) and GO <sub>KOH</sub> (blue). b) TGA and DTA curves of GO. c) TGA and DTA curves of GO <sub>KOH</sub> . ....  | 153 |
| Figure 4.8. Hydrogen permeance and permeability through GO and GO <sub>KOH</sub> membranes of different thickness at a temperature of 30°C.....   | 155 |
| Figure 4.9. a) Conductivity of a GO <sub>KOH</sub> membrane (37 μm thick) in dependence on humidity and temperature. b) Arrhenius plots showing activation energies at different relative humidity. c) Relationship between activation energy and relative humidity...  | 157 |
| Figure 4.10. a) Conductivity of GO <sub>KOH</sub> membranes with different blocking layers. b) Schematic of blocking layer measurements. c) Schematic of a possible reverse Grotthuss mechanism for OH <sup>-</sup> anion diffusion in GO <sub>KOH</sub> . ....   | 159 |
| Figure 4.11. a) Polarization curves and power densities of a GO <sub>KOH</sub> membrane fuel cell at 30°C and 95% RH, before and after durability measurements. b) Durability measurement with a 1 mA constant load current. ....   | 162 |

|  |     |
|--|-----|
| Figure 5.1. Photographs of: a) cellulose nanofiber (CNF) slurry; b) cellulose nanocrystal (CNC) slurry; c) (left to right) conventional cellulose-based paper, CNF paper, and CNC paper. d-e) Optical microscope images of CNF (d) and CNC (e) paper. ....   | 169 |
| Figure 5.2. AFM images of CNF (a,c) and CNC (b,d) paper. ....  | 170 |
| Figure 5.3. XPS spectra of cellulose nanofibers (CNF) and cellulose nanocrystals (CNC): a) wide scan spectra; and b) deconvoluted C 1s spectra. ....   | 172 |
| Figure 5.4. Water uptake (a) and swelling (b) of cellulose nanofiber (CNF) and Nafion. ....  | 173 |
| Figure 5.5. Membrane behaviour during water uptake measurements. a-c) CNF membrane at measurement start (a), after 5 min (b) and after 1 hour (c). d-f) CNC membrane at measurement start (d), after 5 min (e) and after 1 hour (f). ....  | 173 |
| Figure 5.6. Tensile strength (a) and strain until rupture (b) of cellulose nanofiber (CNF) and Nafion.....   | 175 |
| Figure 5.7. Dependence of the hydrogen permeability on temperature for cellulose nanofiber (CNF) and cellulose nanocrystal (CNC) membranes, in comparison to conventional polymer electrolyte membrane, Nafion <sup>®</sup> 212. Dashed lines are linear fits of the measurement data.....   | 177 |
| Figure 5.8. Comparison of hydrogen permeability of cellulose nanofiber (CNF) and cellulose nanocrystal (CNC) membranes with literature data for conventional cellulosic membranes (CA = cellulose acetate, EC = ethyl cellulose, SC = silylated derivatives of cellulose, BEC = butylcarbamate of EC, BCA = butylcarbamate of CA)..... | 178 |
| Figure 5.9. a) Dependence of proton conductivity on humidity for cellulose nanofiber (CNF) and cellulose nanocrystal (CNC) membranes at 30°C. b) Arrhenius plot at 100% RH with activation energies and proton conductivity. ....  | 181 |
| Figure 5.10. Schematic of possible proton conduction mechanisms and pathways in nanocellulose. <sup>26</sup> .....   | 181 |
| Figure 5.11. Photographs of MEAs prepared from: a) a cellulose nanofiber (CNF) membrane; and b) a cellulose nanocrystal (CNC) membrane. Post-operation SEM images of cross-sections of CNF (c) and CNC (d) nanocellulose fuel cells (NCFCs). ....  | 184 |
| Figure 5.12. a) Polarization curves and power densities of a nanocellulose fuel cell (NCFC) operated at 80°C and 95% RH incorporating a 32 µm thick CNF membrane. b) Cell voltage during durability measurements at constant load current of CNF-based NCFC. ....  | 185 |
| Figure 5.13. a) Polarization curves and power densities of a nanocellulose fuel cell (NCFC) operated at 80°C and 95% RH incorporating a 30 µm thick CNC membrane. b) Cell voltage during durability measurements at constant load current of CNC-based NCFC. ....  | 186 |

## List of Tables

|   |     |
|---|-----|
| Table 1.1. Overview of different fuel cell technologies. <sup>11,20,39</sup> .....  | 10  |
| Table 1.2. Overview of some low dimensional proton conductors.....  | 27  |
| Table 2.1. Properties of as-purchased GO dispersion. ....   | 64  |
| Table 2.2. Gas chromatograph operation parameter. ....  | 78  |
| Table 3.1. Position of Raman active bands, intensity ratio I(D)/I(G) and the full width at half maximum of the G peak FWHM (G). All units are in cm <sup>-1</sup> unless otherwise stated. .... | 98  |
| Table 3.2. Relative permittivity of GO paper at 100, 60 and 30% RH from 30 to 90°C. ....  | 117 |
| Table 3.3. Comparison of fuel cell membrane related properties of graphene oxide and Nafion®212.....  | 136 |
| Table 4.1. Comparison of fuel cell membrane related properties of alkaline treated graphene oxide and Tokuyama A 201 anion exchange membrane.....   | 164 |
| Table 5.1. Literature data of hydrogen permeability of various conventional cellulose membranes compared to the CNC and CNF nanocellulose membranes used in this study. ....                    | 178 |
| Table 5.2. Comparison of fuel cell membrane related properties of cellulose nanofibers (CNF), cellulose nanocrystals (CNC) and Nafion®212. ....   | 189 |
| Table 6.1. Fuel cell related properties of Nafion, graphene oxide, cellulose nanofibers (CNF) and cellulose nanocrystals (CNC).....   | 197 |

# 1 Introduction

## 1.1 The Hydrogen Society

Japan introduced a roadmap towards broad utilization of hydrogen as a major energy carrier, in order to become a hydrogen-based society. This long-term strategic roadmap ends in 2050 and is divided into three phases.<sup>1-3</sup>

Phase one is the commercialization of fuel cells and expansion of hydrogen usage, mostly based on fuel cell vehicles. Commercialization of FCVs started in December 2014 with the sale of Toyota's FCV MIRAI.<sup>4</sup> In 2020 the price for fueling a FCV should be comparable or even lower compared to fueling a hybrid car, and in 2025 the price for FCVs should be in the same range as for hybrid vehicles today.

Phase two is the establishment of mass supply of hydrogen gas, and the introduction of hydrogen power generation. Hydrogen will be imported from overseas and by the mid-2020s a price of 30 JPY per Nm<sup>3</sup> hydrogen should be achieved. A demonstration project for importing hydrogen from overseas is planned by Kawasaki Heavy Industries. Liquid hydrogen, produced from lignite in Australia, shall be transported to Japan using a special liquefied hydrogen transport ship.<sup>5</sup> Another possibility to produce and distribute decentralized hydrogen, as shown by Mitsubishi Kakoki Kaisha Ltd. in a sewage treatment plant in Fukuoka, Japan. They constructed and now operate the first hydrogen production plant using biogas from a sewage treatment plant, with a capacity of 65 FCV refills a day.<sup>6</sup> From 2030 hydrogen produced abroad from surplus energy shall be delivered to Japan.

Phase three is the establishment of a CO<sub>2</sub>-neutral hydrogen supply chain. This phase covers R&D and demonstration projects. Establishment of CO<sub>2</sub>-neutral hydrogen production using renewable energy is expected from 2040 (e.g. from wind energy in South America or hydroelectric power in North America).

Hydrogen related markets are expected to increase from approximately 1 trillion JPY in 2030 to 8 trillion JPY in 2050, with large potential for the economy of Japan.<sup>2</sup> Transforming to a hydrogen society will have many benefits for Japan. The high efficiency of fuel cells will lead to a huge energy conservation and thus reduce energy costs for companies and the public.<sup>2</sup> Using hydrogen as a major energy carrier will increase energy security, as it can be

produced from various sources; is a by-product of several processes; and it can be imported from countries with low geopolitical risk. If produced in Japan, the self-sufficiency rate of Japan will be increased and Japan may become fully independent from overseas energy imports in the future.<sup>2</sup> Hydrogen powered fuel cells do not emit harmful exhaust gases such as e.g. CO<sub>2</sub>, leading to a reduction of greenhouse gases and environmental burdens. Even completely CO<sub>2</sub>-neutral hydrogen production could be achieved, if enough renewable energy resources are available.<sup>2</sup> The economy of Japan is strongly dependent on exports, and their previous major industries (e.g. consumer electronics) are struggling due to strong competition from Korea and China. However Japan is leading the world in fuel cell technology and development, having a strong global competitiveness shown by the large amount of patents held.<sup>2</sup> This technological knowhow will preserve existing jobs, create new jobs, and help to strengthen Japan's economy. Additionally, hydrogen production in Japan by renewable energy could help to develop the economy in rural areas with less industry, and could potentially help prevent rural depopulation.

Sales of the Toyota FCV MIRAI have officially started. The Tokyo Olympics in 2020 is a huge chance for Japan to show the world their achievements towards becoming a hydrogen-fueled society. However there are many obstacles to be overcome, and many of these are related to the most important component of the hydrogen society; namely, an electrochemical device that converts the chemical energy of hydrogen into electric energy. This is the fuel cell.

In the following chapters, the definition, history, theory, and general overview of fuel cell types and operation principles will be explained in detail. In particular the two kinds of fuel cell used in this work will be focused upon.

## **1.2 Fuel Cell - Definition and History**

A fuel cell is an electrochemical device that converts the chemical energy of a fuel directly and continuously into electrical energy, as long as the reactants are supplied to the cell and the products are removed.<sup>7-9</sup> An important difference compared to regular batteries is that the reactants are not stored inside the fuel cell but are supplied from outside the cell.<sup>9</sup> Fuel cells offers several advantages compared to other power generators, such as high efficiency,

pollution-free operation (when operated with hydrogen), low noise and low maintenance due to reduced numbers of moving parts.<sup>10,11</sup>

The history of the fuel cell started about 170 years ago. The German scientist Christian Friedrich Schönbein discovered the fuel cell effect (current produced by the combination of hydrogen and oxygen) and described it in 1839.<sup>8,12–15</sup> Based on Schönbein's work the Englishman Sir William Grove invented his "gas voltaic battery", basically the first working fuel cell (Figure 1.1a), in 1842.<sup>8,14–16</sup> Nearly 100 years later, in 1932, Francis Thomas Bacon developed the precursor of the alkaline fuel cell at Cambridge University, based on the work Ludwig Mond and Charles Langer, and in 1959 his "Bacon cell", the world first alkaline fuel cell was patented (Figure 1.1b).<sup>8,15,17</sup> Also at the end of the 1950s the first proton exchange membrane fuel cells were developed at General Electric and with the development of the proton exchange membrane Nafion<sup>®</sup> (E.I. DuPont de Nemours & Co.) this fuel cell type became one of the most used in a wide area of applications.<sup>8,14</sup> In 1959, the world's first fuel cell powered vehicle was presented by the U.S. machinery manufacturer Allis-Chalmers. They built a fuel cell powered tractor based on Bacon's alkaline fuel cell with a 15 kW stack, capable of pulling ~1.5 tons of weight (Figure 1.2a).<sup>18</sup> In 1967 General Motors unveiled their "Electrovan", a 1966 GMC Handivan powered by a 150 kW alkaline fuel cell system and fueled with liquid hydrogen and pure oxygen (Figure 1.2b). The world's first fuel cell passenger car achieved a maximum speed of 105 km/h and a cruising range of 200 km.<sup>18,19</sup> NASA used fuel cells from 1965 in their Gemini and Apollo missions and an alkaline fuel cell system was used on the Space Shuttles until they were taken out of service in 2011 (Figure 1.1c).<sup>8,14,15,20,21</sup> For other applications the use of fuel cells was still too expensive. With the oil crises in the mid-70s and an increasing environmental awareness, the interest in new energy sources increased and the application of fuel cells in other fields than space applications (e.g. automobile application were investigated).<sup>8,14</sup> First large-scale commercial application of fuel cells were micro combined heat and power plants. Most successful are the ENE-Farm systems in Japan, from companies such as Toshiba, Panasonic, JX Nippon Oil or Aisin.<sup>22</sup> Those systems contain PEMFC or SOFC stacks and have a power output of ~700 W while reaching overall efficiencies of  $\leq 95\%$ , with durabilities of over 60,000 hours.<sup>22</sup> The demonstration project and customer testing of ENE-Farm fuel cell systems started in 2005, leading to their commercialization in 2009.<sup>23</sup> Their sales numbers increased from ~3000

units/year to ~29,000 units/year in 2014, and in September 2014 more than 100,000 units had been sold and installed in Japan in total.<sup>23</sup> In 2009 with the Antares DLR-H2 the first fuel cell powered aircraft performed start, flight and landing using only fuel cell power, showing the suitability of fuel cell systems also for civil aviation.<sup>24</sup> In December 2014, over 170 years after Grove's first fuel cell, Toyota Motor Corporation started after many years of fuel cell development and on-road testing (Figure 1.1d) the commercial sale of their fuel cell vehicle the FCV MIRAI (Figure 1.2c).<sup>4</sup> Over one thousand pre-orders and the upcoming sales start of the FCV MIRAI in US and Europe induced Toyota to increase the production numbers of the FVC MIRAI from 700 in 2015 to 3,000 cars in 2017.<sup>25</sup> It seems that the start of Japan becoming a hydrogen society has been successful. Could this be the road towards a global hydrogen society?

In the following chapter, the theory and operation principles of fuel cells will be explained.

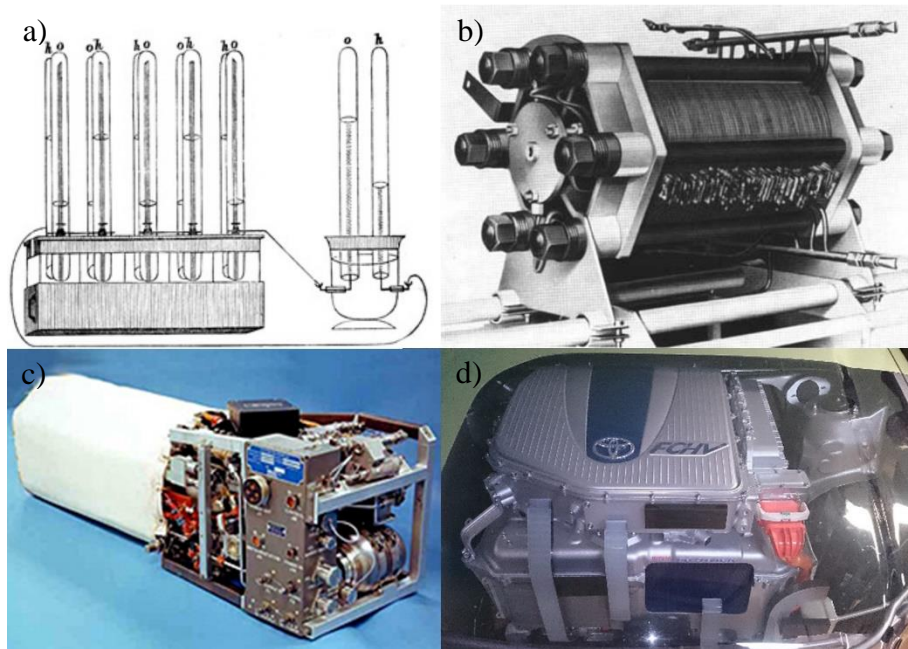


*Figure 1.1. Fuel cell history from the very first fuel cell (1842) to the stack of Toyota's fuel cell car FCHV (2004). a) Schematic of Grove's gas voltaic battery.<sup>16</sup> b) Bacon's alkaline fuel cell (5 kW) from the 1960.<sup>26</sup> c) Fuel Cell system of the Space Shuttle (12 kW).<sup>27</sup> d) Fuel cell stack of Toyota's FCHV (90 kW).*



*Figure 1.2. Generations of fuel cell vehicles. a) The world’s first fuel cell powered vehicle, an Allis-Chalmers tractor with a 15 kW AFC stack, in 1959.<sup>26</sup> b) General Motor’s “Electrovan” with a 150 kW AFC stack, the world’s first fuel cell powered passenger car in 1967.<sup>28</sup> c) Toyota FCV MIRAI with 114 kW PEMFC stack, first commercial fuel cell vehicle in the world, in 2014.*

### **1.3 Fuel Cell - Theory**

Heart of a fuel cell is the so-called membrane electrode assembly (MEA). This consists of two electrodes containing electrocatalyst layers, separated by an electrolyte, as schematically shown in Figure 1.3. Electrochemical reactions take place at the electrodes, while the electrolyte has the task to reliably separate the reactants from each other, and to conduct specific ions. The hydrogen-oxygen reaction is a common example to explain the chemical and thermodynamic reaction in fuel cells and the fuel cell principle is schematically shown in Figure 1.3.<sup>7–9,29–32</sup> Hydrogen is supplied to the anode where it is electrochemically oxidized via the hydrogen oxidation reaction (HOR). The released electrons flow around an external electric circuit and the protons diffuse through the proton-conducting electrolyte to the

cathode. Oxygen (usually air) is supplied to the cathode. Oxygen is electrochemically reduced via the oxygen reduction reaction (ORR) by taking up electrons coming from the anode via the external circuit and recombine with the protons diffusing through the electrolyte, to form water. The reactions occur with corresponding change of Gibbs free energy,  $\Delta G$ , and the resulting electromotive force (EMF), or reversible open circuit voltage,  $E_0$ , can be seen in Figure 1.3.

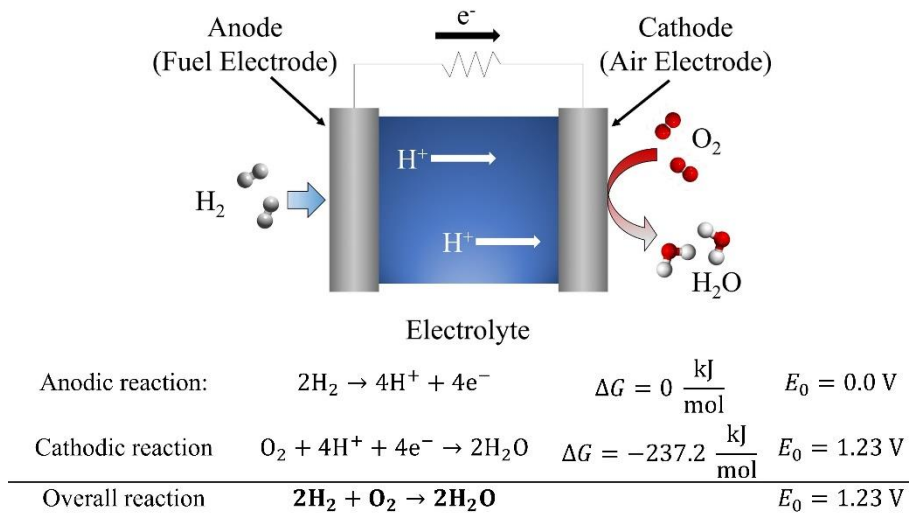


Figure 1.3. Schematic of the working principle of a hydrogen operated fuel cell with electrode reactions; the change in Gibbs free energy; and the resulting theoretical cell voltage.

The theoretical electrical work done by a fuel cell is equal to the change in  $\Delta G$  during the reaction, and the EMF (i.e.  $E_0$ ) and can be calculated by:

$$E_0 = -\frac{\Delta G}{z \cdot F} \quad (1.1)$$

where  $z$  is the number of electrons released by the HOR and  $F$  is the Faraday constant (96,485 C/mol).<sup>7,9,29–32</sup> The EMF for the hydrogen-oxygen reaction is  $\sim 1.23 \text{ V}$ .

The Nernst equation describes the thermodynamic reaction in fuel cells (considering changes in  $\Delta G$  with temperature, reactant pressure and concentration) and can be used to calculate the reversible cell voltage,  $E$ , of a fuel cell:<sup>8,9,11,30</sup>

$$E = E_0 + \frac{R \cdot T}{z \cdot F} \cdot \ln\left(\frac{p_{H_2} \cdot p_{O_2}^{1/2}}{p_{H_2O}}\right) \quad (1.2)$$

with maximum EMF at standard pressure (1 bar) and temperature,  $T$ , (K), gas constant  $R$  (8.314 J K<sup>-1</sup> mol<sup>-1</sup>), and partial pressure,  $p$ , of the gases (reactants and product). The calculated EMF, also known as the Nernst voltage, is the theoretical reversible voltage at any particular temperature and pressure.

Figure 1.4 is a representation of a typical polarization curve of a fuel cell. The open circuit voltage is lower than the theoretical value due to hydrogen crossover, and electrical short circuit current.<sup>11,33–35</sup> The hydrogen cross-over causes a mixed cathode potential due to the formation of a half-cell electrochemical reaction ( $H_2 \leftrightarrow 2H^+ + 2e^-$ ), which is mainly responsible for the large voltage drop. Additional hydrogen reacts directly with oxygen, leading to a reduced O<sub>2</sub> surface concentration and thus lower oxygen partial pressure.<sup>33</sup> The OCV generally decreases with increasing temperature, mainly due to the drop of partial pressure of the reactants.<sup>9,33</sup> When load is applied, the cell voltage drops due to other additional losses, also termed as overvoltage (or overpotential), as can be seen in Figure 1.4. At low current densities the cell voltage drops rapidly and non-linearly, due to activation losses caused by slow electrode kinetics, especially for the ORR.<sup>11,35,36</sup> The activation losses are lower at higher operation temperature, because the reactants have a higher possibility to overcome the necessary activation energy due to higher thermal activity.<sup>36</sup> At intermediate current density, the cell voltage decreases linearly and with lower gradient, due to losses in the electrolyte and electrodes. The voltage drop in this area arises mainly from the electrolyte resistance but also the contact resistance and interfacial resistances between e.g. the electrolyte and the electrocatalyst layer, as well as a minor contribution from the resistance of the electronically conductive components such as the catalyst-support, gas diffusion layer (GDL), and bipolar plates.<sup>11,35–37</sup> At very high current density, the cell voltage drops quickly, caused by limitations in mass transport of reactants at the electrode surface.<sup>11,35,36</sup> At high current densities the reactant consumption is very high and their concentration will drop if

not supplied at a sufficient rate. This concentration decrease reduces the reversible cell voltage (via the Nernst equation), as well as increasing the activation losses.<sup>36</sup>

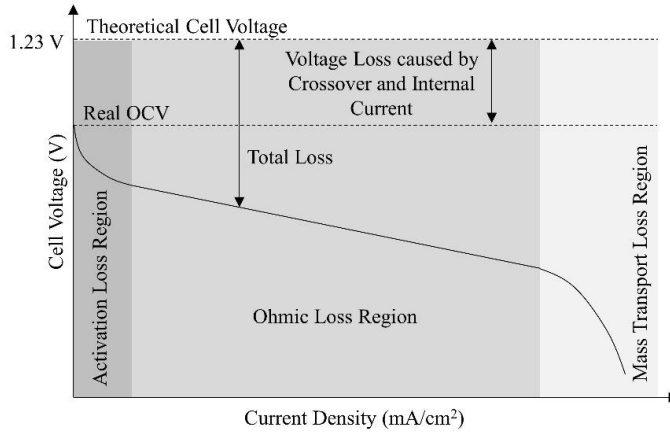


Figure 1.4. Representative polarization curve of a fuel cell, showing regions of different loss mechanisms.

The maximum thermodynamic efficiency of fuel cells is defined as the ratio of Gibbs free energy  $\Delta G$  (the product of temperature  $T$  and entropy,  $\Delta S$ ) and the enthalpy of the reaction,  $\Delta H$ :<sup>7,9,11</sup>

$$\eta = \frac{\Delta G}{\Delta H} \cdot 100\% \quad (1.3)$$

Compared to heat engines, the fuel cell efficiency decreases with increasing operation temperature.<sup>8,11</sup> The highest theoretical efficiency (83%) is obtained when pure hydrogen is reacted with pure oxygen, forming liquid water.<sup>11</sup> Fuel cells achieve electric efficiencies between ~50 and 70%. Compared with large conventional heat engines, even small fuel cells achieve relatively high fuel efficiencies.<sup>7,38</sup>

As the aforementioned efficiency is only a theoretic value, it is more practical to calculate the actual cell efficiency ( $\eta_{cell}$ ), by dividing the cell voltage ( $U_{cell}$ ) by the reversible open circuit voltage ( $E_0$ ):<sup>11</sup>

$$\eta_{cell} = \frac{U_{cell}}{E_0} \cdot 100\% \quad (1.4)$$

In order to increase the useful voltage and power of a fuel cell, single MEAs are usually connected in series to form so-called fuel cell stacks, by using bipolar plates, as schematically shown in Figure 1.5.<sup>8,9,11</sup> The MEA and the bipolar plates form repeat units and the stack is terminated by single flow field and end plates. The flow field, bipolar plates, and end plates are described in more detail in Chapter 1.5.3.

In the next chapter, an overview of the different fuel cell types containing more information on e.g. electrolyte materials and operation temperature will be given.

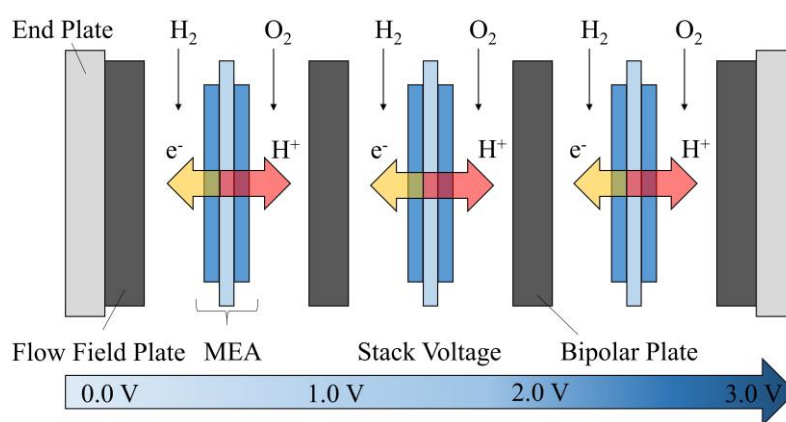


Figure 1.5. Schematic of a fuel cell stack.

## 1.4 Overview of Different Fuel Cell Types and Applications

Fuel cells are commonly named after their electrolyte material, and can be divided into low temperature and high temperature varieties.<sup>8,11,20</sup>

Table 1.1 gives an overview over the different fuel cell types. Figure 1.6 shows the different fuel cell technologies regarding their difference in fuel, water production and ion flow direction. In this work, polymer electrolyte membrane fuel cells (PEMFCs) and alkaline fuel cells (AFCs) are investigated, and therefore these two fuel cell types will be explained in more detail in Chapter 0 and 1.6. In the next chapter the most popular type of fuel cell, the PEMFC will be explained in more detail.

Table 1.1. Overview of different fuel cell technologies.<sup>11,20,39</sup>

| Type                                       | Electrolyte  | Operation Temperature (°C) | Mobile Ion                    | Electrical Efficiency (%) | Fuel                     | Primary applications                                    |
|--|--|----------------------------|-------------------------------|---------------------------|--------------------------|---|
| Alkaline Fuel Cell (AFC)                   | Potassium hydroxide solution (35-50% KOH), or anion exchange membranes | 50 - 200                   | OH <sup>-</sup>               | 50 - 60                   | Hydrogen                 | Spacecraft and military applications                    |
| Proton Exchange Membrane Fuel Cell (PEMFC) | Proton exchange membranes (polymer)                                    | 30 - 100                   | H <sup>+</sup>                | 50 - 60                   | Hydrogen                 | Transportation, stationary, portable devices, submarine |
| Direct Methanol Fuel Cell (DMFC)           | Proton proton exchange membranes (polymer)                             | 20 - 90                    | H <sup>+</sup>                | ~25                       | Methanol                 | Portable power supply and devices                       |
| Phosphoric Acid Fuel Cell (PAFC)           | Concentrated phosphoric acid   | ~220                       | H <sup>+</sup>                | 37 - 55                   | Hydrogen                 | Stationary  |
| Molten Carbonate Fuel Cell (MCFC)          | Carbonate salt mixture   | ~650                       | CO <sub>3</sub> <sup>2-</sup> | 45 - 60                   | Hydrogen or hydrocarbons | Stationary  |
| Solid Oxide Fuel Cell (SOFC)               | Solid ceramics e.g. yttria stabilized zirconia                         | 600 - 1000                 | O <sup>2-</sup>               | 45 - 65                   | Hydrogen or hydrocarbons | Stationary  |

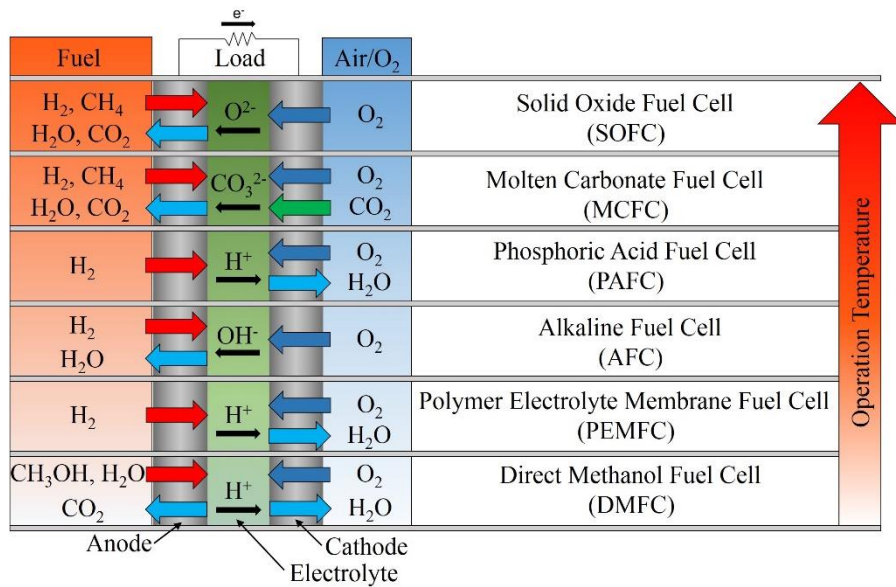


Figure 1.6. Schematic of different fuel cell technologies showing the differences in used fuel and ion flow direction.

## 1.5 Proton Exchange Membrane Fuel Cells

### 1.5.1 Characteristics of Proton Exchange Membrane Fuel Cells

Figure 1.7 shows the principle of a polymer electrolyte membrane fuel cell (PEMFC) with the corresponding electrode reactions. The MEA consists out of two electrodes coated with an electrocatalyst, separated by a proton conducting electrolyte membrane e.g. Nafion<sup>®</sup>. Hydrogen is supplied as the fuel to the anode and at the cathode air or pure oxygen is supplied. At the anode, hydrogen is catalytically split, releasing protons (H<sup>+</sup>) and electrons (HOR). The protons permeate through the electrolyte and the electrons flow via an external electric circuit with load to the cathode. There the oxygen reacts with the electrons and the protons forming water (ORR). The reactions at the electrodes and the overall reaction are shown in Figure 1.7.

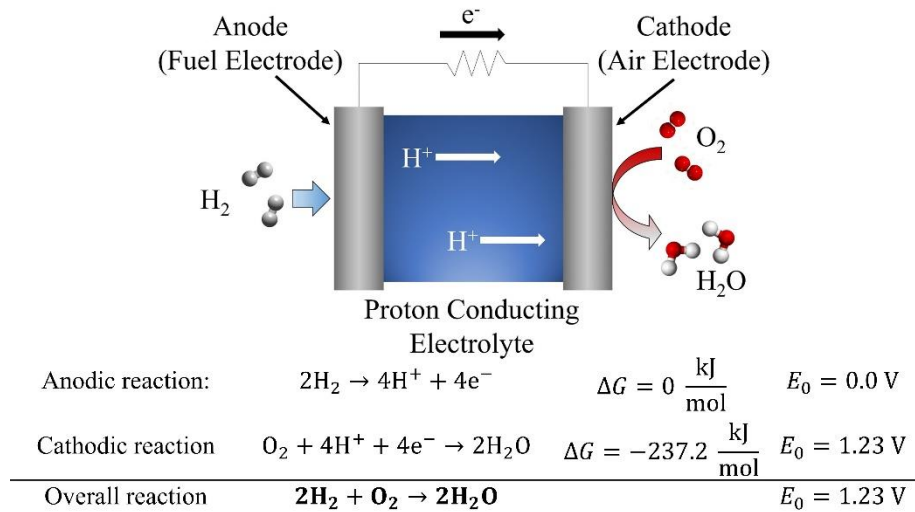


Figure 1.7. Schematic of the working principle of a polymer electrolyte membrane fuel cell (PEMFC) with electrode reactions, change in Gibbs free energy and the resulting theoretical cell voltage.

Currently PEMFCs are one of the most commercially viable fuel cell options and most car manufactures are focusing on PEMFC development, due to the high power density (300-1000 mW/cm<sup>2</sup>), low operation temperature (80 to 100°C), fast start-up (cold-start capability), cycling stability, quick load response and long operation time.<sup>7-9,20</sup>

However PEMFCs have several disadvantages. They are expensive due to the usage of platinum (Pt) as an electrocatalyst, which is necessary due to the relatively low operation

temperature and resulting sluggish cathode kinetics. For example, for an 86 kW PEMFC stack, approximately 50% of the total cost is from the electrocatalyst.<sup>7</sup> Other components such as the proton conducting membrane and the bipolar plates are also expensive.<sup>9,40,41</sup> An operation related problem is water management in PEMFCs, since the proton conductivity of the electrolyte (and thereby the cell performance) strongly depends on adequate humidification. Thus PEMFC systems require active water management.<sup>7,9</sup> Another electrocatalyst related problem is the high sensitivity of Pt to CO poisoning, leading to reduced catalytic activity.<sup>9,20</sup>

In short, the high cost and susceptibility of the Pt electrocatalyst to CO poisoning, are still barriers to wide-spread commercialization of PEMFCs.<sup>42-45</sup> Currently the main commercial application of PEMFCs is in stationary residential combined heat and power fuel cell systems (e.g. Enefarm, Japan), and in fuel cell vehicles (e.g. Toyota FCV MIRAI, Japan).

The following chapters will explain in more detail the components of the membrane electrode assembly and especially the most widely used PEMFC membrane, Nafion<sup>®</sup>.

### 1.5.2 Membrane Electrode Assembly

As mentioned in Chapter 1.5.1, the membrane electrode assembly (MEA) of a PEMFC consists of two electrodes equipped with an electrocatalyst-coated gas diffusion layer, and a proton conducting membrane, as schematically shown in Figure 1.8. In the following chapters properties and function of proton exchange membranes (PEMs), electrocatalysts, and gas diffusion layers (GDLs) will be explained in more detail.

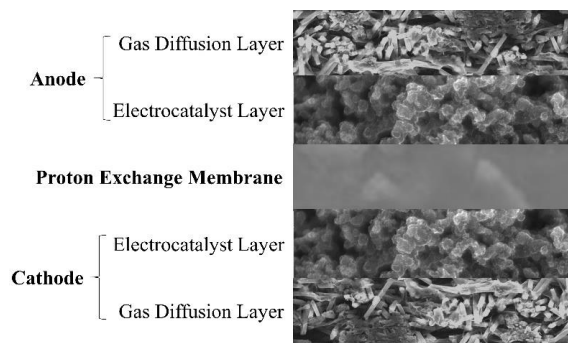


Figure 1.8. Schematic of a membrane electrode assembly (MEA) of a PEMFC.

### 1.5.2.1 Proton Exchange Membranes

The electrolyte is a central part of the fuel cell, and a bottleneck in achieving high performance. Requirements that have to be fulfilled by any electrolyte material are:<sup>7-10</sup>

- High ionic conductivity
- Low electronic conductivity
- Low fuel cross-over (hydrogen)
- Chemical stability in the harsh fuel cell environment
- Sufficient mechanical strength
- Simple fabrication (low cost)
- Ecological compatible

Some of the requirements are easier to fulfill than others. In particular, the requirement of chemical stability in the harsh environment of a fuel cell is very challenging.<sup>9</sup> Additional aspects are low cost and ecologically compatible fabrications, especially in view of commercialization.

Proton exchange membranes (PEM) are permeable to cations but reject anions, due to negatively charged groups, e.g.  $\text{PO}_3^{2-}$  and  $\text{SO}_3^-$ , which are attached to the membranes backbone.<sup>10,46</sup> There are various commercially available proton conducting membranes such as Nafion<sup>®</sup> (E.I. DuPont de Nemours & Co., Inc.), Flemion<sup>™</sup> (Asahi Glass, Japan), Neosepta-F<sup>™</sup> (Tokuyama, Japan) and Aciplex<sup>™</sup> (Asahi Kasei Chemicals Corporation, Japan).<sup>44,47</sup> In particular, they are a fundamental component in PEMFCs, providing mechanical support, sufficient gas barrier, an electron barrier, and high through-plane ionic conductivity.<sup>41,48</sup> Nafion<sup>®</sup> is a perfluorinated ionomer membrane consisting of a fluorinated carbon backbone with perfluoro-side chains, terminating in sulfonic acid groups (it is a registered trademark of E.I. DuPont de Nemours). This is by far the most-used membrane in PEMFCs, due to high proton conductivity ( $> 0.1 \text{ S/cm}$ ), good mechanical properties and excellent chemical stability and durability.<sup>8,41,44,49</sup>

However, also Nafion has several demerits, and therefore the search for alternative electrolyte materials is highly active. A major issue is that the proton conductivity strongly relies on adequate humidification. Dehydration decreases the conductivity, whilst the

changing water content also leads to membrane shrinkage and swelling, in turn leading to deterioration of the electrolyte-electrocatalyst interface.<sup>44,50,51</sup> Additionally, at higher operation temperatures, the mechanical stability of Nafion is reduced due to the low glass transition temperature ( $\sim 110^\circ\text{C}$ ).<sup>52-55</sup> Another temperature-related disadvantage is the increase of fuel cross-over with increasing operation temperature. Fuel cross-over is the movement of fuel from the anode through the membrane to the cathode where it is oxidized, leading to mixed potential at the cathode, resulting in loss of performance and efficiency.<sup>56-58</sup> Furthermore cross-over leads to peroxide radical production at the cathode, and associated catalyst-layer and membrane degradation.<sup>58</sup> The direct reaction of hydrogen and oxygen can also lead to hotspots in the MEA, resulting in pinhole formation in the membrane, destroying gas-tightness, and creating safety problems.<sup>58</sup> Fuel cross-over increases with operation temperature, leading to a conflict.<sup>57</sup> On the one hand, higher temperature is desired in order to facilitate proton conduction and reaction kinetics (in which situation the expensive electrocatalyst could be replaced with non-precious catalysts). On the other hand, fuel cross-over should be kept low for maintaining high efficiency and durability. Finally, the cost of Nafion is still far higher than the targets set by the U.S. Department of Energy (DOE) of  $\sim 20$   $\$/\text{m}^2$ , and the high cost of Nafion is not expected to change, due to the strict reaction conditions and the use of fluorine in the production process.<sup>41,59</sup>

The DOE has set several technical targets for fuel cell membranes in transport applications by 2020 (e.g.  $120^\circ\text{C}$  operation temperature, area-specific proton resistance of  $0.02 \Omega \text{ cm}^2$ , hydrogen and oxygen cross-over of  $2 \text{ mA}/\text{cm}^2$ ).<sup>59</sup> These targets focus on a new generation of PEMFCs, i.e. so-called high temperature polymer electrolyte membrane fuel cells (HT-PEMFCs) in which the operation temperature is between  $100$  to  $200^\circ\text{C}$ .<sup>60</sup> HT-PEMFCs offer several advantages compared with regular PEMFCs, as the reaction kinetics are accelerated, allowing the use of non-precious catalysts. Higher CO tolerance allows the use of reformed fuel. Additionally, system simplification is possible, since active water management is not required at above boiling point.<sup>7,60</sup> However elevated operation temperature exacerbates the aforementioned temperature-related disadvantages of Nafion. Therefore, for next generation fuel cells, new membrane materials are needed, which maintain sufficient proton conductivity, mechanical stability and durability at high temperature and low humidity. Several attempts have been made to find a suitable alternative electrolyte to replace or at least

compete with Nafion. Good reviews on recent developments and methods in this field have been written by Zhang and Shen,<sup>61</sup> and by Peighambardoust et al.<sup>44</sup> Promising materials are polybenzimidazole (PBI), and sulfonated polyether ether ketone (SPEEK). These have sufficiently high proton conductivity and their temperature stability up to 400°C.<sup>44,60,61</sup> The great value of Nafion as electrolyte in PEMFC applications is that it outperforms nearly all other electrolyte materials in a total sum of fuel cell electrolyte requirements mentioned at the beginning of this chapter, especially in terms of conductivity, mechanical stability and durability. For this reason, and maybe also due to the fact that nearly all car manufactures are focused on Nafion-based fuel cell vehicles, is Nafion still the most used membrane in PEMFCs today.

In Nafion, two types of proton conduction contributions have been identified; one inside the pores similar to conduction in bulk water, and the other near the surface of the pores, hopping along  $\text{SO}_3^-$  groups (with higher activation energy).<sup>62</sup> Surface protons are not transported directly between  $\text{SO}_3^-$  groups due to the relatively large distance, therefore a single  $\text{H}_3\text{O}^+$  ion is required to act as a bridge. This can be denoted as a carrier-mediated Grotthuss mechanism.<sup>62,63</sup>

Two basic transport mechanisms are responsible for proton transport in the bulk-like water, depending on the hydration level of the electrolyte: proton hopping (i.e. the Grotthuss mechanism);<sup>64,65</sup> and the vehicle mechanism (i.e. *en masse* movement of ions),<sup>66,67</sup> schematically shown Figure 1.9. In the Grotthuss mechanism, protons hop between water molecules via formation and cleavage of hydrogen bonds. The rate-limiting step is the cleavage of hydrogen bonds, with an activation energy of about 0.11 eV.<sup>65</sup> The Grotthuss mechanism dominates at high water content (where sufficient water pathways result in a bulk-like state) and is much faster than the vehicle mechanism.<sup>68-70</sup> For Nafion, in which the Grotthuss mechanism is dominant at high humidification, the activation energy for proton transport is between 0.05 and 0.15 eV.<sup>51,65,69-72</sup>

In the vehicle mechanism, protons “piggyback” on a diffusing water molecule (e.g. as  $\text{H}_3\text{O}^+$ ), and net transport of protons occurs via a counter diffusion of unprotonated water molecules.<sup>66,67,73</sup> At low water content and elevated temperature this is the dominating

transport process.<sup>67,74,75</sup> The vehicle mechanism has higher activation energy compared to the Grotthuss mechanism (i.e. 0.5 to 0.9 eV).<sup>76,77</sup>

In the next chapter the other two components of the MEAs (the electrocatalyst layer and the GDL) will be briefly explained.

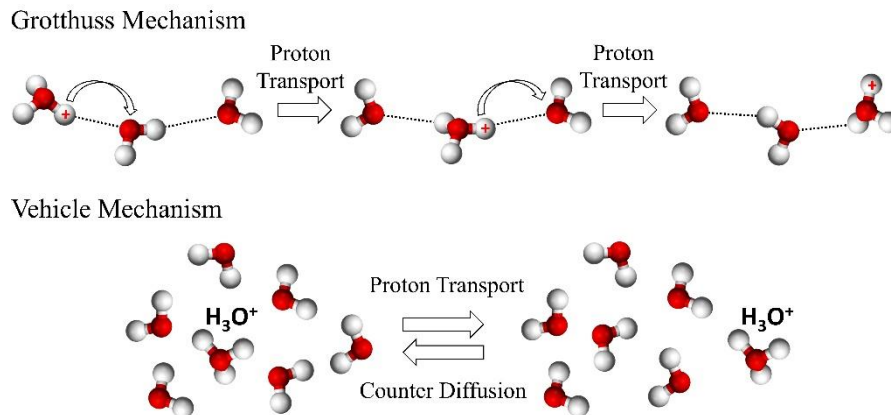


Figure 1.9. Schematic representation of the Grotthuss mechanism and the vehicle mechanism for proton transport in PEMs.

### 1.5.2.2 Electrocatalyst Layer

The electrocatalyst layer is where the chemical reactions in the fuel cell occur. The hydrogen oxidation reaction (HOR) occurs at anode and the oxygen reduction reaction (ORR) occurs at the cathode, as described in Chapter 1.5.1.<sup>7,9</sup> The requirements of the electrocatalyst layer are: high catalytic activity; large surface area; both electric and ionic conductivity; high stability; and resistance to poisoning.<sup>9,40</sup>

A commonly used catalyst in PEMFCs is platinum (Pt).<sup>7,9,11,40</sup> The amount of Pt used in fuel cells has decreased over the years, from ~10 mg<sub>Pt</sub>/cm<sup>2</sup> in the 1960s, to ~0.2 mg<sub>Pt</sub>/cm<sup>2</sup> in recent years.<sup>11</sup> Today, commercial PEMFCs with power densities of 500 to 700 mW/cm<sup>2</sup> contain about 0.2 to 0.4 mg<sub>Pt</sub>/cm<sup>2</sup> of electrode area.<sup>7</sup> Platinum catalyst is still responsible for about 50% of the total fuel cell stack cost, and therefore a lot of research is being performed on non-noble metal catalysts. Graphene has been intensively investigated recently, and Liu et al. recently investigated nitrogen-doped graphene foam as non-precious catalyst for the ORR.

Their catalyst showed a mass activity of  $0.46 \text{ A/g}_{\text{catalyst}}$  (at  $0.6 \text{ V}$ ) indicating the potential of this new noble-metal-free catalyst.<sup>43</sup> Pt particles (2 to 3 nm in diameter) are usually decorated onto a carbon catalyst support material with high surface area, such as carbon black (e.g. Vulcan XC-72).<sup>9,40</sup> SEM and TEM images of carbon black and carbon black decorated with platinum (Pt/CB) are shown in Figure 1.10.

An electrocatalyst ink is formed by mixing the electrocatalyst material with an electrolyte (generally Nafion ionomer solution), alcohol, and water. This ink is then deposited onto the electrolyte membrane via screen printing, spray-deposition or painting, to form a 10 to 30  $\mu\text{m}$  thick electrocatalyst layer.<sup>7,9</sup>

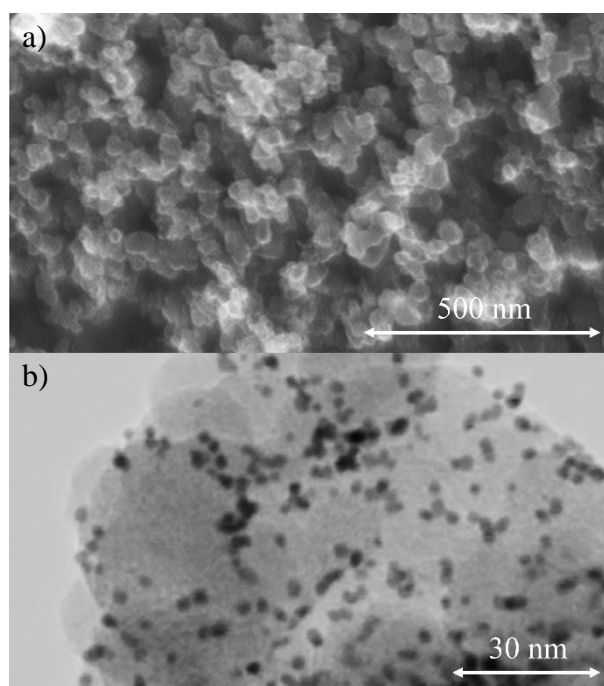
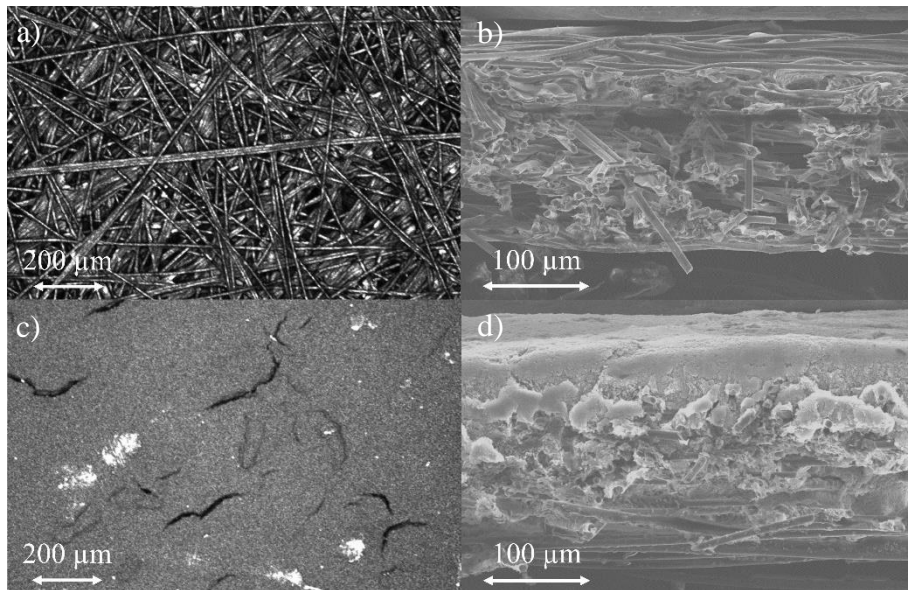


Figure 1.10. a) SEM image of carbon black. b) TEM image of Pt/CB.<sup>78</sup>

### 1.5.2.3 Gas Diffusion Layer

Gas diffusion layers (GDLs) are responsible for distributing the reactant gases across the entire electrocatalyst layer; for the electrical connection between the end plate or the bipolar plate (current collector) and the electrocatalyst layer; draining liquid water from the cathode catalyst layer; and protecting the thin electrocatalyst layer.<sup>7,9,11,79</sup> Typically GDLs consist of

carbon paper or carbon cloth (e.g. 200 to 500 $\mu\text{m}$  thick), with high porosity (> 70%), and can contain a thin microporous layer (for example consisting of carbon powder and a hydrophobic material such as Teflon).<sup>7,9,11,79</sup> The later prevents flooding of the fuel cell at high current densities (e.g. 0.5 to 1 A/cm<sup>2</sup>) by facilitating water removal.<sup>7,9</sup> The GDL is usually attached to the electrocatalyst layer by a hot-pressing process (e.g. at ~130°C and ~7-9 MPa). The ensemble of the above components is called a membrane electrode assembly (MEA).<sup>9</sup> Figure 1.11 shows laser microscope and SEM images of carbon paper without (a-b) and with (c-d) microporous layer.



*Figure 1.11. Laser microscope (left, GDL surface) and SEM images (right, GDL cross-section) of two different gas diffusion layers: a-b) carbon paper made up of randomly orientated carbon fibers; and c-d) carbon paper coated with a microporous layer.*

### 1.5.3 Hardware for Fuel Cell Assembly

The MEA is the central part of a fuel cell, however additional hardware must be used in order to complete the setup and make a complete fuel cell. Figure 1.12a is a schematic of a single cell fuel cell comprising end plates; flow field plates; MEA; and gaskets. Figure 1.12b and 10c show a NEDO single cell holder, with steel end plates, graphite gas flow field plates, and PTFE gaskets. In the following chapters the flow field and end plate will be explained briefly.

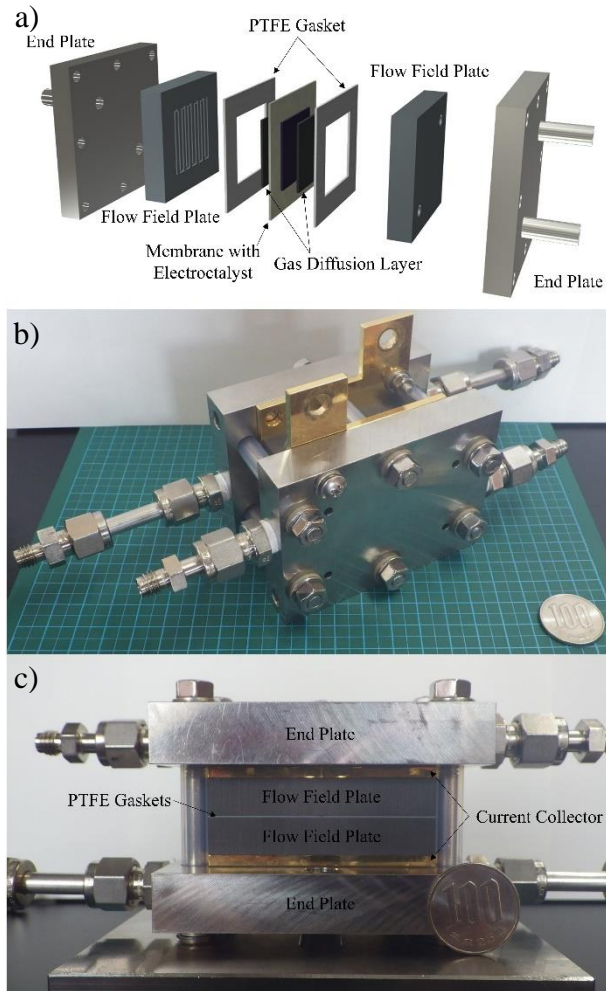


Figure 1.12. a) Schematic of a single cell fuel cell structure. b-c) NEDO single cell holder.

### 1.5.3.1 Flow Field Plates

The flow field plates supply and distribute the reactants across the surface of the electrode, acting as a current collector, mechanical support for the MEA, and for heat management (due to the high thermal conductivity of the materials used).<sup>9,11,80,81</sup> Flow field plates can be divided into monopolar and bipolar plates, depending whether the fuel cell is a single cell with one MEA, or a fuel cell “stack”, consisting of a plurality of MEAs.<sup>9,11,80,81</sup> Flow field plates contain flow channels for the reactants; monopolar plates have channels on one side for only one reactant; and bipolar plates have channels on both sides for both reactants. They can also be equipped with internal channels for liquid/air coolant for additional optimized heat management.<sup>9,11,80,81</sup> Typical gas flow channel geometries are *serpentine flow* which is

most common, *parallel flow*, or *interdigitated flow*.<sup>9,11,80,81</sup> An example of a monopolar flow field plate is shown in Figure 1.13. In the case of a fuel cell stack, bipolar plates are used to connect a plurality of MEAs with each other.<sup>9,11</sup> Compared to monopolar plates, bipolar plates are responsible for distribution of both reactants within the stack and across the electrode area, and they electronically connect the anode and cathode of the two MEAs (hence the term bipolar).<sup>9,11,80-82</sup> Bipolar plates contribute most to the volume and weight of a fuel cell stack (by ~80%), which makes the material selection very important.<sup>11,82</sup> Dense, non-porous graphite, metals (e.g. stainless steel) or composite materials (metal or carbon-based) can be used to fabricate flow field plates.<sup>7,11,80-82</sup> However most car makers use metal-based bipolar plates, as they can be fabricated to be very thin, increasing the volumetric power density of their fuel cell stacks.<sup>7</sup>

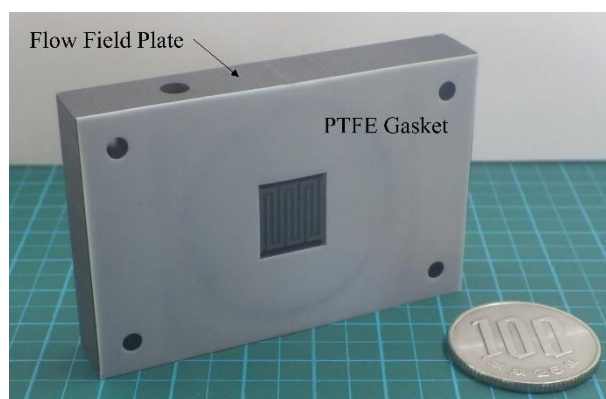
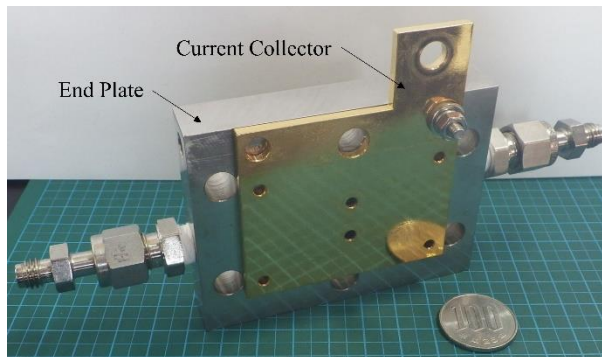


Figure 1.13. Flow field plate (graphite) with a PTFE gasket.

### 1.5.3.2 End Plates

Fuel cell end plates terminate MEAs forming a complete fuel cell unit and have to provide a uniform contact pressure over the whole area and all components in order to achieve low contact resistance and good sealing properties.<sup>83</sup> They are responsible for reactant supply to the flow field plates, current collecting, and heat removal.<sup>11,83</sup> End plates have inlets and outlets for reactants and liquid/air coolant as well as current terminals. Because of the high force required for clamping the fuel cell together, end plates are generally large and usually fabricated from metals such as stainless steel or aluminum.<sup>83</sup> Sometimes additional current

collectors made from e.g. brass may be used. Figure 1.14 shows an example of a stainless steel endplate with additional current collector (brass).



*Figure 1.14. End plate (stainless steel) with an additional current collector (brass).*

## 1.6 Alkaline Fuel Cells

### 1.6.1 Characteristics of Alkaline Fuel Cells

Figure 1.15 shows the principle of an alkaline fuel cell (AFC). Much like a PEMFC, the MEA of an AFC also consists of two electrodes equipped with an electrocatalyst and an electrolyte. However in this case, the electrolyte is an anion conductor, not a proton conductor. Hydrogen is supplied as a fuel to the anode, and in this case pure oxygen rather than air is generally supplied to the cathode. Hydroxyl ions ( $\text{OH}^-$ ) are generated from water and incoming electrons at the cathode, by the ORR. These  $\text{OH}^-$  ions permeate through the electrolyte to the anode. At the anode protons are produced from  $\text{H}_2$  by the HOR, and electrons are released flowing via the external circuit to the cathode. The protons recombine with the hydroxyl ions from the membrane, forming water. Two essential differences of AFCs compared to PEMFCs are that anions move from the cathode to the anode, and that water is produced at the anode and consumed at the cathode.<sup>7-9,11,84,85</sup>

The first practical AFCs utilized aqueous electrolytes e.g. KOH, which presented various challenges in terms of sealing and separation.<sup>8,9,11,84,86,87</sup> Later, alkaline matrix electrolytes and alkaline anion exchange membrane fuel cells (AAEMFCs) were developed, with several advantages over PEMFCs.<sup>84,86-92</sup>

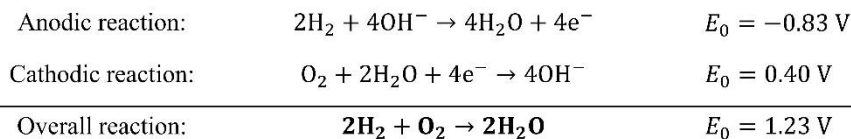
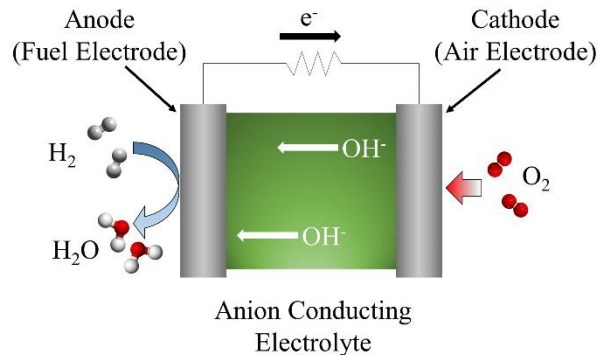


Figure 1.15. Schematic of the working principle of an alkaline fuel cell (AFC) with electrode reactions and the resulting theoretical cell voltage.

Due to lower overpotential for the ORR a high operation voltage, high power densities (e.g. 500 to 800 mW/cm<sup>2</sup>), and high efficiencies (e.g. up to 60%) can be achieved even at relatively low temperature (~60°C).<sup>7,9,85,87</sup> Non-noble metal, or metal-free catalysts can be used due to faster reaction kinetics of the ORR at the cathode.<sup>7-9,11,84,93</sup> The alkaline environment is less corrosive than acid, allowing the usage of iron alloys in AFCs.<sup>8,11</sup> Fuel crossover is reduced because electroosmotic drag is in the opposite direction compared with PEMFCs.<sup>86</sup> These factors can drastically reduce the cost of AAEMFCs compared with PEMFCs.

A major disadvantage of the AFC is the necessity to use pure oxygen instead of air, as CO<sub>2</sub> in the air leads to a rapid formation of carbonate (K<sub>2</sub>CO<sub>3</sub>), which blocks the electrode, destroys the active catalyst layers, and leads to a fast and irreversible performance loss in the cell.<sup>7,9,85,87</sup> Another disadvantage is related to the high rate of water production at the anode. Excess water can dilute the liquid electrolyte, or in case of AAEMFCs flood the electrode, both leading to performance loss.<sup>9,84</sup>

The first fuel cell powered vehicles were the Allis-Chalmers tractor in 1959, and the General Motors Electrovan in 1966, and these both used AFC technology. AFCs were also used in the US space program by NASA from 1965, until the decommissioning of the Space Shuttle

Orbiter in 2011 and were therefore the first long-term application for fuel cell technology.<sup>8,14,15,18–21</sup>

Very recently, the number of publications on AFCs is again increasing, probably due to the fact that AFCs using non-precious catalysts have the potential to result in extremely cheap fuel cells. Development challenges for wide spread commercialization include improving conductivity and stability, as well as fabrication of suitable non-precious catalysts.<sup>85</sup> The Japanese car manufacture Daihatsu Motor Corporation presented a fuel cell truck prototype using an AFCs fueled with hydrazine hydrate at the Tokyo Motor Show in 2013, showing that industry is also very interested in AFC technology.<sup>94</sup>

## **1.6.2 Components of Alkaline Fuel Cells**

### **1.6.2.1 Alkaline Anion Exchange Membranes**

Alkaline anion exchange membranes (AAEMs) have to fulfill the same requirements as PEMs, as listed in Chapter 1.5.2.1, with the difference that in AAEMs the charge carrier is a negatively charged ion such as  $\text{OH}^-$ .<sup>46,48,85,87</sup> There are currently several commercially available anion exchange membranes in production such as Tokuyama A 201 (Tokuyama Co. Ltd.), Aciplex (Asahi Chemical Industry Co.), Selemion (Asahi Glass Co. Ltd.), and FuMA-Tech FAD (FuMA-Tech GmbH).<sup>87</sup> However, none of these dominate in the same way as Nafion does in PEMFCs, since no membrane so far satisfies all the necessary performance requirements in terms of conductivity, durability, gas permeability and cost.

AAEMs have usually a lower conductivity compared to PEMs due to the lower ion mobility ( $\mu$ ) of  $\text{OH}^-$  compared to  $\text{H}^+$  ( $20.64 \times 10^{-8}$  vs  $36.23 \times 10^{-8} \text{ m}^2\text{s}^{-1}\text{V}^{-1}$ ) and lower dissociation level of the ammonium hydroxide groups.<sup>85</sup> The conductivity of the above-mentioned commercially available AAEMs ranges from 6 to 12 mS/cm at 25°C.<sup>87</sup> Non-commercial AAEMs have achieved much higher conductivities, exceeding even those of Nafion. However, they lack in other properties, especially stability, which impedes commercialization.<sup>87</sup> Low conductivity and poor stability are major problems for AAEMs to overcome.<sup>85</sup>

Most commercially available anion exchange membranes are composed of a fluorocarbon or hydrocarbon polymer backbone, with positively charged functional side groups (e.g.  $-\text{NH}_3^+$ ,  $-\text{NRH}_2^+$ ,  $-\text{NR}_3^+$ ), which have a selective permeability for anions.<sup>46,48</sup> Common preparation methods are: grafting vinyl monomers onto polymer films followed by subsequent chemical modification; graft copolymerization of vinyl monomers onto polymers by plasma irradiation; or UV-polymerization methods.<sup>46</sup> The preparation of anion exchange membranes is generally quite complicated and expensive, and the carcinogen chloromethyl methyl ether is often used. Therefore the field is widely open for new membranes with good mechanical, gas barrier, and ion conducting properties. Three different transport mechanisms are assumed to be responsible for  $\text{OH}^-$  transport in alkaline membranes: a Grotthuss-like mechanism similar to proton exchange membranes; diffusion and convection; and surface site hopping.<sup>84,87,95-98</sup> The activation energy for  $\text{OH}^-$  transport is higher compared to  $\text{H}^+$ , ranging from 0.12 to 0.22 eV.<sup>72,97,99</sup>

### 1.6.2.2 Other Components of Alkaline Fuel Cells

The electrode design in AFCs is different depending if the system uses a circulating electrolyte, or a solid AAEM. For AFCs using AAEMs the electrode design is quite simple and similar to PEMFCs. In this case a mixture of electrocatalyst, anion conducting polymer, alcohol and water is directly deposited onto the membrane and the GDL is attached by hot-pressing.

Electrodes used in circulating electrolyte-type AFCs are more complicated and the most commonly used type are PTFE-bonded gas diffusion electrodes.<sup>100</sup> In case of 3 layer design the electrode consists out of an active layer (electrocatalyst layer), gas diffusion layer (GDL) and a backing layer (BL).<sup>92,100,101</sup> The electrocatalyst layer contains the carbon-supported catalyst which is bonded together with small PTFE particles.<sup>11,101</sup> Similar to PEMFCs, the electrocatalyst is deposited on a catalyst support material with high surface area such as carbon black (e.g. Vulcan XC72R).<sup>92,102</sup> As mentioned in Chapter 1.6.1, non-precious catalyst or metal-free catalyst can be used as well as platinum, due to the improved reaction kinetics of the ORR in alkaline media.<sup>7-9,11,84,93</sup> Porous nickel is most commonly used for the HOR at the anode, and silver is a promising catalyst for the cathode due to its high activity

for ORR, high electric conductivity and low cost.<sup>100–102</sup> Manganese oxides or perovskite-type oxide materials are also being investigated as alternative catalysts for AFCs.<sup>101</sup> Recently, carbon-based catalysts (such as nitrogen-doped graphene) is being investigated for the catalytic properties in ORR.<sup>43</sup> In AFCs the GDL has the task of supplying the reactant gases to the catalyst layer, and also preventing electrolyte-leaking (known as weeping).<sup>11,101</sup> Weeping is diffusion of the liquid electrolyte through the electrode, entering the gas stream.<sup>8,101</sup> GDLs are mostly made out of mixtures of porous PTFE and carbon.<sup>11,101</sup> The BL electronically connects the electrode with the flow field/endplate or bipolar plate, and in the case of monopolar design is usually a metal mesh or foam (e.g. nickel). In case of bipolar design, regular carbon paper or carbon cloth can be used.<sup>11,101</sup> Required properties of the BL are high conductivity, mechanical strength, corrosion stability and gas permeability.<sup>92,101</sup> Flow field, bipolar and end plates have the same tasks as those used in PEMFC and similar design as discussed in Chapter 1.5.3. A special component in liquid electrolyte AFCs is the electrolyte frame. This is placed between two electrodes and the liquid electrolyte is circulated through it via an external pump.<sup>11,103</sup> Frame, pump, pipes valves etc. need a high corrosion resistance toward the circulating alkaline electrolyte.<sup>8</sup>

## 1.7 Low Dimensional Proton Conductors

The concept of low dimensional proton conductors has not been widely explored to date, although there are isolated examples of such materials. Low-dimensional proton conductors are defined here as an ionic conductor with at least one spacial dimension lower than 100 nm. For example this could include proton conducting nanoparticles such as one-dimensional proton conducting nanofibers or two-dimensional proton conducting nanosheets. The proton-conducting pathway may be across the surface of individual low dimensional particles, or through a layer comprising a multitude of such particles. The proton conducting network can also be considered to be low-dimensional in the case where e.g. mono- or multilayer water is in between sheet-like structures or crystals, or a 1D network of water “wires” in solid-state nanopores.<sup>104</sup> This is in contrast to the conducting pathways in e.g. Nafion, where large amounts of bulk water (i.e. 3D conduction pathways) in the hydrophilic pores are desired because of the great conductivity contribution of the Grotthuss mechanism.<sup>104,105</sup> Some

examples of low-dimensional proton conductors are minerals, clays, ceramics and metal-organic frameworks.

There are various possible benefits of utilizing low dimensional proton conductors compared with conventional proton conductors. Some of these will be elucidated through the experiments performed in this study. For example, one-dimensional water wires have interesting properties due to the interactions between the water molecules themselves, as well as due to nanoconfinement by the solid-state framework.<sup>106</sup> 1D water wires consist of hydrogen-bonded water molecules oriented parallel with the pore walls and can be found e.g. in zeolites or carbon nanotubes.<sup>106-111</sup> Proton diffusion in 1D water wires occurs via Grotthuss mechanism and is about 40 times faster than in bulk water.<sup>106,107,112</sup> If this effect can be channeled, it could be promising for application in electrochemical devices. However a bottleneck that limits the protonic conduction is the high energy barrier (~10 kcal/mol) that the proton has to overcome to enter the nanoconfined state. 1D water wires are more directional and ordered compared to bulk water, leading to stronger hydrogen bonds.<sup>106</sup> Additional effects such as e.g. van der Waals interactions between the pore and water molecules, or long-range dipolar interactions between water molecules lead to further increased stability of the water chain.<sup>106</sup> Therefore water molecules are difficult to remove from the water wire, which could mean better water retention properties at elevated temperatures. Low-dimensional proton conductors can be used for preparing defined and ordered proton pathways (unidirectional ion transport) and thus artificial ion channels by precise crystal growth (high crystallinity), arrangement and stacking/supramolecular engineering.<sup>113,114</sup> Crystallinity going along with an alignment of the proton conduction planes/pathways can significantly influence the proton conducting properties,<sup>114</sup> and proton conducting properties of material as bulk and incorporated into nanoconfined pores are often different.<sup>115</sup> Compared to PEMs, the mechanical stability can be maintained at temperatures above 120°C due to the higher temperature stability of the framework.<sup>114</sup> Using nanoscale proton conductors offers great possibilities in view of design,<sup>114</sup> e.g. for micro electro mechanical systems (MEMS). Low dimensional proton conductors offer a great opportunity in view of basic science. As it is possible to incorporate proton conducting media into a well-defined and ordered framework, low dimensional proton conductors offer the possibility for

gaining more knowledge and deeper understanding about proton conduction mechanisms as well as system modeling.<sup>114,115</sup>

Despite the potential advantages of low dimensional proton conductors, they have not been applied at a large scale as fuel cell electrolytes because the proton conduction is usually far lower than common PEMs such as Nafion, as shown in Table 1.2. Other problems arise from the open and porous structure, which is not as strong as dense polymeric materials, and may lead to poor gas barrier properties.<sup>114</sup>

Table 1.2 shows an overview of different low dimensional proton conductors listing their class, dimensions, typical observed conductivity range, associated ionic species, assumed conduction mechanism and determined activation energy. In the following Chapters (1.7.1 to 1.7.4) zeolites, zirconium phosphate hydrate, clays and beta-alumina will be described briefly. Graphene oxide and nanocellulose were investigated in this work, and as new materials for fuel cell electrolytes these materials will be described in Chapter 1.8 and 0 in more detail.

*Table 1.2. Overview of some low dimensional proton conductors.*

|  | Class                            | Thickness/Diameter (nm)<br>[Lateral Size (nm)/Aspect ratio]                                    | Conductivity<br>(S/cm)<br>[Temperature]                                       | Ionic<br>Species  | Conduction<br>Mechanism    | Activation<br>Energy<br>(eV) |
|--|----------------------------------|--|---|---|----------------------------|------------------------------|
| Zeolite<br>[116-123]   | Porous<br>Inorganic              | Few to several hundred<br>[Very low aspect ratio]  | $10^{-6}$ - $10^{-4}$ [RT]<br>0.6 [120°C]                                     | Various<br>ions e.g.<br>Na <sup>+</sup> , K <sup>+</sup> ,<br>H <sup>+</sup> and<br>OH  | Vehicle                    | 0.3 - 0.5                    |
| Zirconium<br>phosphate<br>hydrate<br>[104,120,124,125]   | Inorganic<br>metal<br>phosphate  | Amorphous state:<br>< 100<br>Crystalline state:<br>$\sim 10^3$ - $10^6$<br>[High aspect ratio] | $5 \times 10^{-6}$ - $6 \times 10^{-3}$<br>[RT]                               | H <sup>+</sup>  | Vehicle                    | 0.3 - 0.7                    |
| Clay<br>[120,126-131]  | Layered<br>inorganic             | Few nanometer<br>[Ten to several thousand]   | $10^{-4}$ and $10^{-2}$<br>[RT]   | Various<br>cations<br>e.g. Li <sup>+</sup> ,<br>Na <sup>+</sup> and<br>Ca <sup>2+</sup> | Grotthuss                  | 0.06 - 0.17                  |
| $\beta$ -Al <sub>2</sub> O <sub>3</sub> and<br>$\beta^{\prime\prime}$ -Al <sub>2</sub> O <sub>3</sub><br>[120,132-134] | Ceramic<br>metal oxide           | 100 - 10000<br>[Very low aspect ratio]   | $10^{-2}$ - $10^{-1}$ [RT]<br>1 [300]<br>$10^{-11}$ [RT]<br>$10^{-6}$ [500°C] | Na <sup>+</sup><br>H <sub>3</sub> O <sup>+</sup>  | Ion jump<br>+<br>Grotthuss | 0.1 - 0.3                    |
| Graphene<br>oxide<br>[135-137]   | Layered<br>carbon                | $\sim 1$ (monolayer) - $10^5$<br>[< 30 $\mu$ m flake size]                                     | $2 \times 10^{-4}$ [RT]<br>$9 \times 10^{-4}$ [90°C]                          | H <sup>+</sup>  | Grotthuss                  | 0.05 - 0.14                  |
| Nano-<br>cellulose<br>[138]  | Biological<br>organic<br>polymer | Several tens to few hundred<br>[few hundred to several thousand]                               | $10^{-5}$ [RT]<br>$5 \times 10^{-3}$ [120°C]                                  | H <sup>+</sup>  | Grotthuss                  | 0.21 - 0.24                  |

### 1.7.1 Zeolites

Zeolites are hydrated minerals consisting of a three-dimensional negatively charged aluminosilicate anion framework with usually metal cations from the alkaline or alkaline-earth metal group, and water trapped in the microporous 3D structure (at temperatures up to 400°C).<sup>120,139–141</sup> The crystalline structure is ordered at a molecular level, and typical particle sizes range from a few nanometers up to several hundred nanometers with very low aspect ratio, depending on the crystallization time.<sup>116–119</sup> There are over 40 known natural zeolites and a multitude of synthetic zeolites, which may also contain rare earth elements or organic cations.<sup>139–142</sup> Figure 1.16 shows a schematic of the crystal structure and SEM image of the synthetic zeolite ZSM-5. The proton conductivity of zeolites is usually in the range of  $10^{-6}$  to  $10^{-4}$  S/cm and strongly dependent on the hydration state.<sup>120–122</sup> However in tin-mordenite (obtained by heating the zeolite species H-mordenite with tin(II)chloride dihydrate in oxygen atmosphere) a conductivity of 0.6 S/cm was measured at 120 °C.<sup>123</sup> Proton conduction in zeolites is assumed to occur via a vehicular mechanism, due to the measured high activation energies (0.3 to 0.5 eV).<sup>120</sup> Sadakiyo et al. demonstrated the fabrication of an anion conductor by introduction of alkylammonium hydroxide into zeolitic imidazolate, with a OH<sup>-</sup> conductivity of  $2.3 \times 10^{-8}$  S/cm at 25°C.<sup>143</sup> Zeolites, with their molecular sieving properties, are widely used as e.g. hydrocracking catalysts in the oil industry, in automotive emission control, as water filters, in odor control, and for radioactive waste cleanup.<sup>142,144</sup>

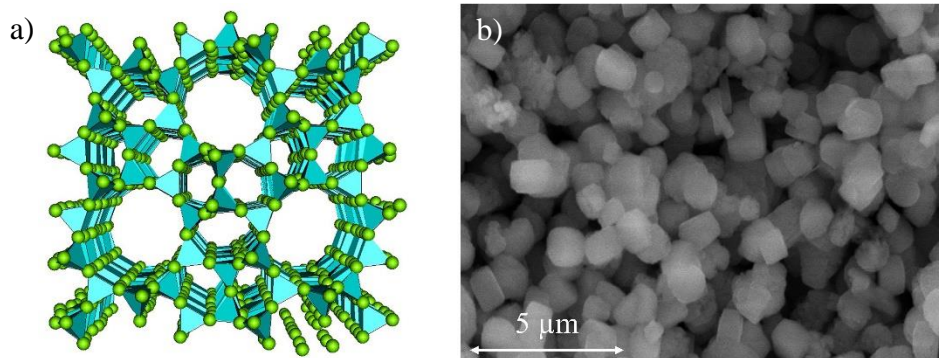


Figure 1.16. a) Schematic of the regular, porous structure of a zeolite crystal (ZSM-5).<sup>145</sup> b) SEM image of ZSM-5 zeolite crystals.<sup>146</sup>

### 1.7.2 Zirconium Phosphate Hydrate

Zirconium phosphate hydrate ( $\text{Zr}(\text{HPO}_4)_2 \cdot n\text{H}_2\text{O}$ ) is a crystalline layered compound and belongs to the group of metal phosphates.<sup>104,120,124,147</sup> It can be synthesized at low temperatures by direct precipitation of soluble zirconium(IV) salts with phosphoric acid, followed by hydrolysis.<sup>147</sup> Their well-ordered structure is determined by the strong interactions between phosphate groups and the metal ions, allowing self-assembly from the nano to macro scale.<sup>124</sup> A typical particle size with high aspect ratio is  $< 0.1 \mu\text{m}$  for more amorphous hydrates, and  $\sim 1 \mu\text{m}$  to  $1 \text{mm}$  for more crystalline state hydrates.<sup>120</sup> Figure 1.17 shows a schematic of the structure and SEM image of  $\alpha$ -zirconium phosphate. The conductivity of zirconium phosphate at room temperature is in the range of  $5 \times 10^{-6}$  to  $6 \times 10^{-3} \text{ S/cm}$ .<sup>104,120</sup> The proton conducting mechanism seems to be a mixture of Grotthuss and vehicular mechanism, since the activation energy of 0.3 eV is too high for a pure Grotthuss-type mechanism, and the strongly increasing activation energy (up to 0.7 eV) at temperatures above  $200^\circ\text{C}$  indicates a dominating vehicular mechanism.<sup>120</sup> Casciola and Constantino observed a strong conductivity decrease by two orders of magnitude with decreasing humidity and an increase in activation energy for pellicular zirconium phosphate in the same range as reported above, indicating the strong dependence of hydration on conductivity, as well as conduction mechanism.<sup>125</sup>

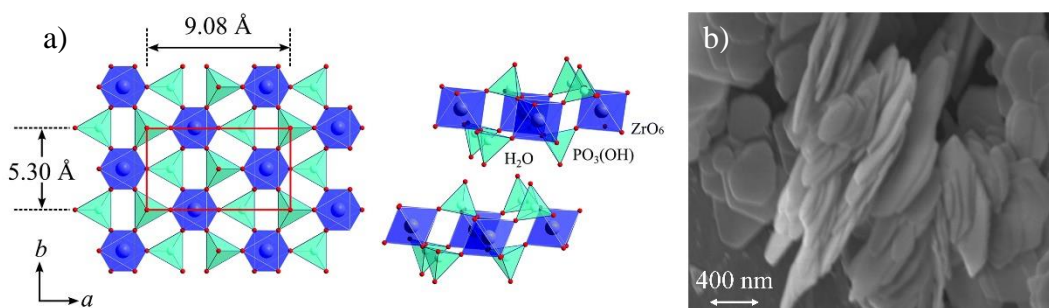


Figure 1.17. a) Structure of  $\alpha$ -zirconium phosphate.<sup>148</sup> b) SEM image of  $\alpha$ -zirconium phosphate.<sup>149</sup>

### 1.7.3 Clays

Clay minerals such as kaolinite, smectite or vermiculite are hydrous aluminium phyllosilicates and can exist in amorphous, disordered or crystalline form.<sup>150</sup> They occur in a stacked multilayer structure of shared tetrahedral and octahedrally structured sheets, and protonated water layers (single and multilayer are formed within the 2-dimensional network, leading to a maximum interlayer spacing of 13 nm).<sup>120,151</sup> Typical particle sizes range from several tens of nanometers to a few microns (e.g.  $\sim 120$  nm to  $\sim 4$   $\mu\text{m}$ ) and the thickness of the individual layers is only a few nanometers.<sup>120,126,127</sup> Figure 1.18 shows a schematic of the structure and SEM image of montmorillonite, which belongs to the group of smectite clays. Ionic conductivity at room temperature varies between  $10^{-4}$  and  $10^{-2}$  S/cm and is strongly dependent on water content (ion exchange can be performed).<sup>120,128-131</sup> Interlayer spacing increases with increasing humidification as mono- and multilayers of water are formed between the clay sheets.<sup>129</sup> Activation energy is in range between 0.055 and 0.17 eV, indicating that a Grotthuss mechanism is the most likely proton transport process.<sup>130,131</sup>

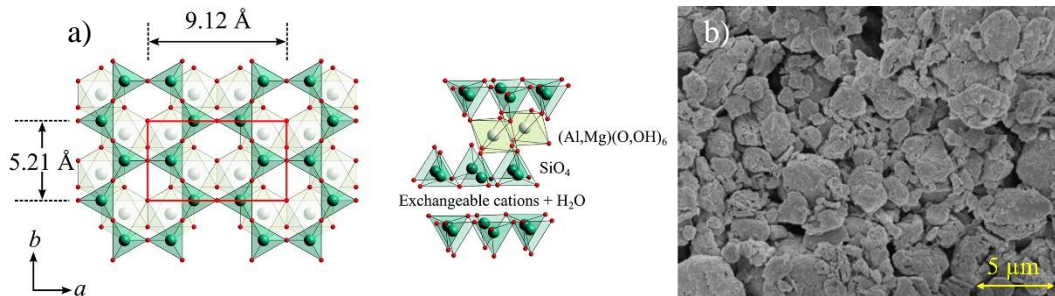


Figure 1.18. a) Structure of the clay material montmorillonite.<sup>148</sup> b) SEM image of montmorillonite clay.<sup>152</sup>

### 1.7.4 Beta-Alumina

$\beta\text{-Al}_2\text{O}_3$  and  $\beta''\text{-Al}_2\text{O}_3$  are proton conducting but electronic insulating ceramics with two different crystal structures ( $\beta\text{-Al}_2\text{O}_3$  hexagonal and  $\beta''\text{-Al}_2\text{O}_3$  rhombohedral), resulting in different chemical stoichiometry and conductivity.<sup>120,133,153</sup> Their structure is characterized by spinel blocks, octahedral and tetrahedral layers of oxygen and aluminum ions, connected via conduction planes that contain highly mobile sodium ions. In the case of a  $\beta\text{-Al}_2\text{O}_3$  unit

cell there are two spinel blocks connected via one conducting plane (Figure 1.19a), whereas in a  $\beta''$ - $\text{Al}_2\text{O}_3$  unit cell three spinel blocks are connected via two conducting planes (Figure 1.19b).<sup>104,133,153</sup> Typical crystal sizes range from a few hundred nanometers to a few microns.<sup>132</sup> Figure 1.19c shows a SEM image of polycrystalline  $\beta''$ - $\text{Al}_2\text{O}_3$ .  $\beta$ - $\text{Al}_2\text{O}_3$  and  $\beta''$ - $\text{Al}_2\text{O}_3$  are sodium ion conductors and were investigated as battery electrolytes in sodium-sulfur or sodium-nickel chloride batteries, but their sodium ions are also exchangeable.<sup>104,120,133</sup> Sodium ion conductivity depends strongly on temperature and increases from 25°C to 300°C by two orders of magnitude. Conductivity is in the range of  $10^{-2}$  to  $3 \times 10^{-1}$  S/cm for single crystal  $\beta$ - $\text{Al}_2\text{O}_3$  and  $10^{-2}$ , to as much as 1 S/cm for single crystal  $\beta''$ - $\text{Al}_2\text{O}_3$ .<sup>133</sup> The conductivity of polycrystalline  $\beta$ - $\text{Al}_2\text{O}_3$  and  $\beta''$ - $\text{Al}_2\text{O}_3$  is lower compared to the single crystalline forms, probably due to an additional grain-boundary effect. The values are in the range of  $10^{-3}$  to  $7 \times 10^{-2}$  S/cm for polycrystalline  $\beta$ - $\text{Al}_2\text{O}_3$ , and around  $4 \times 10^{-1}$  S/cm at 300°C for polycrystalline  $\beta''$ - $\text{Al}_2\text{O}_3$ .<sup>120,133</sup> The activation energy for single and polycrystalline  $\beta$ - $\text{Al}_2\text{O}_3$  and  $\beta''$ - $\text{Al}_2\text{O}_3$  are in the same range ( $\sim 0.1$  to 0.3 eV).<sup>133</sup> Sodium ions are exchangeable with other mono- and bivalent cations, however the resulting ionic conductivity is much less compared to sodium conductivity (e.g. at room temperature  $10^{-11}$  S/cm for  $\text{H}_3\text{O}^+$  and  $6.5 \times 10^{-5}$  S/cm for  $\text{K}^+$ ).<sup>120,154</sup> Activation energy for cation exchanged  $\beta$ - $\text{Al}_2\text{O}_3$  and  $\beta''$ - $\text{Al}_2\text{O}_3$  is 0.15 and 0.24 eV.

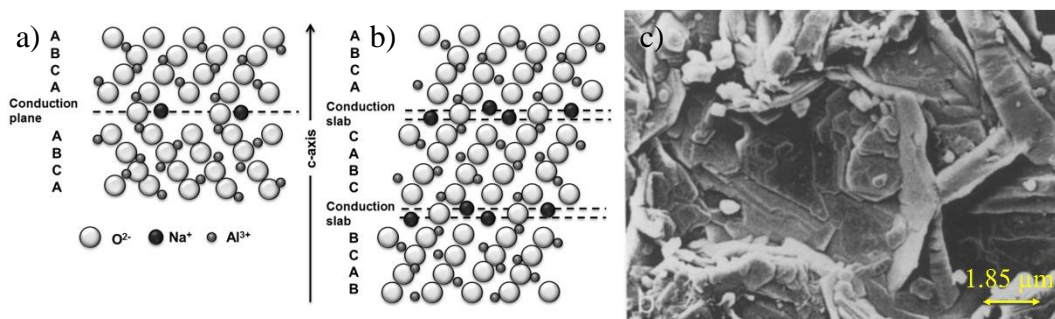


Figure 1.19. a-b) Stacking structure with corresponding conduction planes of  $\beta'$ -alumina (a) and  $\beta''$ -alumina (b).<sup>155</sup> c) SEM image of polycrystalline  $\beta''$ -alumina.<sup>156</sup>

## 1.8 Graphene Oxide

### 1.8.1 Introduction

Graphene is a single layer of graphitic carbon (Figure 1.20a), and since its discovery in 2004 by Geim, graphene has become an intensively researched topic in materials science due to its extraordinary properties, e.g. high intrinsic mobility and high Young's modulus.<sup>157–161</sup>

In graphene each carbon atom is linked to three other carbon atoms via covalent bonding, forming a perfectly planar honeycomb-like hexagonal lattice, due to their planar  $sp^2$ -hybridized carbon.<sup>161,162</sup> Hybridization characterizes the mixing behavior of molecular orbitals and in case of graphene, one 2s-orbital hybridizes with two 2p-orbitals ( $2p_x$  and  $2p_y$ ) to form three planar  $sp^2$ -orbitals, oriented at  $120^\circ$  to each other.<sup>161–163</sup> One electron remains free in the  $2p_z$ -orbital normal to the molecular plane (forming a highly delocalized  $\pi$ -orbital). The  $sp^2$ -orbitals overlap with  $sp^2$ -orbitals of neighboring carbon atoms forming  $\sigma$ -bonds, primarily responsible for the high mechanical stability of graphene. The  $2p_z$ -orbitals ( $\pi$ -orbitals) form  $\pi$ -bonds with  $2p_z$ -orbitals from neighboring carbon atoms. This results in strengthening of the sigma-bonds and thus the structure of graphene. Additionally the  $\pi^*$ - and  $\pi$ -bands fill the band gap between  $\sigma^*$ - and  $\sigma$ -bands, making graphene extraordinary conductive.<sup>161–164</sup>

Despite graphene being only one atom thick ( $\sim 0.1$  nm) and thus the thinnest known material,<sup>157,160,161,165</sup> Lee et al. showed that graphene is the strongest material ever measured, with an intrinsic strength of 130 GPa and a Young's modulus of 1.0 TPa.<sup>166</sup> Chen et al. reported extraordinary high intrinsic electron mobility ( $200\,000\text{ cm}^2\text{ V}^{-1}\text{ s}^{-1}$ ) and charge carrier density ( $10^{12}\text{ cm}^{-2}$ ),<sup>167</sup> the highest ever reported carrier mobility of a semimetal or semiconductor.<sup>161</sup> Graphene is highly transparent e.g. transmittance of 2 nm thick graphene films  $> 95\%$ , and this increases linearly with decreasing thickness.<sup>161,168</sup> Li et al. showed that freshly prepared graphene is more hydrophilic than previously assumed (water contact angle  $\sim 37^\circ$ ), however its hydrophilicity decreases quickly due to hydrocarbon contamination from the ambient air.<sup>169</sup>

Graphene can be prepared by various methods e.g. mechanical exfoliation from graphite, chemical vapor deposition of hydrocarbons on catalytic metal surfaces, annealing of SiC crystals, or reduction of graphite/graphene oxide.<sup>157,158,170</sup>

Applications for graphene range from flexible and transparent electronic devices and circuits,<sup>171</sup> ultracapacitors,<sup>172</sup> membranes for sea water desalination,<sup>173</sup> solar cells,<sup>174</sup> body motion sensors,<sup>175</sup> and medical applications such as composite materials for bone tissue engineering.<sup>176</sup> Graphene is also an interesting material for use in PEMFCs as e.g. a catalyst support, or as a non-precious catalyst due to its large surface area, high conductivity, and chemical stability.<sup>42,177,178</sup> For example, graphene-like foam has been used as catalyst support, showing a high electrochemical surface area and high mass activity compared with carbon black supports.<sup>42,179,180</sup> Liu et al. reported the usage of defective nitrogen-doped graphene foam as cathode catalyst for PEMFC application, showing a promising possibility for metal-free catalysis.<sup>43</sup> Defective nitrogen-doped graphene foam was also investigated as non-precious catalyst in alkaline media, displaying extremely high durability compared with commercial Pt/CB catalysts.<sup>93</sup>

An interesting variation on graphene is graphene oxide (GO),<sup>158,181,182</sup> first reported by Brodie in 1859.<sup>183,184</sup> A commonly accepted model of the structure of GO (Figure 1.20b) is based on the work of Lerf and Klinowski.<sup>185,186</sup> In their model GO is a carbon material that consist of aromatic non-oxidized carbon in a graphene-like structure and oxidized benzene rings. The oxidized region contains epoxy and hydroxyl groups on the basal plane, and carboxyl and hydroxyl groups terminate the edges. GO is thus a structure of mixed  $sp^2$  and  $sp^3$ -hybridized carbon. In  $sp^3$ -hybridized carbon, the 2s orbital hybridizes with all three 2p-orbitals ( $2p_x$ ,  $2p_y$  and  $2p_z$ ) forming four  $sp^3$ -orbitals in tetrahedral arrangement with an angle of  $109.5^\circ$  between the orbitals. Due to this  $sp^3$ -hybridization and the covalently bonded oxygen containing groups, the GO sheets are distorted (whereas in graphene the  $sp^2$ -hybridization results in a perfectly flat lattice).<sup>182,187</sup>  $sp^3$ -hybridized carbon is electronically insulating due to the large energy gap between the  $\sigma^*$ - and  $\sigma$ -bands (5.3 eV) and the loss of the free  $\pi$ -electron.<sup>164,188</sup> GO is often assumed to be completely insulating, however the conductivity is strongly dependent on the  $sp^2/sp^3$  hybridization ratio and thus the oxygen content.

Graphite oxide can be prepared by different methods. In Brodie's preparation method in 1859, graphite powder was treated with potassium chlorate (in a ratio of 1:3) in concentrated fuming nitric acid at 60°C, for four days.<sup>183,189</sup> In 1898 the method was slightly modified and simplified by Staudenmaier, who added concentrated sulfuric acid as an oxidizing agent, adding potassium chlorate in several steps.<sup>189,190</sup> Hummers developed a much faster preparation method in 1958, by oxidizing graphite with potassium permanganate and sodium nitrate in concentrated sulfuric acid.<sup>189,191</sup> His method is currently the most popular due to the fast reaction time (several hours compared to several days) and safer preparation method, since the evolution of explosive chlorine dioxide is avoided and no acid fog formation occurs.<sup>189</sup> The aforementioned methods results in graphite oxide, a three-dimensional structure. To exfoliate the three-dimensional graphite oxide into two-dimensional single layer graphene oxide external energy is applied e.g. ultrasonic treatment or stirring.<sup>182</sup> The lateral dimensions of GO produced via the Hummers method are limited to < 30 μm due to periodic cracking of the topmost GO layer,<sup>135</sup> and the thickness of a monolayer GO produced using this method is approximately 0.67 nm.<sup>136</sup>

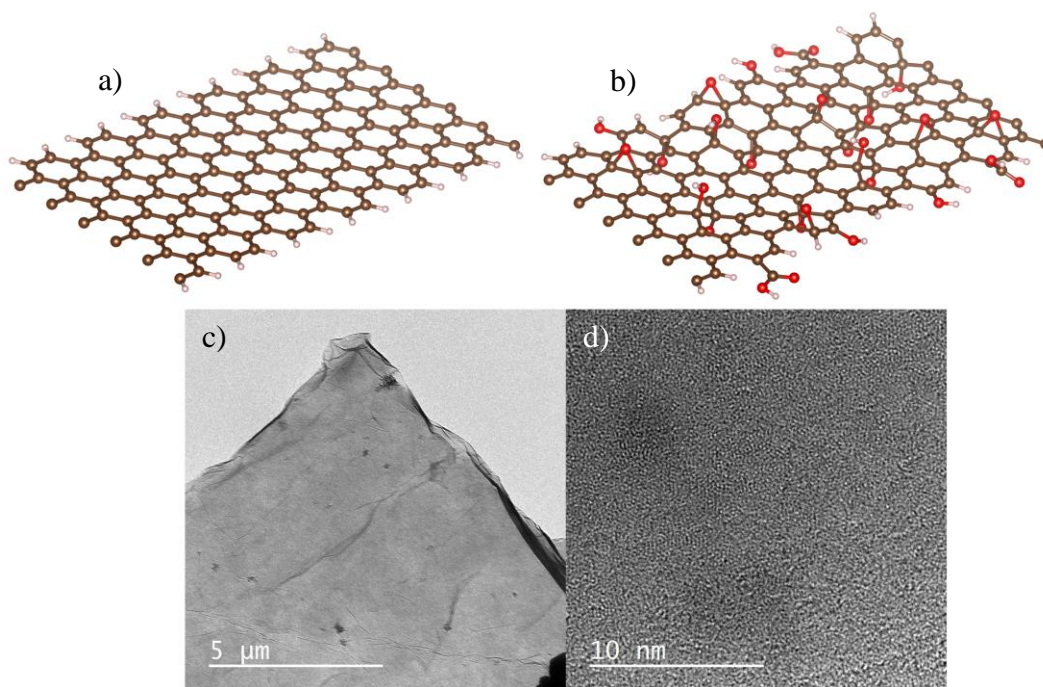


Figure 1.20. Structures of graphene (a) and graphene oxide (b).<sup>192</sup> TEM images of graphene oxide (c,d).

Figure 1.20c-d shows high-resolution TEM images of few-layer GO sheet at different magnification. At the edges, slightly brighter areas indicate thinner regions, a few monolayers thick. Some crumpling and folding is also observed. At high magnification, the hexagonal arrangement of the underlying carbon in GO can be resolved in some regions.

GO has a high hydrophilicity due to hydroxyl groups on the basal plane, and readily forms dispersions e.g. in water or organic solvents such as ethanol or acetone; depending strongly on the oxygen content and the solvent used.<sup>182,193</sup>

Dikin et al. showed that free-standing and flexible GO papers can be easily fabricated by vacuum filtration from dispersion,<sup>194</sup> by flow-directed assembly of GO sheets onto a filter substrate. Cross-sectional investigation by scanning electron microscopy showed that their papers had a layered structure of a multiplicity of GO sheets, with an interlayer distance of ~0.83 nm. The spacing between GO layers in such membranes depends on the degree of oxidation and hydration (i.e. how much water is present between the layers), and is generally around 0.8 to 1.4 nm.<sup>195,196</sup> GO papers have a high Young's modulus (32 GPa) and tensile strength (up to 133 MPa), however also a high stiffness as the elongation is less than 1%.<sup>194</sup>

Since GO can easily be dispersed in water, other thin-film fabrication methods such as bar-coating, inkjet printing and spraying can be used for preparation of few- and multi-layer GO films and membranes.<sup>197-199</sup> Cruz-Silva et al. prepared large-area GO thin films (~1200 cm<sup>2</sup>) by bar coating 0.8 wt% GO dispersion onto a PTFE plate.<sup>197</sup> Their films were less mechanically stable than those reported by Dikin,<sup>194</sup> however they could scroll them up to form GO fibers with high toughness (~17 J/m<sup>3</sup>) and elongation properties (~76% before rupture). Le et al. reported graphene electrodes with high specific capacitance (~132 F/g) fabricated by inkjet-printing of 0.2 wt% GO dispersion onto titanium foils followed by thermal reduction in nitrogen atmosphere.<sup>198</sup> Min et al. reported films prepared by spray coating of reduced GO ethanol dispersion (0.02 mg/ml) on various substrates such as silicon wafers and flexible polycarbonate films. A conductivity of 3 S/cm was achieved for their films, with a transmittance of 80%.<sup>199</sup> GO membranes have been observed to be completely impermeable to many liquids, vapors and gases, whilst allowing unimpeded permeation of water.<sup>200</sup> Daio et al observed reproducible swelling of GO in humid atmosphere due to water

intercalation by using environmental scanning electron microscope, showing GO's strong affinity to water.<sup>201</sup>

GO is widely assumed to be an electronic insulator due to the  $sp^3$ -bonding carbon network,<sup>158,182</sup> however GO has been shown to be a proton conductor. The carboxyl group can act as a proton donor and acceptor, similar to the  $SO_3H$ -groups in Nafion.<sup>62</sup> The through-plane conductivity of GO membranes incorporated in a membrane electrode assembly was reported by Kumar et al. to be 41 to 82 mS/cm (from 25 to 90°C at 100% relative humidity (RH)).<sup>202</sup> Zarrin et al. reported the in-plane conductivity of GO membranes on the order of 100 mS/cm (from 20 to 80°C at 100% RH).<sup>203</sup> Karim et al. reported the in-plane conductivity of GO nanosheets (dropped on a gold electrode and vacuum-dried, measured at 20 to 87°C and 95% RH; and 27°C from 40 to 95% RH) with lower values (15 mS/cm at ~80°C and 95% RH) than previously reported.<sup>204</sup> A fuel cell using GO paper was first reported by Tateishi et al. who also measured the in-plane and through-plane conductivity (at 25°C from 2 to 95% RH; and at 30% RH from 20 to 50°C). They reported a maximum in-plane and through-plane conductivity of ~100 mS/cm and ~1 mS/cm, respectively (25°C, 95% RH).<sup>205</sup> Recently Hatakeyama et al. reported the in-plane conductivity of single and multilayer GO and found an increase in in-plane proton conductivity with increasing membrane thickness (max. ~1 mS/cm, 25°C and ~90% RH).<sup>206</sup>

Several applications for GO have been investigated such as humidity sensing,<sup>207</sup> molecular sieves,<sup>208</sup> dielectrics,<sup>209</sup> and as a precursor for highly conducting flexible films.<sup>210</sup> In the next chapter a short overview of the application of graphene oxide in fuel cells will be given.

### **1.8.2 Graphene Oxide in Fuel Cells**

GO is an interesting alternative membrane material for proton exchange membrane fuel cells due to its gas barrier and proton conducting properties.<sup>200,202</sup> For example, GO has been investigated in composite PEMFC membranes with known proton conductors such as Nafion, sulfonated poly ether ether ketone (SPEEK) and polybenzimidazol (PBI). Kumar et al. reported the preparation of a GO composite membrane by incorporation of 4 wt% GO as a nano-filler in Nafion, and investigated its performance as fuel cell membrane at 100°C and 25% RH.<sup>211</sup> The composite membrane-based PEMFC showed higher performance than a

recast Nafion-based PEMFC (212 vs 56 mW/cm<sup>2</sup>) due to improved conductivity and water retention capability as well as increased mechanical stability. Chien et al. reported the preparation of a GO composite membrane for DMFC applications by dispersion of sulfonated GO into a Nafion matrix.<sup>212</sup> The incorporation of 0.05 to 5 wt% increased the proton conductivity at lower humidity due to improved water retention, whilst leading to lower methanol uptake and swelling. Their composite membrane showed better performance in a DMFC than Nafion<sup>®</sup>115 at 1 and 5 M methanol concentrations, probably related to lower methanol crossover. Jiang et al. reported that the incorporation of sodium dodecylbenzene sulfonate-adsorbed GO (3 to 5 wt%) in SPEEK greatly increased the ion-exchange capacity, water uptake and proton conductivity, whilst reducing methanol permeability.<sup>213</sup> Their membranes showed better performance in DMFCs than Nafion<sup>®</sup>112 (~60 vs 50 mW/cm<sup>2</sup>) due to increased proton conductivity and reduced methanol crossover. Xu et al. reported the incorporation of GO and sulfonated GO (SGO) into phosphoric acid-doped PBI.<sup>214</sup> The incorporation of only 2 wt% SGO increased the proton conductivity compared to pure PBI, e.g. from 23 mS/cm (PBI) to 27 mS/cm (GO) and 52 mS/cm (SGO) at 175°C. They incorporated these composite membranes into a PEMFC resulting in higher power densities (380 mW/cm<sup>2</sup> for GO and 600 mW/cm<sup>2</sup> for SGO) than pure PBI (220 mW/cm<sup>2</sup>) at 175°C. Tseng et al. investigated the suitability of GO-incorporated PBI for DMFC applications.<sup>215</sup> Incorporation of GO leads to increased proton conductivity compared to Nafion<sup>®</sup>117 at 90°C (67 vs 23 mS/cm), while reducing the methanol permeability of the composite membranes. GO was also used as laminate to reduce e.g. methanol crossover in DMFCs. Lin and Lu laminated Nafion<sup>®</sup>115 with a ~1 µm thick GO layer by transfer printing and hot-pressing.<sup>216</sup> Their laminates displayed a 40% lower methanol permeability compared to Nafion (0.93 x 10<sup>-6</sup> vs 1.57 x 10<sup>-6</sup> cm<sup>2</sup>/s) and increased DMFC power density at 8 M methanol concentrations (32 vs 15 mW/cm<sup>2</sup>). Jessie et al. prepared GO-Nafion laminates by drop- and spin-coating a GO-Nafion dispersion onto Nafion<sup>®</sup>212.<sup>217</sup> The laminated membranes show higher DMFC performance (~110 vs 55 mW/cm<sup>2</sup>) and lower fuel permeability (e.g. at 80°C and 2 M methanol concentration 1.72 x 10<sup>-6</sup> vs 5.33 x 10<sup>-6</sup> cm<sup>2</sup>/s) than Nafion<sup>®</sup>212.

The use of membranes in PEMFCs consisting primarily of GO or chemically modified GO have also been investigated, but to a much lesser extent. Tateishi et al. first reported the performance of a fuel cell using a pure GO paper membrane, achieving a maximum power

density of  $\sim 13 \text{ mW/cm}^2$  at room temperature.<sup>205</sup> In their paper they explored the differences in in-plane and through-plane conductivity, as well as the dependence of conductivity on membrane thickness. Additionally the dependence of OCV on electrocatalyst layer thickness was discussed. However their paper lacks discussion on the origin of the low OCV, despite the high gas barrier properties of GO. Additionally, they do not report the performance at typical PEMFC operation temperatures ( $\sim 80^\circ\text{C}$ ), or measure the durability of their MEA, or perform any post-operation characterization. Finally the performance of their Nafion-based fuel cell is much lower than usually reported. Functionalized GO membranes have demonstrated greater promise; for example Scott and Ravikumar reported a freestanding sulfonated GO (SGO) paper membrane achieving an MEA power density of  $113 \text{ mW/cm}^2$  at  $40^\circ\text{C}$  and 25% RH, reaching approximately half the performance of a Nafion-based PEMFC ( $209 \text{ mW/cm}^2$ ). Their SGO fuel cell showed stable operation up to ten hours and sulfonated GO showed higher temperature stability than GO, attributed to stronger interactions between the GO layers.<sup>218</sup> Gao et al. reported ozonated GO as fuel cell membrane. GO was oxidized by passing  $\text{O}_3$  gas through a GO dispersion, resulting in attachment of oxygen atoms to  $\text{sp}^2$ -hybridized carbons, increasing the number of oxygen groups such as e.g. hydroxyl or epoxy. Ozonation lead to an increased in-plane proton conductivity ( $\sim 215$  vs  $150 \text{ mS/cm}$ ) attributed to a smaller sheet size and increased number of pinholes, and better fuel cell performance compared to pure GO. However their membranes showed low durability during fuel cell operation due to partial reduction in the reducing hydrogen atmosphere.<sup>219</sup>

GO has also been investigated for its usage in alkaline anion exchange membrane fuel cells (AAEMFCs). Yang and Wang incorporated graphene and sulfonated graphene obtained by annealing GO into polyvinyl alcohol (PVA)/chitosan composite. Their composite membranes had a maximum ionic conductivity of  $93 \text{ mS/cm}$  at  $80^\circ\text{C}$  and around double the tensile strength of pure PVA ( $62$  vs  $35 \text{ MPa}$ ).<sup>220</sup> Movil et al. incorporated polydiallyldimethylammonium chloride (PDDA)-functionalized GO into PVA-based composite membranes and observed the AAEM performance.<sup>221</sup> The anionic ( $\text{OH}^-$ ) conductivity was  $21 \text{ mS/cm}$  at  $80^\circ\text{C}$ , around twice that of the pure PVA membrane ( $11 \text{ mS/cm}$ ). The achieved power density was around eight times higher ( $17$  vs  $2 \text{ mW/cm}^2$ ). Additionally, the incorporation of functionalized GO increased the thermo-mechanical stability. Liu et al prepared composite membranes by incorporating quarternized graphenes,

obtained by epoxide ring opening reaction of 3-amino-propyltriethoxysilane (APTES)-functionalized graphene, into aryl polymers. Their membranes showed high Young's modulus (5240 MPa) as well as tensile strength (205 MPa) and a bicarbonate conductivity of 18.7 mS/cm was achieved at 80°C, four times higher compared with the pristine reference sample.<sup>222</sup> Zarrin et al. prepared GO with quaternary ammonium groups by using dimethyloctadecyl [3-(trimethoxysilyl)propyl] ammonium chlorite as precursor and incorporated the resulting material as nanofiller in a PBI matrix.<sup>223</sup> A conductivity of 85 mS/cm was achieved at 65°C, around three times higher than the commercial AAEM (FAA FuMa-Tech), and their AAEMFC achieved a power density of 87 mW/cm<sup>2</sup> at 50°C and 100% RH, twice the value of the commercial reference (42 mW/cm<sup>2</sup>). Also, tensile strength and Young's modulus increased with the incorporation of functionalized GO compare to the pristine PBI (43 MPa and 2.1 GPa vs 27 MPa and 1.0 GPa). All the aforementioned work was on composite materials. Pure GO-based AAEMs have not been reported to date.

Such studies in the literature show the potential for GO to be used in fuel cell membranes (PEMFCs and AAEMFCs). However, so far no studies have investigated non-composited GO membranes at higher temperature under PEMFC operating conditions, where electrode kinetics and ionic transport are faster.<sup>177</sup> There has been little or no study of the degradation mechanisms, and no studies have reported the electrical properties and stability of GO in conditions suitable for high temperature proton exchange membrane fuel cell operation (i.e. above 90 °C). Furthermore, a systematic study of the contributions of protonic and electronic conductivity, and GO stability, over the wide humidity and temperature range expected during fuel cell operation, has not been performed. Alkaline fuel cells utilizing a GO-based AAEM have not been reported so far.

## 1.9 Nanocellulose

### 1.9.1 Introduction

Cellulose is the most abundant polymer on earth. It is the major constituent of the cell walls of plants, and provides structural integrity to trees (Figure 1.21). Wood pulp contains around 40-50% cellulose, cotton around 90 wt%, and it can even be produced by bacteria.<sup>224</sup> Cellulose is a simple biopolymer made up of carbon, oxygen and hydrogen (Figure 1.22).<sup>225-227</sup> The polymer chains group together during biosynthesis to form microfibrils via intermolecular hydrogen bonds and van der Waals forces. These microfibrils have diameters up to several tens of nanometers, with lengths of several microns.<sup>225,227-229</sup> Due to the strong intra- and intermolecular hydrogen-bonding network, they exhibit high mechanical strength (up to 1080 MPa) and are highly stable.<sup>227,228</sup> In the presence of pectin or lignin these microfibrils cluster together to form thicker macrofibrils with a diameter of up to about 50 nm. This structure is what gives the cell wall in plants high stiffness and strength.<sup>227,228,230</sup> Cellulose is a renewable, biodegradable and non-toxic polymer that has been utilized by mankind for thousands of years. Papyrus is a cellulose-based paper and was used to write on as early as 3000 BC. With the discovery of papermaking from wood-bark and cloth in China in 105 AD, cellulose became the most important material for writing documents.<sup>229</sup> Pure cellulose was first isolated and named in 1837 by Anselme Payen.<sup>231</sup>

Despite the microstructure of cellulose fibers being known, it was not possible to isolate the individual microfibrils until the late seventies. In 1977 Turbak et al.,<sup>232,233</sup> ran wood pulp fibers through a high pressure milk homogenizer and observed cellulose nanofibers for the first time. This ignited a strong scientific and economic interest in using this material for alternative applications. Cellulose nanofibers (CNFs) are generally produced from purified cellulose fiber pulps by mechanical treatments such as high pressure homogenization, grinding, ultrasonic treatment, or cryocrushing.<sup>225,228,234</sup> The high energy consumption of the mechanical treatment can be reduced by certain pre-treatments e.g. oxidation pre-treatment, which facilitate the process and reduces energy consumption to values around 1000 kWh/ton.<sup>234</sup> CNFs contain both amorphous and crystalline regions of cellulose and have a high aspect ratio.<sup>228,235</sup>

Another form of cellulose can be obtained via hydrolysis of CNFs in e.g. hydrochloric or sulfuric acid, to form cellulose nanocrystals (CNCs).<sup>226,235,236</sup> In this process the amorphous regions of the CNFs are dissolved, leaving only shorter, more crystalline regions. The CNC dimensions can vary depending on the source of cellulose and the hydrolysis conditions (ranging from e.g. 3 to 5 nm width and 50 to 500 nm length).<sup>226,228</sup> Due to their negatively charged surface (sulfuric acid reacts with the hydroxyl groups forming sulfate esters), CNCs can be dispersed readily in water.<sup>226,235,237</sup> Figure 1.22 shows schematics of the chemical structure of natural cellulose, cellulose after the pulping process, and crystalline cellulose (CNC) obtained by acid hydrolysis.

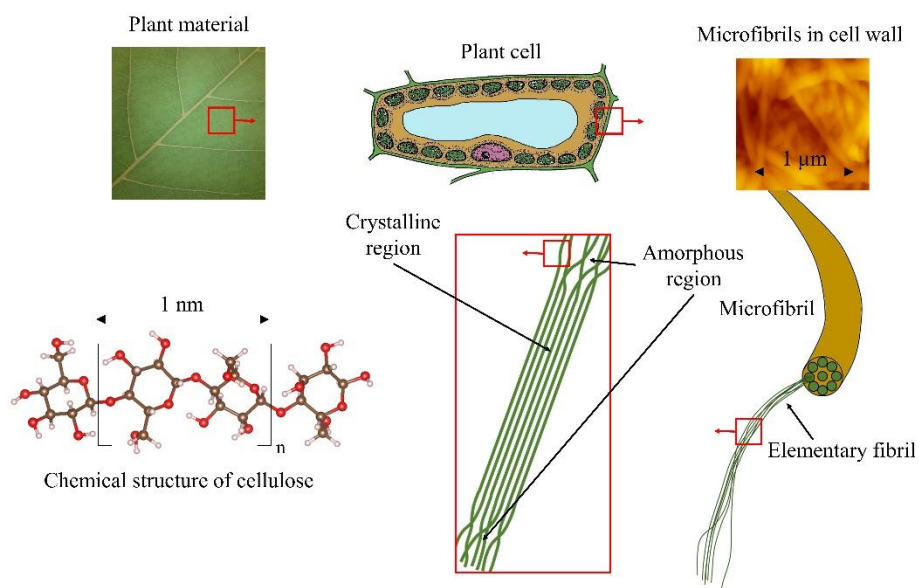


*Figure 1.21. Cellulose, the major constituent of the cell walls of plants.*

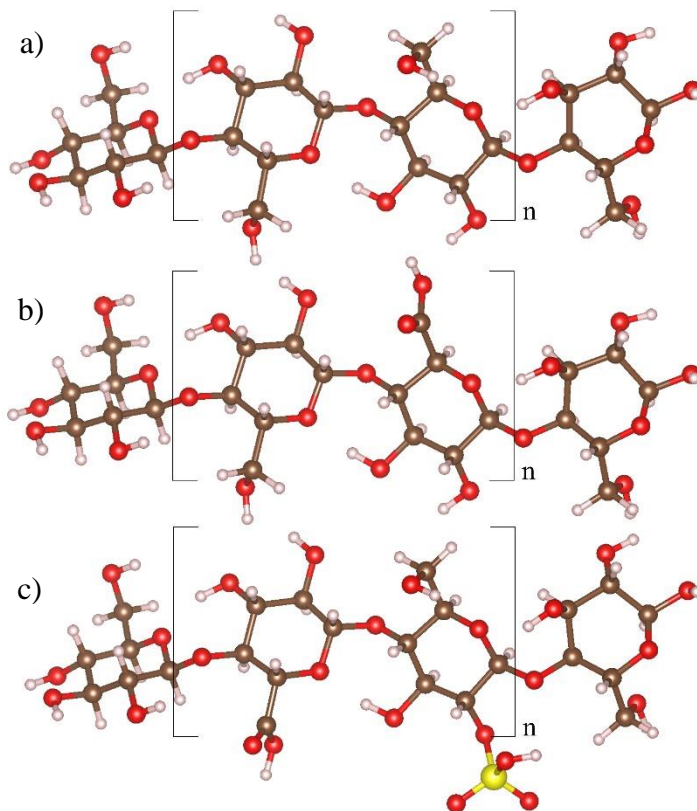


Figure 1.22. Chemical structure of cellulose: a) naturally occurring cellulose; b) with carboxylic acid functional groups formed during the pulping process; c) with sulfate ester groups formed during acid hydrolysis.<sup>192</sup>

Just as conventional wood pulp is used to make paper, nanocellulose can be processed to form “nanocellulose paper”. In 2008 Henriksson reported nanocellulose paper produced from wood pulp via an enzymatic hydrolysis pretreatment, combined with mechanical beating and mechanical homogenization. The resulting paper had very high toughness, a Young’s Modulus of 13.2 GPa, and high tensile strength (214 MPa). The excellent mechanical properties were related to the nanofiber network.<sup>238</sup> In 2009, Nogi et al. fabricated nanocellulose paper with high transparency (71.6% at  $\lambda = 600$  nm), and the optical properties were maintained even after heating up to 150°C.<sup>239,240</sup> They showed that the nanocellulose paper could be written on and folded just like conventional paper. Nanocellulose paper has good oxygen barrier properties, which can be tailored by thermal or chemical treatment.<sup>241,242</sup> Fang et al. used nanocellulose paper as a substrate for solar cells due to their ultrahigh optical transparency and low optical haze.<sup>243</sup> Koga et al. reported the fabrication of highly

transparent conductive networks of silver nanowires and carbon nanotubes on cellulose nanofiber paper, offering new possibilities for future paper electronics.<sup>244</sup> Recently Choi et al. reported the use of nanocellulose as a separator membrane for flexible lithium ion batteries, enabling new possibilities for next-generation energy storage in field of wearable consumer electronics.<sup>245</sup> Other application such as bio-composites, bio-medicine and gas barrier films for e.g. food packaging are also being investigated.<sup>242,246,247</sup>

In the next chapter, the application and investigation of nanocellulose in fuel cells science is reported.

### 1.9.2 Nanocellulose in Fuel Cells

Nanocellulose paper could be an alternative ionomer membrane for fuel cells due to the low cost, good gas barrier properties, mechanical toughness and acidic oxygen functional groups. For example, cellulose has been investigated in composites with Nafion. Jiang et al. blended Nafion with bacterial cellulose resulting in proton conductivity of 71 mS/cm at 100% RH and 30°C.<sup>248</sup> When used in a PEMFC, their membranes exhibited slightly improved power density of 106 mW/cm<sup>2</sup> compared to pristine Nafion (~100 mW/cm<sup>2</sup>) at room temperature, attributed to reduced activation and ohmic overpotentials. However, the OCV was lower (0.91 V) than for pristine Nafion (~1.0 V). Hasani-Sadrabadi et al. incorporated acid-hydrolyzed cellulose nanocrystals into Nafion and investigated the performance as a DMFC membrane.<sup>249</sup> The cellulose-composite maintained its proton conductivity at elevated temperature up to 120°C (~170 mS/cm) as the incorporation of acid-hydrolyzed cellulose nanocrystals prevents dehydration, whereas the conductivity of Nafion decreases at temperatures > 100°C (~120 mS/cm at 120°C) due to loss of water. Methanol cross-over through the composite membrane is approximately one order of magnitude less than for Nafion<sup>®</sup>117 (2.33 x 10<sup>-7</sup> vs 2.0 x 10<sup>-6</sup> cm<sup>2</sup>/s). At 5 M methanol concentration, the power density of the cellulose-composite DMFC (91 mW/cm<sup>2</sup>) was nearly twice that of the performance of a DMFC using Nafion<sup>®</sup>117, attributed to the reduced methanol cross-over.

Jiang et al. immersed bacterial cellulose biofilms into H<sub>3</sub>PO<sub>4</sub> or phytic acid. Their membranes achieved proton conductivities at 20°C of 80 and 50 mS/cm, respectively, and PEMFC power densities of 17.9 and 23 mW/cm<sup>2</sup>, respectively, at 25°C.<sup>250</sup> Durability measurements were

not performed, thus a leaching out of the acid with resulting performance decrease could not be excluded.

Lin et al. modified bacterial cellulose membranes with 2-acrylamido-2-methyl-1-propanesulfonic acid (AMPS) using ultraviolet light-induced grafting polymerization and investigated the performance in a DMFC membrane.<sup>251</sup> Their membranes showed about half the methanol permeability of Nafion<sup>®</sup>115 ( $5.64 \times 10^{-7}$  vs  $1.33 \times 10^{-6}$  cm<sup>2</sup>/s) and a maximum proton conductivity at room temperature of 29 mS/cm, lower than for Nafion<sup>®</sup>115 (39 mS/cm). A power density of only 16 mW/cm<sup>2</sup> was achieved when operated at 2 M methanol concentration, about one third the value achieved by the Nafion-based DMFC ( $\sim 45$  mW/cm<sup>2</sup>), most likely due to the lower proton conductivity.

Kasai et al. showed that cross-linked cellulose sulfate membranes have half the methanol permeation compared to Nafion<sup>®</sup>112 at 3 M methanol concentration, due to reduced solvent uptake ( $\sim 0.7 \times 10^{-6}$  vs  $1.4 \times 10^{-6}$  cm<sup>2</sup>/cm).<sup>252</sup> Conductivity increased with the number of sulfate groups, reaching a maximum of 81 mS/cm at room temperature and approaching the conductivity of Nafion ( $\sim 100$  mS/cm). For some reason their membrane was not assembled into an MEA or investigated in DMFC operation conditions.

Finally, Smolarkiewicz et al. doped cellulose with imidazole, achieving a proton conductivity of approximately  $2 \times 10^{-3}$  mS/cm at 160°C under anhydrous conditions.<sup>253</sup> Despite the fact that their imidazole-doped cellulose membrane exhibits reasonable conductivity under these harsh conditions and are thermally stable up to  $\sim 200^\circ\text{C}$ , it was not investigated as membrane in HT-PEMFCs.

In all the aforementioned studies, dopants were used to increase the proton conductivity, or cellulose was used as a nanofiller to improve the properties of Nafion. Only Smolarkiewicz et al. measured the proton conductivity of a pure cellulose reference sample. Their microcrystalline cellulose pellets, compressed at room temperature under a pressure of 10 MPa, had a maximum conductivity of  $2 \times 10^{-6}$  mS/cm at 70°C (humidity not defined).<sup>253</sup> Most of the above studies were performed at room temperature, whereas PEMFCs generally operate at much higher temperature. To the best of our knowledge the proton conductivity of nanocellulose membranes has not yet been investigated, especially at higher temperature, over a wide range of relative humidity, and with activation energies to give insight into the

conduction mechanism. Pure, unadulterated cellulose or nanocellulose membranes have not been investigated for application in hydrogen fuel cells.

### **1.10 Objectives of this Study**

The objective of this study is the investigation and characterization of two novel low-dimensional proton conductors as fuel cell electrolytes for PEMFCs and AAEMFCs. Specifically graphene oxide (GO) and nanocellulose are investigated for their general fuel cell electrolyte related properties such as proton conductivity, mechanical strength, water uptake gas barrier properties, and performance as membranes in PEMFCs. Additionally, GO is chemically modified and applied as an AAEM. In addition to electrochemical characterization, all materials are characterized for their chemical composition, structure and morphology by aid of methods such as X-ray photoelectron spectroscopy, X-ray diffraction, atomic force microscopy, and scanning electron microscopy.

## References

1. METI has compiled a Strategic Road Map for Hydrogen and Fuel Cells. *Hydrogen and Fuel Cell Promotion Office, Agency for Natural Resources and Energy* (2014). at <[http://www.meti.go.jp/english/press/2014/0624\\_04.html](http://www.meti.go.jp/english/press/2014/0624_04.html)>
2. *Summary of the Strategic Road Map for Hydrogen and Fuel Cells.* (2014). at <[http://www.meti.go.jp/english/press/2014/pdf/0624\\_04a.pdf](http://www.meti.go.jp/english/press/2014/pdf/0624_04a.pdf)>
3. METI has strategic road map for hydrogen and fuel cells in Japan. *Fuel Cells Bull.* **2014**, 9 (2014).
4. Toyota. Toyota Ushers in the Future with Launch of ‘Mirai’ Fuel Cell Sedan. *Toyota Global Newsroom* (2014). at <<http://newsroom.toyota.co.jp/en/detail/4198334/>>
5. Nishimura, M. Hydrogen Technology Roadmap Asia Workshop. in *CO2 Free Energy Supply Chain to Japan with Liquid Hydrogen-included Hydrogen power station, Kawasaki Heavy Industry* (2014). at <<https://www.iea.org/workshop/hydrogen-roadmap--asia-workshop-july-2014.html>>
6. ‘水素リーダー都市プロジェクト’下水バイオガスによる水素ステーション完成記念式典を行います!! *Ministry of Land, Infrastructure, Transport and Tourism* (2015). at <<http://www.city.fukuoka.lg.jp/data/open/cnt/3/48046/1/siryu.pdf>>
7. *Fuel Cells - Selected Entries from the Encyclopedia of Sustainability Science and Technology.* (Springer New York, 2013). at <<http://link.springer.com/10.1007/978-1-4419-0851-3>>
8. Bagotsky, V. S. *Fuel Cells: Problems and Solutions.* (Wiley & Sons, 2009).
9. O’Hayre, R., Cha, S.-W., Colella, W. & Prinz, F. B. *Fuel Cell Fundamentals.* (John Wiley & Sons, Inc., 2008).
10. Zaidi, S. M. J. & Matsuura, T. *Polymer Membranes for Fuel Cells.* (Springer US, 2009). doi:10.1007/978-0-387-73532-0
11. Larminie, J. & Dicks, A. *Fuel Cell Systems Explained, 2nd Edition.* (Wiley, 2003).
12. Schönbein, C. F. On the voltaic polarization of certain solid and fluid substances. *Philos. Mag. Ser. 3* **14**,
13. Bossel, U. *The Birth of the Fuel Cell, 1835-1845: Including the First Publication of the Complete Correspondence from 1839 to 1868 Between Christian Friedrich Schoenbein (discoverer of the Fuel Cell Effect) and William Robert Grove (inventor of the Fuel Cell).* (European Fuel Cell Forum, 2000).

14. Page, K. A., Soles, C. L. & Runt, J. *Polymers for Energy Storage and Delivery: Polyelectrolytes for Batteries and Fuel Cells*. (American Chemical Society, 2012). doi:10.1021/bk-2012-1096
15. Gross, D. Fuel Cells: 170 years of technology development – and Space Age experience! *Cleantech magazine* (2010). at <<http://www.cleantechinvestor.com/portal/2010-issue-5.html>>
16. Grove, W. R. On the Gas Voltaic Battery. Experiments Made with a View of Ascertaining the Rationale of Its Action and Its Application to Eudiometry. *Philos. Trans. R. Soc. London* **133**, 91–112 (1843). Reprinted, not copyrighted.
17. Bacon, F. T. the High Pressure Hydrogen-Oxygen Fuel Cell. *Ind. Eng. Chem.* **52**, 301–303 (1960).
18. Kordesch, K., Hacker, V., Reichmann, K., Cifrain, M. & Hejze, T. The Safe and Economic Revival of Alkaline Hydrogen / Air Fuel Cells with Circulating Electrolytes, Recommended for Vehicles using Battery Hybrid Systems and Hydrogen from Ammonia Crackers. *ECS Trans.* **11**, 167–185 (2008).
19. Marks, C., Rishavy, E. & Wyczalek, F. A. Electrovan - A Fuel Cell Powered Vehicle. *SAE Trans.* **75**, 992–1002 (1967).
20. Busby, R. L. *Hydrogen and Fuel Cells: A Comprehensive Guide*. (PennWell Corporation, 2005).
21. Reaves, W. & Hoberecht, M. Proton Exchange Membrane (PEM) Fuel Cell Status and Remaining Challenges for Manned Space-Flight Applications. in *International Energy Conversion Engineering Conference* (2003).
22. 資源エネルギー庁. 平成26年2月3日 資源エネルギー庁 燃料電池推進室. in 家庭用燃料電池について 34 (METI, 2014). at <[http://www.meti.go.jp/committee/kenkyukai/energy/suiso\\_nenryodenchi/suiso\\_nenryodenchi\\_wg/pdf/002\\_01\\_00.pdf](http://www.meti.go.jp/committee/kenkyukai/energy/suiso_nenryodenchi/suiso_nenryodenchi_wg/pdf/002_01_00.pdf)>
23. Nagata, Y. エネファーム 10万台までの道のりとこれから. in *NEDOフォーラム 24* (Toshiba Fuel Cell Power Systems Corporation, 2015). at <[http://www.nedo.go.jp/nedoforum2015/program/pdf/ts4/yuji\\_nagata.pdf](http://www.nedo.go.jp/nedoforum2015/program/pdf/ts4/yuji_nagata.pdf)>
24. Fuel cells power first takeoff for DLR's Antares aircraft. *Fuel Cells Bull.* **2009**, 3 (2009).
25. Toyota. Toyota to Increase 'Mirai' Production. *Toyota Global Newsroom* (2015).
26. Reprinted with permission from ECS Trans. 11, 167–185 (2008). Copyright 2008, The Electrochemical Society.

27. Hitt, D. NASA Educational Technology Services. *The Science of Space Recycling* (2010). at <[http://www.nasa.gov/audience/foreducators/k-4/features/F\\_Recycling\\_on\\_the\\_ISS.html](http://www.nasa.gov/audience/foreducators/k-4/features/F_Recycling_on_the_ISS.html)>. Reprinted, not copyrighted.
28. GM Heritage Center. *GM Vehicle Technologies* (2015). at <[https://www.gmheritagecenter.com/images/featured/Alt\\_Fuel/full/Electrovan.jpg](https://www.gmheritagecenter.com/images/featured/Alt_Fuel/full/Electrovan.jpg)>. Reprinted with permission from General Motors LLC.
29. Larminie, J. & Dicks, A. *Fuel Cell Systems Explained*. (John Wiley & Sons, Ltd, 2003).
30. Pilatowsky, I. *et al. Cogeneration Fuel Cell-Sorption Air Conditioning Systems*. (Springer London, 2011). doi:10.1007/978-1-84996-028-1
31. *Recent Trends in Fuel Cell Science and Technology*. (Springer-Verlag New York, 2007). doi:10.1007/978-0-387-68815-2
32. Srinivasan, S. *Fuel Cells - From Fundamentals to Applications*. (Springer, 2006).
33. Zhang, J., Tang, Y., Song, C., Zhang, J. & Wang, H. PEM fuel cell open circuit voltage (OCV) in the temperature range of 23°C to 120°C. *J. Power Sources* **163**, 532–537 (2006).
34. Vilekar, S. A. & Datta, R. The effect of hydrogen crossover on open-circuit voltage in polymer electrolyte membrane fuel cells. *J. Power Sources* **195**, 2241–2247 (2010).
35. Ramani, V. Fuel Cells. *Electrochem. Soc. Interface* 41–44 (2006).
36. Revankar, S. T. & Majumdar, P. in *Fuel Cells: Principles, Design and Analysis* 748 (CRC Press, 2014).
37. Mennola, T., Mikkola, M., Noponen, M., Hottinen, T. & Lund, P. Measurement of ohmic voltage losses in individual cells of a PEMFC stack. *J. Power Sources* **112**, 261–272 (2002).
38. DOE. *Fuel Cell Fact Sheet*. (2006). at <[http://www.hydrogen.energy.gov/pdfs/doe\\_fuelcell\\_factsheet.pdf](http://www.hydrogen.energy.gov/pdfs/doe_fuelcell_factsheet.pdf)>
39. Badwal, S. P. S., Giddey, S. S., Munnings, C., Bhatt, A. I. & Hollenkamp, A. F. Emerging electrochemical energy conversion and storage technologies. *Front. Chem.* **2**, 1–28 (2014).
40. Holton, O. T. & Stevenson, J. W. The Role of Platinum in Proton Exchange Membrane Fuel Cells. *Platin. Met. Rev.* **57**, 259–271 (2013).
41. Yee, R. S. L., Rozendal, R. a., Zhang, K. & Ladewig, B. P. Cost effective cation exchange membranes: A review. *Chem. Eng. Res. Des.* **90**, 950–959 (2012).

42. Jianfeng, L., Sasaki, K. & Lyth, S. M. Pt-decorated Graphene-like Foam for Electrochemical Oxygen Reduction with High Mass Activity. *ECS Trans.* **58**, 1751–1762 (2013).
43. Liu, J., Takeshi, D., Orejon, D., Sasaki, K. & Lyth, S. M. Defective Nitrogen-Doped Graphene Foam: A Metal-Free, Non-Precious Electrocatalyst for the Oxygen Reduction Reaction in Acid. *J. Electrochem. Soc.* **161**, F544–F550 (2014).
44. Peighambaroust, S. J., Rowshanzamir, S. & Amjadi, M. *Review of the proton exchange membranes for fuel cell applications. International Journal of Hydrogen Energy* **35**, (Elsevier Ltd, 2010).
45. Baschuk, J. J. & Li, X. Carbon monoxide poisoning of proton exchange membrane fuel cells. *Int. J. Energy Res.* **25**, 695–713 (2001).
46. Xu, T. Ion exchange membranes: State of their development and perspective. *J. Memb. Sci.* **263**, 1–29 (2005).
47. Wang, Y., Chen, K. S., Mishler, J., Cho, S. C. & Adroher, X. C. A review of polymer electrolyte membrane fuel cells: Technology, applications, and needs on fundamental research. *Appl. Energy* **88**, 981–1007 (2011).
48. Strathmann, H., Grabowski, A. & Eigenberger, G. Ion-Exchange Membranes in the Chemical Process Industry. *Ind. Eng. Chem. Res.* **52**, 10364–10379 (2013).
49. *Polymer Membranes for Fuel Cells.* (Springer US, 2009). doi:10.1007/978-0-387-73532-0
50. Li, Q., He, R., Jensen, J. O. & Bjerrum, N. J. Approaches and Recent Development of Polymer Electrolyte Membranes for Fuel Cells Operating above 100 °C. *Chem. Mater.* **15**, 4896–4915 (2003).
51. Blumenthal, G. *et al.* Investigation of the Proton Transport in Nafion | Membranes as a Function of Direction , Temperature and Relative Humidity. *Ionics (Kiel)*. **2**, 102–106 (1996).
52. Yeo, S. C. & Eisenberg, a. Physical properties and supermolecular structure of perfluorinated ion-containing (nafion) polymers. *J. Appl. Polym. Sci.* **21**, 875–898 (1977).
53. Kerr, J. B., Liu, G. & Sun, X. New Polyelectrolyte Materials for High-Temperature Fuel Cells , Membrane Electrode Assemblies and Enhanced Selectivity. *Prog. Rep. - DOE Hydrog. Progr.* 366–372 (2004).
54. Satterfield, M. B., Majsztzik, P. W., Ota, H., Benziger, J. B. & Bocarsly, A. B. Mechanical Properties of Nafion and Titania / Nafion Composite Membranes for Polymer Electrolyte Membrane Fuel Cells. *J. Polym. Sci. Part B Polym. Phys.* **44**, 2327–2345 (2006).

55. Jalani, N. H., Dunn, K. & Datta, R. Synthesis and characterization of Nafion®-MO<sub>2</sub> (M=Zr, Si, Ti) nanocomposite membranes for higher temperature PEM fuel cells. *Electrochim. Acta* **51**, 553–560 (2005).
56. Song, S. Q., Zhou, W. J., Li, W. Z. & Sun, G. Direct Methanol Fuel Cells : Methanol Crossover and its Influence on Single D M F C Performance. *Ionics (Kiel)*. **10**, 458–462 (2004).
57. Baik, K. D., Hong, B. K. & Kim, M. S. Effects of operating parameters on hydrogen crossover rate through Nafion® membranes in polymer electrolyte membrane fuel cells. *Renew. Energy* **57**, 234–239 (2013).
58. Cheng, X. *et al.* Hydrogen crossover in high-temperature PEM fuel cells. *J. Power Sources* **167**, 25–31 (2007).
59. *Fuel Cell Technologies Office: Multi-Year Research, Development, and Demonstration Plan.* (2014). at <<http://energy.gov/eere/fuelcells/downloads/fuel-cell-technologies-office-multi-year-research-development-and-22>>
60. Chandan, A. *et al.* High temperature (HT) polymer electrolyte membrane fuel cells (PEMFC) - A review. *J. Power Sources* **231**, 264–278 (2013).
61. Zhang, H. & Shen, P. K. Recent Development of Polymer Electrolyte Membranes for Fuel Cells. *Chem. Rev.* **112**, 2780–2832 (2012).
62. Eikerling, M., Kornyshev, A. A., Kuznetsov, A. M., Ulstrup, J. & Walbran, S. Mechanisms of Proton Conductance in Polymer Electrolyte Membranes. *J. Phys. Chem. B* **105**, 3646–3662 (2001).
63. Ludue, G. A., Thomas, D. K. & Sebastiani, D. Mixed Grotthuss and Vehicle Transport Mechanism in Proton Conducting Polymers from Ab initio Molecular Dynamics Simulations. 1424–1429 (2011).
64. de Grotthuss, T. Sur la décomposition de l' eau et des corps qu' elle tient en dissolution à l' aide de l'électricité galvanique [On the decomposition of water and ofsolutes by electrical currents]. *Ann. Chim.* **LVIII**, 54–74 (1806).
65. Agmon, N. The Grotthuss mechanism. *Chem. Phys. Lett.* **50**, 456–462 (1995).
66. Kreuer, K.-D., Rabenau, A. & Weppner, W. Vehicle Mechanism , A New Model for the Interpretation of the Conductivity of Fast Proton Conductors Photochemical Oxidative Addition of Chlorine from. *Angew. Chem. Int. Ed. Engl.* **122**, 1981–1982 (1982).
67. Kreuer, K. Proton Conductivity : Materials and Applications. *Chem. Mater.* **8**, 610–641 (1996).

68. Zawodzinski, T. a T., Neeman, M., Sillerud, L. O. & Gottesfeld, S. Determination of water diffusion coefficients in perfluorosulfonate ionomeric membranes. *J. Phys. Chem.* **95**, 6040–6044 (1991).
69. Saito, M., Hayamizu, K. & Okada, T. Temperature dependence of ion and water transport in perfluorinated ionomer membranes for fuel cells. *J. Phys. Chem. B* **109**, 3112–3119 (2005).
70. Choi, P., Jalani, N. H. & Datta, R. Thermodynamics and Proton Transport in Nafion - I. Membrane Swelling, Sorption, and Ion-Exchange Equilibrium. *J. Electrochem. Soc.* **152**, 84–89 (2005).
71. Paul, D. K., McCreery, R. & Karan, K. Proton Transport Property in Supported Nafion Nanothin Films by Electrochemical Impedance Spectroscopy. *J. Electrochem. Soc.* **161**, F1395–F1402 (2014).
72. Varcoe, J. R. Investigations of the ex situ ionic conductivities at 30C of metal-cation-free quaternary ammonium alkaline anion-exchange membranes in static atmospheres of different relative humidities. *Phys. Chem. Chem. Phys.* **9**, 1479–1486 (2007).
73. Knauth, P. & Schoonman, J. *Nanocomposites: Ionic Conducting Materials and Structural Spectroscopies*. (Springer, 2008).
74. Kreuer, K.-D. in *Proton Conductors: Solids, Membranes and Gels - Materials and Devices* 474–486 (Cambridge University Press, 1992).
75. Janik, M. J., Davis, R. J. & Neurock, M. Anhydrous and water-assisted proton mobility in phosphotungstic acid. *J. Am. Chem. Soc.* **127**, 5238–5245 (2005).
76. Pandey, K. & Lakshmi, N. Evidence of failure of hopping model of ionic conductivity in phosphomolybdic acid studied by a.c. conductivity measurements. *J. Mater. Sci.* **4**, 1749–1752 (1999).
77. Tang, Q. *et al.* High Proton Conduction at above 100 ° C Mediated by Hydrogen Bonding in a Lanthanide Metal – Organic Framework. *J. Am. Chem. Soc.* **136**, 12444–12449 (2014).
78. Reprinted with permission from ECS Trans. 58, 1751–1762 (2013). Copyright 2013, The Electrochemical Society.
79. Park, S., Lee, J.-W. & Popov, B. N. A review of gas diffusion layer in PEM fuel cells: Materials and designs. *Int. J. Hydrogen Energy* **37**, 5850–5865 (2012).
80. Hamilton, P. J. & Pollet, B. G. Polymer Electrolyte Membrane Fuel Cell (PEMFC) Flow Field Plate : Design , Materials and Characterisation. *Fuel Cells* **10**, 489–509 (2010).

81. Brett, D. J. L. & Brandon, N. P. Review of Materials and Characterization Methods for Polymer Electrolyte Fuel Cell Flow-Field Plates. *J. Fuel Cell Sci. Technol.* **4**, 29–44 (2007).
82. Hermann, A., Chaudhuri, T. & Spagnol, P. Bipolar plates for PEM fuel cells : A review. *Int. J. Hydrogen Energy* **30**, 1297–1302 (2005).
83. Asghari, S., Shahsamandi, M. H. & Khorasani, M. R. A. Design and manufacturing of end plates of a 5 kW PEM fuel cell. *Int. J. Hydrogen Energy* **35**, 9291–9297 (2010).
84. Wang, Y.-J., Qiao, J., Baker, R. & Zhang, J. Alkaline polymer electrolyte membranes for fuel cell applications. *Chem. Soc. Rev.* **42**, 5768–5787 (2013).
85. Varcoe, J. R. *et al.* Anion-exchange membranes in electrochemical energy systems. *Energy Environ. Sci.* **7**, 3135–3191 (2014).
86. Arges, C. G., Ramani, V. & Pintauro, P. N. Anion Exchange Membrane Fuel Cells. *Interface* **19**, 31–35 (2010).
87. Merle, G., Wessling, M. & Nijmeijer, K. Anion exchange membranes for alkaline fuel cells: A review. *J. Memb. Sci.* **377**, 1–35 (2011).
88. Slade, R. C. T., Kizewski, J. P., Poynton, S. D., Zeng, R. & Varcoe, J. R. in *Fuel Cells: Selected Entries from the Encyclopedia of Sustainability Science and Technology* (ed. Meyers, R. A.) 9–29 (2013). doi:10.1007/978-1-4419-0851-3
89. Bartrom, A. M. & Haan, J. L. The direct formate fuel cell with an alkaline anion exchange membrane. *J. Power Sources* **214**, 68–74 (2012).
90. Zhao, T. S., Li, Y. S. & Shen, S. Y. Anion-exchange membrane direct ethanol fuel cells: Status and perspective. *Front. Energy Power Eng. China* **4**, 443–458 (2010).
91. Ünlü, M., Zhou, J. & Kohl, P. a. Hybrid Anion and Proton Exchange Membrane Fuel Cells. *J. Phys. Chem. C* **113**, 11416–11423 (2009).
92. Strasser, K. The design of Alkaline Fuel Cells. *J. Power Sources* **29**, 149–166 (1990).
93. Liu, J., Sasaki, K. & Lyth, S. M. Defective Nitrogen-Doped Graphene Foam: A Non-Precious Electrocatalyst for the Oxygen Reduction Reaction in Alkaline Medium. *ECS Trans.* **64**, 1161–1172 (2014).
94. Serov, A. *et al.* Anode Catalysts for Direct Hydrazine Fuel Cells : From Laboratory Test to an Electric Vehicle. *Angew. Chemie - Int. Ed.* **53**, 10336–10339 (2014).
95. Grew, K. N., Chu, D. & Chiu, W. K. S. Ionic Equilibrium and Transport in the Alkaline Anion. *J. Electrochem. Soc.* **157**, 1024–1032 (2010).
96. *Electrochemical Polymer Electrolyte Membranes.* (CRC Press, 2015).

97. Tuckerman, M. E., Marx, D. & Parrinello, M. The nature and transport mechanism of hydrated hydroxide ions in aqueous solution. *Nature* **417**, 925–929 (2002).
98. Grew, K. N. & Chiu, W. K. S. A Dusty Fluid Model for Predicting Hydroxyl Anion Conductivity in Alkaline Anion Exchange Membranes. *J. Electrochem. Soc.* **157**, B327 (2010).
99. Pandey, T. P. *et al.* Interplay between water uptake, ion interactions, and conductivity in an e-beam grafted poly(ethylene-co-tetrafluoroethylene) anion exchange membrane. *Phys. Chem. Chem. Phys.* **17**, 4367–4378 (2015).
100. *Materials for Fuel Cells*. (Woodhead Publishing, 2008).
101. Bidault, F., Brett, D. J. L., Middleton, P. H. & Brandon, N. P. Review of gas diffusion cathodes for alkaline fuel cells. *J. Power Sources* **187**, 39–48 (2009).
102. Bidault, F. & Kucernak, A. Cathode development for alkaline fuel cells based on a porous silver membrane. *J. Power Sources* **196**, 4950–4956 (2011).
103. Tomantschger, K., McClusky, F., Oporto, L., Reid, A. & Kordesch, K. DEVELOPMENT OF LOW COST ALKALINE FUEL CELLS. *J. Power Sources* **18**, 317–335 (1986).
104. Knauth, P. & Di Vona, M. L. *Solid State Proton Conductors: Properties and Applications in Fuel Cells*. (John Wiley & Sons, Inc., 2012).
105. Choi, P., Jalani, N. H. & Datta, R. Thermodynamics and Proton Transport in Nafion - II. Proton Diffusion Mechanisms and Conductivity. *J. Electrochem. Soc.* **152**, 123–130 (2005).
106. Köfinger, J., Hummer, G. & Dellago, C. Single-file water in nanopores. *Phys. Chem. Chem. Phys.* **13**, 15333–15728 (2011).
107. Dellago, C., Naor, M. M. & Hummer, G. Proton Transport through Water-Filled Carbon Nanotubes. *Phys. Rev. Lett.* **90**, 1–4 (2003).
108. Fois, E. *et al.* Water Molecules in Single File: First-Principles Studies of One-Dimensional Water Chains in Zeolites. *J. Phys. Chem. B* **105**, 3012–3016 (2001).
109. Quartieri, S. *et al.* One-dimensional ice in bikitaite : single-crystal X-ray diffraction , infra-red spectroscopy and ab-initio molecular dynamics studies. *Microporous Mesoporous Mater.* **30**, 77–87 (1999).
110. Fois, E. *et al.* Dipolar host/guest interactions and geometrical confinement at the basis of the stability of one-dimensional ice in zeolite bikitaite Dipolar host/guest interactions and geometrical confinement at the basis of the stability of one-dimensional ice in zeoli. *J. Chem. Phys.* **111**, 355–359 (1999).

111. Matsui, H. *et al.* Proton tunneling in low dimensional cesium silicate LDS-1 Proton tunneling in low dimensional cesium silicate LDS-1. *J. Chem. Phys.* **143**, 1–12 (2015).
112. Ñ, H. M. A., Hhta, Y. O., Ida, C. I., Orii, M. H. & Adokoro, M. T. Observation of Quasi-One Dimensional Proton Conductions. *J. Phys. Soc. Japan* **79**, 1–4 (2010).
113. Horike, S., Umeyama, D. & Kitagawa, S. Ion Conductivity and Transport by Porous Coordination Polymers and Metal-Organic Frameworks. *Acc. Chem. Res.* **46**, 2376–2384 (2013).
114. Ramaswamy, P., Wong, N. E. & Shimizu, G. K. H. MOFs as proton conductors – challengeves and opportunities. *Chem. Soc. Rev.* **43**, 5913–5932 (2014).
115. Natarajan, S. *et al.* Proton Conduction in Metal – Organic Frameworks and Related Modularly Built Porous Solids. *Angew. Chem. Int. Ed. Engl.* **52**, 2688–2700 (2013).
116. Schoeman, B. J., Sterte, J. & Otterstedt, J. Colloidal zeolite suspensions. *Zeolites* **14**, 110–116 (1994).
117. Zhu, G. *et al.* Synthesis and Characterization of High-Quality Zeolite LTA and FAU Single Nanocrystals. *Chem. Mater.* **10**, 1483–1486 (1998).
118. Castagnola, N. B. & Dutta, P. K. Nanometer-Sized Zeolite X Crystals: Use as Photochemical Hosts. *J. Phys. Chem. B* **102**, 1696–1702 (1998).
119. Taufiqurrahmi, N., Mohamed, A. R. & Bhatia, S. Nanocrystalline Zeolite Y: Synthesis and Characterization. *Mater. Sci. Eng.* **17**, 1–6 (2011).
120. *Proton conductors: Solids, membranes, and gels–materials and devices.* (Cambridge University Press, 1993). doi:10.1002/adma.19930050923
121. Han, W., Ming, S., King, K. & Yeung, L. Zeolite Proton Conducting Membrane for Micro Fuel Cell Applications. *Top. Catal.* **53**, 1394–1400 (2010).
122. Nischwitz, P., Amels, P. & Fetting, F. Studies on the ionic conductivity of zeolitic solids. *Solid State Ionics* **73**, 105–118 (1994).
123. Knudsen, N., Andersen, E. K. R. O. G. H., Andersen, I. G. K. & Skou, E. TIN-MORDENITES, SYNTHESSES AND IONIC CONDUCTIVITY. *Solid State Ionics* **35**, 51–55 (1989).
124. Cao, G., Hong, H. & Mallouk, T. E. Layered Metal Phosphates and Phosphonates: From Crystals to Monolayers. *Acc. Chem. Res.* **25**, 427–432 (1992).
125. Casciola, M. & Constantino, U. Relative Humidity Influence on Proton Conduction of Hydrated Pellicular Zirconium Phosphate in Hydrogen Form. *Solid State Ionics* **20**, 69–73 (1986).

126. Nadeau, P. H. The Physical Dimensions of Fundamental Clay Particles. *Clay Miner.* **20**, 499–514 (1985).
127. Blott, S. J. & Pye, K. Particle size scales and classification of sediment types based on particle size distributions : Review and recommended procedures. *Sedimentology* **59**, 2071–2096 (2012).
128. Poinسیون, C. Protonic conductivity and water dynamics in swelling clays. *Solid State Ionics* **97**, 399–407 (1997).
129. Aliouane, N. *et al.* Investigation of hydration and protonic conductivity of H-montmorillonite. *Solid State Ionics* **148**, 103–110 (2002).
130. Kim, H., Yamazaki, Y., Kim, J., Kudo, T. & Honma, I. High ionic conductivity of Mg – Al layered double hydroxides at intermediate temperature ( 100 – 200 ° C ) under saturated humidity condition ( 100 % RH ). *Solid State Ionics* **181**, 883–888 (2010).
131. Fan, Y. & Wub, H. A new family of fast ion conductor-montmorillonite. *Solid State Ionics* **2738**, 347–354 (1997).
132. Kamaludeen, M., Rencanathan, N. C. & Sundaram, M. Synthesis of Beta-Alumina Solid Electrolyte for Sodium-Sulphur Batteries. *Bull. Electrochem.* **1**, 533–535 (1985).
133. Lu, X., Xia, G., Lemmon, J. P. & Yang, Z. Advanced materials for sodium-beta alumina batteries : Status , challenges and perspectives. *J. Power Sources* **195**, 2431–2442 (2010).
134. Farrington, G. C., Briant, J. L., Breiter, M. W. & Roth, W. L. Ionic Conductivity in H<sub>3</sub>O<sup>+</sup>Beta Alumina. *J. Solid State Chem.* **24**, 311–319 (1978).
135. Pan, S. & Aksay, I. A. Factors Controlling the Size of Graphene Oxide Sheets Produced via the Graphite Oxide Route. *ACS Nano* **5**, 4073–4083 (2011).
136. Pandey, D., Reifengerger, R. & Piner, R. Scanning probe microscopy study of exfoliated oxidized graphene sheets. *Surf. Sci.* **602**, 1607–1613 (2008).
137. Bayer, T., Bishop, S. R., Perry, N., Sasaki, K. & Lyth, S. M. Tunable Mixed Ionic/Electronic Conductivity and Permittivity of Two Dimensional Graphene. *Submitted*
138. Bayer, T. *et al.* High Temperature Proton Conduction in Nanocellulose Membranes: Paper Fuel Cells. *Nat. Energy* **1**, (2016).
139. Davis, M. E. & Lobo, R. F. Zeolite and Molecular Sieve Synthesis. *Chem. Mater.* **11**, 756–768 (1992).
140. Tschernich, R. W. *Zeolites of the World.* (Geoscience Press, 1992).
141. *Handbook of Zeolite Science and Technology.* (CRC Press, 2003).

142. Sherman, J. D. Synthetic zeolites and other microporous oxide molecular sieves. *Proc. Natl. Acad. Sci. U. S. A.* **96**, 3471–3478 (1999).
143. Sadakiyo, M., Kasai, H., Kato, K., Takata, M. & Yamauchi, M. Design and Synthesis of Hydroxide Ion – Conductive Metal – Organic Frameworks Based on Salt Inclusion. *J. Am. Chem. Soc.* **136**, 8–11 (2014).
144. *Zeolites in Industrial Separation and Catalysis*. (Wiley VCH, 2010).
145. Price, G. L. Representative Structures. *TU Chemical Engineering Zeolite Page* (2015). at <http://www.personal.utulsa.edu/~geoffrey-price/zeolite/>. Reprinted with permission from Geoffrey L. Price. Copyright, Geoffrey L. Price.
146. Nano ZSM-5. *ACS Material* (2015). at <http://www.acsmaterial.com/product.asp?cid=33&id=141>. Reprinted with permission from Richard Ploss, CEO, ACS Material, LCC.
147. Trobajo, C., Khainakov, S. A., Espina, A. & García, J. R. On the Synthesis of  $\alpha$ -Zirconium Phosphate. *Chem. Mater.* **7**, 1787–1790 (2000).
148. Reproduced from *Dalt. Trans.* 43, 10642–10650 (2014) with permission from the Royal Society of Chemistry.
149. Reprinted (adapted) with permission from Wang, L. et al. Stable Organic – Inorganic Hybrid of Polyaniline /  $\alpha$ -Zirconium Phosphate for Efficient Removal of Organic Pollutants in Water Environment. *ACS Appl. Mater. Interfaces* **4**, 2686–2692 (2012). Copyright (2012) American Chemical Society.
150. Tan, K. H. *Principles of Soil Chemistry*. (Marcel Dekker Inc., 1998).
151. SPOSITO, G. *et al.* Surface geochemistry of the clay minerals. *Proc. Natl. Acad. Sci. U. S. A.* **96**, 3358–3364 (1999).
152. Reprinted from *Journal of Hazardous Materials*, 160, Wang L. and Wang A., Adsorption properties of Congo Red from aqueous solution onto surfactant-modified montmorillonite, 173-180, Copyright (2008), with permission from Elsevier.
153. *Encyclopedia of Electrochemical Power Sources*. (Elsevier, 2009).
154. Farrington, G. C. Solid Ionic Conductors. *Sensors and Actuators* **1**, 329–346 (1981).
155. *Strontium Aluminate - Cement Fundamentals, Manufacturing, Hydration, Setting Behaviour and Applications*. (InTech, 2014). doi:DOI: 10.5772/57363. Reprinted, unrestricted use permitted.
156. Reprinted from *Solid State Ionics*, 67, Tan A., Kuo, C. K. and Nicholson, P. S., Formation and characterization of Na- $\beta$ "-alumina single crystal films, 131-136, Copyright (1993), with permission from Elsevier.

157. Geim, A. K. & Novoselov, K. S. The rise of graphene. *Nat. Mater.* **6**, 183–91 (2007).
158. Zhu, Y. *et al.* Graphene and graphene oxide: synthesis, properties, and applications. *Adv. Mater.* **22**, 3906–3924 (2010).
159. Novoselov, K. S. *et al.* Electric Field Effect in Atomically Thin Carbon Films. *Science* (80-. ). **306**, 666–669 (2004).
160. Geim, A. K. Graphene: status and prospects. *Science* **324**, 1530–1534 (2009).
161. Soldano, C., Mahmood, A. & Dujardin, E. Production , properties and potential of graphene. *Carbon N. Y.* **48**, 2127–2150 (2010).
162. Katsnelson, M. I. *Graphene - Carbon in Two Dimensions*. (Cambridge University Press, 2012).
163. Fuhrer, M. S., Lau, C. N. & Macdonald, A. H. Graphene: Materially Better Carbon. *MRS Bull.* **35**, 289–295 (2010).
164. Takai, K., Oga, M., Sato, H. & Enoki, T. Structure and electronic properties of a nongraphitic disordered carbon system and its heat-treatment effects. *Phys. Rev. B* **67**, 1–11 (2003).
165. Kim, S. Y. & Park, H. S. On the effective plate thickness of monolayer graphene from flexural wave propagation. *J. Appl. Phys.* **110**, 1–6 (2011).
166. Lee, C., Wei, X., Kysar, J. W. & Hone, J. Measurement of the Elastic Properties and Intrinsic Strength of Monolayer Graphene. *Science* (80-. ). **321**, 385–388 (2008).
167. Chen, J.-H., Jang, C., Xiao, S., Ishigami, M. & Fuhrer, M. S. Intrinsic and extrinsic performance limits of graphene devices on SiO<sub>2</sub>. *Nat. Nanotechnol.* **3**, 206–209 (2008).
168. Eda, G., Fanchini, G. & Chhowalla, M. Large-area ultrathin films of reduced graphene oxide as a transparent and flexible electronic material. *Nat. Nanotechnol.* **3**, 270–274 (2008).
169. Li, Z. *et al.* Effect of airborne contaminants on the wettability of supported graphene and graphite. *Nat. Mater.* **12**, 925–931 (2013).
170. Avouris, P. & Dimitrakopoulos, C. Graphene : synthesis and applications. *Mater. Today* **15**, 86–97 (2012).
171. Chen, B. J. *et al.* Printed Graphene Circuits. *Adv. Mater.* **19**, 3623–3627 (2007).
172. Stoller, M. D., Park, S., Zhu, Y., An, J. & Ruoff, R. S. Graphene-Based Ultracapacitors. *Nano Lett.* **8**, 3498–3502 (2008).

173. Cohen-Tanugi, D. & Grossman, J. C. Water Desalination across Nanoporous Graphene. *Nano Lett.* **12**, 3602–3608 (2012).
174. Song, Y. *et al.* Role of Interfacial Oxide in High-Efficiency Graphene – Silicon Schottky Barrier Solar Cells. *Nano Lett.* **15**, 2104–2110 (2015).
175. Boland, C. S. *et al.* Sensitive, High-Strain, High-Rate Bodily Motion Sensors Based on Graphene-Rubber Composites. *ACS Nano* **8**, 8819–8830 (2014).
176. Lalwani, G. *et al.* Two-Dimensional Nanostructure- Reinforced Biodegradable Polymeric Nanocomposites for Bone Tissue Engineering. *Biomacromolecules* **14**, 900–909 (2013).
177. Lyth, S. M., Jianfeng, L. & Sasaki, K. Electrochemical Oxygen Reduction on Metal-Free Nitrogen-Doped Graphene Foam in Acidic Media. *ECS Trans.* **58**, 1529–1540 (2013).
178. Stephen M. Lyth, Y. Nabae, N. M. Islam, T. Hayakawa, S. Kuroki, M. Kakimoto, S. M. Solvothermal Synthesis of Nitrogen-Containing Graphene for Electrochemical Oxygen Reduction. *eJournal Surf. Sci. Nanotechnol.* **10**, 29–32 (2012).
179. Liu, J., Takeshi, D., Sasaki, K. & Lyth, S. M. Platinum-Decorated Nitrogen-Doped Graphene Foam Electrocatalysts. *Fuel Cells* **14**, 728–734 (2014).
180. Liu, J., Takeshi, D., Sasaki, K. & Lyth, S. M. Defective Graphene Foam: A Platinum Catalyst Support for PEMFCs. *J. Electrochem. Soc.* **161**, F838–F844 (2014).
181. Boehm, H. P., Clauss, A., Fischer, G. O. & Hofmann, U. Das Adsorptionsverhalten sehr dünner Kohlenstoff-Folien. *Zeitschrift für Anorg. und Allg. Chemie* **316**, 119–127 (1962).
182. Dreyer, D. R., Park, S., Bielawski, C. W. & Ruoff, R. S. The chemistry of graphene oxide. *Chem. Soc. Rev.* **39**, 228–240 (2010).
183. Brodie, B. C. On the atomic weight of potassium. *Philos. Trans.* **149**, 249–259 (1859).
184. Ciszewski, M. & Mianowski, A. Survey of graphite oxidation methods using oxidizing mixtures in inorganic acids. *CHEMIK* **4**, 267–274 (2013).
185. He, H., Klinowski, J., Forster, M. & Lerf, A. A new structural model for graphite oxide. *Chem. Phys. Lett.* **287**, 98–101 (1998).
186. Lerf, A., He, H., Forster, M. & Klinowski, J. Structure of Graphite Oxide Revisited |. **5647**, 4477–4482 (1998).
187. Pei, S. & Cheng, H. The reduction of graphene oxide. *Carbon N. Y.* **50**, 3210–3228 (2012).

188. Sreeprasad, T. S. & Berry, V. How do the electrical properties of graphene change with its functionalization? *small* **9**, 341–50 (2013).
189. Chen, J., Yao, B., Li, C. & Shi, G. An improved Hummers method for eco-friendly synthesis of graphene oxide. *Carbon N. Y.* **64**, 225–229 (2013).
190. Staudenmaier, L. Verfahren zur Darstellung der Graphitsäure. *Berichte der Dtsch. Chem. Gesellschaft* **32**, 1394–1399 (1899).
191. Hummers, W. s. & Offeman, R. E. Preparation of Graphitic Oxide. *Am. Chem. Soc.* **80**, 1339 (1957).
192. Momma, K. & Izumi, F. VESTA 3 for three-dimensional visualization of crystal, volumetric and morphology data. *J. Appl. Crystallogr.* **44**, 1272–1276 (2011).
193. Wang, G. *et al.* Synthesis of enhanced hydrophilic and hydrophobic graphene oxide nanosheets by a solvothermal method. *Carbon N. Y.* **47**, 68–72 (2009).
194. Dikin, D. A. *et al.* Preparation and characterization of graphene oxide paper. *Nature* **448**, 457–60 (2007).
195. Bayer, T., Bishop, S. R., Nishihara, M., Sasaki, K. & Lyth, S. M. Characterization of a Graphene Oxide Membrane Fuel Cell. *J. Power Sources* **272**, 239–247 (2014).
196. Yoo, B. M., Shin, H. J., Yoon, H. W. & Park, H. B. Graphene and graphene oxide and their uses in barrier polymers. *J. Appl. Polym. Sci.* **131**, n/a–n/a (2014).
197. Cruz-Silva, R., Morelos-Gomez, A., Kim, H., Jang, H.-K. & Tristan, F. Superstretchable Graphene Oxide Macroscopic Fibers with Outstanding Knotability Fabricated by Dry Film Scrolling. *ACS Nano* **8**, 5959–5967 (2014).
198. Le, L. T., Ervin, M. H., Qiu, H., Fuchs, B. E. & Lee, W. Y. Graphene supercapacitor electrodes fabricated by inkjet printing and thermal reduction of graphene oxide. *Electrochem. commun.* **13**, 355–358 (2011).
199. Min, K. *et al.* A facile route to fabricate stable reduced graphene oxide dispersions in various media and their transparent conductive thin films. *J. Colloid Interface Sci.* **383**, 36–42 (2012).
200. Nair, R. R., Wu, H. A., Jayaram, P. N., Grigorieva, I. V. & Geim, A. K. Unimpeded Permeation of Water Through Helium-Leak-Tight Graphene-Based Membranes. *Science (80-. ).* **335**, 442–444 (2012).
201. Daio, T. *et al.* In-Situ ESEM and EELS Observation of Water Uptake and Ice Formation in Multilayer Graphene Oxide. *Sci. Rep.* **5**, 11807 (2015).
202. Kumar, R., Mamlouk, M. & Scott, K. A Graphite Oxide Paper Polymer Electrolyte for Direct Methanol Fuel Cells. *Int. J. Electrochem.* **2011**, 1–7 (2011).

203. Zarrin, H., Higgins, D., Jun, Y., Chen, Z. & Fowler, M. Functionalized Graphene Oxide Nanocomposite Membrane for Low Humidity and High Temperature Proton Exchange Membrane Fuel Cells. *J. Phys. Chem. C* **115**, 20774–20781 (2011).
204. Karim, M. R. *et al.* Graphene Oxide Nanosheet with High Proton Conductivity. *J. Am. Chem. Soc.* **135**, 8097–8100 (2013).
205. Tateishi, H. *et al.* Graphene Oxide Fuel Cell. *J. Electrochem. Soc.* **160**, F1175–F1178 (2013).
206. Hatakeyama, K. *et al.* Proton Conductivities of Graphene Oxide Nanosheets: Single, Multilayer, and Modified Nanosheets. *Angew. Chemie* **126**, 7117–7120 (2014).
207. Borini, S. *et al.* Ultrafast Graphene Oxide Humidity Sensors. *ACS Nano* **7**, 11166–11173 (2013).
208. Joshi, R. K. *et al.* Precise and ultrafast molecular sieving through graphene oxide membranes. *Science* **343**, 752–4 (2014).
209. Wang, D.-W., Du, A., Taran, E., Lu, G. Q. (Max) & Gentle, I. R. A water-dielectric capacitor using hydrated graphene oxide film. *J. Mater. Chem.* **22**, 21085–21091 (2012).
210. Pei, S., Zhao, J., Du, J., Ren, W. & Cheng, H.-M. Direct reduction of graphene oxide films into highly conductive and flexible graphene films by hydrohalic acids. *Carbon N. Y.* **48**, 4466–4474 (2010).
211. Kumar, R., Xu, C. & Scott, K. Graphite oxide/Nafion composite membranes for polymer electrolyte fuel cells. *RSC Adv.* **2**, 8777 (2012).
212. Chien, H. C. *et al.* Sulfonated graphene oxide/Nafion composite membranes for high-performance direct methanol fuel cells. *Int. J. Hydrogen Energy* **38**, 13792–13801 (2013).
213. Jiang, Z., Zhao, X., Fu, Y. & Manthiram, A. Composite membranes based on sulfonated poly(ether ether ketone) and SDBS-adsorbed graphene oxide for direct methanol fuel cells. *J. Mater. Chem.* **22**, 24862 (2012).
214. Xu, C. *et al.* A polybenzimidazole/sulfonated graphite oxide composite membrane for high temperature polymer electrolyte membrane fuel cells. *J. Mater. Chem.* **21**, 11359–11364 (2011).
215. Tseng, C.-Y. *et al.* Sulfonated Polyimide Proton Exchange Membranes with Graphene Oxide show Improved Proton Conductivity, Methanol Crossover Impedance, and Mechanical Properties. *Adv. Energy Mater.* **1**, 1220–1224 (2011).
216. Lin, C. W. & Lu, Y. S. Highly ordered graphene oxide paper laminated with a Nafion membrane for direct methanol fuel cells. *J. Power Sources* **237**, 187–194 (2013).

217. Jessie, S., Pai, Y., Shih, C., Wu, M. & Lai, S. Novel bilayer well-aligned Nafion/graphene oxide composite membranes prepared using spin coating method for direct liquid fuel cells. *J. Memb. Sci.* **493**, 212–223 (2015).
218. Scott, K. & Ravikumar. Freestanding sulfonated graphene oxide paper: a new polymer electrolyte for polymer electrolyte fuel cells. *Chem. Commun.* **48**, 5584–5586 (2012).
219. Gao, W. *et al.* Ozonated graphene oxide film as a proton-exchange membrane. *Angew. Chemie - Int. Ed.* **53**, 3588–3593 (2014).
220. Yang, J. & Wang, S. Preparation of graphene-based poly(vinylalcohol)/chitosan nanocomposites membrane for alkaline solid electrolytes membrane. *J. Memb. Sci.* **477**, 49–57 (2015).
221. Movil, O., Frank, L. & Staser, J. a. Graphene Oxide-Polymer Nanocomposite Anion-Exchange Membranes. *J. Electrochem. Soc.* **162**, F419–F426 (2015).
222. Liu, L., Tong, C., He, Y., Zhao, Y. & Lü, C. Enhanced properties of quaternized graphenes reinforced polysulfone based composite anion exchange membranes for alkaline fuel cell. *J. Memb. Sci.* **487**, 99–108 (2015).
223. Zarrin, H. *et al.* Quaternized Graphene Oxide Nanocomposites as Fast Hydroxide Conductors. *ACS Nano* **9**, 2028–2037 (2015).
224. Jonas, R. & Farah, L. F. Production and application of microbial cellulose. *Polym. Degrad. Stab.* **59**, 101–106 (1998).
225. Chirayil, C. J., Mathew, L. & Thomas, S. Review of Recent Research in Nano Cellulose Preparation From Different Lignocellulosic Fibers. *Adv. Mater. Sci.* **37**, 20–28 (2014).
226. Peng, B. L., Dhar, N., Liu, H. L. & Tam, K. C. Chemistry and applications of nanocrystalline cellulose and its derivatives: A nanotechnology perspective. *Can. J. Chem. Eng.* **89**, 1191–1206 (2011).
227. Gibson, L. J. The hierarchical structure and mechanics of plant materials. *J. R. Soc. Interface* **9**, 2749–2766 (2012).
228. Moon, R. J., Martini, A., Nairn, J., Simonsen, J. & Youngblood, J. *Cellulose nanomaterials review: structure, properties and nanocomposites*. *Chemical Society Reviews* **40**, (2011).
229. Hon, D. N. S. Cellulose: a random walk along its historical path. *Cellulose* **1**, 1–25 (1994).
230. Beck, C. B. *An Introduction to Plant Structure and Development*. (Cambridge University Press, 2010).

231. Payen, A. Mémoire sur la composition du tissu propre des plantes et du ligneux. *Comptes Rendus l'Académie des Sci.* **7**, 1052–1056 (1838).
232. Turbak, A. F., Snyder, F. W. & Sandberg, K. R. Microfibrillated Cellulose, a New Cellulose Product: Properties, Uses, and Commercial Potential. in *Proceedings of the Ninth Cellulose Conference, Applied Polymer Symposia, 37, New York, N.Y., USA* 815–827 (1983).
233. Turbak, A. F. Birth of Nanocellulose. (2011). at <<http://www.naylornetwork.com/PPI-OTW/articles/?aid=150993&issueID=22333>>
234. Siró, I. & Plackett, D. Microfibrillated cellulose and new nanocomposite materials: a review. *Cellulose* **17**, 459–494 (2010).
235. Dufresne, A. Nanocellulose: a new ageless bionanomaterial. *Mater. Today* **16**, 220–227 (2013).
236. Jiang, F., Esker, A. R. & Roman, M. Acid-catalyzed and solvolytic desulfation of H<sub>2</sub>SO<sub>4</sub>-hydrolyzed cellulose nanocrystals. *Langmuir* **26**, 17919–17925 (2010).
237. Habibi, Y., Lucia, L. A. & Rojas, O. J. Cellulose Nanocrystals : Chemistry , Self-Assembly , and Applications. *Chem. Rev.* **110**, 3479–3500 (2009).
238. Henriksson, M., Berglund, L. A., Isaksson, P., Lindstro, T. & Nishino, T. Cellulose Nanopaper Structures of High Toughness. *Biomacromolecules* **9**, 1579–1585 (2008).
239. Nogi, M., Iwamoto, S., Nakagaito, A. N. & Yano, H. Optically Transparent Nanofiber Paper. *Adv. Mater.* **21**, 1595–1598 (2009).
240. Nogi, M. *et al.* High thermal stability of optical transparency in cellulose nanofiber paper. *Appl. Phys. Lett.* **102**, 181911 (2013).
241. Nair, S. S., Zhu, J., Deng, Y. & Ragauskas, A. J. High performance green barriers based on nanocellulose. *Sustain. Chem. Process.* **2**, 1–7 (2014).
242. Dufresne, A. *Nano-Cellulose: From nature to High Performance Tailored Materials.* (Walter de Gruyter, 2012).
243. Fang, Z. *et al.* Novel nanostructured paper with ultrahigh transparency and ultrahigh haze for solar cells. *Nano Lett.* **14**, 765–73 (2014).
244. Koga, H. *et al.* Uniformly connected conductive networks on cellulose nanofiber paper for transparent paper electronics. *NPG Asia Mater.* **6**, 1–8 (2014).
245. Choi, K. *et al.* Heterolayered, One-Dimensional Nanobuilding Block Mat Batteries. *Nano Lett.* **14**, 5677–5686 (2014).

246. Lee, K.-Y., Aitomäki, Y., Berglund, L. a., Oksman, K. & Bismarck, A. On the use of nanocellulose as reinforcement in polymer matrix composites. *Compos. Sci. Technol.* **105**, 15–27 (2014).
247. Lin, N. & Dufresne, A. Nanocellulose in biomedicine: Current status and future prospect. *Eur. Polym. J.* **59**, 302–325 (2014).
248. Jiang, G. *et al.* Bacterial nanocellulose/Nafion composite membranes for low temperature polymer electrolyte fuel cells. *J. Power Sources* **273**, 697–706 (2015).
249. Hasani-Sadrabadi, M. M. *et al.* Cellulose nanowhiskers to regulate the microstructure of perfluorosulfonate ionomers for high-performance fuel cells. *J. Mater. Chem. A* **2**, 11334–11340 (2014).
250. Jiang, G., Qiao, J. & Hong, F. Application of phosphoric acid and phytic acid-doped bacterial cellulose as novel proton-conducting membranes to PEMFC. *Int. J. Hydrogen Energy* **37**, 9182–9192 (2012).
251. Lin, C. W., Liang, S. S., Chen, S. W. & Lai, J. T. Sorption and transport properties of 2-acrylamido-2-methyl-1-propanesulfonic acid-grafted bacterial cellulose membranes for fuel cell application. *J. Power Sources* **232**, 297–305 (2013).
252. Kasai, Y., Akahira, A., Abdulla, A., Urayama, K. & Takigawa, T. Proton Conductivity and Methanol Permeability of Cellulose Sulfate Membranes. *Kobunshi Ronbunshu* **66**, 130–135 (2009).
253. Smolarkiewicz, I. *et al.* Proton-conducting Microcrystalline Cellulose Doped with Imidazole. Thermal and Electrical Properties. *Electrochim. Acta* **155**, 38–44 (2015).

## 2 Experimental

### 2.1 Sample Preparation

#### 2.1.1 Graphene Oxide Membranes

Graphene oxide (GO) membranes were prepared by vacuum-filtration from GO dispersion onto Millipore filters (pore size 0.025  $\mu\text{m}$ , 35 mm diameter), as shown Figure 2.1a. After filtration and 48 hours drying at room temperature the GO membranes could be easily peeled off the filter yielding freestanding and flexible membranes (Figure 2.1b-c). The thickness of the membranes was adjusted by varying the amount of GO dispersion used for filtration. The approximate relationship was that 1 mg GO corresponded to 0.6  $\mu\text{m}$  membrane thickness.

For this work, GO dispersions were purchased from *Graphene Supermarket*. The properties of the dispersion were provided by the supplier (apart from the oxygen content which was measured in our lab) and are listed in Table 2.1.

*Table 2.1. Properties of as-purchased GO dispersion.*

| Supplier                     | Graphene Supermarket |
|------------------------------|----------------------|
| Monolayer Content (%)        | > 60                 |
| C/O ratio                    | 3.95                 |
| Flake Size ( $\mu\text{m}$ ) | 0.5 - 5              |
| Concentration (mg/ml)        | 5                    |
| Price per 100 ml (JPY)       | 10,200               |
| Oxygen Content (at%)*        | 22.5                 |
| *Measured in our lab         |                      |

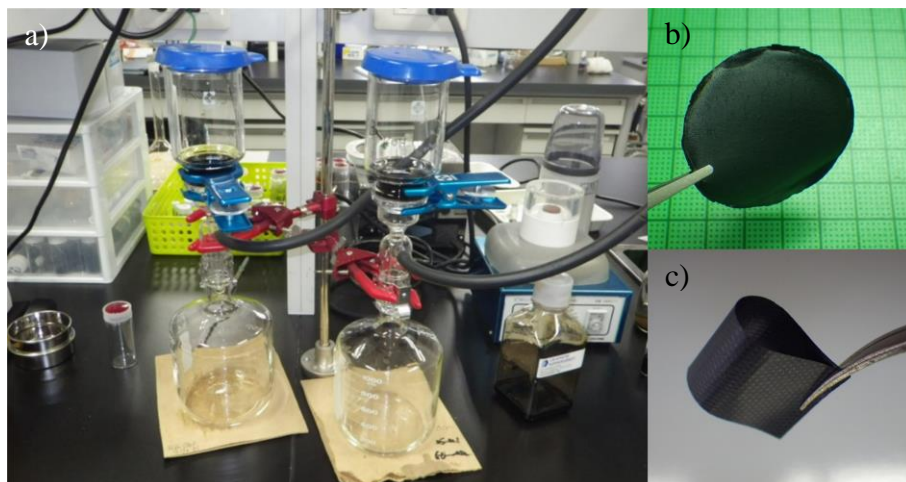


*Figure 2.1. a) Vacuum-filtration of graphene oxide (GO) dispersion. b-c) Free-standing and flexible GO membranes.*

### **2.1.2 Nanocellulose Membranes**

Cellulose nanofiber (CNF) and cellulose nanocrystal (CNC) slurry (3.0 wt% and 11.8 wt% solids, respectively, shown in Figure 2.2a-b) was purchased from the University of Maine, US. Both slurries were diluted with purified water as follows:

100.2 g of the CNF slurry was mixed with 500 ml of purified water and magnetically stirred for 24 hours at 500 rpm. The dispersion was vacuum-filtered onto Millipore filters (pore size 0.1  $\mu\text{m}$ , 35 mm diameter). After filtration the CNF membranes were hot-pressed for 20 min (110°C at 1.1 MPa) and then carefully peeled from the filter. The resulting membranes are freestanding, flexible and foldable like regular cellulose-based paper. 1 mg of CNF corresponds to an average membrane thickness of 0.12  $\mu\text{m}$ .

52.9 g of the CNC slurry was mixed with 500 ml of purified water and stirred for 24 hours at 500 rpm. The dispersion was vacuum-filtered onto Millipore filters (pore size 0.1  $\mu\text{m}$ , 35 mm diameter). After filtration the CNF membranes were dried for 24 hours at room temperature and then carefully peeled of the filter. The resulting membranes are freestanding, but quite brittle and highly transparent. 1 mg of CNC corresponded to an average membrane thickness of 0.09  $\mu\text{m}$ .

Figure 2.2c shows CNF and CNC nanocellulose membranes/paper in comparison with regular printer paper (all similar thickness,  $\sim 90\mu\text{m}$ ).

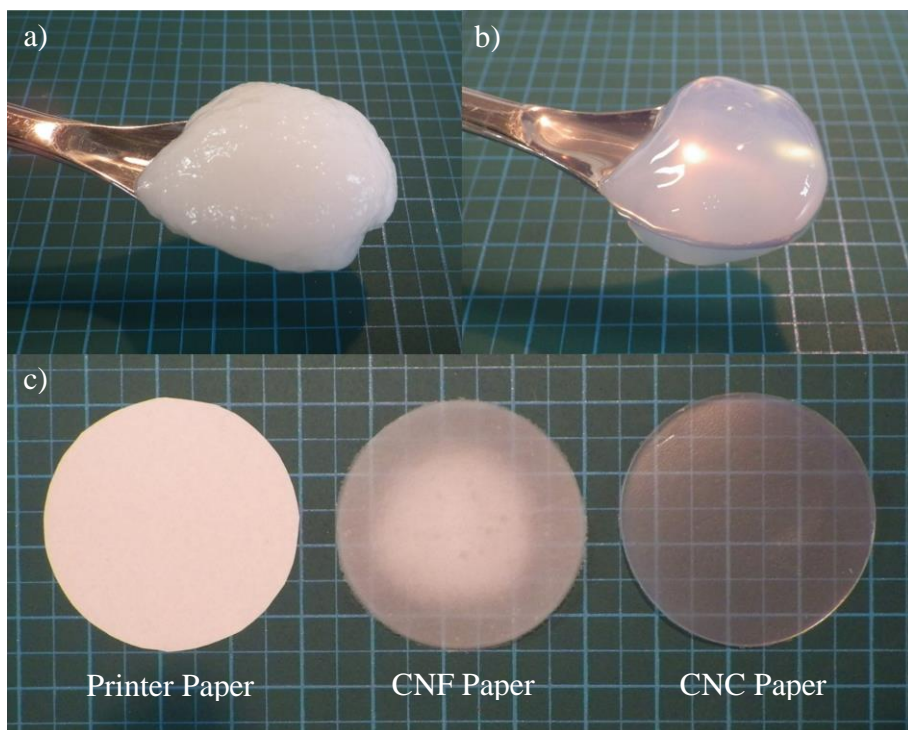


Figure 2.2. a) CNF slurry (3.0 wt% solids). b) CNC slurry (11.8 wt% solids). c) Appearance of prepared CNF and CNC papers in comparison to regular printer paper (all similar thickness,  $\sim 90 \mu\text{m}$ ).

## 2.2 Experimental Techniques for Material Characterization

### 2.2.1 Scanning Electron Microscopy

Scanning electron microscopy (SEM) is a useful measure to investigate the topography of material. Instead of light it uses electrons to scan the sample and forms a highly magnified image with possible resolution up to 10 or 50 Å.<sup>2,3</sup> The first SEM was invented in Germany by Manfred von Ardenne in 1937.<sup>4-6</sup> Figure 2.3a-b shows the principle of SEM. High vacuum environment is used to avoid interaction with other molecules in the air. An electron gun produces and accelerates electrons to a typical energy of 1 to 40 keV. Via a combination of lenses and objective apertures this electron beam is focused on the sample surface. Scan-coils precisely control the electron beam position to allow controlled scanning of the sample surface. Secondary electrons, backscattered electrons and characteristic x-rays (produced by interaction of electron beam with the sample surface) are detected, amplified and the signal

is converted into an image. In this work a *Hitachi SEM S-5200* (Figure 2.3c) was used to investigate surface and cross-section of membranes and membrane electrode assemblies.

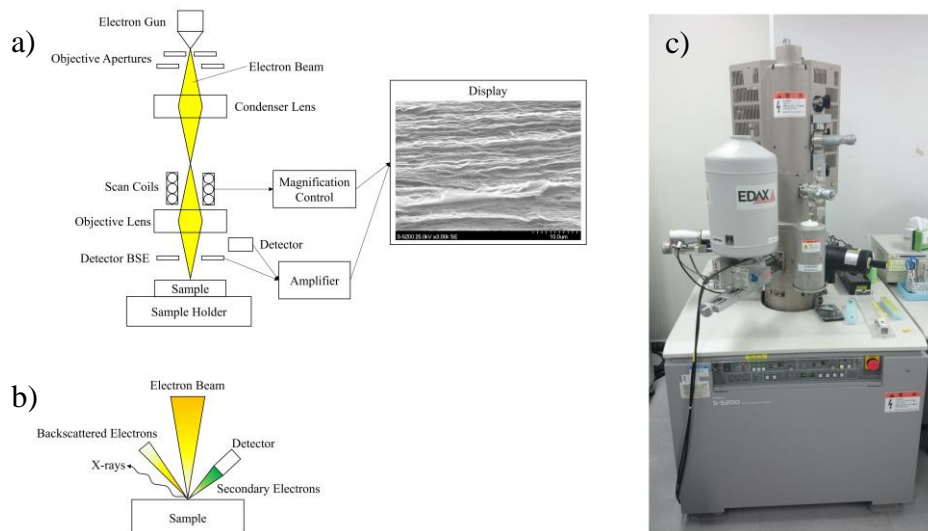


Figure 2.3. a-b) Principle of scanning electron microscopy. c) Hitachi SEM S-5200.

## 2.2.2 Laser Scanning Microscopy

Laser scanning microscopy is a non-destructive technique for investigation of surfaces, with the ability of quantifying surface features.<sup>6,7</sup> Confocal microscopy, the basic concept of laser microscopy was developed at in the mid-1950s by Marvin Minsky, a postdoctoral student at Harvard University.<sup>6</sup> Compared to conventional optical microscopy, laser scanning microscopy offers several advantages such as e.g. the capability to collect serial optical sections from the sample as well as analysis of three-dimensional (3D) surface structures, including surface roughness.<sup>6,7</sup>

The principle of laser scanning microscopy is shown in Figure 2.4a. A laser is used as a light source for contrast improvement, as it reduces unnecessary scattered light due to high light density on a small point.<sup>8</sup> The laser is beamed onto the sample via a pinhole aperture, dichromatic mirror and an objective lens, and the sample surface is scanned in a defined focal plane. The reflected light from the sample (fluorescence emission light) passes back through the dichromatic mirror towards the detector pinhole aperture. The light-source pinhole

aperture, the scanning point and the detector pinhole aperture are confocal i.e. they have the same focus point. Reflected fluorescence emission light outside the focal position is blocked at the detector pinhole, resulting in a clear and high contrast image.<sup>6-8</sup>

In this work, the surface roughness of samples was observed using an *Olympus LEXT 3D OLS 4000* laser scanning microscope (Figure 2.4b). For determination of the roughness profile, a short wave Gaussian profile filter with a cut-off length of  $\lambda = 80 \mu\text{m}$  and an evaluation length of  $700 \mu\text{m}$  was used.

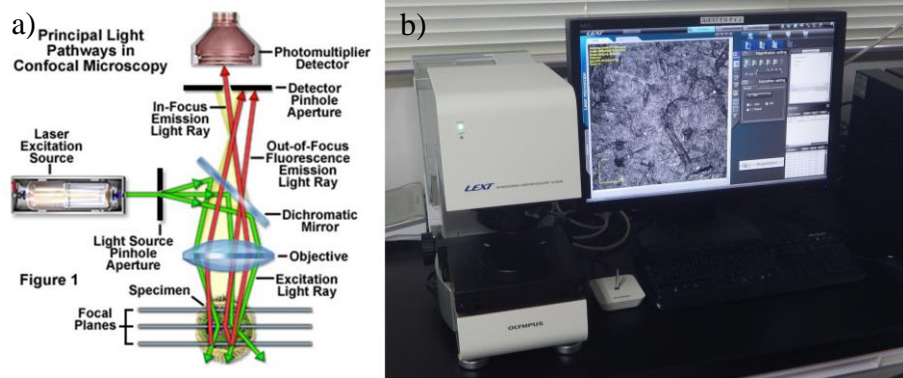


Figure 2.4. a) Principle of laser scanning microscopy.<sup>9</sup> b) Olympus LEXT 3d OLS 4000.

### 2.2.3 X-Ray Photoelectron Spectroscopy

X-ray photoelectron spectroscopy (XPS) is a powerful technique to determine the chemical composition (elemental analysis and chemical bonding states) of near the surface of materials, to a depth of 2 to 5 nm.<sup>10,11</sup> It was developed in the 1960s at University of Uppsala (Sweden) by the Nobel prize winner Kai Siegbahn and his research group.<sup>12,13</sup> Its principle is based on the photoelectric effect,<sup>14,15</sup> as shown in Figure 2.5a. A sample material is irradiated with X-rays; common X-ray sources are Mg K $\alpha$  (1253.6 eV) and Al K $\alpha$  (1486.6 eV).<sup>10</sup> The incident X-rays hit the surface and excite electrons in the atoms of the material. These excited electrons gain enough energy to escape from the sample surface if their binding energy is lower than the energy of the incident X-ray energy (in case of Al K $\alpha$  this is 1486 eV), and if they are near the surface. The kinetic energy of an ejected photoelectron is determined by an analyzer and the binding energy  $E_b$  is calculated using  $E_{kin} = h \cdot \nu - E_b$ ,<sup>16</sup> with kinetic

energy of the photoelectron  $E_{kin}$ , X-ray energy  $h \cdot \nu$  and the electron binding energy  $E_b$ . Each element has a characteristic binding energy, and thus it is possible to determine the chemical composition of the sample. The measurement is conducted in ultrahigh vacuum in order to reduce the impact of surface contamination e.g. absorbed gases, and to avoid energy loss of electrons.<sup>10</sup>

In this work two XPS devices were used; *KRATOS Analytical ESCA-3400* (Figure 2.5b) with Mg K $\alpha$  radiation (12 kW, 10mA) and *ULVAC-PHI 5000 Versa Probe II* (Figure 2.5c) with Al K $\alpha$  radiation (15 kV, 25 W).

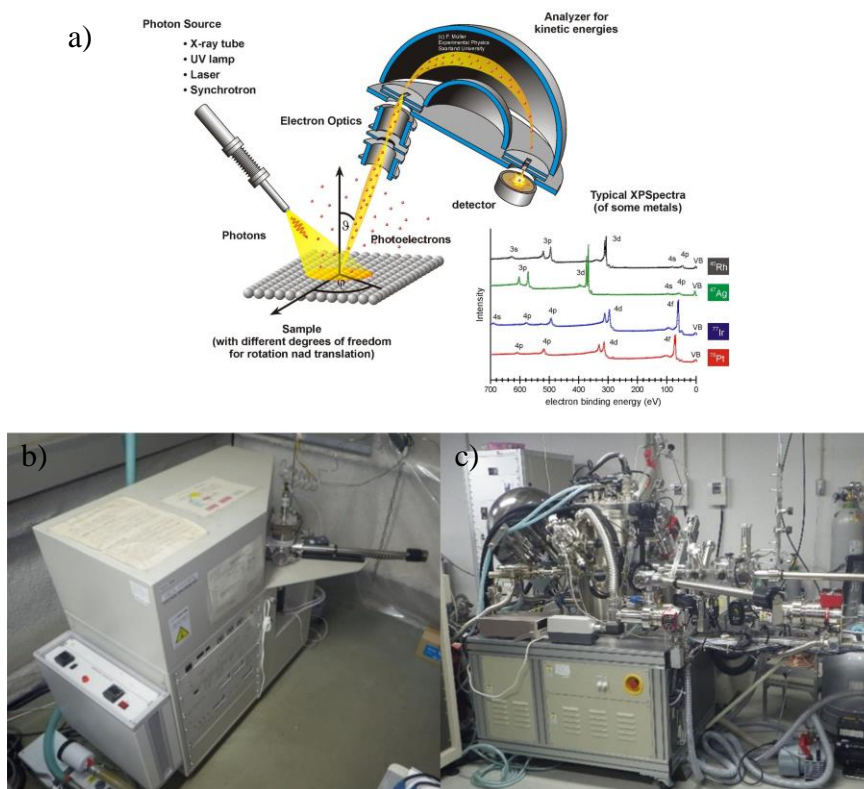


Figure 2.5. a) Principle of X-ray photoelectron microscopy (XPS).<sup>17</sup> b) *KRATOS Analytical ESCA-3400* c) *PHI 5000 Versa Probe II*.

## 2.2.4 X-Ray Diffraction

X-ray diffraction (XRD) is a measurement technique which uses X-rays to investigate the crystallinity of a material, i.e. the crystal structure and orientation, or the spaces between atomic layers.<sup>18</sup> The principle is based on the Bragg equation (W.H. and W.L. Bragg, 1913, Nobel prize in 1915), which describes the position of X-ray scattering peaks in angular space:<sup>18,19</sup>

$$2d \cdot \sin(\theta) = n \cdot \lambda \quad (2.1)$$

with interlayer spacing  $d$ , angle between incident and scattering X-ray  $\theta$ , positive integer  $n$  and X-ray wavelength  $\lambda$ . XRD apparatus consists of three main parts: an X-ray source (in case of our device Cu  $K\alpha$  radiation), a sample stage, and an X-ray detector. The sample is irradiated with X-rays. When hitting an atom in the lattice/crystal structure of the sample, the X-rays are reflected, i.e. diffracted. The intensity of diffracted X-rays is measured by the detector. In order to investigate different diffraction angles, the X-ray source and the detector are rotated as schematically shown in Figure 2.6a. The X-rays are diffracted from many locations/atoms in the sample, resulting in scattering in all directions. However the diffracted X-rays are in phase at certain angles, and these are dependent on the spacing between atomic layers. At this angle the X-ray signal is amplified, giving a characteristic high intensity diffraction peak.<sup>20</sup> For example, the interlayer spacing between GO sheets can be obtained from the diffraction peak angle by using Bragg's equation.<sup>21</sup> X-ray diffraction was measured using a *Rigaku Smartlab* X-ray Diffractometer (Figure 2.6b) with Cu  $K\alpha$  radiation ( $\gamma = 1.5418$  Å,  $0.01^\circ/\text{step}$ ).

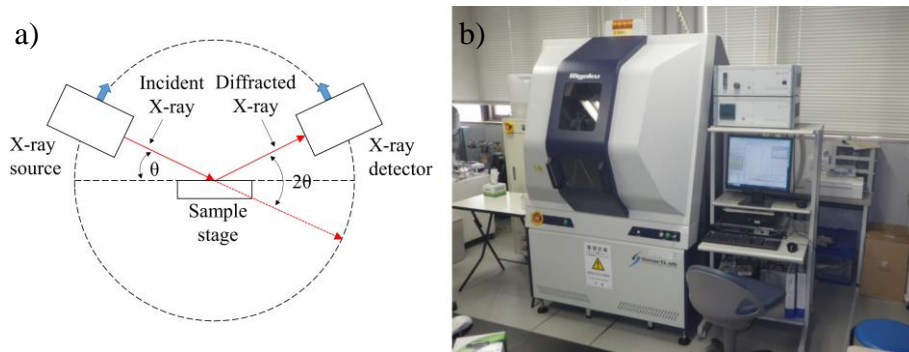


Figure 2.6. a) Principle of X-ray diffraction (XRD). b) Rigaku Smartlab X-ray Diffractometer.

### 2.2.5 Raman Spectroscopy

Raman spectroscopy is a technique used to investigate vibrational motions in molecules in order to obtain information about chemical structures, physical forms and material properties such as e.g. crystallinity.<sup>22</sup> The principle, schematically shown in Figure 2.7a, is based on inelastic scattering of monochromatic light and it is named after inventor and Physics Nobel Prize winner Sir Chandrasekhara Venkata Raman, who discovered inelastic scattering of light in 1923.<sup>22,23</sup>

A Raman system comprises a laser source, sample lighting and collection optics, a wavelength filter and a CCD detector. Laser light is irradiated onto a sample and interacts with the molecules (absorption or scattering). Most of the light is scattered back unchanged (Rayleigh scattering), however a very small amount is scattered at a different wavelength (Raman scattering and anti-Stokes scattering). Rayleigh and anti-Stokes scattered light are filtered from the signal using a notch filter, and remaining Raman signal is detected.<sup>22,24,25</sup> The Raman spectrum, a characteristic fingerprint of an observed material, is obtained by plotting the intensity of the Raman scattered light as a function of its frequency difference from the excitation wavelength (wavenumber shift). In this work a *RENISHAW* inVia Raman Microscope (Figure 2.7b) with 532 nm laser excitation wavelength was used.

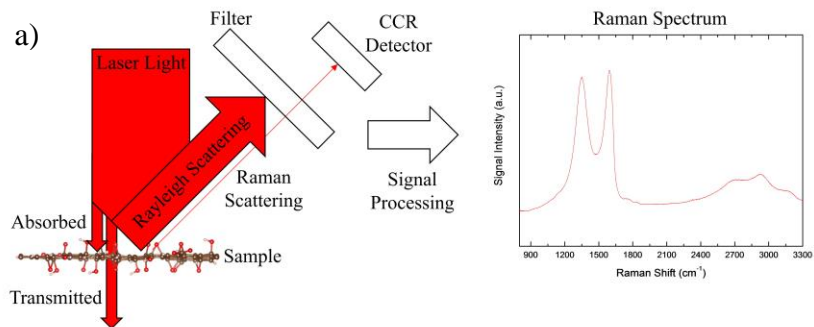


Figure 2.7. a) Principle of Raman spectroscopy. b) RENISHAW inVia Raman Microscope.

## 2.2.6 Atomic Force Microscopy

Atomic force microscopy (AFM) is a non-destructive method to investigate surfaces of conducting and insulating materials on an atomic scale.<sup>26–29</sup> AFM was invented in 1985 by Binnig et al. at Stanford University, and its principle is based on Hooke’s law.<sup>28–30</sup> Figure 2.8a shows the principle of AFM with beam-deflection method (the most commonly used method).<sup>26</sup> The main components of the device are the cantilever with a scanning tip (usually silicon or silicon nitride), a laser source, a position-sensitive detector (quartered photodiode) with evaluation electronics and a 3-axis-movable sample stage. The sample stage moves slowly in the horizontal direction and the sample surface is scanned with the tip of the cantilever. During scanning, normal and lateral forces act on the tip, leading to bending and torsion of the cantilever.<sup>26,27</sup> A laser beam is focused onto the upper side of the cantilever, where it is reflected. The deflection of the laser beam is detected by the photodiode and a topographic image is created by plotting the position of the scanning tip versus the

deflections.<sup>26,27,29</sup> AFM has a very high resolution (vertical resolution  $\sim 1 \text{ \AA}$ , lateral resolution  $\sim 30 \text{ \AA}$ ),<sup>29,30</sup> allowing the structural investigation of nanomaterials.

In this work a *Seiko Instruments* scanning probe microscope unit (SPA300HV, Figure 2.8c) with a SPI 3800 N probe-station (Figure 2.8d) and SN-AF01 cantilevers (SiN, 100  $\mu\text{m}$  tip height, Figure 2.8b) was used to investigate the surface of nanocellulose for their morphology and surface roughness. AFM samples were prepared by dropping 100  $\mu\text{l}$  of nanocellulose dispersion onto 1  $\text{cm}^2$  silicon substrates and the assessed area was 4  $\mu\text{m}$  x 4  $\mu\text{m}$ . The average roughness was calculated by using 10 horizontal and 10 vertical line roughness profiles.

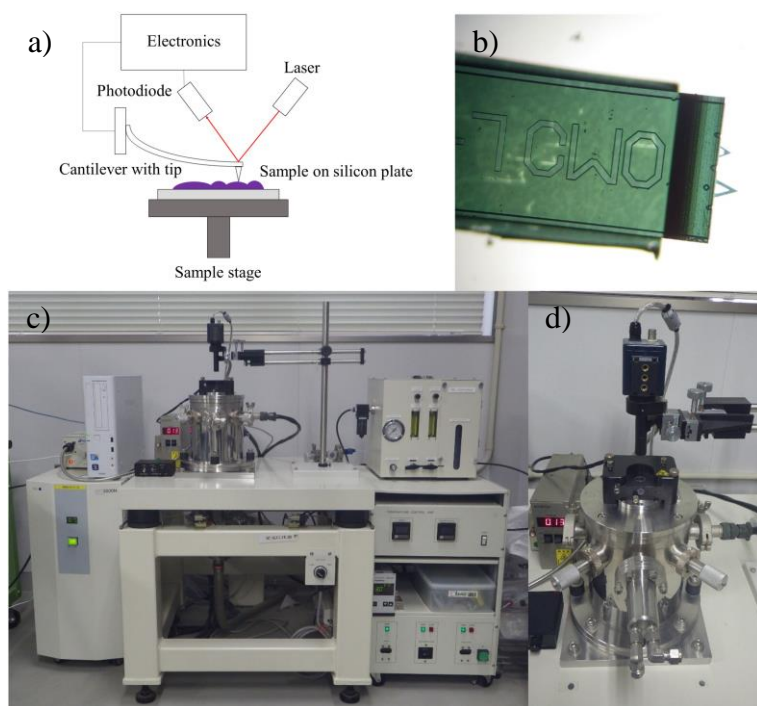


Figure 2.8. a) Principle of atomic force microscopy. b) Microscope image of an SN-AF01 cantilever (SiN, 100 $\mu\text{m}$  height). c) Seiko Instruments scanning probe microscope unit SPA300HV with SPI 3800 N probe station. d) SPI 3800 N probe station with laser attachment and camera unit.

### 2.2.7 Thermogravimetric Analysis

Thermo-gravimetric analysis (TGA) and differential thermal analysis (DTA) are used to investigate the behavior of materials during combustion and pyrolysis, by measuring the

change in sample mass (TGA) and the temperature difference between the sample and an inert reference material (DTA) during heating at a constant rate.<sup>31,32</sup>

The device consists of a highly precise balance (e.g.  $\pm 0.1 \mu\text{g}$ ) with two sample holders containing thermocouples, within a furnace (Figure 2.9a).<sup>31</sup> The sample crucible comprises ceramic (e.g.  $\text{Al}_2\text{O}_3$ ) or metal (e.g. Pt, or aluminum), depending on the operation temperature. The furnace is flooded with gas to create a specific atmosphere, usually air or nitrogen. Mass change during heating occurs when the sample e.g. loses water by evaporation, oxidative decomposition in air, or thermal decomposition in nitrogen atmosphere.<sup>31</sup> The TGA curve is usually normalized and starts at 100% sample weight. Difference in temperature between sample and reference may occur from processes such as glass transition, melting or evaporation of incorporated water. The exothermic or endothermic character of the process is shown by the DTA curve and characteristic temperatures e.g. glass transition temperature can be determined.<sup>31</sup>

In this work a Thermo plus EVO2 TG8121 (*Rigaku*, Figure 2.9b) with a constant heating rate of 5 K/min was used. Samples were placed in  $\text{Al}_2\text{O}_3$  crucibles (5 mm diameter, 5 mm height, Figure 2.9c). The data was evaluated using the program Thermo plus EVO Analysis.

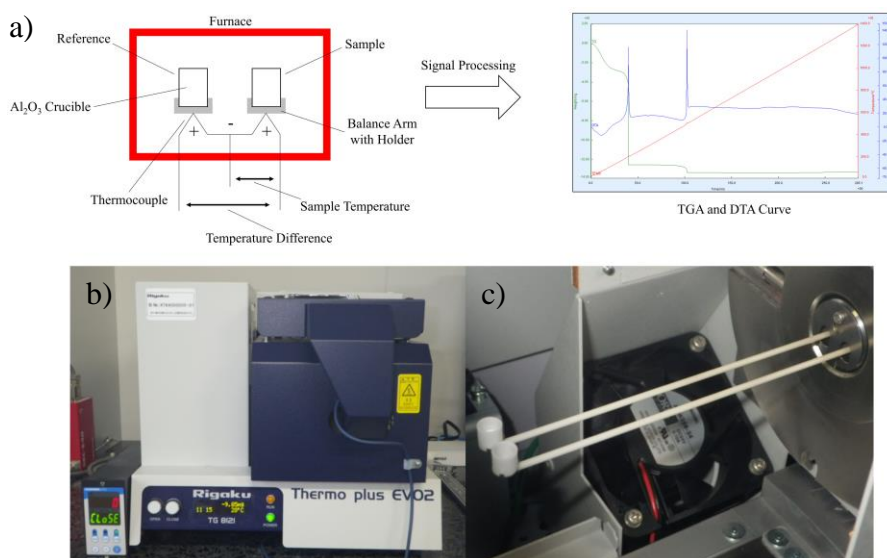


Figure 2.9. a) Schematic of a TGA Device. b) Rigaku Thermo plus EVO2 TG8121; c) internal balance beams with holders.

### 2.2.8 Ion Exchange Capacity Measurements

The H<sup>+</sup> IEC of GO membranes was performed by immersing and sonicating the dry GO membrane in 1M NaCl solution to exchange the acidic protons of GO with Na<sup>+</sup>. The released protons were titrated to neutral pH with 0.01 M NaOH solution. The OH<sup>-</sup> IEC was obtained by redispersing a dry GO<sub>KOH</sub> membrane in 15 mL of milli-Q H<sub>2</sub>O with the assistance of sonication. The dispersion was titrated back to the original pH of GO solution ( $\approx 3.5$ ) using 0.01 M HCl solution. The IECs (in mmol/g) were determined from the following equation, where  $V_x$  and  $C_x$  are the volume and concentration, respectively, of NaOH or HCl:

$$E = \frac{V_x \times C_x}{\text{Membrane Weight}} \quad (2.2)$$

### 2.2.9 Water Uptake and Swelling Measurements

Water-uptake is an important factor in fuel cell membranes, since the proton conductivity usually strongly relates to the amount of absorbed water. Strong swelling on the other hand can lead to deterioration of the electrolyte-electrocatalyst interface.

In this work, water uptake and swelling (i.e increase in thickness) were measured on samples with a size of 10 x 10 mm. For each material, five samples were measured for reproducibility. Samples were first vacuum dried at 60°C for two hours. The mass was then determined using an analytical balance (*Mettler Toledo*,  $\pm 0.1$  mg, Figure 2.10a) and the thickness was determined using a micrometer (*Mitutoyo*,  $\pm 1$   $\mu\text{m}$ , Figure 2.10b). Samples were then placed into a water bath at room temperature for one hour. After saturation, excess surface water was removed carefully with a tissue, and the mass and thickness were measured again. The alkaline GO membranes displayed strong swelling in water, affecting the mechanical properties to the extent that handling freestanding samples was impossible. Therefore the membranes in Chapter 4.3.5 were supported on silicon wafers and a water droplet was placed over the membrane covering it completely. After saturation, excess water was carefully removed using a tissue and the mass was measured. Water uptake (*WU*) was calculated using Equation ( 2.3 ), where  $m_{\text{wet}}$  and  $m_{\text{dry}}$  are the wet and dry masses, respectively:

$$WU (\%) = \frac{m_{\text{wet}} - m_{\text{dry}}}{m_{\text{dry}}} \cdot 100\% \quad (2.3)$$

Swelling ( $S_w$ ) was calculated by using Equation ( 2.4 ), where  $T_{wet}$  and  $T_{dry}$  are the wet and dry thicknesses of the samples, respectively:

$$S_w (\%) = \frac{T_{wet} - T_{dry}}{T_{dry}} \cdot 100\% \quad (2.4)$$

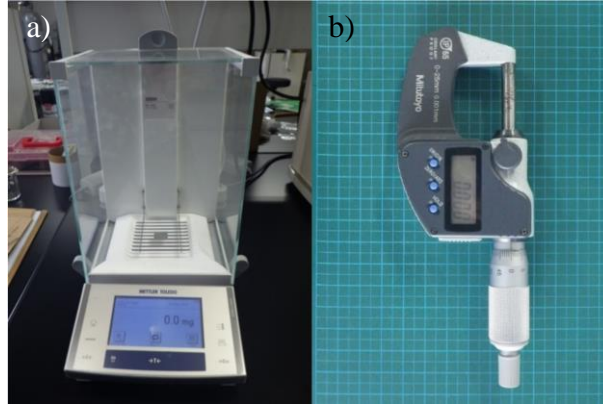


Figure 2.10. Mettler Toledo analytic balance. b) Mitutoyo micrometer.

### 2.2.10 Gas Barrier Measurements

Gas barrier properties of fuel cell electrolytes are important, as fuel crossover reduces the performance and efficiency of fuel cells, as well as compromising safety.

Permeability ( $P$ ) can be expressed as the product of the diffusion ( $D$ ) and solubility ( $S$ ) coefficient and the dependence of transport parameters in organic polymers is typically described by Arrhenius-van't Hoff equations:<sup>33,34</sup>

$$P = D \cdot S \quad (2.5)$$

$$S = S_0 \cdot e^{-\Delta H_S / R \cdot T} \quad (2.6)$$

$$D = D_0 \cdot e^{-\Delta E_D / R \cdot T} \quad (2.7)$$

$$P = P_0 \cdot e^{-\Delta E_P / R \cdot T} \quad (2.8)$$

where  $\Delta H_S$  is the enthalpy of sorption and  $E_D$  and  $E_P$  are respectively the activation energies of diffusion and permeation. From the four formulas  $E_P = E_D + \Delta H_S$  can be received by transformation. In general diffusion coefficient is stronger dependent on temperature than the

solubility coefficient and  $E_D$  is therefore bigger than the absolute value of  $\Delta H_s$ . For organic polymers a typically observed behavior is therefore that permeability increases with increasing temperature.<sup>33,34</sup>

For gas permeance measurements, the membrane area was masked with kapton and alumina tapes to provide a sample circle of desired diameter and area ( $d = 1$  cm,  $A = 0.785$  cm<sup>2</sup>) as shown in Figure 2.11a. To prevent bending under vacuum, the membrane is placed on a porous polycarbonate support filter (1.2  $\mu$ m pore size). Dry hydrogen permeation through the test membranes was measured at different temperatures using a GTR-11A/31A gas barrier testing system (*GTR Tec Corporation*, Japan, Figure 2.11c). The part of the machine where test gas is sampled (GTR-31AKU, Figure 2.11b) uses differential-pressure method for film permeability testing where gas permeation is induced by the vacuum on the permeate side and extra pressure applied at the feed side, as shown in Figure 2.11d. Total pressure difference was set to 200 kPa. In order to obtain gas concentration sufficient for detection using gas chromatography, the sample collection time after vacuuming the sweep side of the membrane was 30 minutes. The gas collected was transferred to a gas chromatograph and the volume of gas was measured. The gas sampling system is combined with a gas chromatograph, with a thermal conductivity detector (TCD) (*Yanaco G3700T*, Japan), as shown in Figure 2.11e. Operation parameters of the gas chromatograph are listed in the Table 2.2. Both permeance in GPU units and permeability in barrer units were estimated for membranes of different thickness,<sup>35</sup> and compared to the reference Nafion membrane. Operation parameter of the gas chromatograph are shown in Table 2.2.

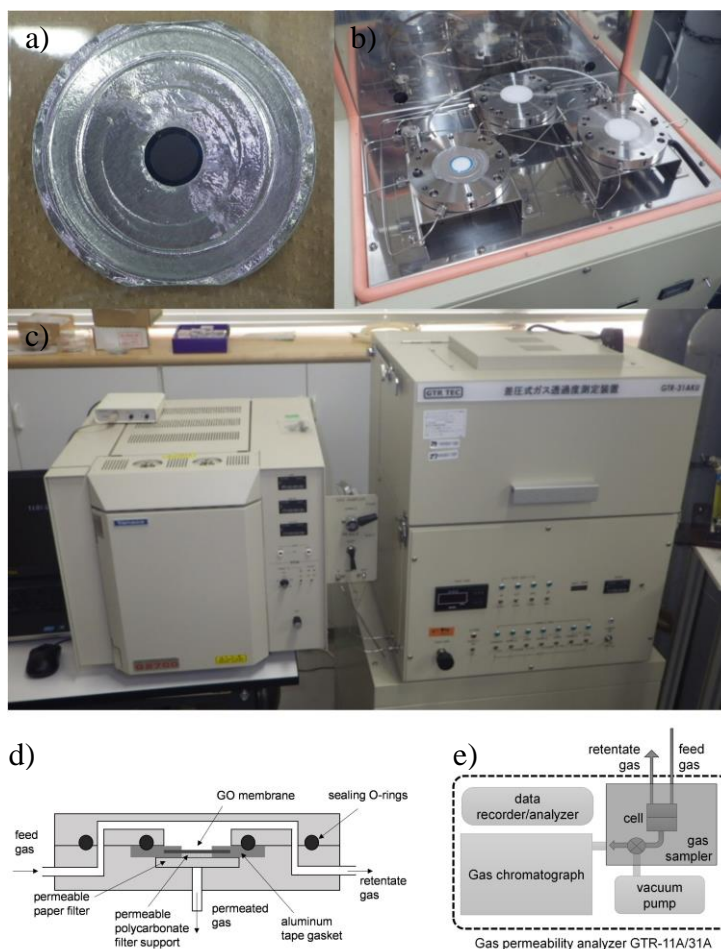


Figure 2.11. Gas permeation measurement system: a) Schematic of the permeation cell; b) Schematic of the GTR-11A/31A gas permeation measurement system; c) Graphene oxide membrane mounted in the system; d) Permeation cells of the gas permeability analyzer; e) Schematic of gas permeability analyzer GTR-11A/31A.

Table 2.2. Gas chromatograph operation parameter.

|                            |   |
|----------------------------|---|
| Column                     | Porapak Q packed column,<br>2 m, 1/8 inch, mesh 50/80 |
| Oven temperature (°C)      | 60  |
| Detection method           | TCD   |
| Detector temperature (°C)  | 150   |
| Detector current (mA)      | 40  |
| Current polarity           | Negative  |
| Carrier gas                | Ar  |
| Carrier gas pressure (kPa) | 110   |
| Carrier gas flow (cc/min)  | 30  |

### 2.2.11 Tensile Strength Testing

Tensile strength and elongation (strain) until rupture are both important mechanical properties regarding membrane-handling, MEA preparation and cell longevity, because they give information about the “work performance” (i.e. the amount of deformation the membrane will bear without failure). Tensile strength testing is a method to determine mechanical properties such as tensile strength, Young’s Modulus and flexibility of a material. A specimen with defined length, width and thickness is slowly extended until rupture, while monitoring the tension with a force gauge. The tensile strength at rupture ( $\sigma$ ) was calculated using:

$$\sigma = \frac{F}{A} \quad (2.9)$$

where  $F$  is the applied force, and  $A$  is the initial cross-sectional area of the sample. Strain ( $\varepsilon$ ) was calculated using:

$$\varepsilon = \frac{L}{L_0} \cdot 100\% \quad (2.10)$$

where  $L$  is the length of the sample during elongation and  $L_0$  is the initial sample length. Elastic modulus  $E$  is defined as the slope of the stress-strain curve in the elastic region and was calculated using:

$$E = \frac{\sigma}{\varepsilon} \quad (2.11)$$

In this work a hydraulic testing machine with 5 N force gauge (*SHIMPO* FGO-C-TV, Figure 2.12a) was used with an elongation speed of 10 mm per minute. Samples can be cutted by using a dumbbell shape specimen cutter (Figure 2.12b).

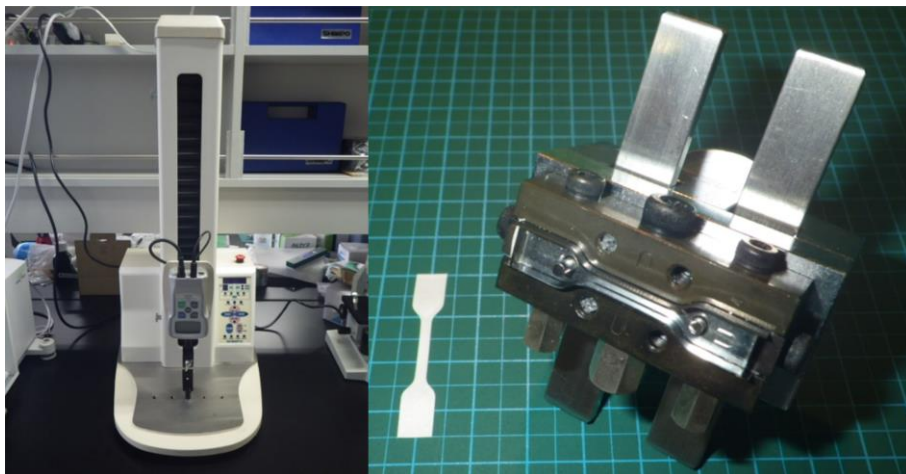


Figure 2.12. a) Hydraulic Testing Machine SHIMPO FGO-C-TV with 5 N force gauge. b) Dumbbell shape specimen cutter.

### 2.2.12 Impedance Spectroscopy

Impedance spectroscopy is a small-signal excitation technique with the assumption of a linear current-voltage relation. It is a non-destructive technique that can also provide valuable information about electrochemical systems such as batteries and fuel cells.<sup>36-39</sup>

An AC amplitude voltage ( $\pm 10$  mV to ensure a pseudo-linear response) with changing frequency is applied to a conducting sample and its response, i.e. a phase-shifted AC current signal is measured and converted into impedance. This is usually plotted as Nyquist plot, with both real and imaginary impedences.<sup>36,40,41</sup> The use of impedance spectroscopy to determine the conductivity of solid electrolytes was first used by Bauerle in 1969 when investigating yttria-stabilized zirconia,<sup>36,42</sup> and is now a common technique to precisely investigate the conductivity of new fuel cell electrolytes.<sup>43</sup>

To investigate the conductivity of the electrolytes studied here, impedance spectroscopy measurements were performed using a commercially available membrane testing system shown in Figure 2.13a (*Scribner Associates Inc.*, MTS 740) coupled with an impedance analyser (*TOYO Corporation*, Solartron SI 1260). For through-plane conductivity membranes with 10 x 30 mm sample size were measured over an AC frequency range of 30 MHz to 1 Hz, with an AC amplitude of  $\pm 10$  mV. Gas diffusion electrodes (*E-TEK*, High Temperature ELAT, E-W, 18 x 5 mm) between the membrane and platinum electrodes of the

testing rig (Figure 2.13b) were attached using conductive carbon paint (*SPI Supplies*, colloidal graphite, Part #05006-AB). The cell was uniaxially compressed with a pressure of 1.074 MPa to obtain a good contact between the membrane and electrodes. A schematic of the 2-electrode/4-terminal cell setup is shown in Figure 2.13e. This electrode-membrane arrangement comprises two electrode-membrane interfaces and the membrane as bulk. For in-plane conductivity measurement another testing rig (Figure 2.13c) was used, with a total distance of 5 mm between the platinum electrodes.

The impedance spectra were evaluated using *Zview* (*Scribner Associates Inc.*). The frequency dependent data is fitted using equivalent circuits to determine membrane resistance and capacitance. This analysis is aided by the use of Nyquist plots where the X-axis represents the real part of the impedance, and Y-axis represents the imaginary part. The Nyquist plots of our measurements generally show two semicircles, dependent on the measured frequency. Due to the larger capacitance of the thin electrode/membrane interface as compared to the relatively thicker membrane, the time constant (given by resistance multiplied by capacitance) is typically larger for the electrodes. Therefore, the impedance arc attributed to the electrode typically occurs at low frequency (i.e. the inverse of time constant), and the membrane impedance is found at higher frequency, as depicted by the right and left arcs in Figure 2.13d.<sup>39,40</sup> The diameter of this high frequency semicircle is equivalent to the resistance of the membrane. This simplified impedance plot can be modeled by an equivalent circuit comprising a series of two parallel RC-circuits, with the possibility in replacing the capacitor by a constant phase element (Figure 2.13d).

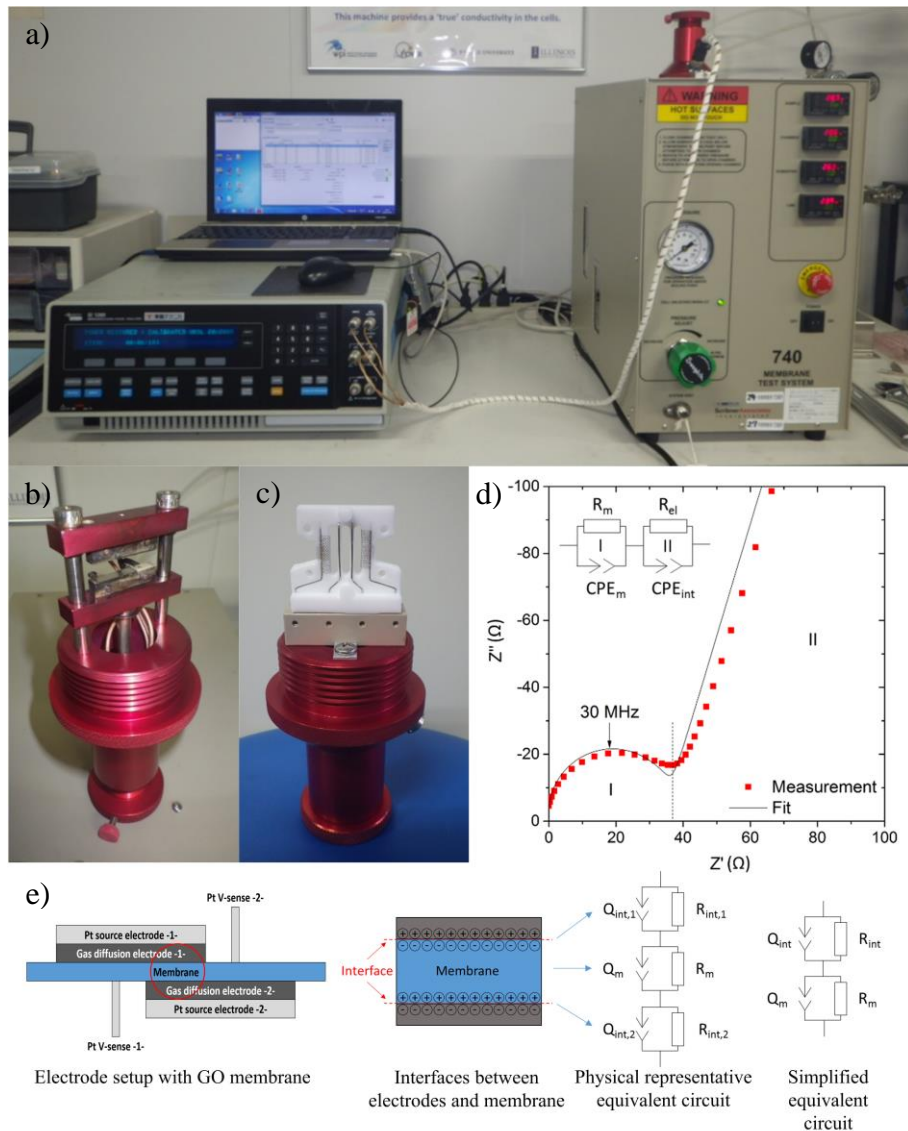


Figure 2.13. a) Membrane test system MTS 740 (right) with Solartron impedance analyzer (left). b) Electrode setup of the MTS 740 for through-plane conductivity measurements with Pt-blocking electrodes. c) Electrode setup of the MTS 740 for in-plane conductivity measurements. d) Representative impedance spectra of GO membrane at 30°C and 100% RH showing measurement data and fitting curve with equivalent circuit. e) Schematic of the MTS 740 electrode setup for through-plane conductivity measurement with corresponding electrode/membrane interfaces and representative equivalent circuits.

## 2.3 Membrane Electrode Assembly Fabrication and Characterization

### 2.3.1 Membrane Electrode Assembly Fabrication

The membrane electrode assembly (MEA) fabrication process for Nafion-based, GO-based and nanocellulose-based MEAs is nearly identical and is schematically shown in Figure 2.14a. Electrocatalyst ink was prepared by mixing Pt/C electrocatalyst (Tanaka Kikinzoku Kogyo K.K., 46.2 wt% Pt) with 5 wt% Nafion solution (*Wako*, Japan), ethanol (*Chameleon*, Japan), and deionized water. The Nafion to catalyst mass ratio utilized was 0.28 : 0.72. For example, 100 mg Pt/C was mixed with 836  $\mu\text{l}$  Nafion solution, 475  $\mu\text{l}$  deionized water and 4274  $\mu\text{l}$  ethanol. The catalyst ink was stirred overnight, then sonicated before use for 30 min (*SMT Corporation*, Ultra Sonic Homogenizer UH-600). The membranes were placed onto a movable hot-plate (60°C), covered with a PET mask to create an electrode size of 0.5 cm<sup>2</sup> and the catalyst ink was sprayed directly onto the membranes (*Nordson K.K.* Spraying Device with an A7A spray gun, nozzle size 0.5 mm, Figure 2.14b) by using pulse spray mode (spray cycle 100 ms, 15 ms “gun delay”, 50 ms “gas on” and 20 ms “gun on” setting). Two carbon papers with the same size of electrode area were placed next to the electrode as a reference, in order to determine the amount of electrocatalyst deposited onto the electrode area. The deposited electrocatalyst weight was determined by using an analytical balance (*Mettler Toledo*, XP2UV,  $\pm 0.1 \mu\text{g}$ ). The catalyst loading was 0.3 mg<sub>Pt</sub>/cm<sup>2</sup> for both electrodes. For all MEAs (apart from GO-based MEAs), hydrophobic carbon paper (*E-Tek*, EC-TP1-060T, d = 0.8 cm, thickness ~180  $\mu\text{m}$ ) gas diffusion layers (GDLs) were attached to the electrocatalyst layers by a two-step hot-pressing process (*sinto* Digital Press CYPT-10, Figure 2.14c). In the first step the MEA was pre-hot-pressed without a GDL at 132°C and 0.3 kN for 180s. Then the GDLs were attached by hot-pressing at 132°C and 0.6 kN for 20s. For GO-based MEAs gas diffusion layers (GDLs) were precisely positioned over the electrocatalyst layers, but not hot-pressed to avoid loss of oxygen in the GO, which can occur at temperatures as low as 70°C.<sup>44</sup>

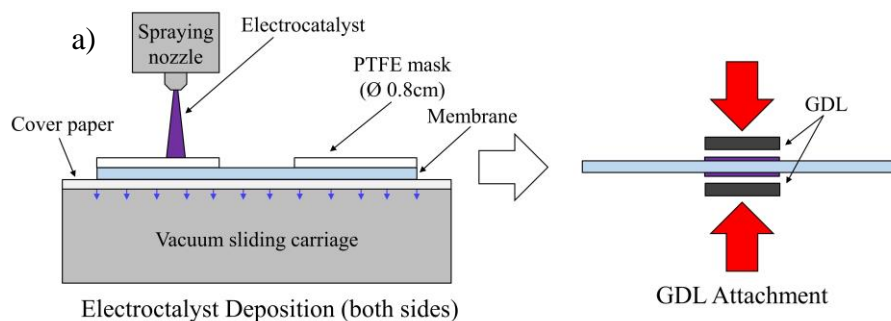


Figure 2.14. a) General fabrication process of a membrane electrode assembly. b) Nordson K.K. Spraying Device. c) Sinto Digital Press CYPT-10.

### 2.3.2 Membrane Electrode Assembly Characterization

The prepared MEAs ( $0.5 \text{ cm}^2$  electrode size,  $\sim 35 \text{ mm}$  diameter) were placed into a single cell holder (Figure 2.15a). A rubber o-ring was placed between the anode flow field and the anode of the MEA, and the cell was compressed with a force of  $0.5 \text{ N}$  by using a torque-gauge. The o-ring is necessary to seal the anode side and prevent hydrogen leakage. The fuel cell was then installed in a home-made PEMFC test system comprising an oven, heated gas pipes, and a humidifier (heated water bath and gas bubbler). Depending on the electrolyte, different preconditioning steps were used.

GO-based MEAs were preheated at  $30^\circ\text{C}$  (no gas flow) for one hour, followed by preconditioning (i.e. humidification) for 30 minutes at  $30^\circ\text{C}$  and a nitrogen gas flux of  $100 \text{ ml/min}$  (at 95% RH). The gas flux was changed to hydrogen and air ( $100 \text{ ml/min}$ , 95% RH) and after 15 minutes a performance test was conducted.

Nanocellulose-based MEAs were preheated at 80°C (no gas flow) for two hours, followed by preconditioning (i.e. humidification) for one hour at 80°C and a nitrogen gas flux of 100 ml/min (95% RH). The gas flux was changed to hydrogen and air (100 ml/min, 95% RH) and after 15 minutes a performance test was conducted.

Polarization curves, power density and durability of MEAs in this work were investigated using a potentiostat (*Amtek*, VersaSTAT 4). Polarization curve measurements were performed at different load current rates (i.e. from 0.1 to 0.5 mA/s), depending on the performance of the MEA. The measurement is performed starting from OCV with 0 mA load current. With increasing load current e.g. at 0.5 mA/s, the cell voltage drops, resulting in a typical polarization curve shape with steep and strongly changing slope at low current density due to activation losses and a linear region due to ohmic losses of the cell (compare Figure 1.4). At high current density, a strong drop in cell voltage is generally observed due to mass transport losses. The minimum cell voltage at which the measurement is terminated is 0.16 V. Three to five measurements, depending on if the power density further increased or not, were performed before the durability of the MEAs was observed.

For the prepared MEAs durability measurements were conducted as follows. From the previously measured polarization curves and power density measurements the load current at a cell voltage of 0.5 V was selected to be used as constant load current value. The measurement started from OCV with 0 mA load current, then the electric load with determined current value was connected to the fuel cell in one step. The measurement was stopped when the cell voltage dropped under 0.3 V, or after at least 10 hours in case of better durability. 15 min after the durability measurement, the OCV was noted and a polarization curve measurement was performed. To evaluate changes in performance before and after durability measurement, the OCV and power density were compared with pre-measurement values.



Figure 2.15. a) Cell holder used in our laboratory. b) Potentiostat VersaSTAT 4 (Amtek).

## References

1. Reimschuessel, A. C. Scanning Electron Microscopy-part 1. *Chem. Instrum.* **49**, (1957).
2. *Scanning Electron Microscopy and X-Ray Microanalysis*. (Springer US, 2003). doi:10.1007/978-1-4615-0215-9
3. McMullan, D. Scanning electron microscopy 1928–1965. *Scanning* **17**, 175–185 (1995).
4. von Ardenne, M. Improvements in electron microscopes. (1937).
5. von Ardenne, M. *Die praktische Ausführung der Elektronensonden-Mikroskope. Elektronen Übermikroskopie* (1940).
6. Claxton, N. S., Fellers, T. J. & Davidson, M. W. Laser Scanning Confocal Microscopy. *Encycl. Med. Devices Instrum.* **1979**, 1–37 (2006).
7. Tomovich, S. J. & Peng, Z. Optimised reflection imaging for surface roughness analysis using confocal laser scanning microscopy and height encoded image processing. *J. Phys. Conf. Ser.* **13**, 426–429 (2005).
8. Principles of Laser Scanning Microscopes. *Olympus Corporation Webpage* 2015.05.28 at <[http://www.olympus-ims.com/de/knowledge/metrology/lex\\_t\\_principles/basic/](http://www.olympus-ims.com/de/knowledge/metrology/lex_t_principles/basic/)>
9. MicroscopyU. *Confocal Microscopy - Basic Concepts* at <<http://www.microscopyu.com/articles/confocal/confocalintrobasics.html>>. Reprinted with permission from Eric Flem, Communication & CRM Manager, Nikon Instruments Incorporation.
10. Oswald, S. *Encyclopedia of Analytical Chemistry. X-Ray Photoelectron Spectroscopy in Analysis of Surfaces*. *Encyclopedia of Analytical Chemistry* (2013). doi:10.1002/9780470027318
11. Watts, J. F. & Wolstenholme, J. *An Introduction to Surface Analysis by XPS and AES*. (John Wiley & Sons, Ltd, 2013). doi:10.1002/0470867930
12. Siegbahn, K. *et al.* ESCA. Atomic, molecular and solid state structure studied by means of electron spectroscopy. *Nov. acta Regiae Soc. Sci. Ups.* **20**, (1967).
13. Siegbahn, K. M. *Electron spectroscopy for atoms, molecules and condensed matter. Nobel Lecture - Physics* (1981). doi:10.1126/science.217.4555.111
14. Hertz, H. Ueber einen Einfluss des ultravioletten Lichtes auf die electriche Entladung. *Ann. der Phys. und Chemie* **267**, 983–1000 (1887).

15. Einstein, A. Über einen die Erzeugung und Verwandlung des Lichtes betreffenden heuristischen Gesichtspunkt. *Annalen der Physik* **17**, 132–148 (1905).
16. Rutherford, E. The Origin of  $\beta$  and  $\gamma$  Rays from Radioactive Substances. *Philos. Mag. Ser. 6* **28**, 305–319 (1914).
17. Müller, F. Ultra High Vacuum Lab. *Universität Saarland* at <<http://jacobs.physik.uni-saarland.de/english/instrumentation/uhvl.htm>>. Reprinted with permission from Frank Müller, Universität Saarland. Copyright, Frank Müller.
18. Birkholz, M. *Principles of X-ray Diffraction. Thin Film Analysis by X-Ray Scattering* (2006). doi:DOI: 10.1002/3527607595
19. Bragg, W. H. & Bragg, W. L. The Reflection of X-rays by Crystals. *Proc. R. Soc. London A Math. Phys. Eng. Sci.* **88**, 428–438 (1913).
20. Schaetzl, R. & Thompson, M. L. *Soils - Genesis and Geomorphology*. (Cambridge University Press, 2015).
21. Short, M. a. & Walker, P. L. Measurements of Interlayer Spacings and Crystal Sizes in Turbostratic Carbons. *Carbon N. Y.* **1**, 3–9 (1963).
22. Smith, E. & Dent, G. *Modern Raman Spectroscopy—A Practical Approach. Journal of Raman Spectroscopy* **36**, (John Wiley & Sons, Ltd, 2005).
23. Raman, C. V. & Krishnan, K. S. A New Type of Secondary Radiation. *Nature* **121**, 501–502 (1928).
24. *Raman Spectroscopy Basics*. at <[http://web.pdx.edu/~larosaa/Applied\\_Optics\\_464-564/Projects\\_Optics/Raman\\_Spectroscopy/Raman\\_Spectroscopy\\_Basics\\_PRINCETON-INSTRUMENTS.pdf](http://web.pdx.edu/~larosaa/Applied_Optics_464-564/Projects_Optics/Raman_Spectroscopy/Raman_Spectroscopy_Basics_PRINCETON-INSTRUMENTS.pdf)>
25. Halvorson, R. a. & Vikesland, P. J. Surface-enhanced Raman spectroscopy (SERS) for environmental analyses. *Environ. Sci. Technol.* **44**, 7749–7755 (2010).
26. Meyer, E., Hug, H. J. & Bennewitz, R. *Scanning Probe Microscopy*. (Springer, 2003).
27. Butt, H. J., Cappella, B. & Kappl, M. Force measurements with the atomic force microscope: Technique, interpretation and applications. *Surf. Sci. Rep.* **59**, 1–152 (2005).
28. García, R. *Dynamic atomic force microscopy methods. Surface Science Reports* **47**, (2002).
29. Cappella, B. & Dietler, G. Force-distance curves by atomic force microscopy. *Surf. Sci. Rep.* **34**, 1–104 (1999).
30. Binnig, G. & Quate, C. F. Atomic Force Microscope. *Phys. Rev. Lett.* **56**, 930–933 (1986).

31. *Principles and Applications of Thermal Analysis*. (Wiley-Blackwell, 2007).
32. Bhadeshia, H. K. D. H. *Thermal Analysis Techniques*. (2002). at <http://www.msm.cam.ac.uk/phase-trans/2002/Thermal1.pdf>
33. Matteucci, S., Yampolskii, Y., Freeman, B. & Pinnau, I. *Materials Science of Membranes for Gas and Vapor Separation*. (John Wiley & Sons Ltd., 2006).
34. Ghosal, K. & Freeman, B. D. Gas Separation Using Polymer Membranes: An Overview. *Polym. Adv. Technol.* **5**, 673–697 (1994).
35. Recommended Units for Key Parameters. *J. Memb. Sci.* **443**, II (2013).
36. Barsoukov, E. & Macdonald, J. R. *Impedance Spectroscopy: Theory, Experiment, and Applications*. (John Wiley & Sons, Ltd, 2005).
37. Wagner, N. Characterization of membrane electrode assemblies in polymer electrolyte fuel cells using a . c . impedance spectroscopy q. *J. Appl. Electrochem.* **32**, 859–863 (2002).
38. Wagner, N. Application of Electrochemical Impedance Spectroscopy for Fuel Cell Characterization Presentation outline. (2010).
39. Tuller, H. L. & Bishop, S. R. Point Defects in Oxides: Tailoring Materials Through Defect Engineering. *Annu. Rev. Mater. Res.* **41**, 369–398 (2011).
40. Macdonald, J. R. Impedance Spectroscopy. *Ann. Biomed. Eng.* **20**, 289–305 (1992).
41. Cogger, N. D. & Evans, N. J. *An Introduction to Electrochemical Impedance Measurement*. (1999). at <http://www.kmyocorrosionlab.duzce.edu.tr/Dokumanlar/fac74bb6-84be-4640-93de-810cc3176267.pdf>
42. Bauerle, J. E. Study of solid electrolyte polarization by a complex admittance method. *Solid State Commun.* **7**, 2657–2670 (1969).
43. Cooper, K. R. Progress Toward Accurate Through-Plane Membrane Resistance and Conductivity Measurement. *ECS Trans.* **25**, 1–19 (2009).
44. Jung, I. *et al.* Reduction Kinetics of Graphene Oxide Determined by Electrical Transport Measurements and Temperature Programmed Desorption. *J. Phys. Chem. C* **113**, 18480–18486 (2009).

## 3 Graphene Oxide Membrane Fuel Cells

### 3.1 Introduction and Motivation

As described in the introductory Chapter 1.5.2.1, the development of novel fuel cell membranes is necessary for accelerating the commercialization of fuel cells and the realization of a hydrogen society. Graphene oxide (GO) was mentioned as a potential material for fuel cell membrane application, due to its proton conduction, mechanical strength, and high gas barrier properties.

Here we present a detailed characterization of GO membranes via scanning electron microscopy (SEM), laser microscopy, X-ray photoelectron spectroscopy (XPS), Raman spectroscopy, and X-ray diffraction (XRD). We report water-uptake, tensile strength, and gas barrier properties of GO compared to Nafion.

A detailed analysis of the through-plane electrical conductivity of GO paper is performed by aid of electrical impedance spectroscopy, relevant to fuel cell and ionomer applications, over a wide temperature range (30 to 120°C) and humidity range (0 to 100% RH). By aid of blocking layer measurements the mixed electronic-protonic conductive behavior of GO is examined. The capacitance is extracted from impedance data, and related to the water content of the GO paper, measured using *in situ* gravimetric analysis.

Performance of a pure graphene oxide membrane fuel cell (GOMFC) operating at up to 80°C is investigated. Lastly an electrode-supported GOMFC with high power density is prepared by a novel spraying process, a step towards fully-printable fuel cells.

### 3.2 Sample Preparation and Nomenclature

GO membranes with various thicknesses were prepared from a graphene oxide (GO) solution (*Graphene Supermarket*, 5 mg/ml, flake size 0.5 to 5  $\mu\text{m}$ ) by vacuum-filtration onto Millipore membrane filters (35 mm diameter, 0.025  $\mu\text{m}$  pore size). After filtration the membranes were dried at room temperature for 48 hours and then peeled-off the filter resulting in freestanding and flexible pure GO membranes. Herein the face of the membrane previously attached to the filter is referred to as the underside, and the air-exposed face is referred to as the upper

side. Membrane thickness was measured with a micrometer, and 10 ml GO suspension (i.e. 50 mg) led to a membrane thickness of around 36  $\mu\text{m}$ , corresponding to a density of 1.44  $\text{g}/\text{cm}^3$ . The detailed fabrication process for Nafion-based and GO-based membrane electrode assemblies (MEAs) is described in the experimental Chapter 2.3.1.

### **3.3 General Material Characterization**

#### **3.3.1 Scanning Electron Microscopy**

SEM was used to probe the morphology and structure of the GO membrane surface and cross-section. *Figure 3.1a-c* shows the upper side of the membrane. A wrinkled surface with structural features of approximately 20  $\mu\text{m}$  in length and several  $\mu\text{m}$  in width is observed. The reason for this wrinkled surface can be attributed to the tetrahedral structure of  $\text{sp}^3$ -hybridized carbon; surface tensions introduced during drying; and/or surface charges. The underside of the membrane is smoother and nearly featureless (*Figure 3.1d*). This is attributed to the flow-directed assembly onto a smooth filter surface, leading to a flat arrangement of GO sheets over the whole filter area. On the upper side, the GO sheets are not confined by a flat surface and are therefore more exposed to surface tensions and configuration change to minimize stress. *Figure 3.1e-f* shows the cross-section of the GO membrane. It can be clearly seen that the GO membrane consists of a plurality of graphene oxide layers closely stacked together. The single GO layers have wrinkled edges as a result of the  $\text{sp}^3$ -hybridization.

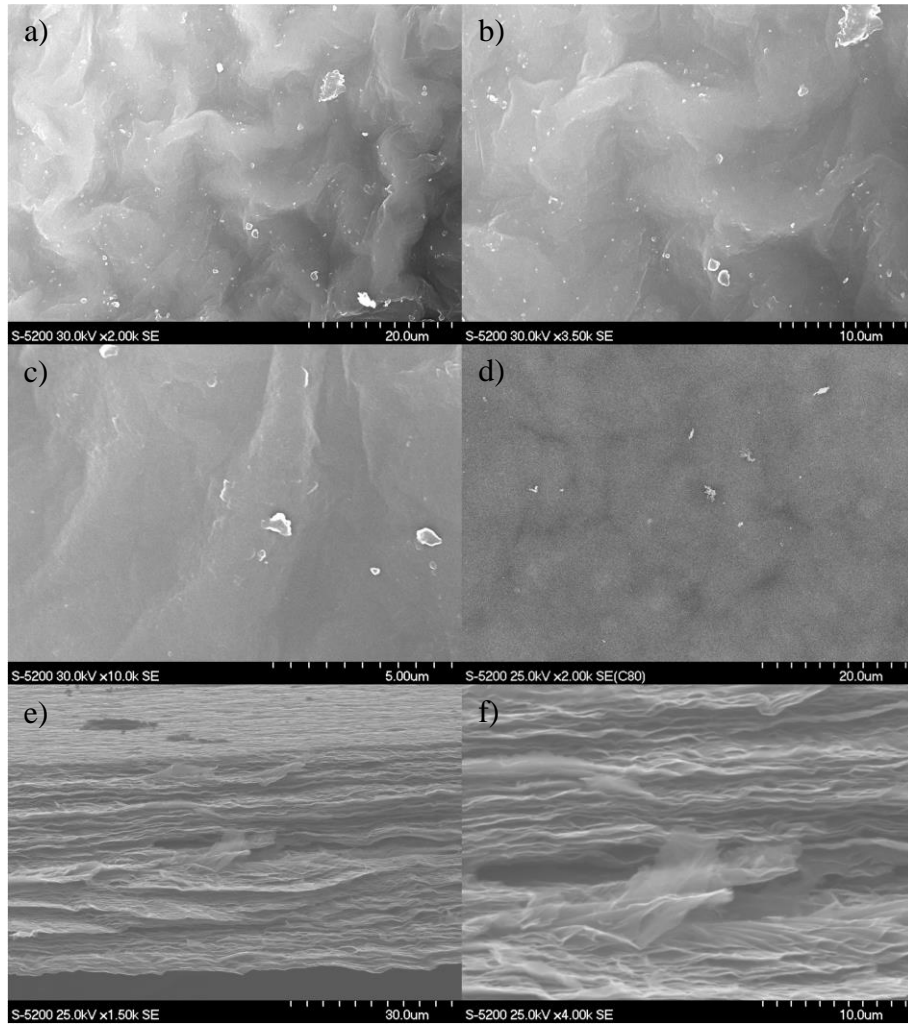


*Figure 3.1. SEM images of a GO membrane. a-c) Upper side surface at different magnifications. d) Surface of the underside. e-f) Cross-section of a GO membrane at different magnifications showing the layered structure.*

### 3.3.2 Laser Microscopy and Surface Roughness

Linear roughness measurements were conducted using laser microscopy. *Figure 3.2a* shows the GO surface at 5x magnification (upper side). Wrinkles are uniformly distributed across the surface, likely induced by stresses imposed by surface tension during drying. At 100x magnification (*Figure 3.2b*), the wrinkles can be seen in greater detail, and are very similar to the SEM image. The 3D projection in *Figure 3.2c* illustrates the wrinkled texture more clearly and *Figure 3.2d* shows height distribution over the measured area. Both 3D images are magnified by 3x in the z-axis to display the structure more clearly. The peak to trough distance is approximately 4  $\mu\text{m}$ .

For a quantitative evaluation of the membrane surfaces, roughness measurements were conducted. The arithmetic average height  $R_a$ , defined as the average absolute deviation of the roughness irregularities from the mean line, is 0.5062 ( $\pm 0.0261$ )  $\mu\text{m}$  for the upper side of the membrane, and 0.1832 ( $\pm 0.0150$ )  $\mu\text{m}$  for the underside. This surface roughness is larger than that measured for Nafion (0.052  $\mu\text{m}$ ). This increased roughness and thus the total area of the interface, possibly leading to increased mechanical interaction between the membrane and the electrocatalyst layer, resulting in improved adhesion and reduction of the contact resistance.<sup>1</sup>

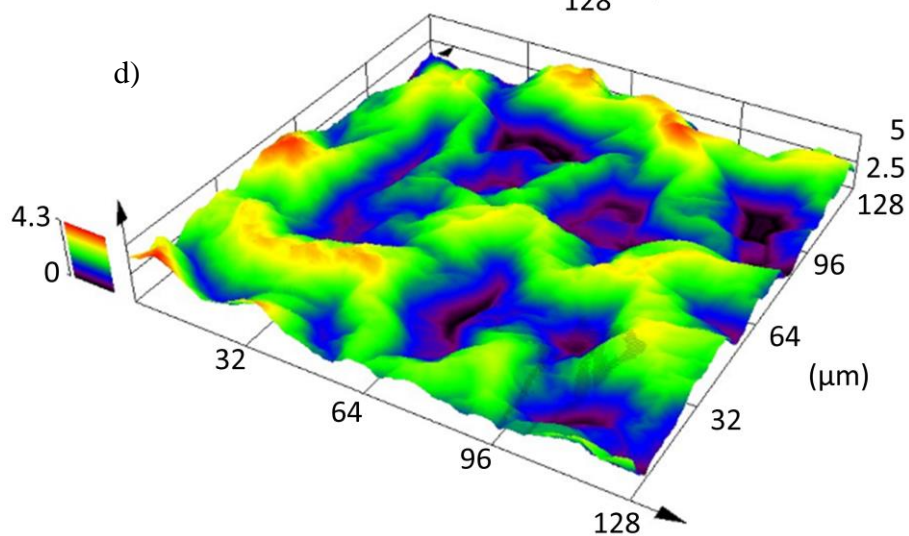
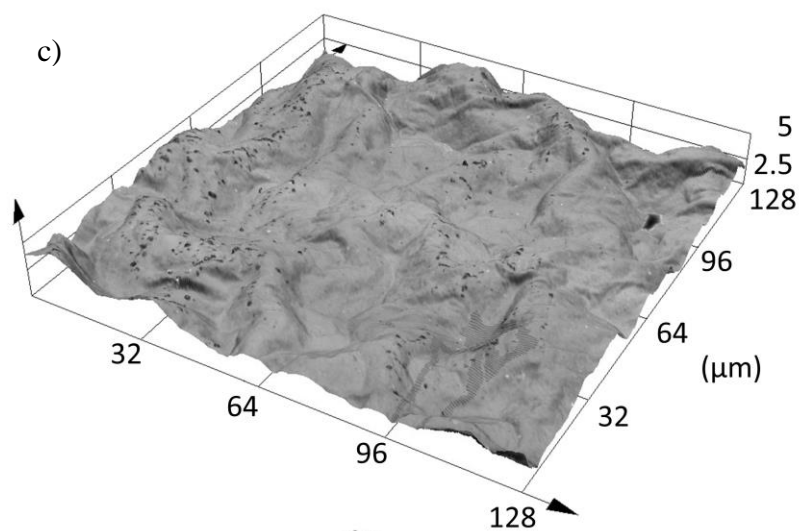
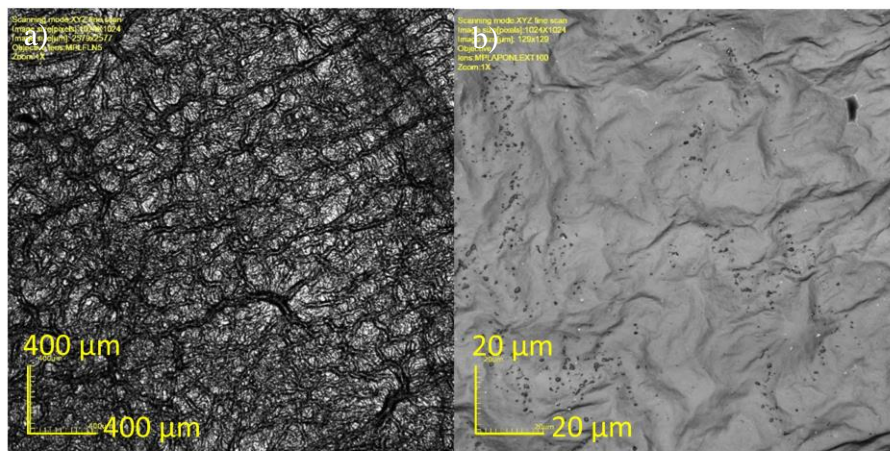


Figure 3.2. Laser microscopy images of the GO membrane surface: a) 5x magnification; b) 100x magnification; c) 3D projection; and d) Colored 3D projection with height profile.

### 3.3.3 X-Ray Photoelectron Spectroscopy

XPS was measured for elemental and chemical analysis. In the wide scan, two major peaks at binding energies of approximately 284.5 and 532.0 eV are observed (*Figure 3.3a*), attributed to C1s (74.8 at%) and O1s (25.2 at%) components. The peak at ~480 eV is noise. *Figure 3.3b* shows the C1s spectrum of GO, deconvoluted into six peaks, attributed to different types of C bonds. The C1s related peaks assigned in the following paragraph are in accordance with Tien et al. observations.<sup>2</sup> The largest peak is attributed to sp<sup>3</sup>-hybridized C-C/C-H bonds at 284.2 eV (41.0%) and thus to the carbon backbone of GO. The next largest peak is attributed to epoxy groups C-O-C at 286.1 eV (24.5%), followed by hydroxyl groups C-OH at 285.1 eV (15.7%). Epoxy and hydroxyl groups are thought to be the dominant species on the basal plane of GO, resulting in strong binding to water via hydrogen bonds.<sup>3</sup> Carbonyl C=O at 287.1 eV (8.3%) and carboxyl groups O-C=O at 288.2 eV (5.5%) are also present with lower intensities. The lowest peak in the C 1s spectrum is attributed to sp<sup>2</sup>-hybridized C=C bond at 283.5 eV (5.0%), and due to its small magnitude, this indicates that the proportion of free electrons is very low, in contrast with the significantly larger peaks typically observed in unoxidized graphene. The O 1s (*Figure 3.3c*) signal is deconvoluted into five peaks. The strongest peak at 531.9 eV is attributed to C-O bonds (38.0%), followed by O-H at 532.8 eV (22.4%), and C-OH at 531.1 eV (21.0%). C=O bonds at 530.2 eV (9.3%) and adsorbed water at 533.7 eV (9.3%).<sup>4</sup> The higher energy oxygen groups (e.g. epoxides) in this GO sample are potentially easily removed in reducing conditions (e.g. PEMFC anode operating conditions), with consequent modification of GO electrical properties, as discussed in the MEA characterization section (3.5).

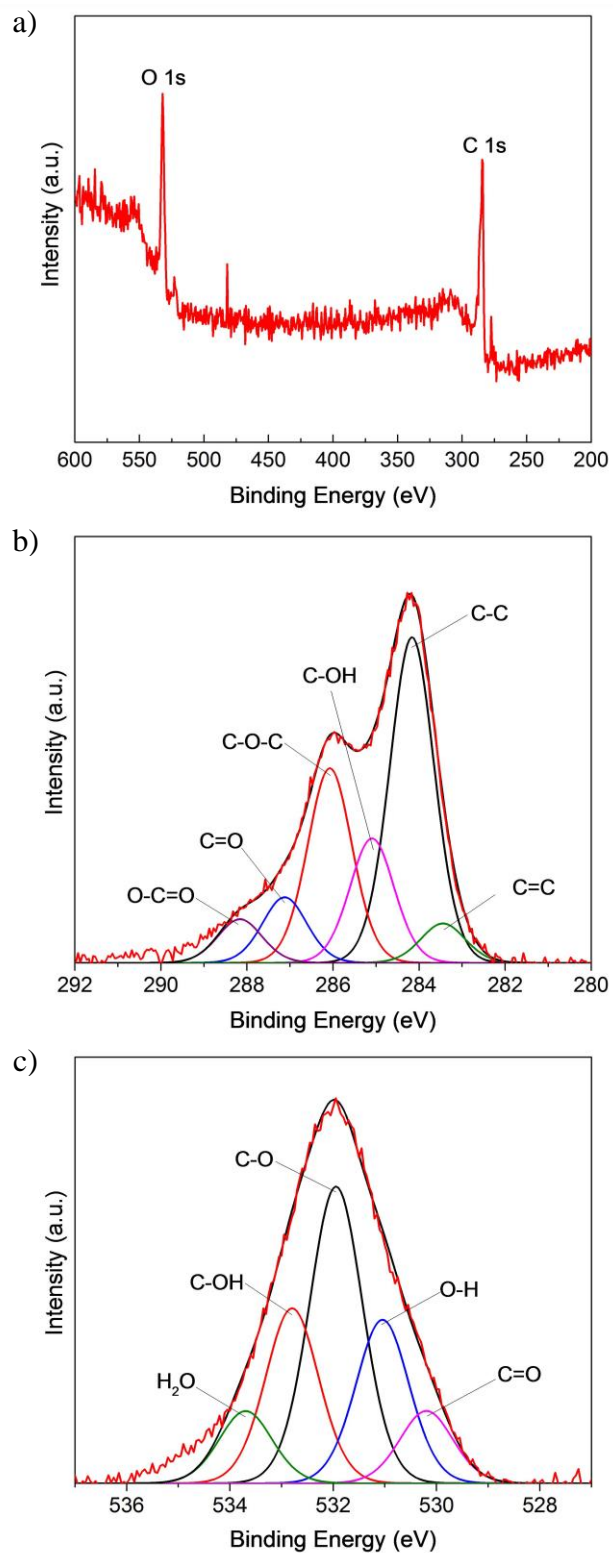


Figure 3.3. a) XPS wide scan spectra of GO. b) Component analysis of the C 1s peak of GO. c) Component analysis of the O 1s peak of GO.

### 3.3.4 Raman Spectroscopy

Raman spectroscopy was used to compare the atomic and electronic properties of GO with graphene.<sup>5</sup> Raman spectra of GO and graphene are shown in *Figure 3.4* and the position of Raman active bands, intensity ratio  $I(D)/I(G)$  and the full width at half maximum (FWHM) of the G peak (G) can be seen in *Table 3.1*. Raman spectra of GO shows two strong Raman-active bands. The G band ( $\sim 1594\text{ cm}^{-1}$ ) represents in-phase vibrations of the  $\text{sp}^2$ -carbon network. The D band ( $\sim 1347\text{ cm}^{-1}$ ) is due to the breathing mode of six-atom rings, and represents the disorder caused by edges or defects in the carbon network.<sup>6-8</sup> The G band is actually made up of both a G and D' band, but due to the effect of broadening it appears as a single band.<sup>8</sup> At higher wave numbers ( $> 2600\text{ cm}^{-1}$ ) three less intense, overlapping peaks are observed. The 2D and 2D' peaks are second order bands of the D and D' band, and they are inversely proportional to the number of defects. Their intensity drops severely as the  $\text{sp}^2$  carbon network is destroyed, and thus in  $\text{sp}^3$ -dominated GO their intensity is relatively low.<sup>8</sup> There is a clearly visible D+D' band, indicating a high concentration of defects.<sup>5,8</sup> Because the 2D, D+D' and 2D' bands strongly overlap, it was not possible to determine exactly the 2D and 2D' positions. The intensity ratio of the D and G peaks [ $I(D)/I(G)$ ] is an indicator of the proportion of defects.<sup>5,9,10</sup> For comparison we measured a commercially available graphene powder sample (*CheapTubes.com*, Grade 4) herein defined as  $\text{G}_{\text{G4}}$ , which displayed three strong Raman-active bands; the G band ( $\sim 1572\text{ cm}^{-1}$ ); the 2D band ( $\sim 2696\text{ cm}^{-1}$ ) and the D band ( $\sim 1344\text{ cm}^{-1}$ ). Due to the strong 2D band, the low intensity D band, and the narrow G band with small D' band (which is related to defect concentration, e.g  $\text{sp}^3$ ), we can assume that  $\text{G}_{\text{G4}}$  has a very low defect concentration compared to GO and thus the nearly perfect  $\text{sp}^2$  network of graphene.<sup>7</sup> The D+D' and 2D' bands are not visible in  $\text{G}_{\text{G4}}$ . The full width at half maximum (FWHM) of the G band ( $22\text{ cm}^{-1}$ ) is smaller than in GO ( $69\text{ cm}^{-1}$ ), with a lower  $I(D)/I(G)$  ratio, indicating less disorder.<sup>5</sup> In conclusion, GO is as expected highly defective compared to  $\text{G}_{\text{G4}}$ . However, these defects are an indicator of a greater proportion of hydrophilic oxygen groups, and therefore a greater number of potential proton conduction sites. The spurious peak at  $\sim 2380\text{ cm}^{-1}$  in the  $\text{G}_{\text{G4}}$  signal is noise, most likely generated from interaction of the detector with a cosmic ray.

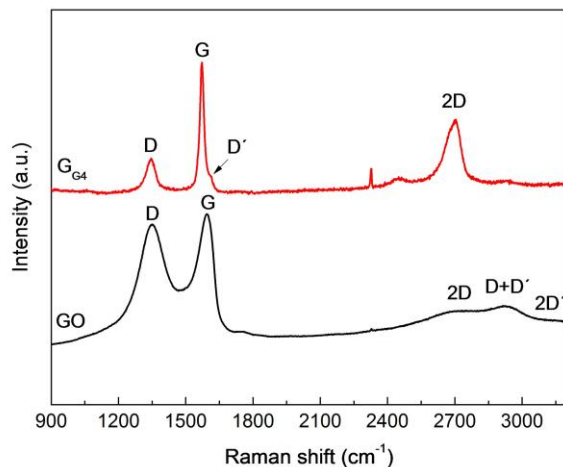


Figure 3.4. Wide scan Raman spectra of GO and GG4.

Table 3.1. Position of Raman active bands, intensity ratio  $I(D)/I(G)$  and the full width at half maximum of the G peak FWHM (G). All units are in  $\text{cm}^{-1}$  unless otherwise stated.

|                             | GO    | GG4   |
|-----------------------------|-------|-------|
| D band                      | 1347  | 1344  |
| G band                      | 1594  | 1572  |
| D + D''                     | -     | 2449  |
| 2D band                     | 2700  | 2696  |
| D + D' band                 | 2914  | -     |
| $I(D)/I(G)$ [dimensionless] | 0.932 | 0.365 |
| FWHM (G)                    | 69    | 22    |

### 3.3.5 X-Ray Diffraction

Figure 3.5 shows the XRD pattern of GO measured in ambient air (~60% RH). There is a broad major peak at  $2\theta = 11.6^\circ$ , corresponding to an inter-planar distance between the GO layers of 0.761 nm, which is in the range of reported values in literature (6 to 12 Å).<sup>3,11-14</sup> The broad peak of GO in comparison to graphene and graphite arise from the more amorphous nature of GO.<sup>15</sup> The inter-planar distance is more than twice as large as the interlayer spacing for graphene/graphite (peak at  $26.5^\circ$  and 0.336 nm), due to the presence of the surface oxygen groups, which act as spacers between the layers,<sup>16</sup> further confirming a significant level of bound oxygen in GO, as well as intercalated water.<sup>3,14,17</sup> Lerf et al. showed by aid of XRD analysis that the interlayer spacing of graphitic oxide increases with increasing

humidity and they reported interlayer spacings of 8 Å at 45% RH, 9 Å at 75% RH, and 11.5 Å at 100% RH.<sup>12</sup> Daio et al. performed in-situ SEM and in-situ STEM investigation on the swelling behavior of a GO membrane at different temperatures and humidity.<sup>17</sup> They reported reproducible thickness increase (increasing RH) and decrease (decreasing RH) with a swelling amplitude of ~10 μm from 30 to 95% RH.

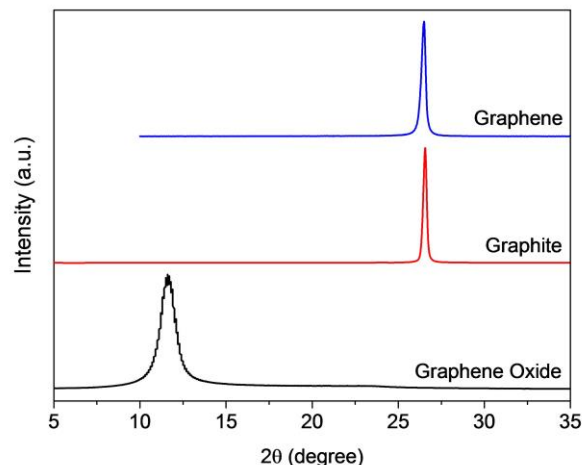


Figure 3.5. XRD patterns graphene (Grade 4), graphite and graphene oxide.

### 3.3.6 Water Uptake and Swelling

Water uptake and swelling measurements were performed because proton conductivity is generally attributed to a water-mediated proton transport mechanism (e.g. the Grotthuss mechanism),<sup>18,19</sup> and is expected to improve with increasing hydration. The change in physical dimensions with increasing humidity and the corresponding strain can impact fuel cell applications. For example, excessive swelling may lead to deterioration of the membrane-electrocatalyst interface, or membrane failure.<sup>20</sup> Figure 3.6 shows the water uptake and swelling of GO and Nafion. The water uptake of GO is approximately 20 times higher than Nafion ( $325.6 \pm 22.1$  wt% compared to  $15.4 \pm 0.6$  wt%). Swelling (i.e. the increase in thickness of the GO membrane) was  $197.8 \pm 39.4\%$ ; also around 20 times higher than that of Nafion ( $10.4 \pm 1.1\%$ ), and GO resembles a hydrogel-like structure. The higher water uptake of GO compared with Nafion indicates a larger driving force for water absorption, meaning that the GO membrane may maintain high proton conductivity even

under lower humidity conditions. For example Kumar et al. reported strongly increased fuel cell performance for GO-Nafion composite membranes compared to recast Nafion at 120°C and 25% RH (212 vs 56 mW/cm<sup>2</sup>), explained by the increased water retention properties and thus maintained proton conductivity.<sup>21</sup>

On the other hand, the greater degree of swelling of GO might increase the risk of deterioration of the membrane-catalyst interface if the membrane is repeatedly hydrated and dried and warrants further study.<sup>20</sup>

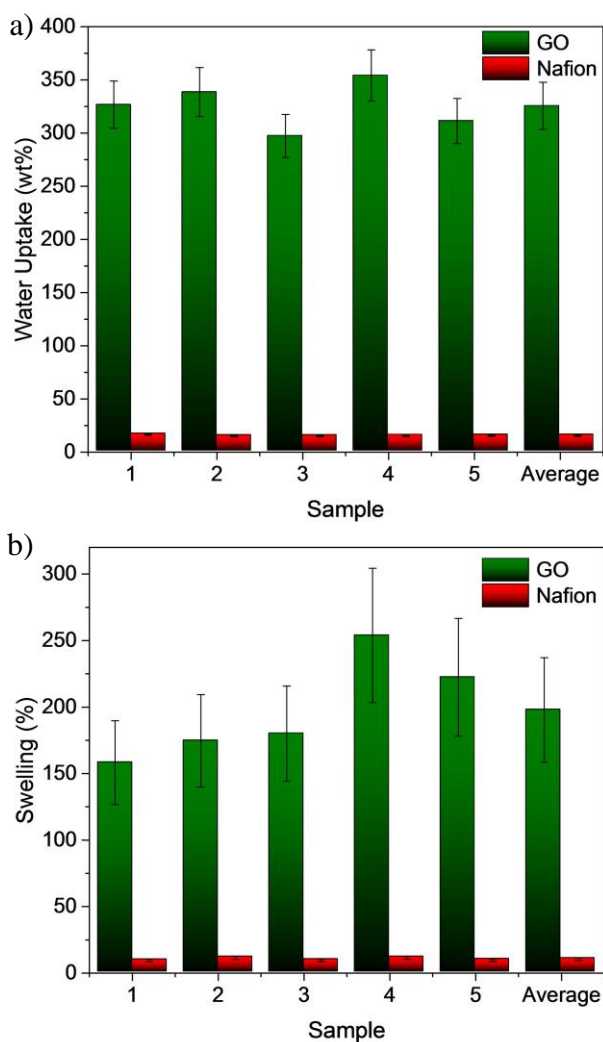
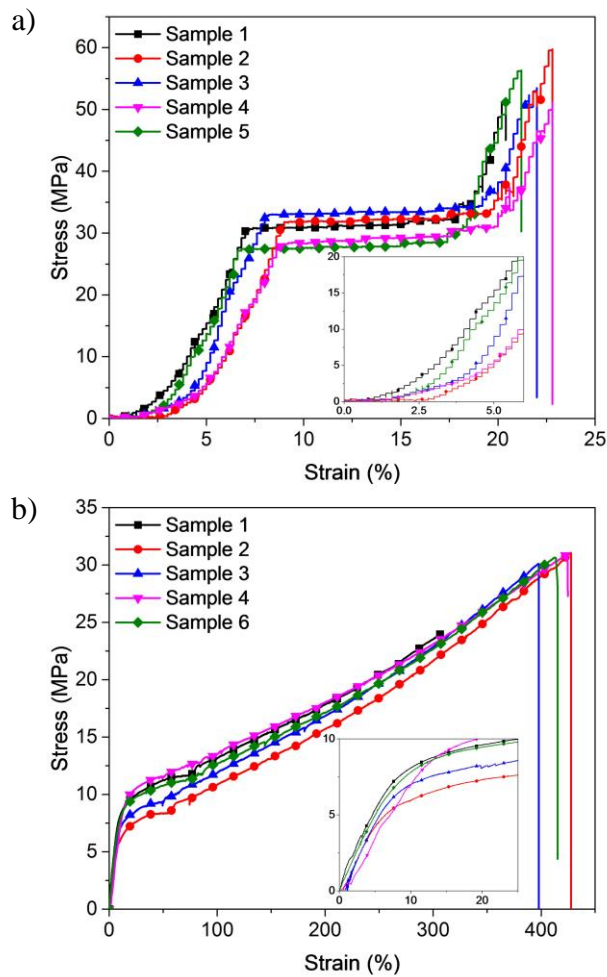


Figure 3.6. Water uptake (a) and swelling (b) of graphene oxide and Nafion.

### 3.3.7 Tensile Strength Measurements

Tensile strength and elongation (strain) until rupture are both important mechanical properties regarding membrane handling, MEA preparation and fuel cell longevity, because they give information about the “work performance” (i.e. the amount of deformation the membrane will bear without failure). *Figure 3.7a* shows the stress-strain curves for five GO membrane samples. All the curves have similar shape, confirming the reproducibility of the measurement. The curve progression can be divided into four different regions: a straightening region; an elastic region; an extended elastic limit (where plastic deformation begins); and a plastic region up until fracture. At low stress, GO displays a non-linear elastic elongation up to a stress of approximately 10 MPa. This straightening region is suggested to be induced by a high concentration of water molecules in the interlayer spacing.<sup>22,23</sup> Based on their hydrogen bonds with the GO sheets, water molecules respond to the applied strain by reorientation, decreasing the elastic modulus of the membrane.<sup>23</sup> At higher stress, an approximately linear elastic elongation occurs, up to around 28 to 32 MPa, and 6.5 to 8.5% strain. A stretching of the wrinkled GO sheets is assumed to be responsible for this elastic elongation.<sup>23</sup> After this elastic elongation region, there is an extended tensile elastic limit (from approximately 7 to 18% strain) where the strain increases rapidly with only a very small increase in force. It is proposed that this phenomenon is a result of individual GO sheets sliding over each other in the presence of water molecules, which act as a lubricant.<sup>11,23</sup> Finally there is a region where the GO sheets appear to grip again possibly because the density of water molecules decreases to a point where the lubrication effect no longer dominates (above 30 MPa), before plastic elongation continues forming microcracks within the GO sheets,<sup>23</sup> with a fast increase in stress until rupture at around 50 MPa and 20% strain. The stress-strain curves of Nafion (*Figure 3.7b*) can be separated into two regions: an elastic region, and a plastic region up until rupture. The Nafion samples exhibit an elastic elongation until around 6 MPa and 7% strain, after which the stress increased with plastic elongation nearly linearly until rupture at approximately 30 MPa stress and 400 to 425% strain, which is similar to values mentioned in literature.<sup>24</sup> The average tensile strength of GO membranes was  $54.5 \pm 3.3$  MPa, compared with  $30.7 \pm 0.4$  MPa for Nafion (nominal value 32 MPa).<sup>25</sup> The GO membrane has approximately double the strength of Nafion. However, as can be observed in the stress-strain curve, the elasticity of the GO membrane is very low compared

to Nafion (*Figure 3.7*). The strain of the GO membrane before rupture is only  $22 \pm 1\%$ , compared with  $411 \pm 14\%$  in Nafion. The elastic modulus of the GO membrane (i.e. the slope of the stress-strain curve in the elastic region) is  $680 \pm 9.7$  MPa for GO, compared with  $94.9 \pm 8.5$  MPa for Nafion (nominal value 266 MPa, measured at lower humidity).<sup>25</sup> Summarizing these tensile strength results (*Figure 3.8*), Nafion exhibits lower tensile strength and elastic modulus than GO membranes, but exhibits much higher elongation and therefore can resist more deformation before failure occurs. However, it is noted that the electrodes and the interface between electrodes and Nafion will likely not tolerate such extreme deformations. GO membranes exhibit a very large tensile strength and elastic modulus, but are very stiff, characterized by fracture at only 20% elongation, and are thus less resistant to severe deformation.



*Figure 3.7. Stress-strain curve of GO (a) and Nafion (b) membranes. The insets show an enlarged plot of low strain regions for both samples.*

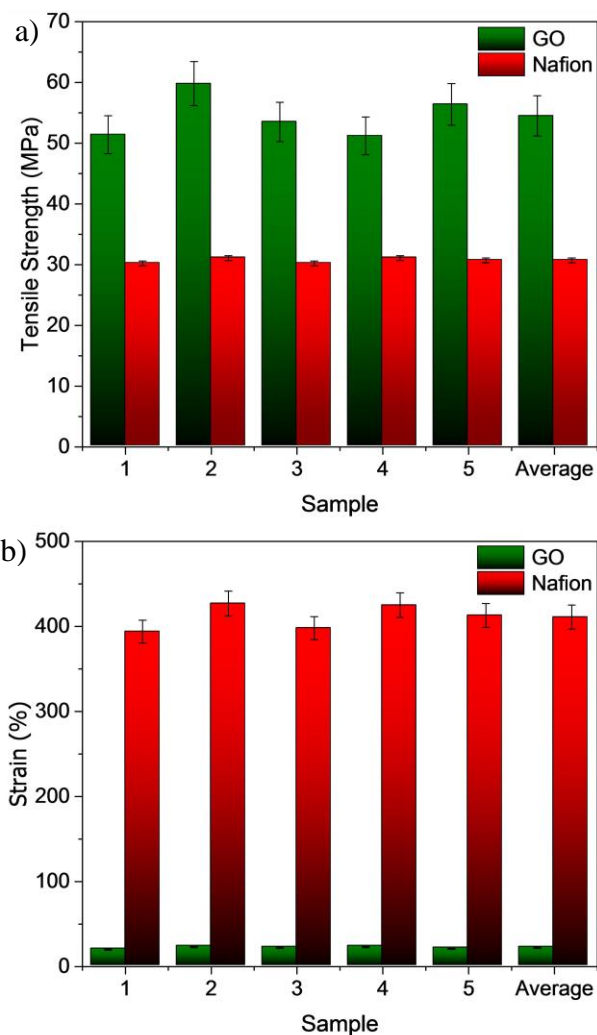


Figure 3.8. Tensile strength (a) and strain until rupture (b) of GO and Nafion.

### 3.3.8 Gas Barrier Properties

For fuel cell applications, crossover of fuel from the anode to cathode is an important issue as it reduces the OCV and leads to performance loss,<sup>26-28</sup> and should therefore be avoided. Gas barrier properties are therefore an important criteria for a membrane to be suitable as fuel cell electrolyte. Figure 3.9 shows the hydrogen gas barrier properties of GO and Nafion and their dependence on temperature. GO has higher hydrogen gas barrier properties compared with Nafion by approximately three orders of magnitude. However, this is contrary to a previous study by Nair et al., which claims that GO is completely impermeable to liquids and gases except water.<sup>16</sup> In their work permeability was investigated using two different

approaches. In the first approach small containers were filled with gas at low over pressure ( $< 100$  mbar) and the pressure change was recorded. Over several days no noticeable changes were observed. In a second approach gas permeation was tested by mass spectrometer, however, again, no permeation was detected. The reason for the contrary results can simply be related to the difference in the magnitude of pressures used. Nair et al. used a pressure  $< 100$  mbar whereas in our work a total pressure difference between feed and permeate side was 200 kPa, thus 20 times higher. Therefore we conclude that our results are reliable due to higher amount of detectable permeate.

For both samples the permeability increases with increasing temperature. This is typical behavior for organic polymers.<sup>29</sup> As described in the experimental Chapter 2.2.10, permeability is a product of the diffusion and solubility coefficients. Since this increases with temperature we can conclude that the diffusion increase with temperature is faster than the decrease in solubility. The higher gas barrier properties in GO compared with Nafion should result in a higher OCV in MEAs. Additionally GO could be used as coating layer for increasing hydrogen barrier of hydrogen-storages or pipes.

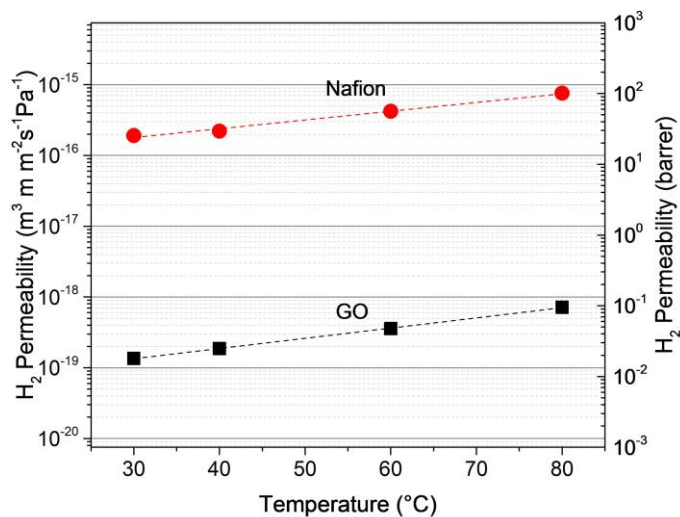


Figure 3.9. Dependence of the hydrogen permeability on temperature for graphene oxide and Nafion. Dashed lines are linear fits of the measurement data.

## 3.4 Impedance Spectroscopy

### 3.4.1 Electrical Conductivity

Graphene oxide paper has a multilayer structure, providing mechanical strength as well as the porosity necessary for hydration.<sup>30</sup> For good proton conductivity, and low electronic conductivity, it is assumed that a high degree of oxidation is preferable. Conductivity measurements were performed through-plane, i.e. normal to the orientation of the GO sheets. Typical impedance spectra are semicircular at high frequencies and have a larger “tail” at low frequencies, as shown in *Figure 3.10a*. In order to obtain an equivalent circuit to fit the membrane resistance, a model of the electrode setup was developed. The sample setup in the MTS 740 electrical measurement device is shown in *Figure 3.10b*.<sup>31</sup> The distance between the anode source electrode and the cathode sensor electrode is very large (~3 mm) relative to the membrane thickness (~10 to 100  $\mu\text{m}$ ). Therefore the cathode voltage sensor electrode measures the potential of the cathode current source electrode, and vice versa for the anode electrodes. In essence, these are effectively two-electrode measurements with four leads, used in order to minimize lead resistance.

Therefore the electrical measurements measure two electrode impedances in series with the GO electrolyte impedance (*Figure 3.10b*). These resistances can be modelled by a series of three R//CPE circuits (a resistor, R, in parallel with a constant phase element, CPE). For the symmetric electrodes studied here, this can be further simplified to two R//CPE circuits in series.<sup>32</sup> The membrane and electrode CPE values are denoted as  $Q_m$  and  $Q_{int}$ , respectively. CPEs are used rather than capacitors to model the slightly depressed nature of the semicircle arcs, which typically arise from a distribution of time-constants resulting from heterogeneous physical properties, e.g. dielectric constant and resistivity.<sup>33,34</sup>

Fits to the impedance spectra are shown in *Figure 3.10a* (solid lines). The electrical conductivity ( $\sigma$ ) of the high frequency (left-most) arc was calculated from the extracted resistance  $R$  ( $\Omega$ ) by using the membrane thickness  $L$  (cm), the effective cross-sectional area  $A$  ( $\text{cm}^2$ ) and Equation ( 3.1 ):

$$\sigma = \frac{L}{R \cdot A} \quad (3.1)$$

The corresponding capacitance was derived from the CPE elements using Equation ( 3.2 ), see references.<sup>34,35</sup>

$$C_{GO\ Paper} = (Q)^{\frac{1}{n}} \cdot R^{\frac{1-n}{n}} \cdot \sin\left(\frac{n \cdot \pi}{2}\right) \mid \omega = \omega_p \quad (3.2)$$

where  $n$  and  $Q$  are extracted from the fitting routine, and  $n$  represents the deviation from purely capacitive (i.e., when  $n = 1$ ) behavior. Angular frequencies ( $\omega$ ) have to be in the range of the angular frequency at the highest point of the impedance arc ( $\omega_p$ ). In the present measurement, values for  $n$  of the membrane impedance were approximately 0.9, representing close to ideal capacitive behavior.

The diameter of the high frequency impedance arc, corresponding to the resistance, increases approximately linearly with increasing membrane thickness (*Figure 3.10a*). This demonstrates that this contribution to the impedance spectra arises from the membrane, while the low frequency arc (corresponding to the electrode) remains nearly constant in diameter. Since the electrode/membrane interface is very thin compared to the thickness of the membrane, the measured interface capacitance ( $C_{int} \sim 10$  nF) is expected to be much larger than that of the membrane ( $C_m \sim 0.1$  nF), resulting in a larger time constant  $\tau (= RC)$ , and thus lower characteristic frequency ( $1/\tau$ ) for the electrode contribution, as indeed is found.<sup>36,37</sup> The electrode impedance is not discussed further in this thesis. Taking the ratio of membrane resistances (14.70, 18.67 and 29.82  $\Omega$ ) to membrane thickness (29, 42, and 64  $\mu\text{m}$ ) and cross-sectional area (0.45  $\text{cm}^2$ ) yields an average GO resistivity of 2.1  $\text{k}\Omega \text{ cm}$  at 30°C and 100% RH. In the cases of low humidity and elevated temperature, a second, smaller high frequency arc was observed, which is related to electronic conduction and discussed later in Chapter 3.4.2.

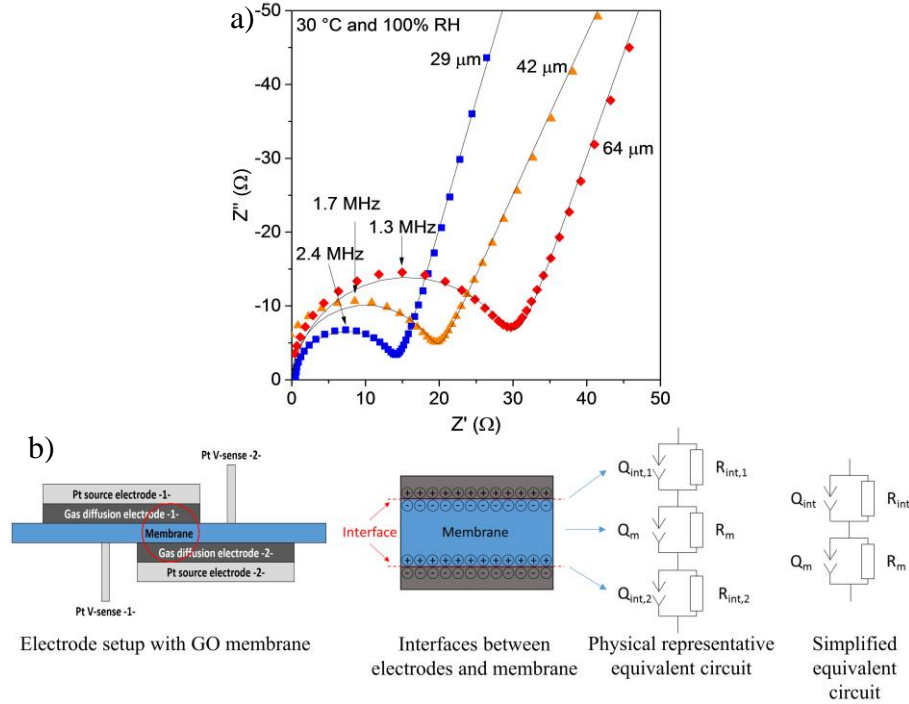


Figure 3.10. a) Impedance spectra for 29, 42 and 64  $\mu\text{m}$  thick GO paper at 30°C and 100% RH. The diameter of the high frequency arc increases with increasing membrane thickness, confirming that it corresponds to conduction within the GO paper. b) Electrode setup of the membrane test system MTS 740 with corresponding electrode/membrane interfaces and representative equivalent circuits.

The humidity and temperature dependence of conductivity was investigated for a 14  $\mu\text{m}$  thick GO paper (Figure 3.11a). The temperature was increased from 30 to 90°C whilst humidity was decreased isothermally at each temperature, after pre-treatment for four hours at 100% RH at each temperature. The conductivity decreases slightly with decreasing humidity from 100% to 40% RH for all temperatures, indicating water-mediated proton transport, as previously suggested by other studies<sup>38–42</sup>, and denoted “high RH” in the figure. Furthermore, the large electrode resistance (e.g. see Figure 3.10a) is consistent with a conduction mechanism that is associated with ion transport, as opposed to electronic transport, in which ohmic contacts are expected to result in much smaller electrode impedance. For RH < 40%, the conductivity surprisingly increases by approximately one order of magnitude with decreasing RH, denoted “low RH” in the figure. Additionally, conductivity increases with increasing temperature in all cases (except at 90°C, as discussed later), reaching maximum values of 0.5 mS/cm at 90°C and 100% RH (high RH), and 5.7 mS/cm at 80°C and 0% RH

(low RH). Arrhenius plots of conductivity are shown in *Figure 3.11b*, and activation energies ( $E_A$ ), consistent with the following equation for hopping type conduction,<sup>43</sup> were extracted from the Arrhenius plots, as shown in *Figure 3.11c*:

$$\sigma = \frac{\sigma_0}{T} \exp\left(-\frac{E_A}{kT}\right) \quad (3.3)$$

where  $\sigma_0$  is a pre-exponential factor and  $k$  is the Boltzmann constant. Partial fitting of the data was performed at high temperatures and low humidity due to conductivity outliers in this range. A significant increase in slope in the Arrhenius plot at 60°C is observed, indicating two thermally activated regimes. As reported in the figure,  $E_A \sim 0.05$  to 0.14 eV were observed at low temperature (regime 1), in good agreement with values reported for proton conductivity in Nafion (0.093 to 0.145 eV)<sup>44,45</sup>, as well as the energy required for cleaving hydrogen-bonds in the Grotthuss conducting mechanism ( $\sim 0.113$  eV).<sup>19</sup> At higher temperature (regime 2),  $E_A$  is approximately 0.25 eV, increasing to 0.88 eV with decreasing humidity. At high RH, the larger activation energy indicates a change in proton conduction mechanism, as described later in the discussion. Finally, at low RH, electronic conductivity becomes dominant, as elaborated on later with electron blocking measurements.

As opposed to the trends for other temperatures, the conductivity at 90°C and low humidity exhibited lower values than expected. In order to explore this behavior further, measurements were performed at higher temperature (120°C) on the same membrane, following the 90°C measurement. As shown in *Figure 3.12a*, at 120°C the conductivity increases with decreasing humidity over the entire RH range. Under these conditions, the impedance spectra no longer exhibited semi-circular arcs; instead all the data points fell on approximately the same point on the real axis with approximately zero imaginary impedance (*Figure 3.12b*). Furthermore, after testing, the GO paper was metallic-grey in color as opposed to the typical starting matte-black color (inset *Figure 3.12a*). These observations are consistent with reduction of the graphene oxide paper (i.e. formation of rGO), with a consequent dramatic increase in electronic conduction. There is further evidence for this in the fuel cell measurements, as discussed later.<sup>30</sup> The activation energy at 0% RH during cool down from 120 to 30°C was found to be  $\sim 3$  meV, around one order of magnitude less than before the 120°C measurement step, and in range of the activation energy expected for semiconductor behavior.<sup>46</sup>

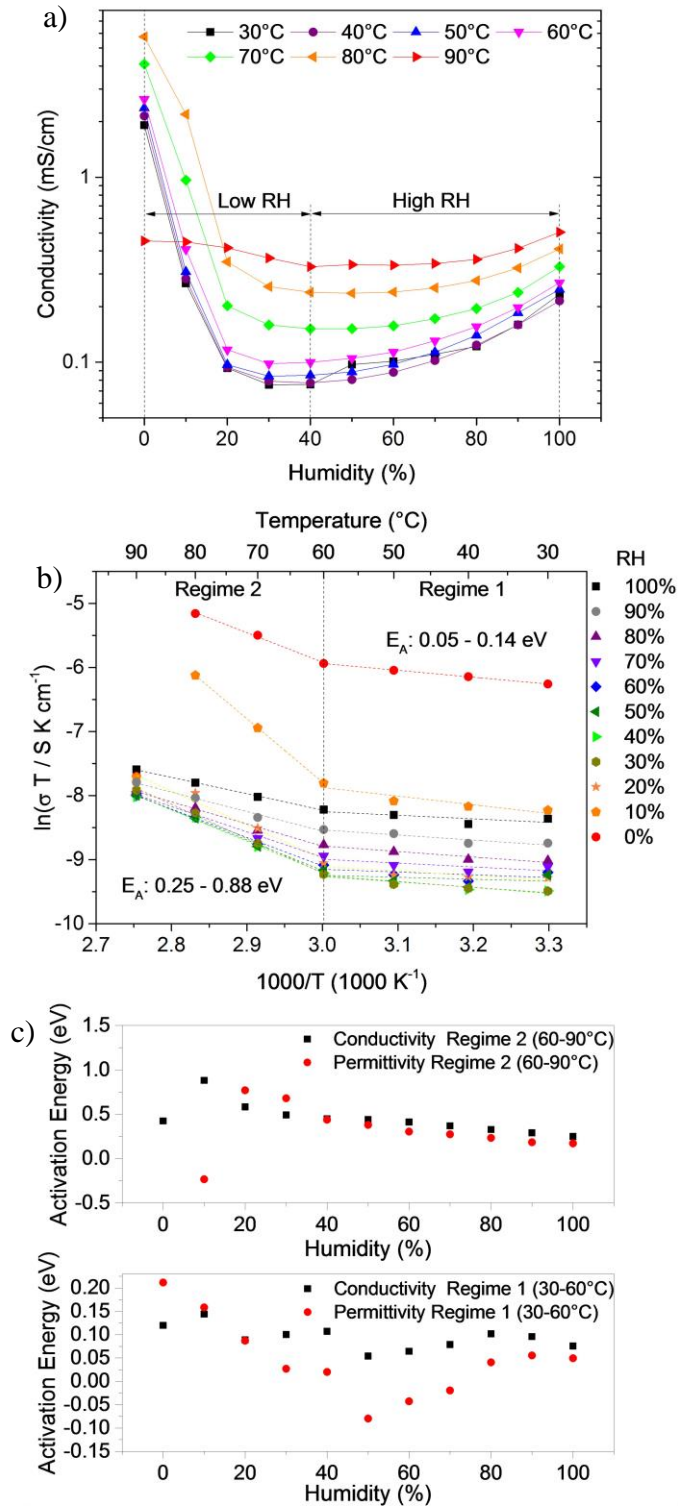


Figure 3.11. a) GO membrane paper conductivity dependence on humidity at different temperatures. Measurements were performed using isothermal steps of high to low humidity with increasing temperature. b) Arrhenius plot of conductivity for 100 to 0% RH (with steps of 10% RH). Dashed lines are linear fits from which the slope yields the activation energy. c) Activation energy of conductivity and capacitance extracted from Arrhenius plots.

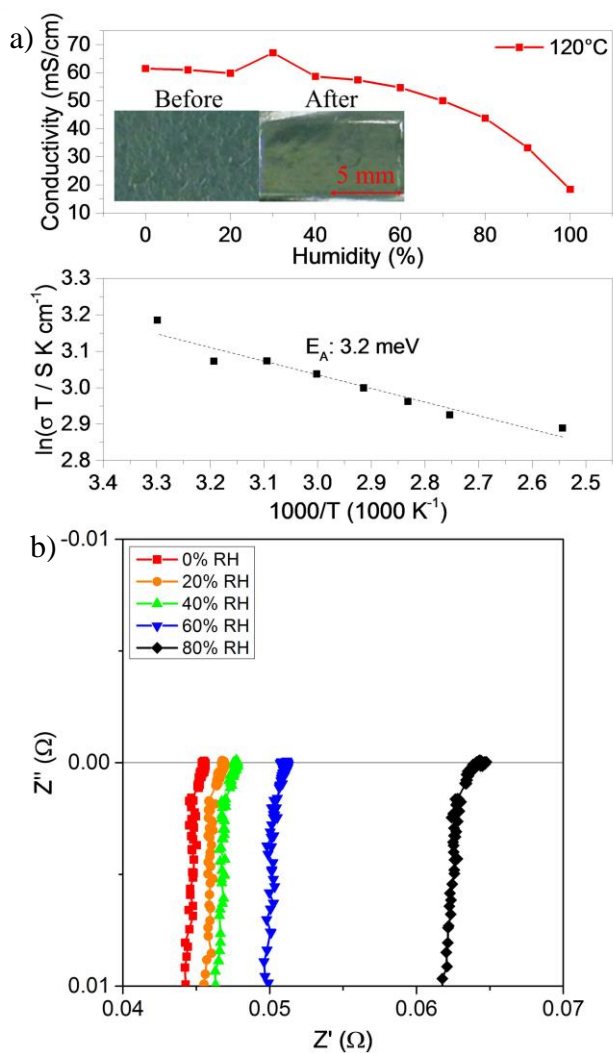


Figure 3.12. a) Upper graph shows conductivity dependence on humidity at 120°C. The chamber was pressurized at 230 kPa total pressure. The inset image shows the membrane before and after measurement. The lower graph shows an Arrhenius plot obtained during a cool down process at 0% RH (120 to 30°C). b) Impedance spectra of GO at 120°C. Disappeared low frequency semi-circle indicates dominating electronic conductivity.

### 3.4.2 Electron Blocking Measurements

In order to separate the electronic and protonic contributions from the total conductivity, electron blocking (proton conducting) layers were employed on both sides of the GO membrane. A 10  $\mu m$  thick GO paper sample was sandwiched between two Nafion<sup>®</sup>212 membranes which act as electron blocking layers, schematically shown in *Figure 3.13a-b*. The impedance of this layered structure was measured using similar procedures as described

above. This method is not commonly utilized in the measurement of PEMs, but gives a vital insight into the conduction mechanisms at play. At intermediate to low frequencies during the impedance measurement, protons pass through the Nafion layer into the GO layer and then into the other Nafion layer. Considering that the resistance to the redox reaction at the interfaces ( $Z_{int,e/i}$ ) is expected to be quite large (no catalysts are present), the resistance to ion transport in this frequency range is expected to be equal to the resistive components of the sum of Nafion ( $Z_{i,naf}$ ), GO ( $Z_{i,GO}$ ), and their interfacial ( $Z_{int,i2}$ ) ionic impedances. At lower frequencies, electrode impedances are expected to become evident (as shown in *Figure 3.10a* for non-blocked membranes). This type of cell and impedance measurement has previously been discussed and used to examine the ionic conductivity of oxide ion conductors.<sup>47-51</sup>

The impedance spectra for the non-blocked and blocked measurements are shown in *Figure 3.13c-d* (a small, additional high frequency contribution is found for the non-blocked measurements, discussed later). After subtracting the resistance of Nafion (determined from measurements on a Nafion membrane), the pure ionic conductivity of GO was calculated from the blocking measurements and is shown in *Figure 3.14a*. At high humidity, the conductivity of the unblocked and electronically blocked membrane are nearly identical, as expected for dominant proton conduction and indicating that the interfacial ionic resistance (given in  $Z_{int,i2}$ ) is indeed negligible. As humidity decreases, the blocked conductivity decreases by about four orders of magnitude, yet the conductivity of the unblocked membrane at first slightly decreases but then increases. These results are consistent with a loss of proton conductivity with decreasing humidity (as expected for water-mediated proton conduction), and a rise in electronic conduction via the  $sp^2$  regions of the GO sheets. Furthermore, the activation energy,  $E_a$ , for ionic conduction (*Figure 3.14b*), agrees well with the values expected for proton conduction, as described above. *Figure 3.14c* shows the calculated electronic conductivity and the dependence of ionic transference number (i.e. the ratio of ionic to total conductivity) on humidity, derived from the blocking measurements. The electronic contribution decreases and the ionic transference number increases with increasing humidity. At higher temperatures, higher RH's are required to achieve the same ionic transference number, consistent with the loss of water upon heating to higher temperatures for a given RH (discussed later in Chapter 3.4.5).

Turning back to the impedance spectra in *Figure 3.13*, a small additional high frequency contribution to the total impedance was found for non-blocked samples measured in low humidity. The additional response is not observed in the electronic blocking measurements, also shown in the figure. Considering that the dominant conduction mechanism in low humidity is electronic, and the feature is not present in electronic blocking measurements, the additional arc is likely related to an electronic conduction process. Two separate contributions to the impedance spectra for electronic conduction may be expected: one for conduction within the GO sheets at high frequency, and another for conduction between GO sheets, across an interface.<sup>52,53</sup> The activation energy for the small high frequency component in low RH (10 to 50% RH) is approximately 0.1 to 0.3 eV.

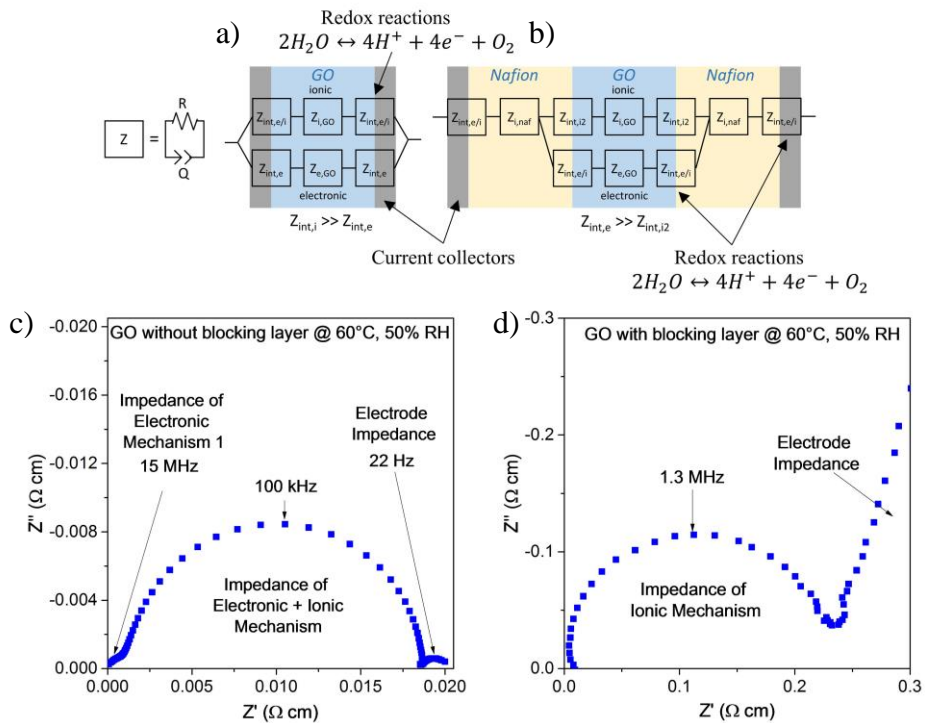


*Figure 3.13. Equivalent circuits for (a) the non-blocking case, and (b) with the addition of Nafion “blocking” electrodes. These appear to be blocking by virtue of the large interfacial impedance for electronic incorporation into GO ( $Z_{int,i,2}$ ) via water redox reactions. c-d) Impedance spectra of GO without (c) and with Nafion blocking layer (d) at 60°C and 50% RH.*

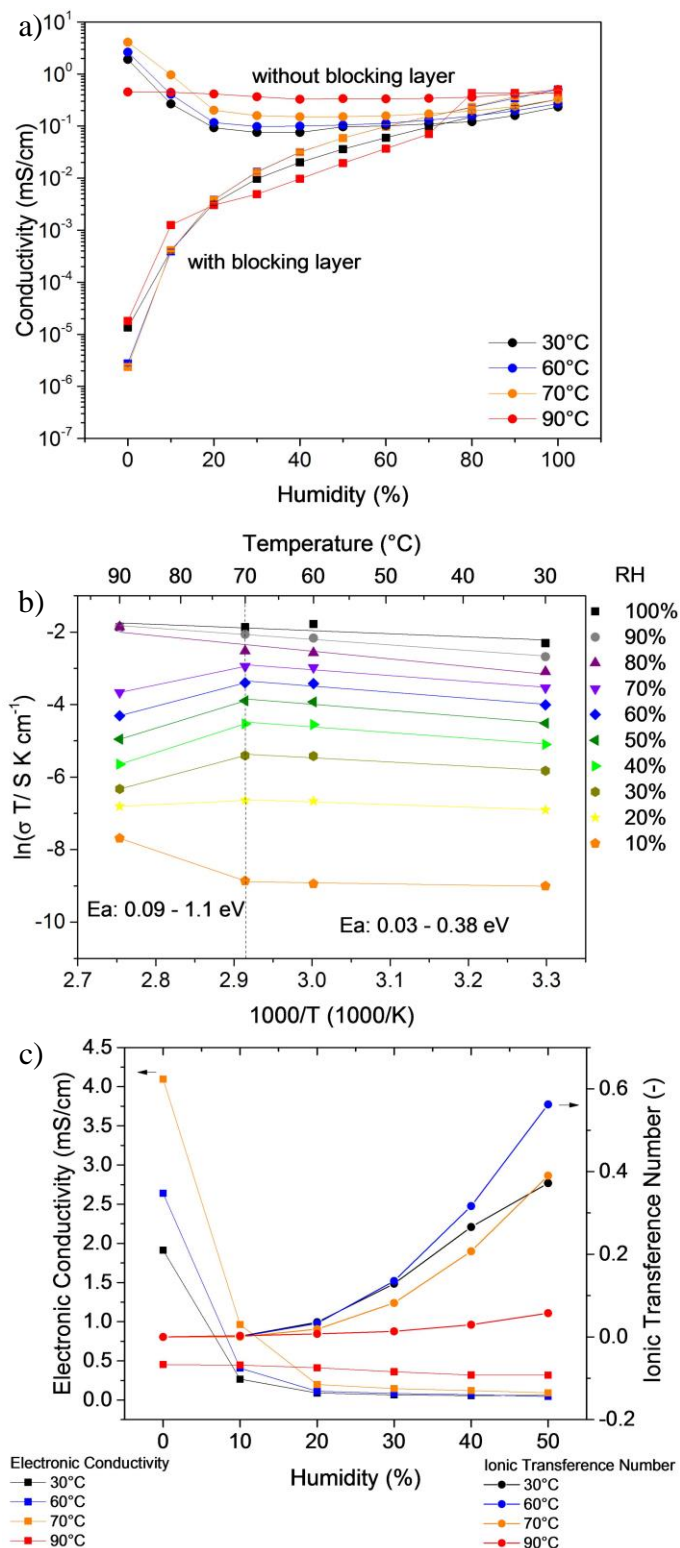


Figure 3.14. a) Conductivity of GO with and without Nafion blocking layers, showing the prevalence of electronic conductivity at low humidity. b) Arrhenius plot of the GO membrane covered with Nafion blocking layers and activation energy. c) Electronic contribution to overall conductivity and ionic transference number in dependence on humidity.

### 3.4.3 In-plane Proton Conductivity

In order to determine if the proton conductivity within GO paper is isotropic or anisotropic, the in-plane proton conductivity ( $\sigma_{IP}$ ) was measured at 100% RH from 30 to 90°C and compared to the values of the through-plane conductivity ( $\sigma_{TP}$ ). The sample had a width of 5 mm and a thickness of 18  $\mu\text{m}$ , and the  $\sigma_{IP}$  was calculated using following equation:

$$\sigma_{IP} = \frac{L}{R \cdot A} \quad (3.4)$$

where  $L$  is the distance between the two platinum electrodes (5 mm),  $R$  the measured resistance and  $A$  the cross-sectional area of the sample (0.09  $\text{mm}^2$ ).

Figure 3.15 shows the in-plane and through-plane conductivity of GO and Nafion. The in-plane proton conductivity of GO is around two orders of magnitude higher compared to through-plane conductivity over the whole temperature range, in agreement with previously reported values.<sup>41,54</sup> The conductivity anisotropy of GO is  $\sigma_{IP}/\sigma_{TP} = 155$  on average, much higher than in Nafion ( $\sigma_{IP}/\sigma_{TP} = 2.9$ ). The measured value for Nafion is in range of anisotropy values mentioned in literature ( $\sigma_{IP}/\sigma_{TP} = 1.8$  to 5),<sup>55-57</sup> however no values for comparison are to be found for GO.

The high anisotropy in conductivity for GO is linked to the large anisotropy in the dimensions of the GO sheets (i.e nanoscale thickness versus microscale lateral size) as well as the highly lamellar structure of the multilayer GO paper. This model supports the role of functional groups on the surface of the GO sheets acting as hopping sites as compared with bulk Grotthus water-mediated proton transfer, as schematically shown in *Figure 3.16*, and also assumed by Ravikumar and Scott.<sup>58</sup> This could also be indicated by the slightly higher activation energy (*Figure 3.15*) compared with the pure Grotthus-type conduction mechanism. In the case of through-plane conductivity, protons must repeatedly hop from one GO layer to the next in a tortuous route via pores, defects and edges.<sup>54</sup> In the case of in-plane conduction, protons can travel in a single plane of water molecules between GO sheets, with dense hydrogen-bonding network enabling fast proton transport. The in-plane conductivity reaches a maximum of 49.8  $\text{mS/cm}$  at 70°C, and decreases with further increase in temperature. The reason for this decrease may be due to reduced water uptake at elevated

temperature, as later shown in Chapter 3.4.5, resulting in a discontinuous hydrogen-bonding network, as well as missing water bridges for surface hopping along functional groups. It is important to mention that the in-plane conductivity of GO is approximately as high as the through-plane conductivity of Nafion. If this can be exploited, GO could become highly competitive as a proton conductor. However it is an engineering challenge to construct devices utilizing the in-plane conductivity of GO rather than the through-plane conductivity.

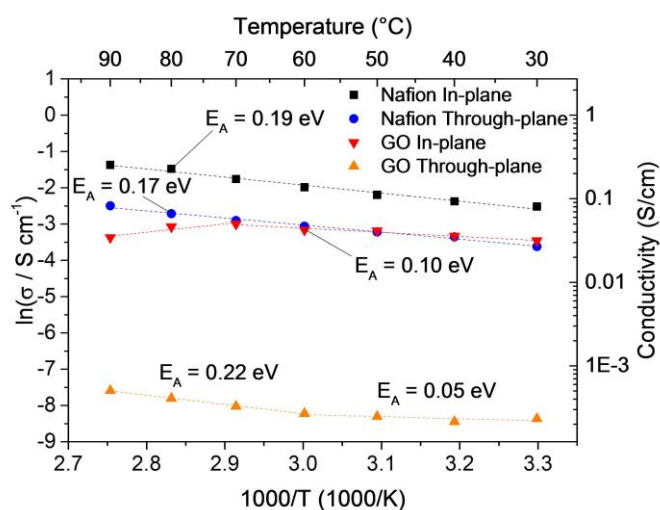


Figure 3.15. Conductivity and Arrhenius plot of the in-plane and through-plane conductivity of Nafion and graphene oxide at 100% RH. Dashed lines are linear fits from which the slope yields the activation energy.

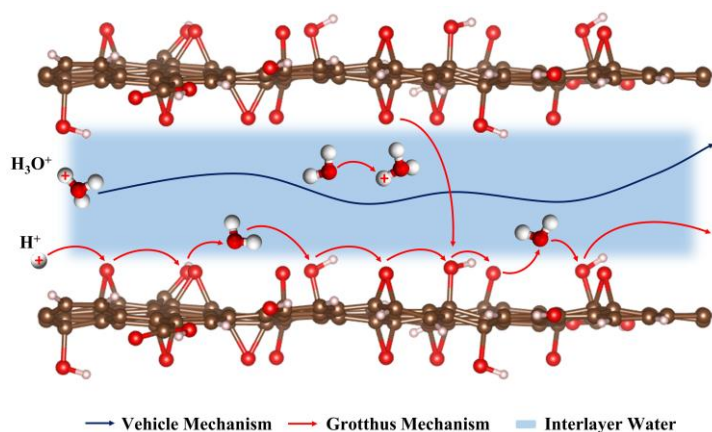


Figure 3.16. Proton transport in GO. Proton conduction modes in the interlayer water (bulk water) and transport along the oxygen groups on the surface.<sup>59</sup>

### 3.4.4 Capacitive Contributions

In addition to the conductivity discussed above, trends in the capacitive behavior of GO paper with temperature and relative humidity were also analyzed from the same set of measurements. The capacitance was determined from impedance measurements with the aid of Equation ( 3.2 ). This shows a strong increase by around two orders of magnitude with decreasing humidity for all temperatures, and is in range of several hundreds of pF to several hundreds of nF, as shown in *Figure 3.17*. Previous researchers have observed a similar trend with Nafion, though with capacitance changes only on the order of tens of percent.<sup>45,60</sup> The relative permittivity of GO paper ( $\epsilon_{GO}$ ) was calculated from the capacitance using the following equation, with membrane thickness ( $d$ ), permittivity of vacuum ( $\epsilon_0 \sim 8.85 \times 10^{-12}$  F/m) and active electrode area ( $A$ ).

$$\epsilon_{GO} = \frac{C_{GO} \cdot d}{\epsilon_0 \cdot A} \quad ( 3.5 )$$

*Figure 3.17a* shows the  $\epsilon_{GO}$  dependence on humidity and temperature (also reported in *Table 3.2*). The permittivity has a wide range (around two orders of magnitude) from  $\sim 10$  at 100% RH to several thousand at 10% RH, exceeding the typical permittivity of Nafion (7 to 30),<sup>61</sup> and water ( $\sim 80$ )<sup>62</sup> by a hundred-fold.

The activation energy for capacitance was extracted from the Arrhenius plot of *Figure 3.17b* and reported along with the values for conductivity in *Figure 3.11c*. Within error, the trend and absolute values for capacitance and conductivity activation energies are similar, indicating the same source, namely displacement of protons and/or electrons. Similar to the Arrhenius plot for conductivity, the Arrhenius plot for the capacitance related activation energy can be divided into two regimes: one ranging from 30 to 60°C with relatively low activation energies close to zero (regime 1), and one from 60 to 90°C, with larger activation energies (regime 2). In regime 2 the activation energy increases with decreasing humidity from 0.17 to 0.77 eV.

Capacitance at 0% RH is not reported, as instrumental contributions to capacitance and/or inductance distorted the small impedance response from the sample caused by the high electronic conductivity in this condition.

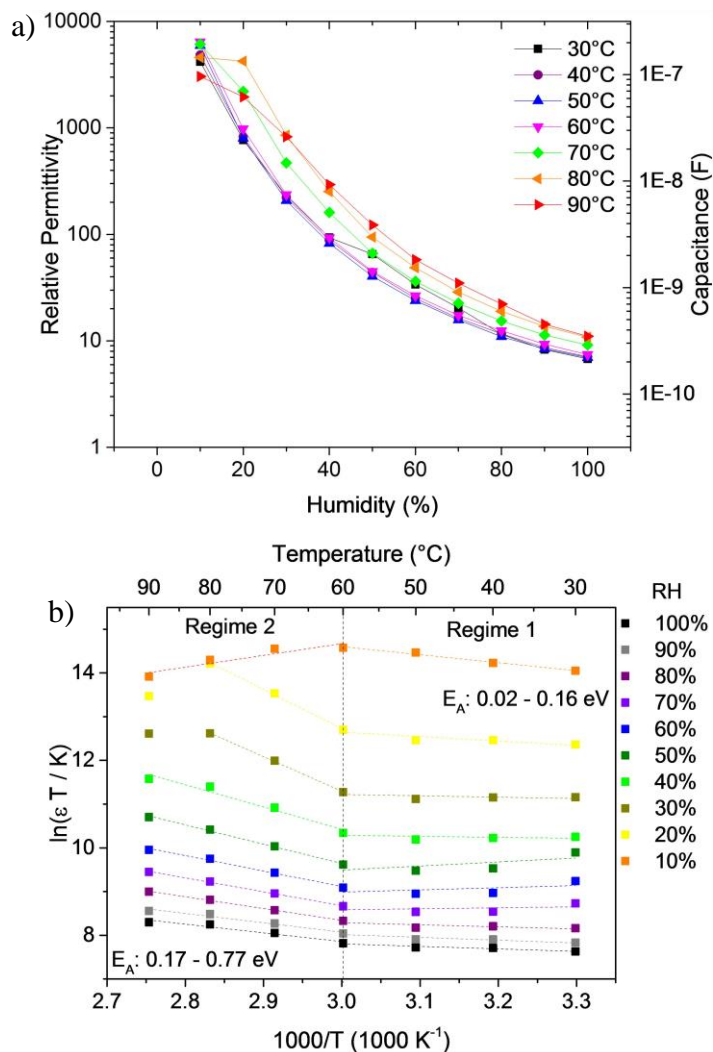


Figure 3.17. a) Dependence of permittivity of GO on temperature and humidity. b) Arrhenius plot of permittivity for 100 to 10% RH (with steps of 10% RH). Activation energy for permittivity values is shown in Figure 3.11c.

Table 3.2. Relative permittivity of GO paper at 100, 60 and 30% RH from 30 to 90°C.

| Temperature<br>(°C) | Humidity |       |     |      |
|---------------------|----------|-------|-----|------|
|                     | 100%     | 60%   | 30% | 10%  |
| 30                  | 6.8      | 65.2  | 231 | 4174 |
| 40                  | 7.1      | 43.9  | 223 | 4835 |
| 50                  | 7        | 40.4  | 208 | 5932 |
| 60                  | 7.4      | 45    | 237 | 6431 |
| 70                  | 9.1      | 66.5  | 469 | 6107 |
| 80                  | 10.8     | 94.3  | 853 | 4582 |
| 90                  | 11       | 122.5 | 826 | 3044 |

### 3.4.5 Water Content Measurements

Due to the dependence of capacitance and conductivity on water content, water uptake (mass of water divided by mass of GO) measurements using TGA were performed as a function of relative humidity at two temperatures, as shown in *Figure 3.18a*. The membrane was pretreated with dry nitrogen for 24 h and it is assumed to be fully dehydrated (except for an assumed physisorbed monolayer of water which is difficult to remove).<sup>17,63,64</sup> For the room temperature data, two separate measurements on the same sample were performed, both showing the reproducible linear trend. Extrapolating the room temperature values to 100% RH yields a 33 wt% water uptake, which is only ten percent of the value we observed previously for GO after immersion in water at room temperature and measured ex situ (325.6 wt%). Reason for this difference might be a higher driving force for water uptake in liquid water compared to humidified air. For the higher temperature measurement, the amount of adsorbed water is about 1/3 of that measured at room temperature for the same RH (i.e. 30%). In Nafion, a decrease in water content with increasing temperature was also reported.<sup>65,66</sup>

The change in the number of water molecules absorbed per unit cell of GO ( $\Delta\lambda$ ) was calculated from the following equation. This equation is analogous to the  $\lambda$  reported for Nafion,<sup>67</sup> though in this case it is based on GO concentration and not acid group concentration.

$$\lambda = \frac{\text{Water Molecules}}{\text{GO Cell Unit}} = WU_{\text{H}_2\text{O}/\text{GO}} \cdot \frac{M_{\text{GO, Unit Cell}}}{M_{\text{H}_2\text{O}}} \quad (3.6)$$

where  $WU_{\text{H}_2\text{O}/\text{GO}}$  is the water uptake in weight fraction of water to GO,  $M_{\text{GO, Unit Cell}} = 220.1$  g/mol is the molar mass of a unit cell GO and  $M_{\text{H}_2\text{O}} = 18.02$  g/mol is the molar mass of water. Pandey et al. reported a unit cell for GO, containing 6 carbon, 9 oxygen and 4 hydrogen atoms, with a dimension of approximately 0.273 x 0.406 nm and an individual GO sheet thickness of ~0.67 nm.<sup>68</sup> The molar mass of one unit cell GO  $M_{\text{GO, Unit Cell}}$  is therefore 220.1 g/mol, though it is noted that depending on unintentional functional groups and oxygen content, this value may vary.

Excluding the potential for an unknown monolayer water concentration, the number of water molecules per unit cell GO at room temperature ranges from 2.40 at 30% RH to 3.56 at 76% RH, and by extrapolation, ~4 water molecules at 100% RH. It's noted that this is about 1/4

that reported for the ratio of water per SO<sub>3</sub>H-group in Nafion.<sup>69,70</sup> At 71°C the water uptake is strongly decreased and ranges from 0.47 at 12% RH to 0.72 at 30% RH, and by extrapolation, only ~1.7 at 100% RH. The increase in permittivity with decrease in water content is evident when relative permittivity (from *Figure 3.17a*) is replotted against  $\lambda$ , using the permittivity values at 30 and 70°C respectively, as shown in *Figure 3.18b*. Extrapolated values for  $\lambda$  at 100% RH taken from linear fits to the data in *Figure 3.18a* are also shown.

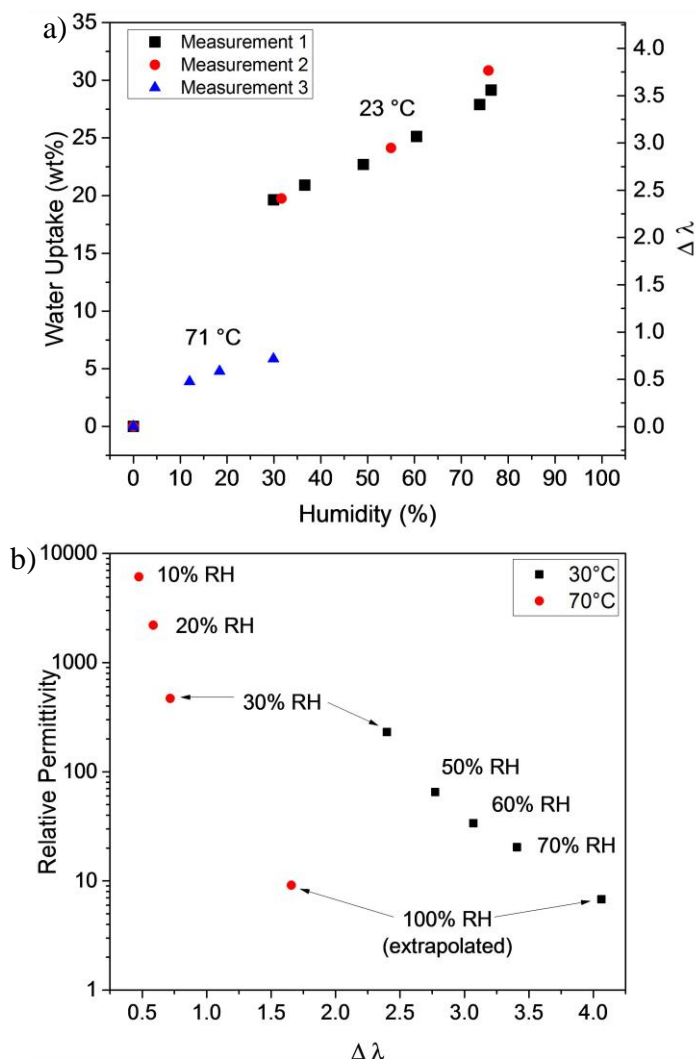


*Figure 3.18. a) Water uptake of GO at different relative humidity reported in mass of water per mass of GO (left axis) and number of water molecules per GO unit cell ( $\lambda$ , right axis). b) Permittivity dependence on the number of water molecules per GO unit cell ( $\lambda$ ).*

### 3.4.6 Discussion: Electronic and Capacitive Behaviour of Graphene Oxide

With the aid of blocking measurements, proton conductivity was clearly established in the GO membranes. As expected, in the high RH range, proton conductivity increased with increasing RH, and below 60°C, the activation energies for proton migration agreed well with those typically ascribed to the Grotthuss type mechanism. At temperatures above about 60°C in high RH, activation energies increased, indicating a change in conduction mechanism to e.g. the vehicle or proton surface hopping mechanisms.<sup>45,71,72</sup> The former mechanism is suggested to be more accessible at higher temperatures due to increased molecular mobility, while the latter mechanism may arise from the loss of water observed in *Figure 3.18*. Similar observations have been made for Nafion, where surface bound water at low RH (i.e. low water content) is suggested to have a high activation barrier for proton hopping.<sup>73</sup> *Figure 3.16* shows a schematic representation of proton transport in GO via the vehicle mechanism, Grotthuss type mechanism, and proton hopping along functional groups on the surface.

Turning to the low RH range, a significant contribution from electronic conductivity is clearly apparent, becoming the dominant charge carrier at the lowest RH's. The increase in electronic conductivity with decreasing RH is believed to arise from a loss of the insulating water phase between the GO sheets, and thus reduced barrier to electron transport between sheets.<sup>74</sup> It is worth noting that the spacing between GO sheets is expected to decrease with water loss in the spring-loaded setup, as observed previously.<sup>17</sup> A similar RH dependence is also observed for the membrane partially reduced at 120°C, where a higher RH leads to a decrease in electronic conductivity. The relatively steep activation energy at 0% RH in the higher temperature regime may arise from semiconducting behavior of the GO and/or behavior consistent with the sample becoming increasingly reduced (and therefore increasingly electronically conductive) upon heating.

Transport in reduced GO (rGO) has been found to occur via variable-range hopping and in the case of well-reduced GO by band-like transport.<sup>75</sup> In other words, one might expect a higher activation energy for electronic conductivity in GO with higher oxygen contents. After partial reduction at 120°C, the electronic conductivity still shows a slight thermal activation (*Figure 3.12a*), albeit lower than the steep temperature dependence described above, consistent with the above interpretation. Interestingly, in the range of 40 to 60% RH in *Figure*

3.14, GO is a mixed ionic and electronic conductor (MIEC). Hatakeyama et al. recently suggested that reduced GO with added sulfonate groups exhibits MIEC behavior.<sup>76</sup> MIEC materials are attractive as single phase electrodes due to their ability to provide electrons and carry protons, simultaneously needed for the oxygen reduction reaction (ORR).

Dielectric permittivity was found to increase by more than 2 orders of magnitude with decreasing RH. While Nafion also exhibits an increase in capacitance with decreasing RH, the relative change is only a few tens of percent, as mentioned earlier.<sup>45,60</sup> In the present mixed conducting system, the mechanism for the large permittivity change with decreasing RH is not known, although the similarity of permittivity and conductivity activation energies (*Figure 3.11c*) suggests that the mechanisms for both processes may be related. In other words, the permittivity may reflect contributions from both the water-like layers (e.g. dipolar relaxation involving proton motion) and the GO itself (e.g. “pseudo-capacitance” described later and/or electrical double layer capacitance), with relative contributions dependent on humidity. The following discussion hypothesizes possible causes for the behavior; further work beyond the purview of the present study would be needed to confirm mechanisms.

In terms of the contribution from water: under the highest RH, the water content is large in the GO paper, and as a result one expects dipolar polarization within water layers to dominate the permittivity. Since the values are lower than for pure water, dipoles may be hindered from fully polarizing in response to the electric field, leading to a lower permittivity. Loss of water may alleviate the water rotational confinement, leading to the initial observed increase in permittivity. The large increase in permittivity upon dehydration may be related to changes that take place within the 2D layered structure of the GO paper membrane. For example, at high RH, the GO platelets which make up the paper are largely isolated via the proton conducting water interlayer. Upon partial loss of water, some of the platelets may be expected to become electronically connected, leading to: 1) the increased electronic conductivity observed in *Figure 3.14*; and 2) a possible interdigitated network of electrically connected GO sheets similar to that used in multilayer capacitors.<sup>77</sup> This latter possibility may give rise to the very large increase in GO permittivity with water loss.

Additionally, the capacitance of carbon-based materials has been reported to consist of double-layer capacitance due to charge accumulation in the electrode-electrolyte-interface

and a pseudo-capacitance, which is induced by faradaic reactions involving oxygen groups.<sup>78–80</sup> The double-layer capacitance was shown to increase with increasing electronic conductivity whereas the pseudo-capacitance strongly depends on the oxygen groups. However, synergistic effects of electronic conductivity and defect density were also observed.<sup>78,79</sup> If such mechanisms are active in the present study, one may expect the double-layer capacitance to dominate in lower humidity conditions and in reduced samples with lower oxygen contents. Since the above capacitance sources are electrode related, this effect is more likely evident at low frequency.

### 3.5 Membrane Electrode Assembly Characterization

A GO membrane was assembled into an MEA to test the performance in a GOMFC (*Figure 3.19a*), i.e. a PEMFC analogue in which the Nafion membrane is replaced with GO, in a temperature range from 30 to 80°C. This is the first time that a GOMFC operated at elevated temperature has been reported in the literature.<sup>30</sup>

*Figure 3.20* shows the dependence of the polarization curve and the current-power density curve, on temperature. The high open circuit voltage (OCV) of 1.01 V at 40°C (compared to Nafion, equal to 0.98 V) is very promising. This high OCV clearly indicates that this membrane is a predominant protonic conductor under these conditions, as any dominant electron transport through the membrane would result in a significant voltage drop. Additionally, it also indicates low fuel crossover. The OCV, however, decreases from a maximum of 1.01 V at 40°C, to 0.42 V at 80°C. This potential drop may be partly due to a loss of oxygen groups with a corresponding decrease in proton conductivity as discussed in detail above, as well as an increase in electronic conductivity.

From 30 to 80°C, the gradient of the slope of the polarization curve (i.e. the resistance) increases, behavior that is not in agreement with the expected increase in conductivity with increasing temperature observed in *Figure 3.11a*. We propose that the GOMFC may suffer a loss of oxygen-containing groups due to the strongly reducing hydrogen conditions at the anode. A partial reduction of the GO membrane could also result in an increase in electronic conductivity, leading to a direct flow of electrons from the anode to the cathode, correspondingly reducing the OCV.<sup>81</sup> Additionally, rupture of the membrane may occur

under reducing conditions, resulting in gas leakage across the membrane, with a corresponding drop in OCV.

The maximum power density (MPD) at 30°C is 33.8 mW/cm<sup>2</sup>, the highest reported value in the literature for a pure GOMFC. The improved performance compared to a previously reported value (13 mW/cm<sup>2</sup>, for a ~20 µm thick membrane)<sup>41</sup> could be attributed to the fact that the GO membrane in this work is thinner, as discussed later. For comparison, a Nafion-based PEMFC was fabricated and operated under the same conditions (*Figure 3.21a*), and the MPD was found to be only twice the value for the present GOMFC. With increasing temperature the MPD decreases to 23.2 mW/cm<sup>2</sup> at 40°C, and 5.5 mW/cm<sup>2</sup> at 50°C. At 80°C the MPD is just 0.18 mW/cm<sup>2</sup>. Again, the degradation in fuel cell performance with increasing temperature may be due to loss of oxygen-containing groups such as epoxy and hydroxyl in the reducing hydrogen atmosphere, even at temperatures as low as 40°C. In support of this hypothesis, a discoloration of the membrane was clearly observed after the measurement, especially on areas exposed to hydrogen (*Figure 3.22*). To investigate this discoloration, we conducted XPS measurements on the membrane after MEA operation. At the anode, the discolored region had an oxygen content of 15.0 at%, whilst at the cathode the oxygen content was 24.3 at%. This decrease in oxygen content of the GO membrane at the anode (from 25.2 at% before MEA tests) supports the idea that reduction of the GO occurs at elevated temperature, and the reduction is more pronounced under reducing hydrogen gas conditions. It is worth reiterating, that these are the first reported elevated temperature measurements of a GOMFC, possibly due to a reluctance to report this observed deterioration in performance.

Lastly, the thickness dependence of GO membrane fuel cell performance was investigated using a thicker, 50 µm membrane (as opposed to the 16 µm membrane discussed above). In *Figure 3.21a*, the thicker membrane clearly has a much lower maximum power density (~3.5 mW/cm<sup>2</sup>) which indicates that membrane thickness plays a key role in performance of these cells (as opposed to being limited by electrode kinetics). Additionally, the performance of a GOMFC with thinner membrane is approaching the performance of Nafion-based PEMFCs at room temperature (membrane thickness 50.1 µm) prepared under the same conditions (namely that the GDL was not attached by hot-pressing). If hot-pressed, power density of

Nafion PEMFCs is about twice the value of not hot-pressed MEAs. This highlights the advantage of creating thin, mechanically robust, and gas tight GO membranes.

A durability test was performed on the 50  $\mu\text{m}$  thick GO membrane under constant load (2 mA), at 30°C (*Figure 3.21b*). The cell voltage decreased steadily to just 26% of the initial value after 80 minutes. After the durability test, the maximum power density decreased to  $\sim 0.5 \text{ mW/cm}^2$ . This decrease in performance over time is attributed to reduction of the GO, as previously discussed. However, the high OCV measured after the load was removed indicates that the membrane maintained its gas barrier properties. We are currently investigating methods to increase the stability of the oxygen functional groups to offer better resistance to reduction and high temperature stability.

Post-operation SEM investigation of the MEA cross-sections was performed. *Figure 3.19b* shows the strong variation in thickness of GDL, electrocatalyst layers and GO membrane. *Figure 3.19c-d* shows clearly the layered structure of the GO membrane.

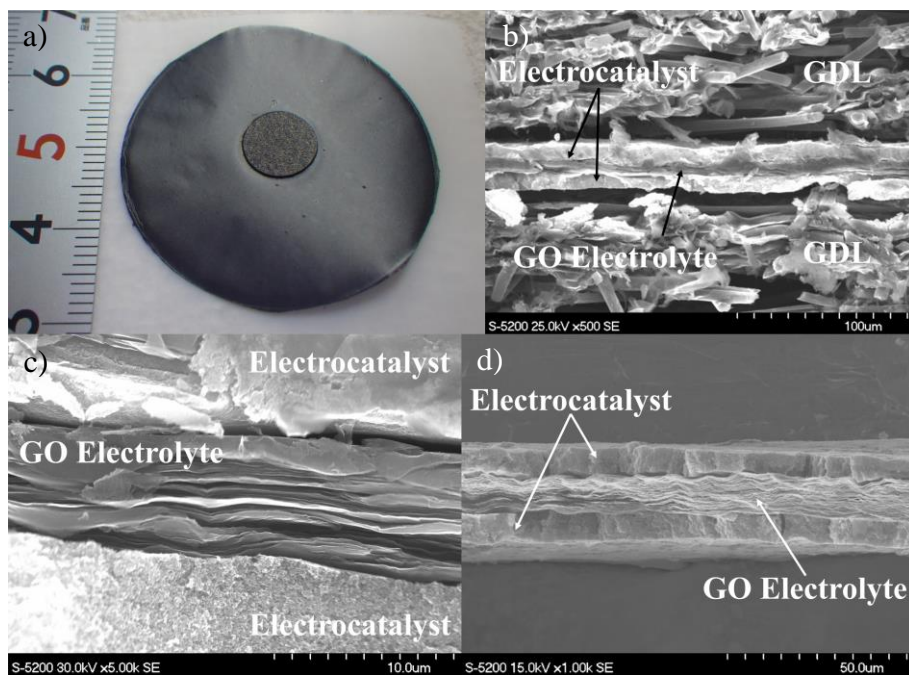


*Figure 3.19. a) Graphene oxide membrane fuel cell (GOMFC). b) Cross-section of the GOMFC shown in Image (a). c-d) Cross-section of a GOMFC showing the layered structure of the GO membrane.*

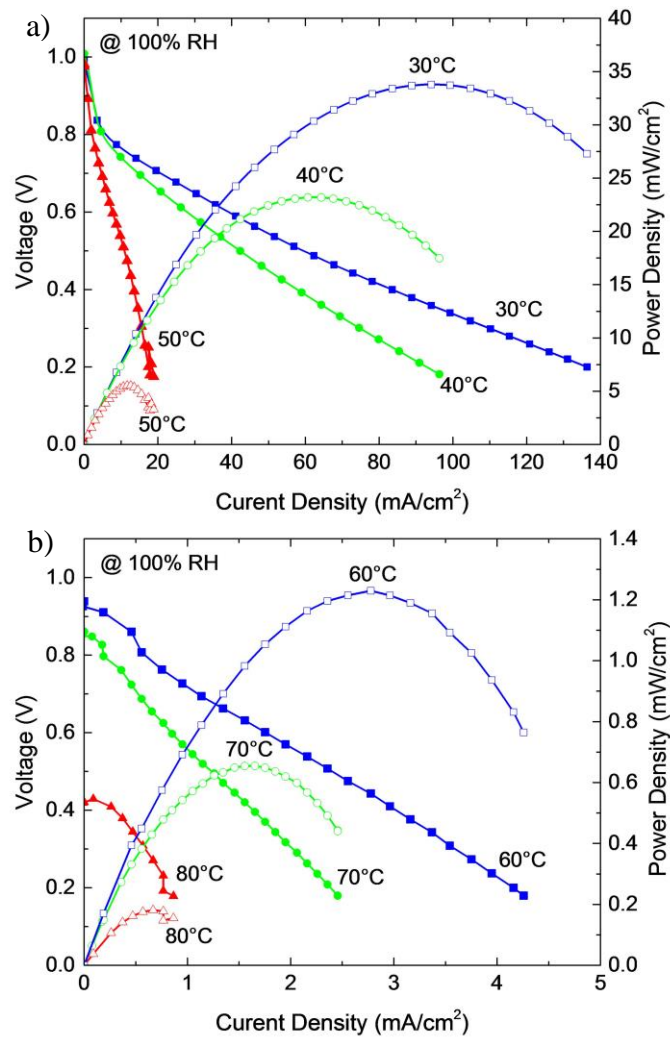


Figure 3.20. Polarization curves and power density of the GOMFC at different temperatures: a) 30 to 50°C; and b) 60 to 80°C.

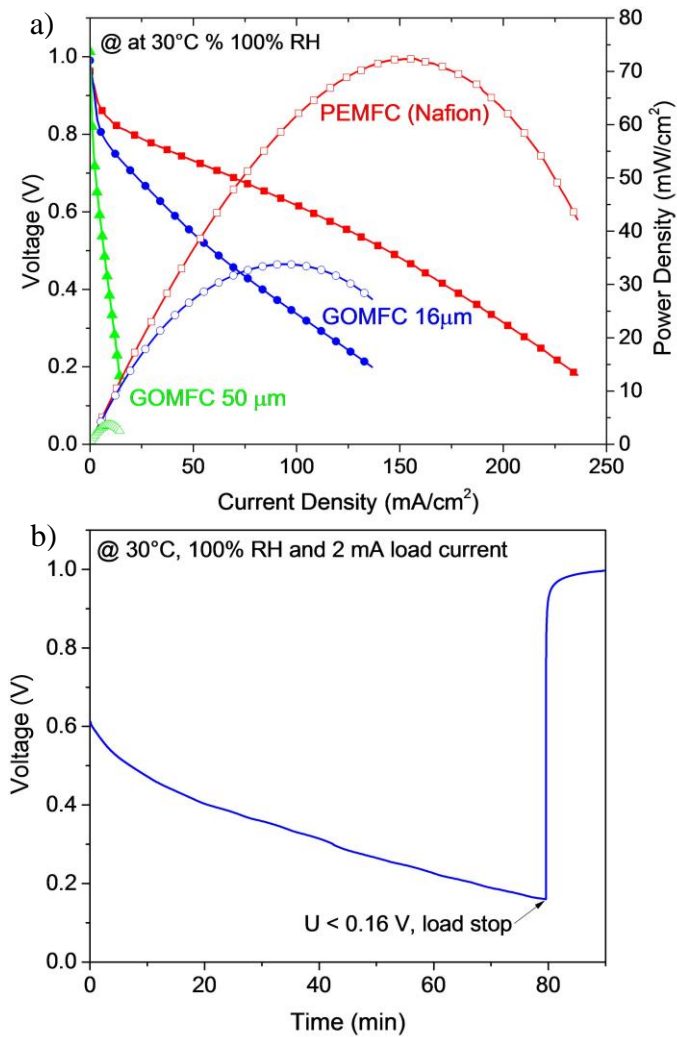


Figure 3.21. Polarization curves and power density for 16 and 50  $\mu\text{m}$  thick GOMFCs, and a 50.1  $\mu\text{m}$  thick Nafion-based PEMFC at 30°C. b) Durability measurement of a 50  $\mu\text{m}$  thick GOMFC with 2 mA load current at 30°C.

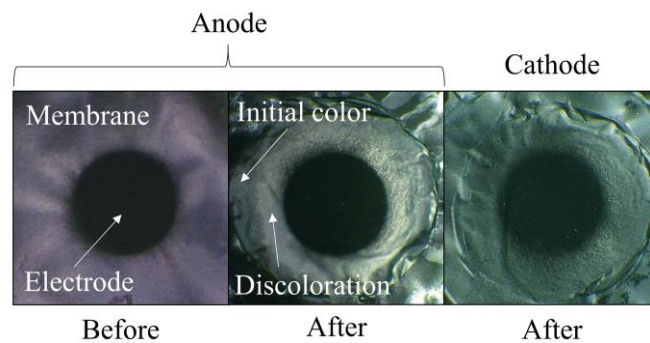


Figure 3.22. Discoloration of the GO membrane after fuel cell operation.

## 3.6 Electrode-supported Fuel Cells: Sprayed Membranes

### 3.6.1 Introduction

As shown in the previous chapter, GOMFCs with thin membranes are approaching the power density of Nafion-based fuel cells at low operation temperatures. Therefore a way to increase power density for a fuel cell using a compared to Nafion less proton conductive membrane is to reduce the electrolyte thickness. However thin electrolytes might have problems with mechanical stability and handling of freestanding membranes during fabrication would be difficult. A new concept for thin film electrolytes is the electrode-supported electrolyte. In solid oxide fuel cells (SOFCs) electrode-supported designs are quite common, and are used in order to decrease voltage loss along the electrolyte and to decrease the operation temperature of the cell.<sup>82-87</sup> For example yttria-stabilized zirconia (YSZ) electrolytes with thicknesses of 0.1 to 10 microns have been successfully fabricated.<sup>85</sup> Reducing the electrolyte thickness not only decreases the ohmic losses and therefore increases the power density of the cell, but also reduces the material costs. For PEMFCs, the concept of electrode-supported membranes is almost unknown. The reason for this may be the assumption that fuel crossover increases drastically with decreasing membrane thickness.<sup>26</sup> However, Klingele et al. recently reported the fabrication of an inkjet-printed electrode-supported Nafion MEA with an electrolyte thickness of 8 to 28  $\mu\text{m}$ , with extraordinarily high power density ( $4 \text{ W/cm}^2$ ) and negligible fuel crossover.<sup>88</sup> Their method is a great leap forward in MEA fabrication, but still requires an additional subgasket to prevent gas leakage, as well as hot-pressing.

In order to improve fabrication process and reduce fabrication time for mass production, it would be beneficial if a complete MEA could be fabricated in one fabrication device, and without additional hot-pressing, or the need for sub-gaskets. Printing technologies e.g. 3D printing, can be used to fabricate various kind of products, including foodstuffs, drug delivery vehicles, medical implants, and customized labware.<sup>89,90</sup> Printing technologies are methods for large area processing and cost reduced production. Recently Lyth and Silva reported the preparation and investigation of cathodes produced by deposition of water-based multiwall carbon nanotube inks on various substrates. They showed that water-based ink processing could be used as large-scale manufacturing technique in e.g. field emission technologies.<sup>91</sup>

In the previous chapter, GO was investigated as promising fuel cell membrane and also other researchers showed the application of GO as fuel cell membranes.<sup>30,38,54,58</sup> All of these previous reports were for membrane-supported cells, thus using relatively thick electrolytes with high ohmic losses. However the high gas barrier properties (as shown in *Figure 3.9*) make it interesting as a thinfilm electrolyte in electrode-supported fuel cells.<sup>16,92</sup> Here we present the fabrication and characterization of an ultra-thin electrode-supported GOMFC fabricated by spraying.

### 3.6.2 Fabrication Method

For the fabrication of electrode-supported GOMFCs, a *Nordson K.K.* spraying device with an A7A spray gun was utilized. The fabrication process is schematically shown in *Figure 3.23*. Catalyst ink was prepared as described in Section 2.3.1. The catalyst ink was sprayed onto carbon paper (*Sigracet*<sup>®</sup> GDL 25 BC with microporous layer, 4x4 cm, electrode size 0.5 cm<sup>2</sup>, 0.3 mg platinum loading) in order to fabricate the cathode. Following this, GO-water-ethanol dispersion (herein referred to as GO ink) was sprayed over the masked cathode in several steps in order to fabricate an ultrathin electrolyte layer. The final electrolyte thickness depends on the amount of spraying steps, as seen schematically in *Figure 3.23c*. Approximately 9.54 ml of GO ink (corresponding to approximately 9.88 mg of GO) was sprayed over a total area of 22 cm<sup>2</sup>. Therefore for the masked area (14.44 cm<sup>2</sup>) the total loading of GO was 6.5 mg, or 0.45 mg/cm<sup>2</sup>. The deposited electrolyte thickness was calculated to be ~3.9 μm (0.6 μm per mg of GO). Then a second layer of electrocatalyst ink was sprayed onto a masked portion of the GO in order to fabricate the anode, directly opposite the cathode. A gas diffusion layer was placed on the anode (without hot-pressing) and the MEA was fitted into a NEDO cell holder (1 cm<sup>2</sup> flow field size).

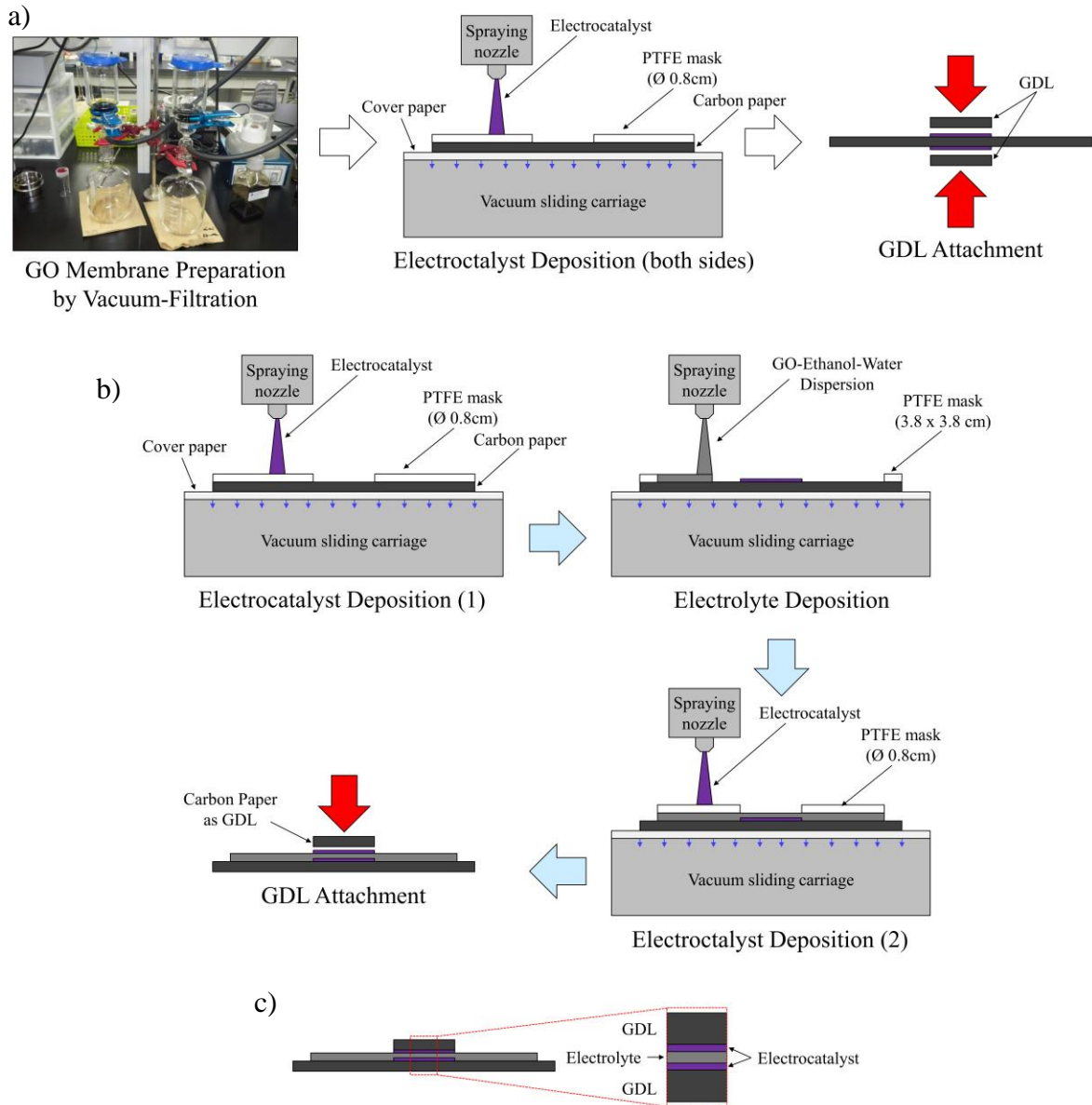


Figure 3.23. a-b) Fabrication process of electrolyte-supported (a) and electrode-supported (b) GOMFCs. c) Structure of the electrode-supported GOMFC.

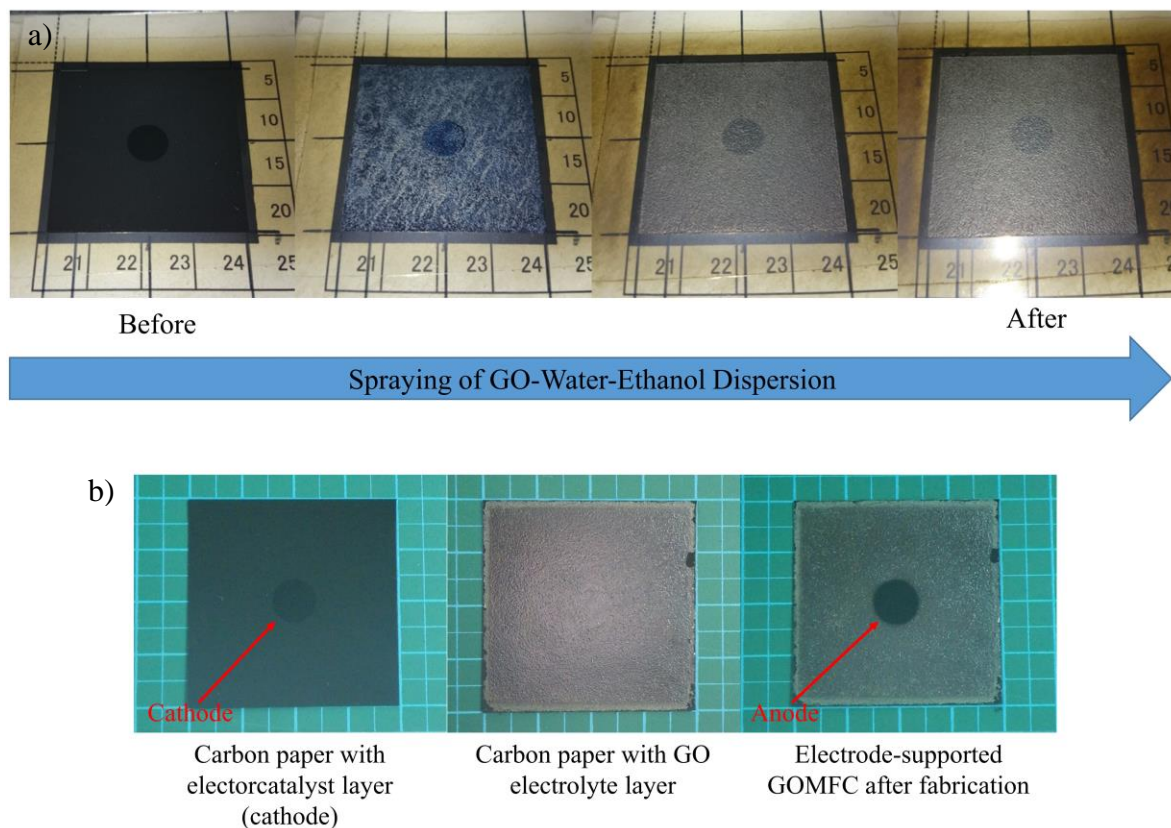


Figure 3.24. a) Schematic of the spray deposition of GO electrolyte onto the cathode-containing carbon paper (electrode), showing the increasing electrolyte thickness with several spraying steps. b) Fabrication of electrode-supported GOMFC. From left to right: After cathode preparation, after GO electrolyte deposition and after anode preparation.

### 3.6.3 Characterization of Electrode-Supported GOMFC

Figure 3.25a shows polarization curves and power densities of three different GOMFCs; two electrolyte-supported MEAs using 50 and 16  $\mu\text{m}$  thick membranes; and a printed thin-film electrolyte fabricated according to the steps above. The performance is compared with two Nafion-based PEMFCs: one prepared with hot-pressing, and one without.

Both electrolyte-supported GOMFCs have a high open circuit voltage (OCV) of  $\sim 1.0$  V, indicating high gas barrier and good catalytic activity of the catalyst. The sprayed GOMFC has a much lower OCV of 0.57 V. The ex-situ gas barrier properties of GO were shown to be high in Chapter 3.3.8. However, the fabrication process and the very thin nature of the films may lead to pinholes and therefore hydrogen cross-over. The sprayed GOMFC showed

a much higher power density ( $\sim 79 \text{ mW/cm}^2$ ) compared to electrolyte-supported GOMFCs ( $\sim 4$  and  $34 \text{ mW/cm}^2$ ). This is due to its low electrolyte resistance, calculated from the slope of the polarization curve ( $0.89 \text{ } \Omega \text{ cm}^2$  compared to  $4.15$  and  $43.0 \text{ } \Omega \text{ cm}^2$  respectively). The electrode-supported GOMFC showed slightly higher power density than Nafion-based PEMFC ( $\sim 72 \text{ mW/cm}^2$ ) prepared in a similar manner (i.e. GDL not hot-pressed). However compared to PEMFCs fabricated by hot pressing, the power density is only around half. This may be due to reduced contact resistance between the GDL and the electrocatalyst layer, as well as better catalytic activity, since hot-pressing leads to a good coverage of the electrocatalyst by Nafion ionomer.

A durability measurement was performed with  $100 \text{ mA}$  constant load current and the cell voltage was monitored (Figure 3.25b). Within one hour, the cell voltage drops from a starting value of  $\sim 0.5 \text{ V}$  to  $0.16 \text{ V}$ . The durability of the electrode-supported GOMFC is worse than the electrolyte-supported GOMFC (Figure 3.21b), probably due to the fact that an electronically conducting pathway can be formed more quickly through a thin GO layer than through the thicker layers.

Figure 3.25b shows the relationship between electrolyte thickness and resulting power density. It can be clearly seen that decreasing the electrolyte thickness results in a profound increase in the power density of fuel cells. From our experience, GO membranes less than  $10 \text{ } \mu\text{m}$  are difficult to handle and break easily during MEA fabrication. Therefore for thinner electrolytes, the electrode-supported preparation method is strongly recommended.

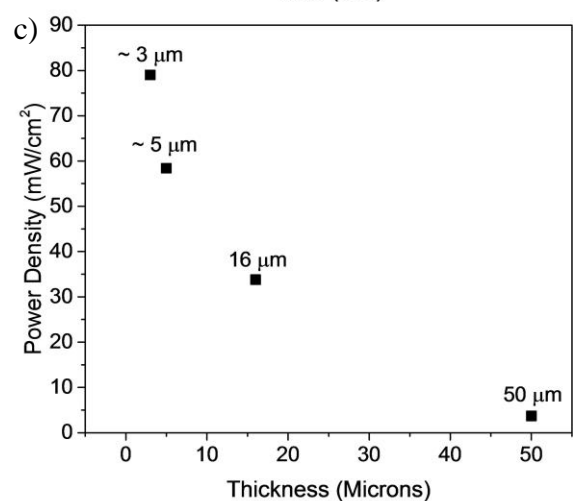
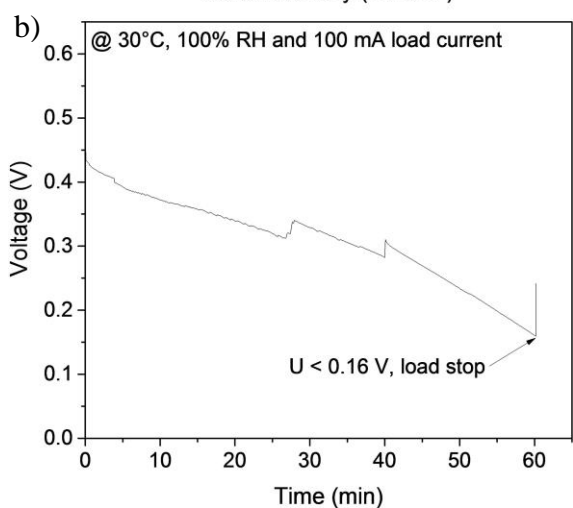
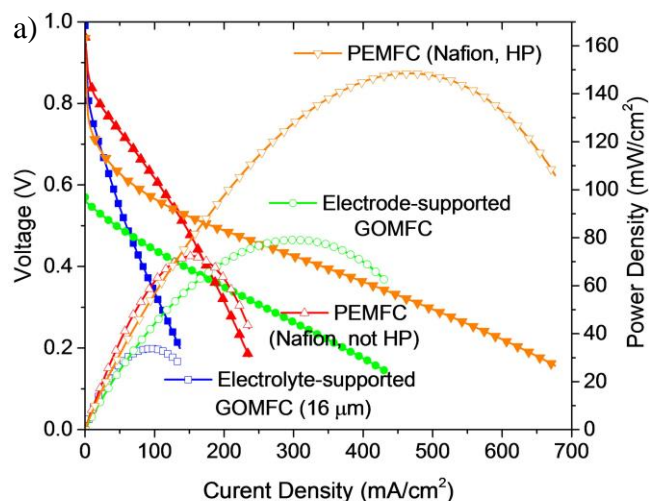
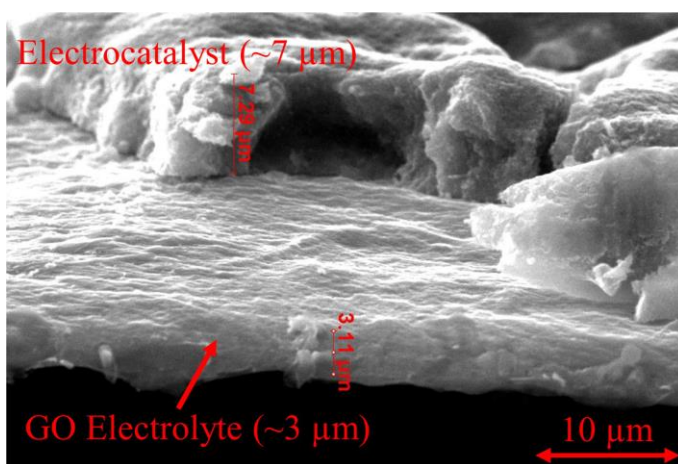


Figure 3.25. a) Polarization curves and power density of electrolyte- and electrode supported GOMFCs in comparison to Nafion-based PEMFCs. b) Durability measurement of the electrode-supported GOMFC at 100 mA constant load current. c) Power density in dependence on electrolyte thickness showing the strong performance of electrode-supported GOMFCs.

After the performance test, the cross-section of the electrode-supported GOMFC was investigated in order to determine the electrolyte thickness. The sample was cut using a scalpel, but during this process the carbon paper became detached from the GO membrane. *Figure 3.26* shows a cross-section of the electrode-supported GOMFC. It can be seen that the GO electrolyte has a thickness of  $\sim 3 \mu\text{m}$ , and is approximately half as thick as the electrocatalyst layer ( $\sim 7 \mu\text{m}$ ). Due to the same amount of catalyst ink used for electrode deposition height of anode and cathode is assumed to be similar. During spraying the electrolyte onto the anode containing carbon paper the high catalyst-layer (height difference between carbon paper and electrolyte surface) might lead to tensions within the GO electrolyte resulting in pinholes and micro cracks reducing the gas barrier properties of the electrolyte.



*Figure 3.26. SEM image of the cross-section (post-operation) showing the ultrathin GO electrolyte in comparison to the electrocatalyst layer.*

### 3.7 Conclusions

GO membranes prepared by vacuum filtration from aqueous solution were investigated. The morphology was studied by SEM and laser microscopy. XPS revealed an oxygen content of 25.2 at%, mainly in the form of epoxy and hydroxyl groups. XRD analysis revealed an interlayer spacing of 0.761 nm. The fuel cell-related properties of GO are compared with Nafion<sup>®</sup>212 in Table 3.3. GO had much higher water uptake than Nafion, which may lead to better water retention for high temperature operation. However, the membrane swelled to a greater degree than Nafion, increasing the risk of deterioration under hydration. GO has higher tensile strength and elastic modulus than Nafion. Hydrogen permeability of GO is approximately three orders of magnitude less compared to Nafion.

GO shows clear humidity- and temperature-dependent conductivity with two maxima at 5.74 mS/cm (80°C, 0% RH) and 0.51 mS/cm (90°C, 100% RH). With the aid of blocking layer measurements, GO was shown to be a mixed electronic-protonic conductor, with transference numbers depending on humidity. Proton conductivity with corresponding activation energies (0.05 to 0.88 eV) was observed at high humidity, whereas at low humidity (< 40%) electronic conductivity dominates, leading to conductivities exceeding those of proton conduction. At temperatures > 90°C GO is partially irreversibly reduced, and electronic conduction dominates, indicated by increased conductivity with decreasing humidity. Cool-down at 0% RH after measurement at 120°C shows that GO is transformed to a more electronic conductor (i.e. rGO) with a positive temperature coefficient of conduction. The through-plane proton conductivity of GO is < 1% than the highest values of Nafion. This is also reflected by the lower power densities achieved in GO-based PEMFCs. GO on the other hand showed a very high in-plane conductivity due to the fast proton transport in the low dimensional conduction pathway (mono- or multilayer of water), approaching the values of the through-plane conductivity of Nafion.

A maximum power density of 33.8 mW/cm<sup>2</sup> was obtained at 30°C for a membrane-supported MEA made using a GO membrane, approaching the power density for a Nafion based PEMFC prepared in a similar manner (i.e. without hot pressing). The OCV was 1.01 V, higher than for the Nafion-based PEMFCs (0.98 V). This is probably due to the high gas barrier properties of GO and thus low gas crossover-related overvoltage. At elevated

temperature, and also during durability tests, the GOMFC performance suffered, probably due to partial reduction of GO and thus loss of oxygen groups, as evidenced by post-test XPS. An electrode-supported GOMFC with thin electrolyte ( $\sim 3 \mu\text{m}$ ) was prepared by using a novel spray-deposition technique. The resulting power density was  $\sim 79 \text{ mW/cm}^2$ , around twice that of the thicker, electrolyte-supported GOMFCs, and approaching that of Nafion-based PEMFCs. This high power density is attributed to the decreased electrolyte resistance in thinner membranes. The OCV was  $\sim 0.57 \text{ V}$ , much lower than observed for the electrolyte-supported GOMFCs. This is attributed to fuel crossover due to the very thin nature of the membranes, and possible pinholes resulting from the fabrication process. If these engineering issues can be solved, power densities exceeding those of Nafion-based fuel cells should be achievable. Although this technology is still at a very early stage of development, and despite the low proton conductivity compared with Nafion, electrode-supported, printed GO ionomer membranes are promising for future fuel cell applications, as well as other electrochemical membrane applications. Further, the spray deposition techniques developed in this work could help to automate and accelerate fuel cell production and commercialization.

Even the raw material costs of GO are higher, cheap membranes can be fabricated as the high gas barrier properties allow usage of thinner membranes compared to Nafion, which reduce the amount of necessary membrane material. Additionally, the price of GO varies between different suppliers and is decreasing over time. If this work used materials from e.g. *Graphenea*, the membrane costs would be decreased to  $\sim 35 \text{ \$/m}^2$ . Thus there are reasonable possibilities for cost reduction in graphene oxide membranes.

Although GO could not outperform Nafion in overall performance, this study unveiled several interesting features of GO, opening up a variety of application possibilities and further research topics. Due to the high gas barrier properties, GO could be used as thin coating material e.g. in hydrogen storage vessels and hydrogen pipelines in order to avoid hydrogen leakage and embrittlement. Thin layers of GO coated on Nafion could help to maintain high gas barrier whilst thinning down the Nafion layer, potentially resulting in high open circuit voltage, lower membrane resistance, and thus higher power density. The high in-plane conductivity in combination with mixed ionic-electronic conductivity and surface proton transport make GO to an interesting mixed ionic-electronic conductor (MIEC). MIEC

materials are attractive as e.g. single phase electrodes due to their ability to provide electrons and carry protons, simultaneously needed for the oxygen reduction reaction (ORR). GO could have applications in fields where surface/grain boundary conductivity is required e.g. catalysis and sensor technologies. If the in-plane proton conduction could be utilized in fuel cells, high power densities would be achievable, most likely comparable with Nafion-based PEMFCs.

*Table 3.3. Comparison of fuel cell membrane related properties of graphene oxide and Nafion®212.*

| <b>Property</b>                                  | <b>Nafion®212</b>      | <b>GO</b>              |
|--|------------------------|------------------------|
| Mechanica Strength (MPa)                         | 30.7                   | 54.5                   |
| Water Uptake (wt%)                               | 25.6                   | 31.1                   |
| H <sub>2</sub> Permeability at 80°C (barrer)     | 1.01 x 10 <sup>2</sup> | 9.5 x 10 <sup>-2</sup> |
| Proton Conductivity $\sigma_{TP}$ (mS/cm):       |                        |                        |
| -At 30°C   | 26.8                   | 0.23                   |
| -Max.  | 108.3 [120°C]          | 0.51 [90°C]            |
| Proton Conductivity $\sigma_{IP}$ (mS/cm):       | 251.4 [120°C]          | 51.5 [70°C]            |
| Max. Power Density at 30°C (mW/cm <sup>2</sup> ) | 149                    | 79                     |
| Durability                                       | Good                   | Poor                   |
| Raw Material Cost (\$/kg)                        | 24 445                 | 200 000                |
| Membrane Cost (\$/m <sup>2</sup> )               | 2 445 (50 $\mu$ m)     | 880 (3 $\mu$ m)        |

## References

1. Kim, J. Y., Cha, H. S. & Joe, Y. II. Characteristics of Pt-Nafion Composite Prepared by Sputtering-Chemical Reduction. in *203rd ECS Meeting* 1287 (2003).
2. Tien, H.-W., Huang, Y.-L., Yang, S.-Y., Wang, J.-Y. & Ma, C.-C. M. The production of graphene nanosheets decorated with silver nanoparticles for use in transparent, conductive films. *Carbon N. Y.* **49**, 1550–1560 (2011).
3. Dreyer, D. R., Park, S., Bielawski, C. W. & Ruoff, R. S. The chemistry of graphene oxide. *Chem. Soc. Rev.* **39**, 228–240 (2010).
4. Heo, Y., Im, H., Kim, J. & Kim, J. The influence of Al(OH)<sub>3</sub>-coated graphene oxide on improved thermal conductivity and maintained electrical resistivity of Al<sub>2</sub>O<sub>3</sub>/epoxy composites. *J. Nanoparticle Res.* **14**, 1196 (2012).
5. Ferrari, A. C. & Basko, D. M. Raman spectroscopy as a versatile tool for studying the properties of graphene. *Nat. Nanotechnol.* **8**, 235–46 (2013).
6. Zhu, Y. *et al.* Graphene and graphene oxide: synthesis, properties, and applications. *Adv. Mater.* **22**, 3906–3924 (2010).
7. Kudin, K. N. *et al.* Raman Spectra of Graphite Oxide and Functionalized Graphene Sheets. 1–6 (2008).
8. Xu, L. & Cheng, L. Graphite Oxide under High Pressure : A Raman Spectroscopic Study. *J. Nanomater.* **2013**, (2013).
9. Das, A., Chakraborty, B. & Sood, a. K. Raman spectroscopy of graphene on different substrates and influence of defects. *Bull. Mater. Sci.* **31**, 579–584 (2008).
10. Dong, X. *et al.* Ultra-large single-layer graphene obtained from solution chemical reduction and its electrical properties. *Phys. Chem. Chem. Phys.* **12**, 2164–9 (2010).
11. Dikin, D. A. *et al.* Preparation and characterization of graphene oxide paper. *Nature* **448**, 457–60 (2007).
12. Lerf, A. *et al.* Hydration behavior and dynamics of water molecules in graphite oxide. *J. Phzsics Chem. Solids* **67**, 1106–1110 (2006).
13. Seung Hun, H., Hae-Mi, J. & Sung-Ho, C. X-ray Diffraction Patterns of Thermally-reduced Graphenes. *J. Korean Phys. Soc.* **57**, 1649 (2010).
14. Park, S. *et al.* Colloidal Suspensions of Highly Reduced Graphene Oxide in a Wide Variety of Organic Solvents. *Nano Lett.* **9**, 1593–1597 (2009).
15. Marcano, D. C. *et al.* Improved Synthesis of Graphene Oxide. *ACS Nano* **4**, 4806–4814 (2010).

16. Nair, R. R., Wu, H. A., Jayaram, P. N., Grigorieva, I. V. & Geim, A. K. Unimpeded Permeation of Water Through Helium-Leak-Tight Graphene-Based Membranes. *Science* (80-. ). **335**, 442–444 (2012).
17. Daio, T. *et al.* In-Situ ESEM and EELS Observation of Water Uptake and Ice Formation in Multilayer Graphene Oxide. *Sci. Rep.* **5**, 11807 (2015).
18. Kreuer, K.-D., Paddison, S. J., Spohr, E. & Schuster, M. Transport in proton conductors for fuel-cell applications: simulations, elementary reactions, and phenomenology. *Chem. Rev.* **104**, 4637–78 (2004).
19. Agmon, N. The Grotthuss mechanism. *Chem. Phys. Lett.* **50**, 456–462 (1995).
20. Li, Q., He, R., Jensen, J. O. & Bjerrum, N. J. Approaches and Recent Development of Polymer Electrolyte Membranes for Fuel Cells Operating above 100 °C. *Chem. Mater.* **15**, 4896–4915 (2003).
21. Kumar, R., Xu, C. & Scott, K. Graphite oxide/Nafion composite membranes for polymer electrolyte fuel cells. *RSC Adv.* **2**, 8777 (2012).
22. Park, S. *et al.* The effect of concentration of graphene nanoplatelets on mechanical and electrical properties of reduced graphene oxide papers. *Carbon N. Y.* **50**, 4573–4578 (2012).
23. Gao, Y. *et al.* The effect of interlayer adhesion on the mechanical behaviors of macroscopic graphene oxide papers. *ACS Nano* **5**, 2134–2141 (2011).
24. in *Fluorinated Ionomers (Second Edition)* (ed. Grot, W.) 251–257 (William Andrew Publishing, 2011). doi:<http://dx.doi.org/10.1016/B978-1-4377-4457-6.10022-6>
25. Du Pont. DuPont™ Nafion PFSA Membranes NRE-211 and NRE-212 Perfluorosulfonic acid polymer. *Product Information* 1–6 (2004). at <<http://www.fuelcellmarkets.com/content/images/articles/nae201.pdf>>
26. Baik, K. D., Hong, B. K. & Kim, M. S. Effects of operating parameters on hydrogen crossover rate through Nafion® membranes in polymer electrolyte membrane fuel cells. *Renew. Energy* **57**, 234–239 (2013).
27. Song, S. Q., Zhou, W. J., Li, W. Z. & Sun, G. Direct Methanol Fuel Cells : Methanol Crossover and its Influence on Single D M F C Performance. *Ionics (Kiel)*. **10**, 458–462 (2004).
28. Cheng, X. *et al.* Hydrogen crossover in high-temperature PEM fuel cells. *J. Power Sources* **167**, 25–31 (2007).
29. Matteucci, S., Yampolskii, Y., Freeman, B. & Pinnau, I. *Materials Science of Membranes for Gas and Vapor Separation*. (John Wiley & Sons Ltd., 2006).

30. Bayer, T., Bishop, S. R., Nishihara, M., Sasaki, K. & Lyth, S. M. Characterization of a Graphene Oxide Membrane Fuel Cell. *J. Power Sources* **272**, 239–247 (2014).
31. Cooper, K. R. Progress Toward Accurate Through-Plane Membrane Resistance and Conductivity Measurement. *ECS Trans.* **25**, 1–19 (2009).
32. Huggins, R. A. Simple Method to Determine Electronic and Ionic Components of the Conductivity in Mixed Conductors A Review. *Ionics (Kiel)*. **8**, 300–313 (2002).
33. Hirschorn, B. *et al.* Constant-Phase-Element Behavior Caused by Resistivity Distributions in Films. *J. Electrochem. Soc.* **157**, C452 (2010).
34. Shoar Abouzari, M. R., Berkemeier, F., Schmitz, G. & Wilmer, D. On the physical interpretation of constant phase elements. *Solid State Ionics* **180**, 922–927 (2009).
35. Yadav, R. & Fedkiw, P. S. Analysis of EIS Technique and Nafion 117 Conductivity as a Function of Temperature and Relative Humidity. *J. Electrochem. Soc.* **159**, B340–B346 (2012).
36. Macdonald, J. R. Impedance Spectroscopy. *Ann. Biomed. Eng.* **20**, 289–305 (1992).
37. Tuller, H. L. & Bishop, S. R. Point Defects in Oxides: Tailoring Materials Through Defect Engineering. *Annu. Rev. Mater. Res.* **41**, 369–398 (2011).
38. Kumar, R., Mamlouk, M. & Scott, K. A Graphite Oxide Paper Polymer Electrolyte for Direct Methanol Fuel Cells. *Int. J. Electrochem.* **2011**, 1–7 (2011).
39. Zarrin, H., Higgins, D., Jun, Y., Chen, Z. & Fowler, M. Functionalized Graphene Oxide Nanocomposite Membrane for Low Humidity and High Temperature Proton Exchange Membrane Fuel Cells. *J. Phys. Chem. C* **115**, 20774–20781 (2011).
40. Karim, M. R. *et al.* Graphene Oxide Nanosheet with High Proton Conductivity. *J. Am. Chem. Soc.* 0–3 (2013). doi:10.1021/ja401060q
41. Tateishi, H. *et al.* Graphene Oxide Fuel Cell. *J. Electrochem. Soc.* **160**, F1175–F1178 (2013).
42. Hatakeyama, K. *et al.* Proton Conductivities of Graphene Oxide Nanosheets: Single, Multilayer, and Modified Nanosheets. *Angew. Chemie* **126**, 7117–7120 (2014).
43. *Proton conductors: Solids, membranes, and gels—materials and devices.* (Cambridge University Press, 1993). doi:10.1002/adma.19930050923
44. Blumenthal, G. *et al.* Investigation of the Proton Transport in Nafion | Membranes as a Function of Direction , Temperature and Relative Humidity. *Ionics (Kiel)*. **2**, 102–106 (1996).

45. Paul, D. K., McCreery, R. & Karan, K. Proton Transport Property in Supported Nafion Nanothin Films by Electrochemical Impedance Spectroscopy. *J. Electrochem. Soc.* **161**, F1395–F1402 (2014).
46. Taychatanapat, T. & Jarillo-Herrero, P. Electronic transport in dual-gated bilayer graphene at large displacement fields. *Phys. Rev. Lett.* **105**, (2010).
47. Eguchi, K., Setoguchi, T., Inoue, T. & Arai, H. Electrical properties of ceria-based oxides and their application to solid oxide fuel cells. *Solid State Ionics* **52**, 165–172 (1992).
48. Inoue, T., Kamimae, J., Ueda, M., Eguchi, K. & Arai, H. Ionic and electronic conductivities of LaCoO<sub>3</sub>- and LaMnO<sub>3</sub>-based perovskite-type oxides measured by the a.c. impedance method with electron-blocking electrodes. *J. Mater. Chem.* **3**, 751–754 (1993).
49. Jak, M. J. G., Riess, I. & Schoonman, J. Combination of ac-impedance spectroscopy and short circuiting measurements applied on YBa<sub>2</sub>Cu<sub>3</sub>O<sub>7-δ</sub>. *Solid State Ionics* **86-88**, 1409–1413 (1996).
50. Vischjager, D. J., van der Put, P. J., Schram, J. & Schoonman, J. Oxygen Diffusion in YBa<sub>2</sub>Cu<sub>3</sub>O<sub>7-x</sub>; An Impedance Spectroscopy Study. *Solid State Ionics* **27**, 199–205 (1988).
51. Riess, I. Review of the limitation of the Hebb-Wagner polarization method for measuring partial conductivities in mixed ionic electronic conductors. *Solid State Ionics* **91**, 221–232 (1996).
52. Reiss, G., Vancea, J. & Hoffmann, H. Grain-Boundary Resistance in Polycrystalline Metals. *Phys. Rev. B* **56**, 2100–2103 (1986).
53. Strunk, H. P., Werner, J. H., Fortin, B. & Bonnaud, O. Origin of Curved Arrhenius Plots for the Conductivity of Polycrystalline Semiconductors. *Solid State Phenom.* **37-38**, 213–218 (1994).
54. Gao, W. *et al.* Ozonated graphene oxide film as a proton-exchange membrane. *Angew. Chemie - Int. Ed.* **53**, 3588–3593 (2014).
55. Gardner, C. L. & Anantaraman, A. V. Studies on ion-exchange membranes . II . Measurement of the anisotropic conductance of Nafion®. *J. Electrochem. Soc.* **449**, 209–214 (1998).
56. Casciola, M., Alberti, G., Sganappa, M. & Narducci, R. On the decay of Nafion proton conductivity at high temperature and relative humidity. *J. Power Sources* **162**, 141–145 (2006).
57. Ma, S., Siroma, Z. & Tanaka, H. Anisotropic Conductivity Over In-Plane and Thickness Directions in Nafion-117. *J. Electrochem. Soc.* **153**, 2274–2281 (2006).

58. Scott, K. & Ravikumar. Freestanding sulfonated graphene oxide paper: a new polymer electrolyte for polymer electrolyte fuel cells. *Chem. Commun.* **48**, 5584–5586 (2012).
59. Momma, K. & Izumi, F. VESTA 3 for three-dimensional visualization of crystal, volumetric and morphology data. *J. Appl. Crystallogr.* **44**, 1272–1276 (2011).
60. Yadav, R. & Fedkiw, P. S. Analysis of EIS Technique and Nafion 117 Conductivity as a Function of Temperature and Relative Humidity. *J. Electrochem. Soc.* **159**, B340–B346 (2012).
61. Paddison, S. J., Reagor, D. W. & Jr, T. A. Z. High frequency dielectric studies of hydrated Nafion® 1. **459**, 91–97 (1998).
62. Malmberg, C. G. & Maryott, A. A. Dielectric Constant of Water from 0 to 100 C. *J. Res. Natl. Bur. Stand. (1934)*. **56**, 1–8 (1956).
63. Szabó, T., Berkesi, O. & Dékány, I. DRIFT study of deuterium-exchanged graphite oxide. *Carbon N. Y.* **43**, 3186–3189 (2005).
64. Bi, H. *et al.* Ultrahigh humidity sensitivity of graphene oxide. *Sci. Rep.* **3**, 2714 (2013).
65. Broka, K. & Ekdunge, P. Oxygen and Hydrogen Permeation Properties and Water Uptake of Nafion 117 membrane and recast film for PEM fuel cell. *J. Appl. Electrochem.* **27**, 117–123 (1997).
66. Rieke, P. C. & Vanderborgh, N. E. Temperature Dependence of Water Content and Proton Conductivity in Polyperfluorsulfonic Acid Membranes. *J. Memb. Sci.* **32**, 313–328 (1987).
67. Hwang, G. S. *et al.* Role of water states on water uptake and proton transport in Nafion using molecular simulations and bimodal network. *Polymer (Guildf)*. **52**, 2584–2593 (2011).
68. Pandey, D., Reifenger, R. & Piner, R. Scanning probe microscopy study of exfoliated oxidized graphene sheets. *Surf. Sci.* **602**, 1607–1613 (2008).
69. Slade, S., Campbell, S. a., Ralph, T. R. & Walsh, F. C. Ionic Conductivity of an Extruded Nafion 1100 EW Series of Membranes. *J. Electrochem. Soc.* **149**, A1556 (2002).
70. Onishi, L. M., Prausnitz, J. M. & Newman, J. Water - Nafion Equilibria. Absence of Schroeder's Paradox. *J. Phys. Chem. B* **111**, 10166–10173 (2007).
71. Eikerling, M., Kornyshev, A. A., Kuznetsov, A. M., Ulstrup, J. & Walbran, S. Mechanisms of Proton Conductance in Polymer Electrolyte Membranes. *J. Phys. Chem. B* **105**, 3646–3662 (2001).

72. Pandey, K. & Lakshmi, N. Evidence of failure of hopping model of ionic conductivity in phosphomolybdic acid studied by a.c. conductivity measurements. *J. Mater. Sci.* **4**, 1749–1752 (1999).
73. Choi, P., Jalani, N. H. & Datta, R. Thermodynamics and Proton Transport in Nafion - I. Membrane Swelling, Sorption, and Ion-Exchange Equilibrium. *J. Electrochem. Soc.* **152**, 84–89 (2005).
74. Wang, D.-W., Du, A., Taran, E., Lu, G. Q. (Max) & Gentle, I. R. A water-dielectric capacitor using hydrated graphene oxide film. *J. Mater. Chem.* **22**, 21085–21091 (2012).
75. Eda, G., Mattevi, C., Yamaguchi, H., Kim, H. & Chhowalla, M. Insulator to Semimetal Transition in Graphene Oxide. *J. Phys. Chem. C* **113**, 15768–15771 (2009).
76. Hatakeyama, K. *et al.* Super proton / electron mixed conduction in graphene oxide hybrids by intercalating sulfate. *J. Mater. Chem. A Mater. energy Sustain.* **3**, 20892–20895 (2015).
77. Kishi, H., Mizuno, Y. & Chazono, H. Base-Metal Electrode-Multilayer Ceramic Capacitors: Past, Present and Future Perspectives. *Jpn. J. Appl. Phys.* **42**, 1–15 (2003).
78. Bleda-Martínez, M. J. *et al.* Role of surface chemistry on electric double layer capacitance of carbon materials. *Carbon N. Y.* **43**, 2677–2684 (2005).
79. Zhang, W. *et al.* Insight into the capacitive properties of reduced graphene oxide. *ACS Appl. Mater. Interfaces* **6**, 2248–2254 (2014).
80. Xu, B. *et al.* What is the choice for supercapacitors: graphene or graphene oxide? *Energy Environ. Sci.* **4**, 2826 (2011).
81. Cooper, K. R. In Situ PEMFC Fuel Crossover & Electrical Short Circuit Measurement. *Fuel Cell Magazine* 1–2 (2008).
82. Srivastava, P. *et al.* Electrode supported solid oxide fuel cells: Electrolyte films prepared by DC magnetron sputtering. *Solid State Ionics* **99**, 311–319 (1997).
83. Su, S., Gao, X., Zhang, Q., Kong, W. & Chen, D. Anode- Versus Cathode-Supported Solid Oxide Fuel Cell : Effect of Cell Design on the Stack Performance. *Int. J. Electrochem. Sci.* **10**, 2487–2503 (2015).
84. Basu, R. N. *et al.* Simplified processing of anode-supported thin film planar solid oxide fuel cells. *J. Eur. Ceram. Soc.* **25**, 463–471 (2005).

85. Zuo, C., Liu, M. & Liu, M. *Sol-Gel Processing for Conventional and Alternative Energy*. (Springer, 2012). at <http://www.springerlink.com/content/r501048714370703/>
86. Larminie, J. & Dicks, A. *Fuel Cell Systems Explained, 2nd Edition*. (Wiley, 2003).
87. Will, J., Mitterdorfer, A., Kleinlogel, C., Perednis, D. & Gauckler, L. J. Fabrication of thin electrolytes for second-generation solid oxide fuel cells. *Solid State Ionics* **131**, 79–96 (2000).
88. Klingele, M., Breitwieser, M., Zengerle, R. & Thiele, S. Direct deposition of proton exchange membranes enabling high performance hydrogen fuel cells. *J. Mater. Chem. A* **3**, 11239–11245 (2015).
89. Sun, J., Zhou, W., Huang, D., Fuh, J. Y. H. & Hong, G. S. An Overview of 3D Printing Technologies for Food Fabrication. *Food Bioprocess Technol.* (2015). doi:10.1007/s11947-015-1528-6
90. Chen, C., Erkal, J. L., Gross, B. C., Lockwood, S. Y. & Spence, D. M. Evaluation of 3D Printing and Its Potential Impact on Biotechnology and the Chemical Sciences. *Anal. Chem.* **86**, 3240–3253 (2014).
91. Lyth, S. M. & Silva, S. R. P. Electron Field Emission from Water-Based Carbon Nanotube Inks. *ECS J. Solid State Sci. Technol.* **4**, P3034–P3043 (2015).
92. Bayer, T. *et al.* Alkaline Anion Exchange Membranes based on KOH-treated Multilayer Graphene Oxide. *Submitted* (2015).

## 4 Anion Exchange Graphene Oxide Membrane Fuel Cells

### 4.1 Introduction and Motivation

As described in Chapter 1.6.1, alkaline fuel cells (AFCs) offer a big advantage compared to PEMFCs, as the usage of non-precious catalyst is possible due to faster reaction kinetics at the cathode. In Chapter 0, graphene oxide (GO) was successfully tested as membrane material for PEMFCs. With its extraordinary high gas barrier to hydrogen, is GO also very promising for application in AFCs.

Here we report the preparation and characterization of a novel heterogeneous anion exchange membrane based on multilayer graphene oxide paper. Reacting carboxyl or hydroxyl groups with KOH results in the following neutralization reactions, forming a carboxylate salt, or an alkoxide:



In the case of GO, the OH- and COOH-functional groups are attached to the surface of the graphene sheet. Similar surface neutralization reactions have been performed on acid-oxidized multiwall carbon nanotubes.<sup>1</sup> Following this neutralization with excess KOH, the GO dispersion is filtered and dried to form membranes.

A detailed material characterization is performed via scanning electron microscopy (SEM), X-ray photoelectron spectroscopy (XPS) and X-ray diffraction (XRD). We report water-uptake, tensile strength, thermal stability and gas barrier properties of KOH-treated GO compared to unaltered GO. The conductivity is investigated and the performance in a GO-based alkaline anion exchange membrane fuel cell (AAEMFC) is presented.

### 4.2 Sample Preparation and Nomenclature

To make an alkaline GO dispersion, 210.8 mg of potassium hydroxide (*Wako Pure Chemical Industry*, assay value > 85.0%) was dissolved in 43.01 ml graphene oxide dispersion (*Graphene Supermarket*, flake size 0.5. to 5  $\mu\text{m}$ , 5 mg/ml) and stirred at room temperature

for 24 hours. The amount of KOH added to the GO dispersion was calculated to be approximately stoichiometric with the oxygen functional groups on the GO, as calculated from elemental analysis. The pH of the as-purchased GO dispersion was 2.3 before addition of KOH, changing to 12.5 after the cation exchange reaction. Herein, KOH-treated graphene oxide is labelled  $\text{GO}_{\text{KOH}}$ . Membranes were prepared by vacuum-filtration from dispersion onto Millipore filters (pore size 0.025  $\mu\text{m}$ , 35 mm diameter). These were then dried at room temperature for 48 hours and peeled off the filter, yielding freestanding and flexible  $\text{GO}_{\text{KOH}}$  membranes.

### **4.3 General Material Characterization**

#### **4.3.1 Scanning Electron Microscopy**

Figure 4.1 shows surface and cross-sectional SEM images of GO (a-b) and  $\text{GO}_{\text{KOH}}$  (c-d) membranes. Both GO and  $\text{GO}_{\text{KOH}}$  membranes have a layered structure, characteristic of multilayer GO paper. However, the  $\text{GO}_{\text{KOH}}$  membrane surface is more strongly corrugated, with more prominent surface features than the GO membrane. Such corrugation has been observed in, for example, reduced GO.<sup>2</sup> Alternatively, the change in morphology may be induced by the introduction of significantly altered surface charge as a result of the neutralization reaction.

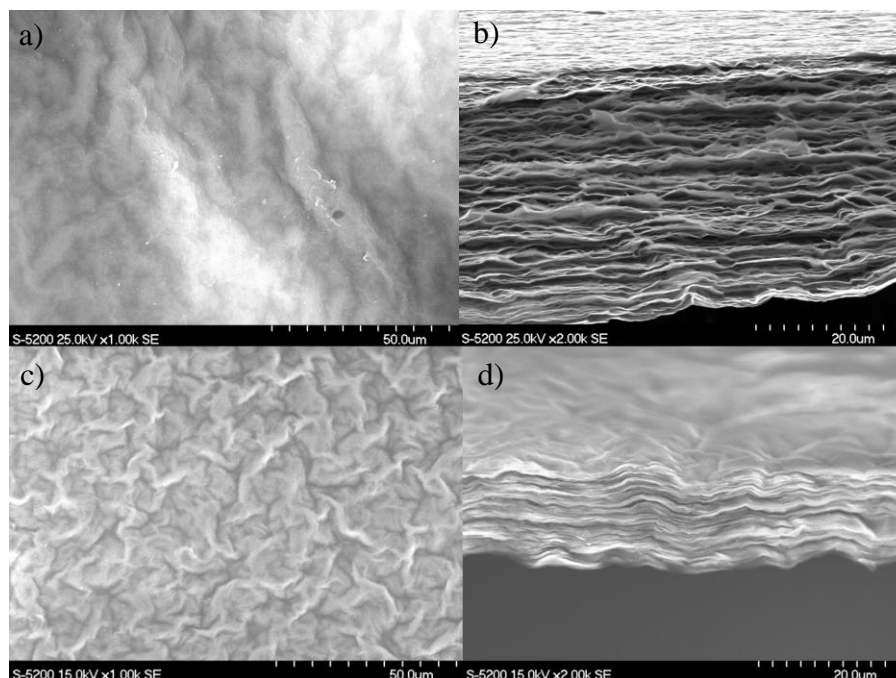


Figure 4.1. SEM images of multilayer (a,b) GO, and (c,d)  $GO_{KOH}$  membranes.

### 4.3.2 X-Ray Photoelectron Microscopy

XPS was performed on GO and  $GO_{KOH}$  for chemical and elemental analysis. Figure 4.2a shows the wide scan spectrum with three major peaks corresponding to O 1s (532 eV), K 2p (292 eV), and C 1s (284 eV). The elemental composition is: 77.5% carbon and 22.5% oxygen for GO; and 78.5% carbon, 15.9% oxygen, and 5.7% potassium for  $GO_{KOH}$ . The oxygen content is slightly lower in  $GO_{KOH}$ . Figure 4.2b shows the C1s spectra deconvoluted into six peaks ascribed to different bonds.  $GO_{KOH}$  shows a clear decrease in the proportion of epoxy groups. The proportion of hydroxyl groups decreases slightly and an energy shift is observed, as a result of the cation exchange reaction. The deconvoluted O 1s spectra are shown in Figure 4.3a. The decreased intensity reflects the decreased oxygen content in  $GO_{KOH}$ . Epoxy groups are highly reactive due to the highly strained bonds, and open up to generate hydroxyls in basic environment.<sup>3</sup> The peak at ~530.6 eV indicates oxygen-alkali bonds, providing evidence of successful cation exchange.<sup>4</sup> Figure 4.3b shows two potassium peaks at 292.8 eV and 295.6 eV attributed to the K 2p<sub>3/2</sub> and K 2p<sub>1/2</sub> spin-orbit-split doublet of potassium oxides and cations. The K 2p<sub>3/2</sub> peak is deconvoluted into two contributions reflecting the different chemical environments of potassium ions. The major assignment is at

292.7 eV for the potassium associated with the carboxylic acid groups of GO, located in a position similar to that of the analogous small molecule potassium acetate,<sup>5</sup> whilst a minor contribution is attributed to unbound KOH. The presence of K-O bonds and the decreased proportion of epoxy and hydroxyl functional groups confirm the successful chemical modification of GO. The decrease in oxygen content, especially of certain functional groups indicates partial reduction of GO in the strongly alkaline environment (pH 12.5), as previously reported.<sup>6,7</sup>

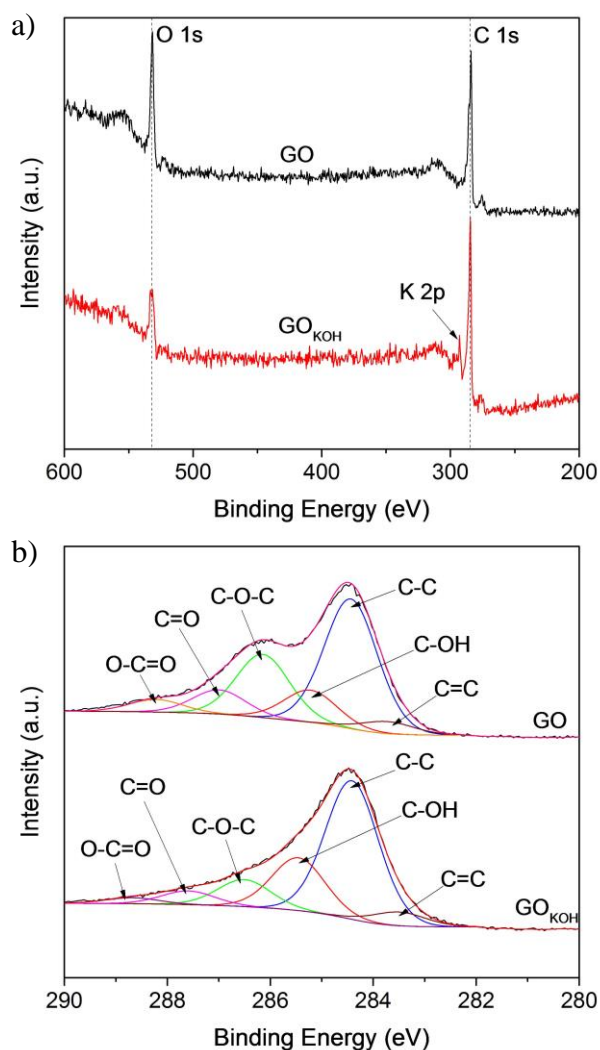


Figure 4.2. XPS of multilayer GO and GO<sub>KOH</sub> membranes. a) Wide scan spectra; b) C 1s spectra with component analysis.

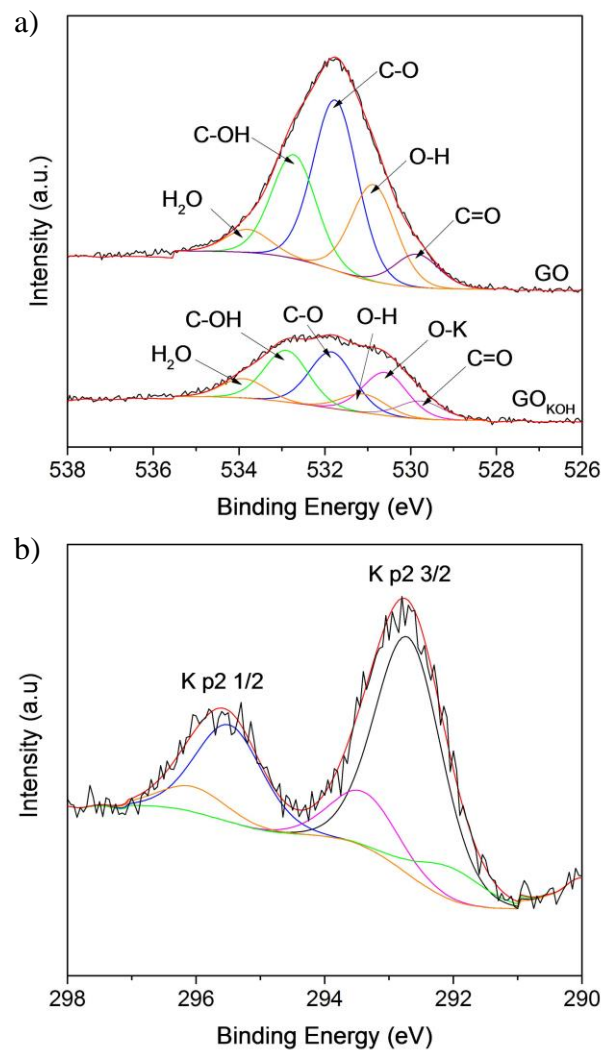


Figure 4.3. XPS of multilayer GO and GO<sub>KOH</sub> membranes. a) O 1s spectra with component analysis. b) K 2p spectra of the multilayer GO<sub>KOH</sub> membrane.

### 4.3.3 X-Ray Diffraction

Figure 4.4 shows XRD spectra of GO and  $\text{GO}_{\text{KOH}}$  measured at ambient temperature and relative humidity. GO has a major peak at  $2\theta = 11.53^\circ$  corresponding to an interlayer distance of 0.77 nm, similar to reported values under similar conditions.<sup>8</sup>  $\text{GO}_{\text{KOH}}$  has a major peak at  $2\theta = 10.32^\circ$  corresponding to a much larger interlayer spacing of 0.86 nm. In general, the interlayer spacing in GO decreases with decreasing oxygen content.<sup>9</sup> The larger interlayer spacing in  $\text{GO}_{\text{KOH}}$  despite the lower oxygen content reflects the much larger ionic radius of  $\text{K}^+$  ions ( $\sim 0.13$  nm),<sup>10</sup> compared with  $\text{H}^+$  ( $\sim 8.4 \times 10^{-7}$  nm).<sup>11</sup> The appearance of a second peak in the  $\text{GO}_{\text{KOH}}$  spectrum at  $2\theta = 21.2^\circ$  corresponds to an interlayer spacing of 0.42 nm. This has been associated with potassium-graphite intercalation compounds,<sup>12</sup> and may be a further indicator of partial reduction of the GO to a graphite-like state. The lack of characteristic Bragg reflections for bulk KOH indicates that little or no excess KOH is present.<sup>13</sup>

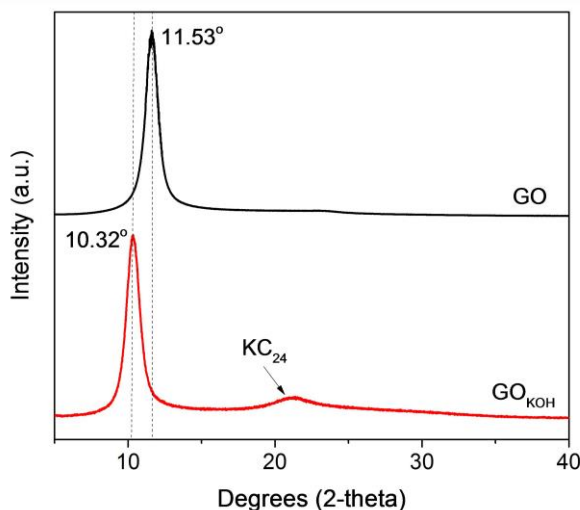


Figure 4.4. XRD spectra of GO and  $\text{GO}_{\text{KOH}}$ . Increased interlayer spacing for  $\text{GO}_{\text{KOH}}$ .

### 4.3.4 Ion Exchange Capacity

The ion exchange capacity (IEC) of the membranes, i.e. the number of moles of charge carrier per unit mass, was determined by titration. The GO and  $\text{GO}_{\text{KOH}}$  membranes have IECs of approximately 2.6 and 6.1 mmol/g for  $\text{H}^+$  and  $\text{OH}^-$  respectively. As there is a slight excess of  $\text{OH}^-$  in the alkaline membrane compared to the  $\text{H}^+$  present in the untreated membrane, we

conclude that there is a small excess of free KOH in the  $GO_{KOH}$  membrane, as confirmed by the K 2p XPS data.

#### 4.3.5 Water Uptake and Swelling

The average water uptake of GO is 1434 wt%, compared with 1099 wt% for  $GO_{KOH}$  (Figure 4.5). The lower water uptake in  $GO_{KOH}$  is attributed to lower oxygen content and therefore reduced hydrophilicity. Both membranes show an extremely high degree of swelling and resembling a hydro-gel.<sup>14</sup> A determination of the swelling (thickness increase) is not possible as the mechanical stability of the samples is very low. The high degree of swelling is in part attributed to the smaller area of the membrane samples allowing water absorption throughout the entire membrane on much faster timescales.

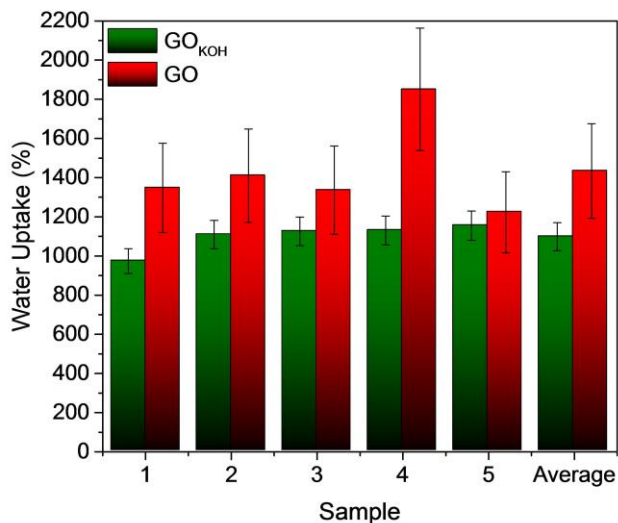


Figure 4.5. Water uptake of GO and  $GO_{KOH}$ .

### 4.3.6 Tensile Strength Measurements

The tensile strength ( $24.5 \pm 2.0$  MPa) and Young's modulus ( $290.3 \pm 66$  MPa) of  $\text{GO}_{\text{KOH}}$  are smaller compared to our previously reported values for GO ( $54.5 \pm 3.3$  MPa and  $680 \pm 9.7$  MPa, respectively), as shown in Figure 4.6a.<sup>8</sup> This may be due to reduced van der Waals forces between the individual  $\text{GO}_{\text{KOH}}$  sheets because of the intercalated potassium ions. However, the values are comparable to conventional ionomer materials. The strain before rupture is shown in Figure 4.6b.  $\text{GO}_{\text{KOH}}$ 's strain before rupture is  $11 \pm 1.6\%$ , significantly lower than previously observed for GO ( $22 \pm 1\%$ ).

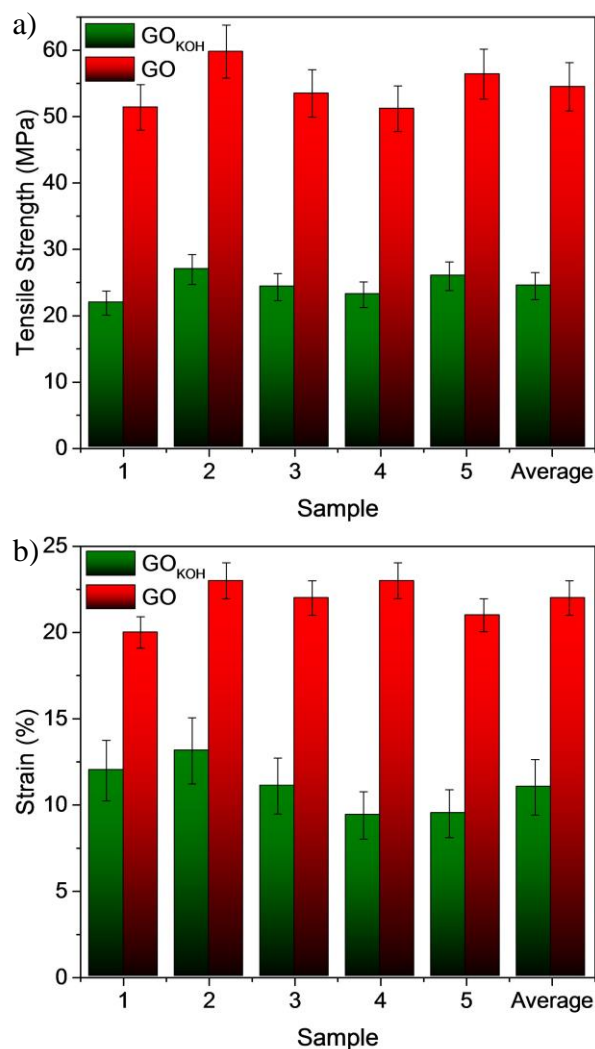


Figure 4.6. Tensile strength (a) and strain until rupture (b) of GO and  $\text{GO}_{\text{KOH}}$ .

### 4.3.7 Thermogravimetric Analysis

The thermal stabilities of GO and GO<sub>KOH</sub> were investigated by thermogravimetric analysis (TGA, Figure 4.7a) and differential thermal analysis (DTA, Figure 4.7b-c) in air, shown in Figure 4.7. GO displays four main weight loss peaks (Figure 4.7a). The endothermic peak centered at ~80°C is associated with evaporation of water intercalated in the GO. There is a small exothermic mass loss peak at around 160°C which we attribute to early onset reduction of the GO, i.e. the decomposition of one of the weakly-bonded functional groups (e.g. -OH). The exothermic mass loss peak at ~220°C is attributed to decomposition of all other oxygen-containing functional groups. The final exothermic mass loss peak at ~520°C is attributed to combustion of the remaining carbon.

GO<sub>KOH</sub> also exhibits four mass-loss steps (Figure 4.7a). The first is related to water evaporation, at ~80°C. A similar small exothermic mass loss occurs at 140°C, again attributed to loss of weakly bound oxygen-containing functional groups. The third, exothermic mass loss peak occurs at ~380°C attributed to the formation of potassium carbonate. This is more thermally stable than carbon and accounts for the stability of this phase up to > 800°C. Finally, two strong endothermic signals corresponding to the glass transition and melting points of K<sub>2</sub>CO<sub>3</sub> are observed,<sup>15</sup> followed by complete mass loss at around 1100°C, corresponding to decomposition of K<sub>2</sub>CO<sub>3</sub>. These results show that GO<sub>KOH</sub> is slightly less thermally stable than GO.

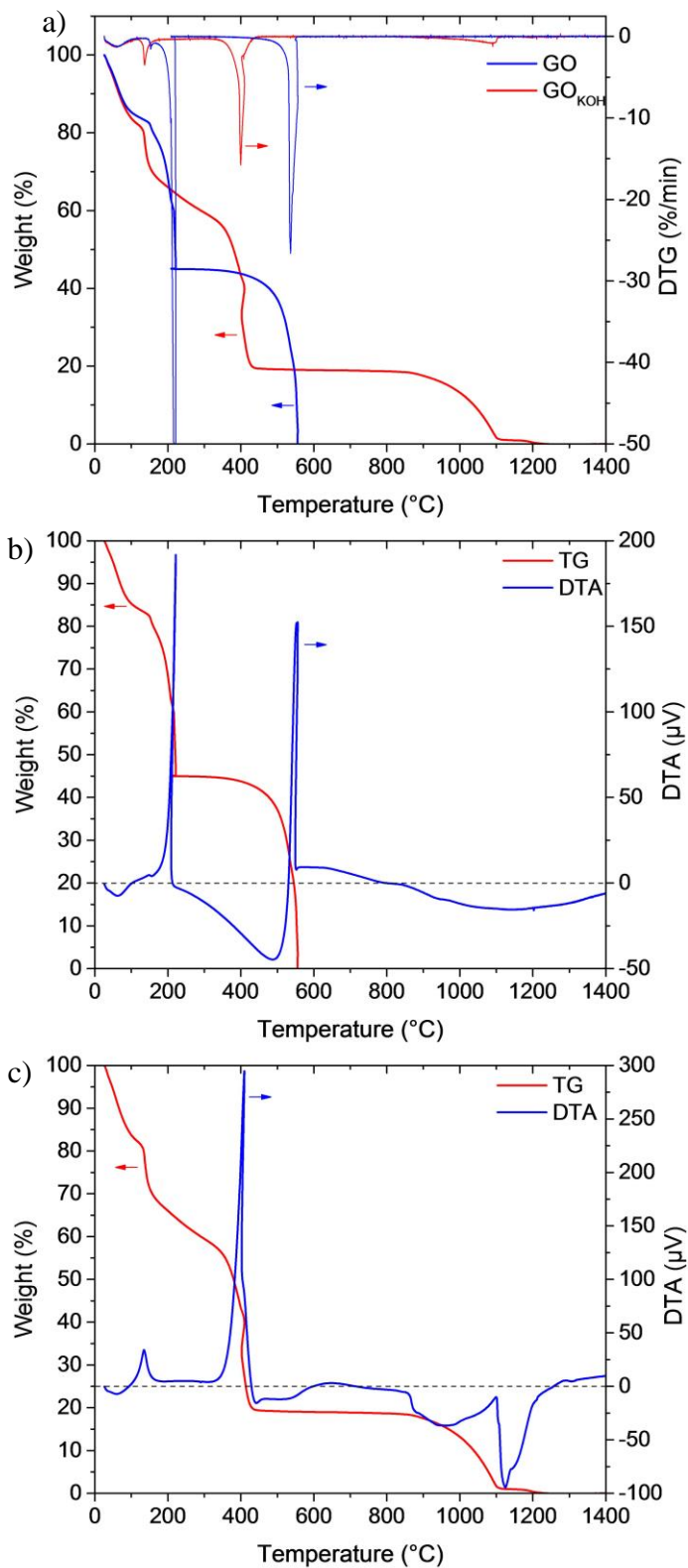


Figure 4.7. a) TGA curves of GO (red) and GO<sub>KOH</sub> (blue). b) TGA and DTA curves of GO. c) TGA and DTA curves of GO<sub>KOH</sub>.

### 4.3.8 Gas Barrier Properties

Crossover of hydrogen from the anode to cathode is an important issue in fuel cells and should be avoided. One of the main advantages of using GO as an ionomer membrane is that it is highly impermeable, and therefore crossover should be minimal. As a result of this, much thinner membranes could be utilized, reducing cell resistance. Here we measure the hydrogen gas barrier properties of membranes with different thickness (GO: 17 and 37  $\mu\text{m}$ ; GO<sub>KOH</sub>: 15 and 37  $\mu\text{m}$ ) at 30°C. Figure 4.8 shows the permeance and permeability. The values are extremely low for both membranes, several orders of magnitude lower than Nafion (~25 barrer). The hydrogen permeance decreases with increasing thickness for both GO and GO<sub>KOH</sub>. This is as expected since the permeance is the pressure-normalized gas flux through the membrane and is dependent on the diffusion coefficient (constant), the concentration of permeate (constant), and the thickness of the membrane. The permeability is approximately constant with thickness, as expected for this thickness-normalized value. These results are contrary to a previous high-profile study which claims that GO is completely impermeable to liquids and gases except water.<sup>16</sup> This disparity is attributed to the much larger pressure differential used in our work, resulting in higher, more measurable hydrogen permeation rates. The permeance and permeability of GO<sub>KOH</sub> are around 5 times lower than in GO, indicating that KOH treatment can improve the hydrogen gas barrier properties, despite the larger interlayer spacing. This may be due to the added effect of potassium ions, which completely change the electronic structure within the membrane. As such, both GO and GO<sub>KOH</sub> membranes are ideally suited to minimize crossover in fuel cells.

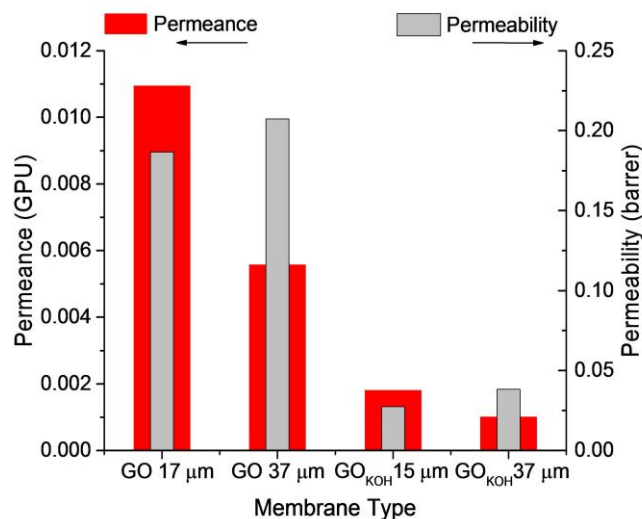


Figure 4.8. Hydrogen permeance and permeability through GO and GO<sub>KOH</sub> membranes of different thickness at a temperature of 30°C.

## 4.4 Impedance Spectroscopy

### 4.4.1 Conductivity of GO<sub>KOH</sub> Membranes

Impedance spectroscopy was used to determine the through-plane ionic conductivity of the membranes. Figure 4.9a shows the dependence of conductivity on humidity and temperature for GO<sub>KOH</sub>. The proton conductivity of GO at 100% RH is included for comparison. In general, the conductivity increases with increasing humidity and increasing temperature. This is as expected for ionic charge carriers, in which higher temperature overcomes the activation barrier for ion mobility and high humidity provides enhanced ion mobility via water-mediated transport mechanisms. The highest anionic conductivity of GO<sub>KOH</sub> is 6.1 mS/cm at 70°C and 100% RH. This is around 20 times higher than the value of proton conductivity of GO, suggesting that the alkaline ion exchange reaction was successful in fundamentally changing the nature of ion transport in the material. It compares well with commercially available AAEMs, e.g. Tokuyama, which has a through-plane conductivity of 7.1 mS/cm.<sup>17</sup>

However, at low humidity and high temperature (70°C) the conductivity of the GO<sub>KOH</sub> membranes increases with decreasing humidity, as also observed for GO membranes.<sup>18</sup> This is indicative of electronic conduction under these conditions. At high humidity electronic conductivity is negligible due to the presence of intercalated water and the large interlayer

spacing, blocking electron-conducting pathways between  $sp^2$  regions of the carbon. At low relative humidity the interlayer spacing decreases as water is removed from the membrane.<sup>19</sup> This provides the opportunity for electron percolation from layer to layer, along a pathway of local  $sp^2$  regions.<sup>20</sup> Although electronic conduction is not desirable in fuel cell membranes, this effect is not observed under fuel cell conditions (i.e. high humidity), and additionally there are potential applications of GO membranes as mixed ionic and electronic conductors. Arrhenius plots of the conductivity data are presented for different humidity in Figure 4.9b. The slopes correspond to activation energies, which are plotted against humidity in Figure 4.9c. Due to the unusual behavior observed at 70°C and attributed to mixed conduction, fitting was limited to the 30 to 60°C range. The activation energies are quite high at high humidity (~0.4 eV, or 38.6 kJ mol<sup>-1</sup>). Generally values of between ~0.1 to 0.2 eV (~10 to 25 kJ/mol),<sup>21,22</sup> are reported for anion conducting membranes. The activation energy gradually decreases with decreasing humidity, possibly related to the gradual change in interlayer spacing with RH. At low RH, the activation energy is just 0.01 eV (1.0 kJ/mol), most likely indicating electron transfer, and confirming that the membranes are mixed ionic conductors when dry.

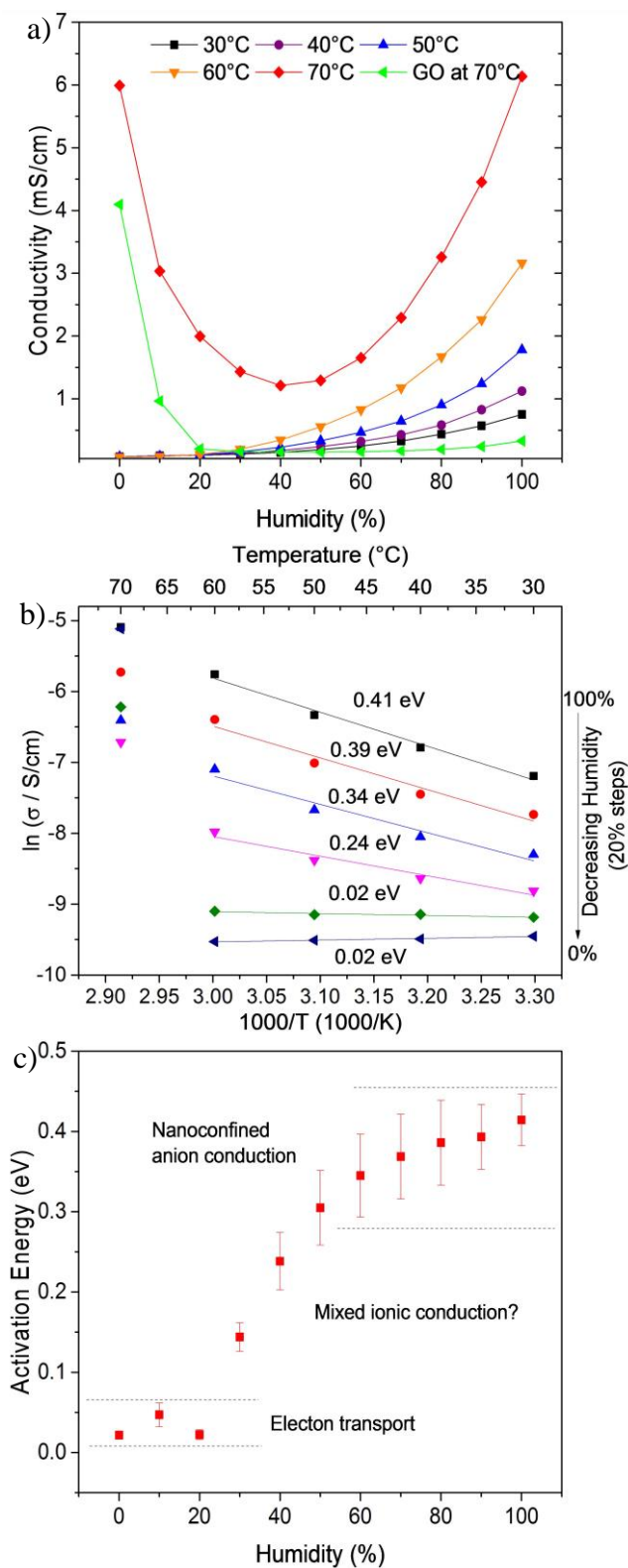


Figure 4.9. a) Conductivity of a  $GO_{KOH}$  membrane ( $37 \mu m$  thick) in dependence on humidity and temperature. b) Arrhenius plots showing activation energies at different relative humidity. c) Relationship between activation energy and relative humidity.

#### 4.4.2 Determination of Dominant Ionic Species

Blocking layer measurements were performed on the membranes in order to confirm the dominance of  $\text{OH}^-$  anion conduction, and to discount proton or  $\text{K}^+$  ion conduction (Figure 4.10a). Accordingly,  $\text{GO}_{\text{KOH}}$  membranes were sandwiched between anion-blocking (Nafion) or cation-blocking (Tokuyama A 201) membranes, as shown schematically in Figure 4.10b. When proton-blocking layers are utilized, the conductivity closely follows that of  $\text{GO}_{\text{KOH}}$  with no blocking layers. When anion-blocking layers are used, the conductivity drops significantly across the whole temperature range. These results confirm that the dominant charge carriers are  $\text{OH}^-$  anions. These results also discount majority  $\text{K}^+$  conduction, since neither blocking layer is a known  $\text{K}^+$  conductor. However, a small proportion of  $\text{H}^+$  conduction appears to occur (~6%). A small discrepancy is observed between the reference sample and the sum of the anion- and proton-blocked samples, especially at higher temperature. This may be due to a small amount of  $\text{K}^+$  conduction; potassium carbonate formation and associated  $\text{CO}_3^{2-}$  ion conduction.<sup>23</sup> However due to the barrier properties of GO and nanoconfinement between the individual GO sheets, movement of such ions through the membrane by the vehicular mechanism is expected to be restricted.<sup>16</sup> The discrepancy may also be attributed to a small proportion of electronic conduction.

The above results confirm that the dominant charge carriers in  $\text{GO}_{\text{KOH}}$  membranes at high humidity are  $\text{OH}^-$  ions. The specific mechanism for  $\text{OH}^-$  conduction in  $\text{GO}_{\text{KOH}}$  is hypothesized to be either vehicular, or reverse Grotthuss. In the vehicular mechanism, an  $\text{OH}^-$  ion physically travels through the membrane. However, this is problematic in the case of GO, since it is widely accepted that due to the highly impermeable nature of this material, only protons and water can pass through the spaces in between individual GO sheets. The reverse-Grotthuss mechanism is related to the conventional Grotthuss mechanism, in which acidic protons hop from e.g. a hydronium ion ( $\text{H}_3\text{O}^+$ ) to a water molecule, forming a new hydronium ion and leaving behind a water molecule. The reverse-Grotthuss mechanism dominates in alkaline conditions, where there is a large excess of  $\text{OH}^-$  ions. Here, protons hop from a water molecule onto an adjacent  $\text{OH}^-$  ion, forming a new water molecule and leaving behind a new  $\text{OH}^-$  ion.<sup>24-26</sup> In this way the diffusion of positively charged protons effectively results in a net backwards movement of  $\text{OH}^-$  ions (schematically represented in Figure 4.10c). This is analogous to the transport of vacancies in p-type semiconductors, or

the transport of  $O^{2-}$  ions in solid oxide fuel cell (SOFC) electrolytes. The activation energy for Grotthuss-type proton hopping is expected to be much lower ( $\sim 0.13$  eV) than the measured  $0.4$  eV.<sup>25</sup> This hints that nanoconfinement between the layers of GO fundamentally affects the activation energy required for ionic transport, due to steric effects.<sup>27</sup>

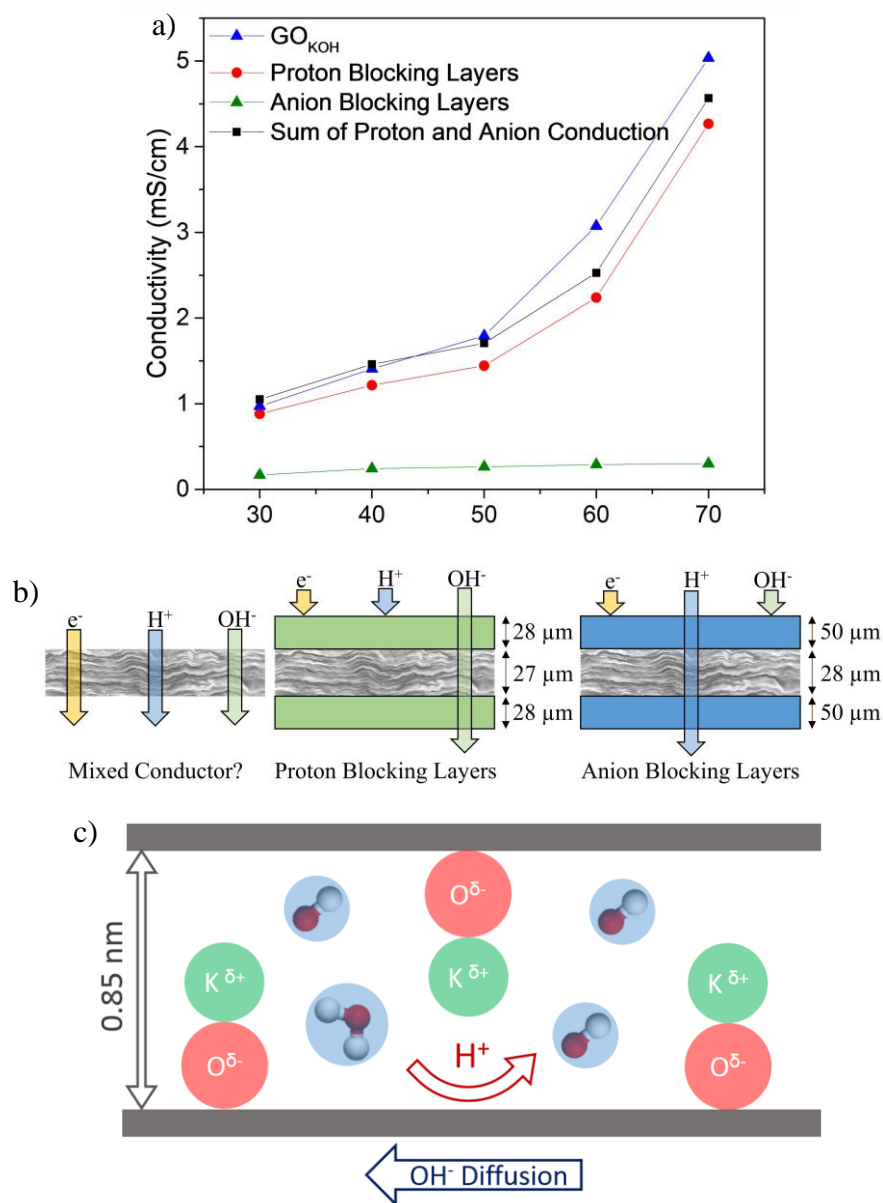


Figure 4.10. a) Conductivity of  $GO_{KOH}$  membranes with different blocking layers. b) Schematic of blocking layer measurements. c) Schematic of a possible reverse Grotthuss mechanism for  $OH^-$  anion diffusion in  $GO_{KOH}$ .

## 4.5 Membrane Electrode Assembly Characterization

Due to the interesting anion conductivity measured in these novel AAEMs, a proof-of-concept AAEMFC was fabricated. A single-cell MEA was prepared using an 18  $\mu\text{m}$  thick  $\text{GO}_{\text{KOH}}$  electrolyte membrane, and installed in a fuel cell test system. Figure 4.11a shows the resulting polarization curves and power density of the cell. The open circuit voltage (OCV) is 0.94 V. This is reasonable, but still lower than for commercially available AAEMs (1.02 V), or for proton-conducting GOMFCs (1.01 V).<sup>8</sup> The low OCV cannot be attributed to fuel crossover, because of the excellent hydrogen barrier properties of the membrane. Therefore, it is attributed to mixed ionic-electronic conductivity, as observed in the blocking layer measurements. There is a small initial voltage drop of  $\sim 0.05$  V attributed to activation losses. This is much smaller than observed in GOMFCs ( $\sim 0.2$  V), reflecting the faster reaction kinetics in alkaline environment. The ohmic region is linear but steep, indicating relatively high ohmic losses. From this slope, the total cell resistance is calculated to be  $204 \Omega \text{ cm}^2$ , around 1000 times higher than in AAEMFCs made with commercially available anion conducting membranes.<sup>28</sup> The resistance of the membrane is calculated to be  $0.48 \Omega \text{ cm}^2$  from the conductivity measurements at  $30^\circ\text{C}$ , so this is clearly not the main contributor to the cell resistance. Therefore it is attributed to the electrocatalyst layer, or the interface between the electrocatalyst layer and the membrane. Hot-pressing is usually utilized during fabrication of MEAs in order to improve contact between ionomer and the electrocatalyst. In  $\text{GO}_{\text{KOH}}$  AAEMFCs the hot-pressing step was omitted, since high temperature reduces GO and destroys the ion-conducting properties. Therefore the interaction between the polymer anion-conducting ionomer and the electrocatalyst is not optimized, increasing the resistance of the layer. Additionally, the presence of KOH in the membrane could lead to the formation of potassium carbonate upon exposure to  $\text{CO}_2$  in the air. Many studies utilize pure oxygen rather than air at the cathode to prevent this, but such conditions are not realistic for practical fuel cell usage. Carbonate formation leads to neutralization of the membrane, quickly decreasing the conductivity (i.e. increasing the resistance) of the membrane.<sup>23</sup> The carbonate could also potentially result in an inert layer at the interface with the electrocatalyst, acting as a barrier to ion conduction and increasing the cell resistance. No mass transport limited region is observed, due to the relatively low power density. The maximum power density is  $0.97 \text{ mW/cm}^2$  at  $2.09 \text{ mA/cm}^2$ . This is much lower than in commercial AAEMFCs operated

under similar condition (e.g. 8 to 100 mW/cm<sup>2</sup>).<sup>29</sup> Improvements in the performance of GO<sub>KOH</sub> AAEMFCs are expected by optimization of the ionomer-catalyst ratio in the electrocatalyst layer; utilizing pure oxygen rather than air; decreasing the membrane thickness; and laminating the GO<sub>KOH</sub> with thin polymeric anion conducting layers.<sup>30</sup> However, despite the relatively low power density at present, this is an important proof-of-concept device.

The durability of the GO<sub>KOH</sub> AAEMFC was investigated at 30°C at a constant load current of 1 mA (Figure 4.11b). The cell voltage drops significantly in the first 5 minutes of operation. After the initial drop in cell voltage, a slower degradation in performance is observed. Similar behavior was reported in acid-based GOMFCs, and related to reduction of GO in the strongly reducing hydrogen atmosphere increasing the proportion of electronic conduction through the membrane.<sup>8</sup> In less than an hour the cell voltage dropped by 0.5 V, to 0.2 V. After the durability measurement, the cell performance was again investigated. The OCV was just 0.65 V, confirming that increased electronic conductivity is a factor in the degradation process. The maximum power density was just 0.44 mW/cm<sup>2</sup> at 1.60 mA/cm<sup>2</sup>.

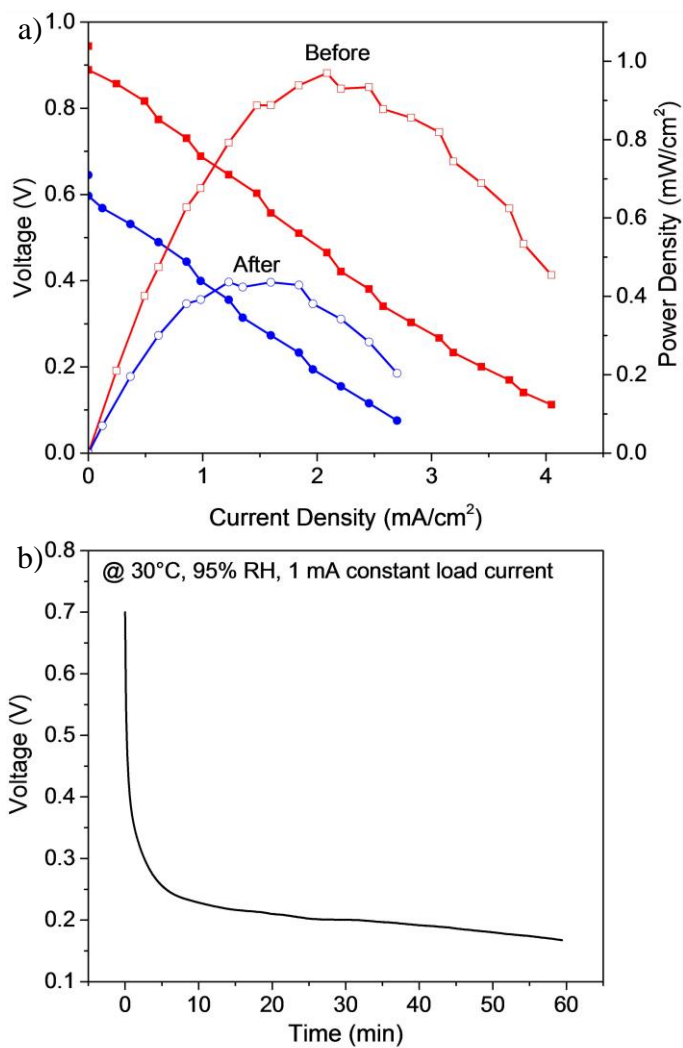


Figure 4.11. a) Polarization curves and power densities of a  $\text{GO}_{\text{KOH}}$  membrane fuel cell at  $30^\circ\text{C}$  and 95% RH, before and after durability measurements. b) Durability measurement with a 1 mA constant load current.

## 4.6 Conclusions

Novel alkali anion exchange membranes were prepared via cation exchange of pure graphene oxide dispersions, followed by simple vacuum-filtration.

A summary of the properties of  $\text{GO}_{\text{KOH}}$  are compared with Tokuyama A 201 anion exchange membrane (AEM) in Table 4.1. No reports about the mechanical properties of Tokuyama A 201 could be found, however due to the fluorinated carbon backbone we assume a tensile strength similar to Nafion. In this case  $\text{GO}_{\text{KOH}}$  has slightly lower tensile strength than the Tokuyama membrane, and approximately half the tensile strength of unaltered GO membranes. The water uptake of  $\text{GO}_{\text{KO}}$  is much larger than for the Tokuyama AEM and unaltered GO, suggesting strong swelling, leading to a hydrogel-like structure. Hydrogen gas permeation through the membranes was several orders of magnitude below that of conventional polymers such as Tokuyama A201. The maximum conductivity was 6.1 mS/cm at 70°C, comparable to commercially available anion conducting membranes, and the dominant charge carrier was confirmed to be  $\text{OH}^-$ , by using careful blocking layer measurements.

A demonstration alkaline fuel cell (AFC) utilizing a  $\text{GO}_{\text{KOH}}$  membrane was fabricated. The initial OCV was 0.94 V, and the maximum power density was  $\sim 1 \text{ mW/cm}^2$ . The relatively low performance is attributed to carbonate formation upon exposure to  $\text{CO}_2$ , and the fact that hot-pressing cannot be used without reducing the graphene oxide, and we are now working on solving these engineering challenges. Despite the performance of the  $\text{GO}_{\text{KOH}}$ -based AFC being much lower than with commercial membranes, this is an original and important proof-of-concept for the application of pure graphene oxide-based alkaline exchange membranes in electrochemical devices.

The cost of the  $\text{GO}_{\text{KOH}}$  membrane is currently much higher than the commercially available membrane. However, this will be improved by using thinner  $\text{GO}_{\text{KOH}}$  membranes and by using a graphene oxide supplier with lower cost for the raw materials.

GO offers various possibilities for surface modification e.g. attaching quaternary ammonium groups. Thus in future work GO-based AEMs with higher ion conductivity and better durability might be prepared. Additionally the high gas barrier properties of  $\text{GO}_{\text{KOH}}$  indicates

electrode-supported AFCs with very thin membranes may be successful, resulting in higher power densities and, making the AFCs more competitive with PEMFCs.

*Table 4.1. Comparison of fuel cell membrane related properties of alkaline treated graphene oxide and Tokuyama A 201 anion exchange membrane.*

| <b>Property</b>  | <b>Tokuyama A201</b> | <b>GO<sub>KOH</sub></b> |
|--|----------------------|-------------------------|
| Mechanical Strength (MPa)                                      | Unknown              | ~24.5                   |
| Water Uptake (wt%) <sup>17</sup>                               | ~50                  | ~1100                   |
| Hydrogen Permeability (barrer) <sup>31</sup>                   | ~30 [70°C]           | ~0.03 [30°C]            |
| Maximum Anion Conductivity $\sigma_{TP}$ (mS/cm) <sup>17</sup> | 7.1 [30°C]           | 6.1 [70°C]              |
| Max. Power Density (mW/cm <sup>2</sup> ) <sup>28</sup>         | ~270 [50°C]          | ~1 [30°C]               |
| Durability <sup>32</sup>                                       | Good                 | Poor                    |
| Membrane Cost (\$/m <sup>2</sup> )                             | 851 (28 $\mu$ m)     | 5280 (18 $\mu$ m)       |

## References

1. Lyth, S. M., Hatton, R. a. & Silva, S. R. P. Efficient field emission from Li-salt functionalized multiwall carbon nanotubes on flexible substrates. *Appl. Phys. Lett.* **90**, 2005–2008 (2007).
2. Abdelkader, A. M., Valle, C., Cooper, A. J., Kinloch, I. A. & Dryfe, R. A. W. Alkali Reduction of Graphene Oxide in Molten Halide Salts : Production of Corrugated Graphene Derivatives for Supercapacitors. *ACS Nano* **8**, 11225–11233 (2014).
3. Thomas, H. R. *et al.* Deoxygenation of graphene oxide: Reduction or cleaning? *Chem. Mater.* **25**, 3580–3588 (2013).
4. Dupin, J., Gonbeau, D., Levasseur, A., Cedex, P. & Cedex, T. Systematic XPS studies of metal oxides , hydroxides and peroxides. *Phys. Chem. Chem. Phys.* **2**, 1319–1324 (2000).
5. Jerome, R., Teyssie, P., Pireaux, J. J. & Verbist, J. J. Surface Analysis of Polymers End-Capped with Metal Carboxylates using X-ray Photoelectron Spectroscopy. *Appl. Surf. Sci.* **27**, 93–105 (1986).
6. Park, S. *et al.* Aqueous Suspension and Characterization of Chemically Modified Graphene Sheets Chemically Modified Graphene Sheets. *Communications* 6592–6594 (2008). doi:10.1021/cm801932u
7. Fan, X. *et al.* Deoxygenation of Exfoliated Graphite Oxide under Alkaline Conditions: A Green Route to Graphene Preparation. *Adv. Mater.* **20**, 4490–4493 (2008).
8. Bayer, T., Bishop, S. R., Nishihara, M., Sasaki, K. & Lyth, S. M. Characterization of a Graphene Oxide Membrane Fuel Cell. *J. Power Sources* **272**, 239–247 (2014).
9. Krishnamoorthy, K., Veerapandian, M., Yun, K. & Kim, S. The chemical and structural analysis of graphene oxide with different degrees of oxidation. *Carbon N. Y.* **53**, 38–49 (2012).
10. Nightingale, E. R. Phenomenological Theory of Ion Solvation . Effective Radii of Hydrated Ions. *J. Phys. Chem.* **63**, 1381–1387 (1959).
11. Pohl, R. *et al.* The size of the proton. *Nat. Lett.* **466**, 213–217 (2010).
12. Nishitani, R., Uno, Y. & Suematsu, H. In situ observation of staging in potassium-graphite intercalation compounds. *Phys. Rev. B* **27**, 6572–6575 (1983).
13. Snyder, R. G. *et al.* Structure of Potassium Hydroxide: An X-Ray and Infrared Study. *J. Chem. Phys.* **33**, 1164–1170 (1960).

14. Talyzin, A. V, Hausmaninger, T., You, S. & Szabó, T. The structure of graphene oxide membranes in liquid water, ethanol and water-ethanol mixtures. *Nanoscale* **6**, 272–281 (2014).
15. Lehman, R. L., Gentry, J. S. & Glumac, N. G. Thermal stability of potassium carbonate near its melting point. *Thermochim. Acta* **316**, 1–9 (1998).
16. Nair, R. R., Wu, H. A., Jayaram, P. N., Grigorieva, I. V. & Geim, A. K. Unimpeded Permeation of Water Through Helium-Leak-Tight Graphene-Based Membranes. *Science* (80-. ). **335**, 442–444 (2012).
17. Faraj, M. *et al.* New Anion Conducting Membranes Based on Functionalized Styrene–Butadiene–Styrene Triblock Copolymer for Fuel Cells Applications. *J. Polym. Sci. Part a-Polymer Chem.* **49**, 3437–3447 (2011).
18. Bayer, T., Bishop, S. R., Perry, N., Sasaki, K. & Lyth, S. M. Tunable Mixed Ionic/Electronic Conductivity and Permittivity of Two Dimensional Graphene. *Submitted*
19. Daio, T. *et al.* In-Situ ESEM and EELS Observation of Water Uptake and Ice Formation in Multilayer Graphene Oxide. *Sci. Rep.* **5**, 11807 (2015).
20. Wang, D.-W., Du, A., Taran, E., Lu, G. Q. (Max) & Gentle, I. R. A water-dielectric capacitor using hydrated graphene oxide film. *J. Mater. Chem.* **22**, 21085–21091 (2012).
21. Ren, X., Price, S. C., Jackson, A. C., Pomerantz, N. & Beyer, F. L. Highly Conductive Anion Exchange Membrane for High Power Density Fuel-Cell Performance. *ACS Appl. Mater. Interfaces* **6**, 13330–13333 (2014).
22. Tanaka, M. *et al.* Anion conductive block poly(arylene ether)s: synthesis, properties, and application in alkaline fuel cells. *J. Am. Chem. Soc.* **133**, 10646–10654 (2011).
23. Varcoe, J. R. *et al.* Anion-exchange membranes in electrochemical energy systems. *Energy Environ. Sci.* **7**, 3135–3191 (2014).
24. *Electrochemical Polymer Electrolyte Membranes.* (CRC Press, 2015).
25. Tuckerman, M. E., Marx, D. & Parrinello, M. The nature and transport mechanism of hydrated hydroxide ions in aqueous solution. *Nature* **417**, 925–929 (2002).
26. Jensen, M. Ø., Röthlisberger, U. & Rovira, C. Hydroxide and Proton Migration in Aquaporins. *Biophys. J.* **89**, 1744–1759 (2005).
27. *Proton conductors: Solids, membranes, and gels–materials and devices.* (Cambridge University Press, 1993). doi:10.1002/adma.19930050923

28. Fukuta, K., Inoue, H., Chikashige, Y. & Yanagi, H. Improved Maximum Power Density of Alkaline Membrane Fuel Cells (AMFCs) by the Optimization of MEA Construction. *ECS Trans.* **28**, 221–225 (2010).
29. Merle, G., Wessling, M. & Nijmeijer, K. Anion exchange membranes for alkaline fuel cells: A review. *J. Memb. Sci.* **377**, 1–35 (2011).
30. Paneri, A. *et al.* Proton selective ionic graphene-based membrane for high concentration direct methanol fuel cells. *J. Memb. Sci.* **467**, 217–225 (2014).
31. Hoefner, T., Schalenbach, M., Carmo, M., Maier, W. & Stolten, D. Development of the Anion Exchange Membrane Water Electrolysis. ECS Meet. Abstr. 3, (2015).
32. Electrochemical Energy: Advanced Materials and Technologies. (CRC Press, 2015).

## **5 Nanocellulose Fuel Cells**

### **5.1 Introduction and Motivation**

As described in the introductory Chapter 0, nanocellulose paper could be an important alternative ionomer membrane for fuel cells due to the low cost, good gas barrier properties, mechanical toughness and possible proton conducting properties, due to acidic oxygen functional groups. However, to the best of our knowledge the proton conductivity of nanocellulose membranes has not yet been investigated, especially at higher temperature, over a wide relative humidity range, with activation energy calculations to give insight into the conduction mechanism. Pure, unadulterated cellulose or nanocellulose membranes have not been investigated for application in hydrogen fuel cells.

Here, nanocellulose paper is prepared from cellulose nanofibers (CNF) and cellulose nanocrystals (CNC). It is characterized in detail for its chemical composition and morphology via X-ray photoelectron spectroscopy (XPS) and atomic force microscopy (AFM). The gas barrier properties of nanocellulose paper are measured at different temperatures and reported, compared to Nafion. The proton conductivity is investigated over a wide temperature and humidity range, giving insights into the conduction mechanism of these novel fuel cell membranes. The application of nanocellulose paper as an ionomer membrane for PEMFC-type hydrogen fuel cells is reported and their cross-section is observed post operationally by scanning electron microscopy.

### **5.2 Sample Preparation and Nomenclature**

Nanocellulose materials (CNF and CNC slurry, 3.0 wt% and 11.8 wt% solids, respectively) were purchased from University of Maine. Nanocellulose slurry (CNF = 100.2 g, CNC = 50.0 g) was mixed with 500 ml of deionized water and stirred for 24 hours at 500 rpm. The dispersions were then vacuum-filtered onto Millipore filters. After filtration the resulting CNF membranes were placed between two Teflon sheets, hot-pressed for 20 min (at 110°C and 1.1 MPa), and then carefully peeled of the filter. CNC membranes were simply peeled of the filter. The resulting CNF papers are free-standing and flexible, whilst the CNC membranes are more brittle and break more easily.

Photographs of the nanocellulose slurries are shown in *Figure 5.1a-b*. Photographs of the CNF and CNC membrane are compared with conventional cellulose-based paper (*Fuji Xerox, G70*) in *Figure 5.1c*. Conventional cellulose paper is completely opaque and white. The CNF paper is slightly transparent, and the CNC paper is more transparent. Both CNF and CNC membranes look very similar under an optical microscope (*Figure 5.1d-e*).

The detailed fabrication process for Nafion-based and GO-based membrane electrode assemblies (MEAs) is described in the experimental Chapter 2.3.1.

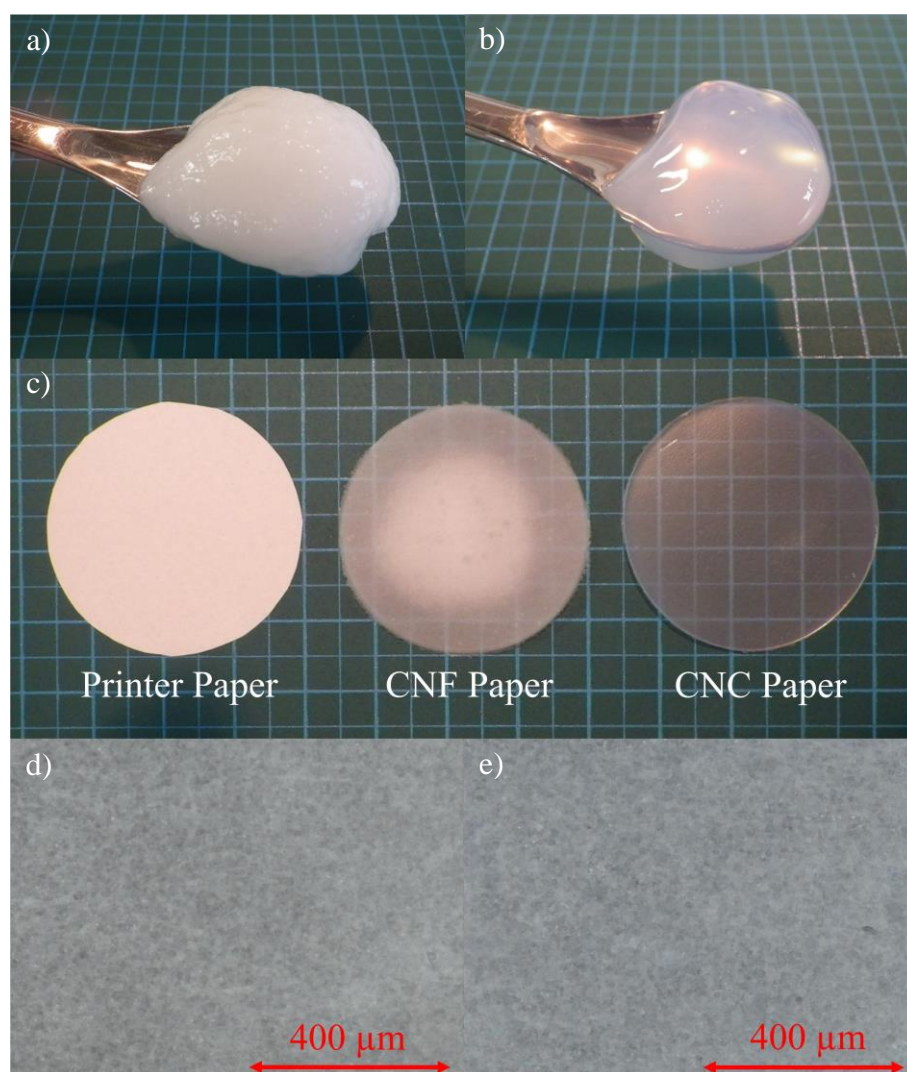


*Figure 5.1. Photographs of: a) cellulose nanofiber (CNF) slurry; b) cellulose nanocrystal (CNC) slurry; c) (left to right) conventional cellulose-based paper, CNF paper, and CNC paper. d-e) Optical microscope images of CNF (d) and CNC (e) paper.*

## 5.3 General Material Characterization

### 5.3.1 Atomic Force Microscopy

AFM images (*Figure 5.2*) show clearly the difference in microstructure between CNF and CNC. The CNF membrane consists of a network of randomly interwoven fibers with large diameters ranging from ~50 to 180 nm, with lengths extending beyond the imaging area. The thicker fibers may comprise bundles of smaller fibers. The surface roughness is  $36.60 \pm 11.25$  nm. In contrast, the CNC membrane comprises more highly aligned fibers with much smaller diameter ( $< 100$  nm) and shorter length (200 to 300 nm). This reflects the removal of amorphous regions of the nanocellulose polymer bundles during acid hydrolysis, with only the crystalline portions of the fibers remaining.<sup>1-3</sup> The high degree of alignment may be due to hydrogen bonding between the molecules,<sup>4,5</sup> or the high aspect ratio and stiffness (as in the case of liquid crystals). The surface roughness is  $4.10 \pm 0.64$  nm, reflecting the smaller feature size compared with CNF.

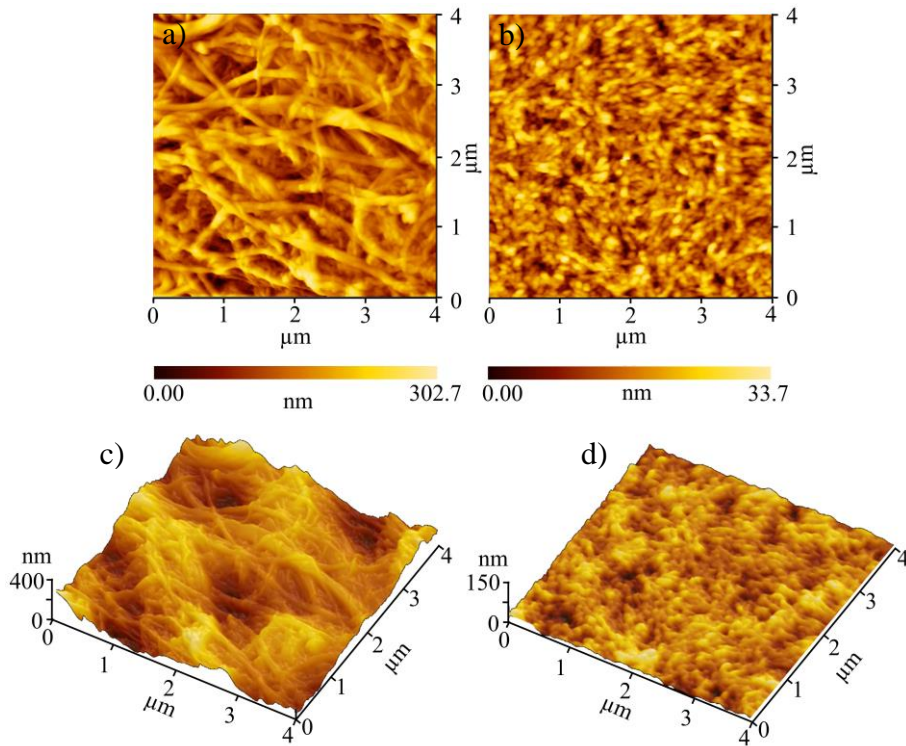


*Figure 5.2. AFM images of CNF (a,c) and CNC (b,d) paper.*

### 5.3.2 X-Ray Photoelectron Spectroscopy

*Figure 5.3a* shows the XPS wide scan spectrum for both CNF and CNC. The two major peaks correspond to C 1s (285 eV) and O 1s (532 eV) excitations. CNF has a small F 1s peak at 689 eV, attributed to contamination from Teflon sheets during hot-pressing. The elemental composition of the CNF surface is 62.0% C, 36.4% O, and 1.6% F. The CNC signal has minor peaks at 496 and 62 eV corresponding to Na KLL and Na 2s, respectively attributed to contamination from the acid hydrolysis process, in which NaOH is used for neutralization.<sup>6</sup> Two peaks are also observed at 231 and 167 eV in the CNC wide scan, corresponding to S 2s and S 2p peaks. The presence of S is introduced during the sulfuric acid hydrolysis process in which sulfate ester groups are introduced via condensation esterification between hydroxyls of the cellulose polymer and a sulfuric acid molecule.<sup>7,8</sup> The elemental composition of CNC is 57.5% C, 41.0% O, 0.8% Na, and 0.8% S.

The C 1s spectra reveal the difference between CNF and CNC in more detail (*Figure 5.3b*). The C 1s peak of CNF can be deconvoluted into 4 sub-peaks ascribed to different types of carbon bonds. The major peak at 284.8 eV corresponds to C-C bonds from the polymer backbone. The shoulder at 286.6 eV corresponds to C-O bonds, representing the hydroxyl groups of cellulose. The peak at 288.2 eV corresponds to the epoxy groups (C-O-C), and the smallest sub-peak at 289.8 eV to the carboxyl functional group. Carboxyl groups are formed during the pulping and bleaching processes.<sup>9</sup> The C 1s peak of CNC is similar, but displays an additional peak at 287.3 eV corresponding to the ester functional group (O=C-O-R) introduced during acid hydrolysis. Both C 1s spectra correspond well with the known chemical structure of nanocellulose, as shown schematically in *Figure 1.22*.

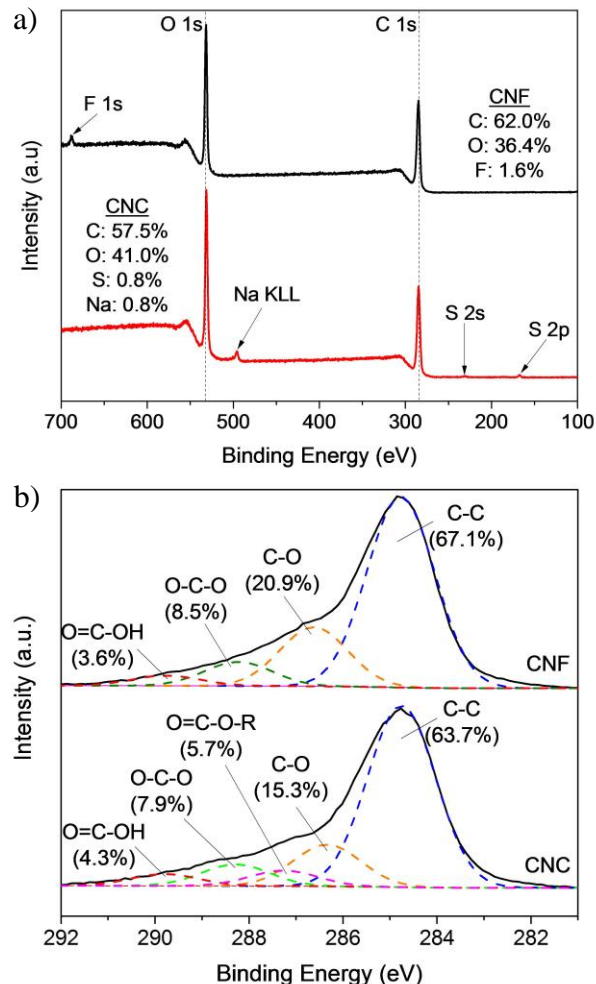


Figure 5.3. XPS spectra of cellulose nanofibers (CNF) and cellulose nanocrystals (CNC): a) wide scan spectra; and b) deconvoluted C 1s spectra.

### 5.3.3 Water Uptake and Swelling

The average water uptake of CNF is 126 wt%, compared with 15 wt% for Nafion, indicating a higher hydrophilicity for CNF (Figure 5.4a). When immersed into water, CNF membranes swell strongly in thickness (61 vs 10% for Nafion, Figure 5.4b), yet not as strong in longitudinal direction (Figure 5.5), and maintaining sufficient mechanical stability. The stronger rate of swelling of CNF compared to Nafion is in accordance with the observed increased water uptake. For CNC membranes water uptake and swelling could not be determined as they easily dissolve when immersed into water, as shown in Figure 5.5.

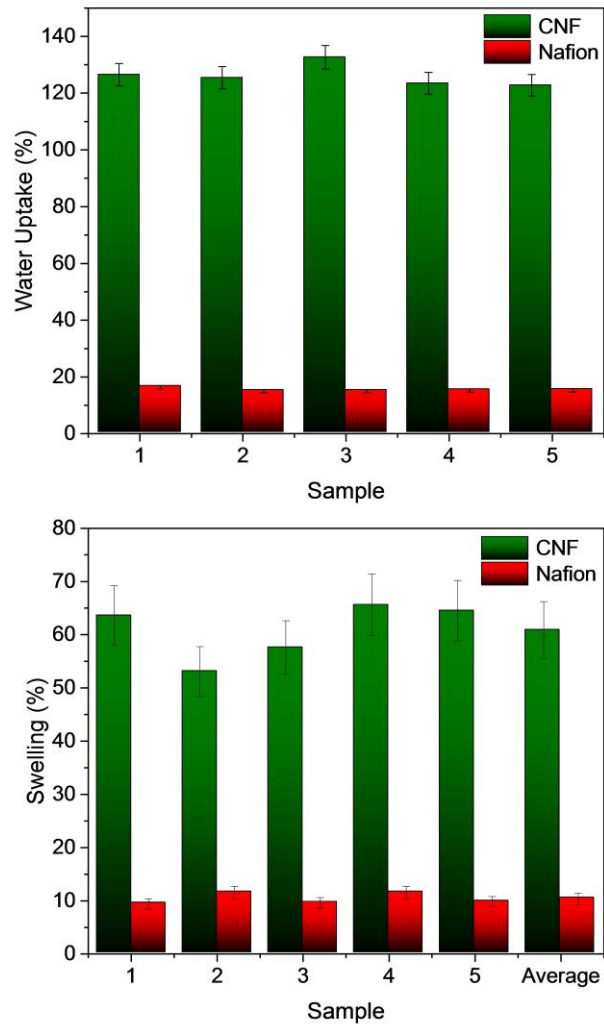


Figure 5.4. Water uptake (a) and swelling (b) of cellulose nanofiber (CNF) and Nafion.

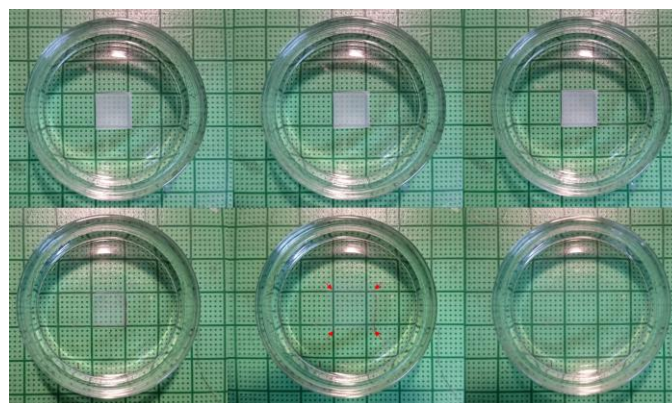


Figure 5.5. Membrane behaviour during water uptake measurements. a-c) CNF membrane at measurement start (a), after 5 min (b) and after 1 hour (c). d-f) Nafion membrane at measurement start (d), after 5 min (e) and after 1 hour (f).

### 5.3.4 Tensile Strength Measurements

The tensile strength ( $122.8 \pm 4.8$  MPa) of CNF is approximately four times higher compared to Nafion, as shown in Figure 5.6a. Also Elastic modulus of CNF is with  $1494.7 \pm 194$  MPa clearly higher than for Nafion ( $94.9 \pm 8.5$  MPa). The elongation (strain) before rupture is shown in Figure 4.6b. At an average strain of  $7.2 \pm 0.9\%$  CNF specimen ruptured, significantly lower than previously observed for Nafion ( $411 \pm 14\%$ ). Despite this low strain value, CNF is foldable like regular paper and is easy to handle e.g. during membrane electrode assembly fabrication. CNC paper on the other hand is very brittle and breaks easily during specimen fabrication and sample attachment to the tensile strength testing machine. Tensile strength values between 3.5 and 27.2 MPa were determined. Reason for this big difference might be due to micro cracks, which occur during specimen fabrication and sample attachment, influencing the repeatability of the tensile testing enormously. Therefore we conclude that the tensile strength values for CNC are not reliable.

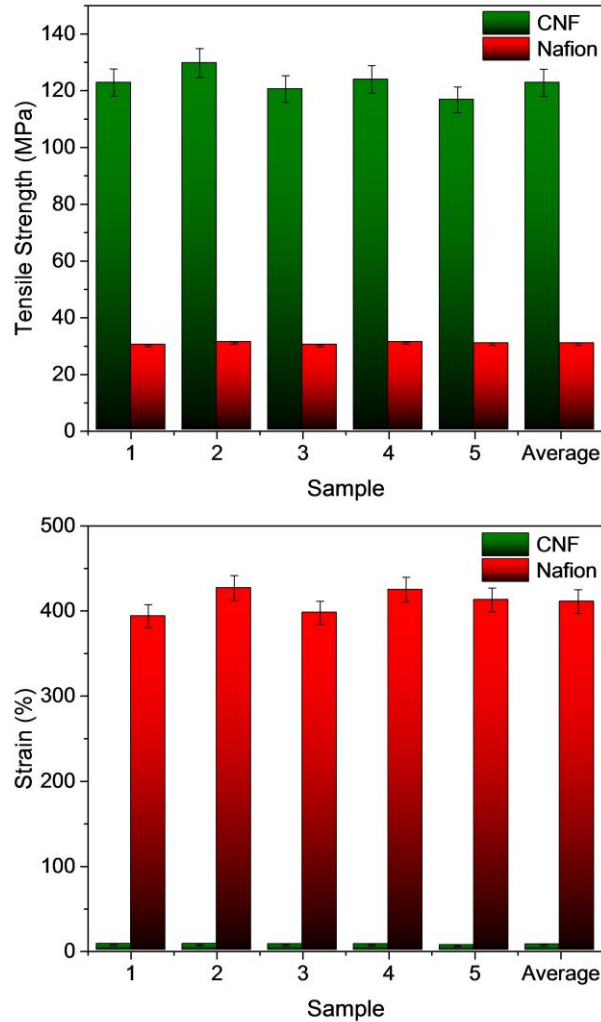


Figure 5.6. Tensile strength (a) and strain until rupture (b) of cellulose nanofiber (CNF) and Nafion.

### 5.3.5 Gas Barrier Properties

Figure 5.7 shows the hydrogen permeability of nanocellulose papers compared with Nafion, which is the most commonly utilized proton conducting membrane for PEMFCs. Both CNF and CNC membranes have very low hydrogen permeability; around three orders of magnitude lower than Nafion. The CNF membrane has slightly higher permeability than the CNC membrane. The opposite trend was previously observed for oxygen, nitrogen and carbon dioxide, where membrane made of microfibrillated cellulose (similar to CNF) has displayed *ca.* three orders of magnitude lower permeability compared to one made of sisal

cellulose whiskers (CNC).<sup>10</sup> The authors of reference 10 stated however that their films were very brittle and hydrogen permeation was not measured. Similarly high gas barrier (for H<sub>2</sub>, O<sub>2</sub>, N<sub>2</sub> and CO<sub>2</sub>) was reported by Fukuzumi et al. for membranes prepared of TEMPO-oxidized cellulose nanofibrils deposited on plasma-treated poly(ethylene terephthalate).<sup>11</sup>

The improved hydrogen barrier properties of CNC compared with CNF may be due to the higher crystallinity and tightly-packed nature of CNC (as observed in AFM), since gas permeation in polymer membranes occurs preferentially in lower density, i.e. more amorphous regions.<sup>12-14</sup> In support of this, the densities of the CNF and CNC membranes are 1.004 and 1.348 g/cm<sup>3</sup>, respectively.

For all samples the permeability increases with increasing temperature. This is typical behavior for organic polymers,<sup>15</sup> including cellulose-based materials.<sup>16</sup> Gas permeability depends on both the diffusion and solubility coefficients. The diffusion coefficient increases with temperature, whilst the solubility decreases with temperature. Therefore we can conclude that diffusion rate increases with temperature faster than the solubility decreases.

It is important to point that gas permeability in dry membranes is expected to increase significantly in humidified atmosphere. Wu et.al reported ca. 15 times increased permeability of cellulose membrane for H<sub>2</sub>, O<sub>2</sub>, N<sub>2</sub> and CO<sub>2</sub> at 25°C under humid condition, while the difference is only ca. 3 to 5 times at 80°C.<sup>17</sup> Therefore, despite the increase of permeability in humidified conditions the gas barrier is expected to remain much higher than the reference Nafion membrane.

To the best of our knowledge the H<sub>2</sub> permeability of these nanocellulose membranes is the lowest reported in literature to date. However, there is still very little data reported on membranes with consideration of nanostructure, i.e. made from carefully processed nanocellulose. Compared to conventional cellulosic membranes (*Figure 5.8* and *Table 5.1*) CNF and CNC membranes have ca. three orders of magnitude lower hydrogen permeability. Comparable H<sub>2</sub> gas barrier properties of TEMPO-oxidized cellulose nanofibrils films in the work of Fukuzumi et al. cannot be clearly attributed to the nanocellulose layer as they were deposited on plasma-treated PET which also contributes to the barrier properties.<sup>11</sup> The extremely high barrier properties of nanocellulose membranes are perhaps the consequence of the dense packing of the individual fibers/crystals with virtual absence of free volume

compared with conventional cellulose material. As a result, the permeation is governed mainly by diffusion between nanofibrils or nanocrystals rather than through pores and/or voids. Investigation of the gas permeability of other gases (i.e. CO<sub>2</sub>, N<sub>2</sub> and O<sub>2</sub>) results in even lower values (data not shown, will be reported elsewhere) further suggesting a fundamental difference in permeation mechanism between nanocellulose and conventional cellulose, since CO<sub>2</sub> is normally expected to have the highest permeability. Similarly, oxygen had permeability an order of magnitude lower than hydrogen, leading to the conclusion that the nanocellulose membranes studied here are highly uniform and structurally intact, with no pinholes or microdefects leading to uncontrolled gas leaks.

The promising gas barrier properties of nanocellulose are highly suited for use in hydrogen PEMFC membrane applications. Additionally, nanocellulose could be applied as a low-cost coating to prevent hydrogen leakage and/or hydrogen embrittlement in gas pipelines, hydrogen storage vessels, or high pressure gas delivery systems.<sup>18,19</sup>

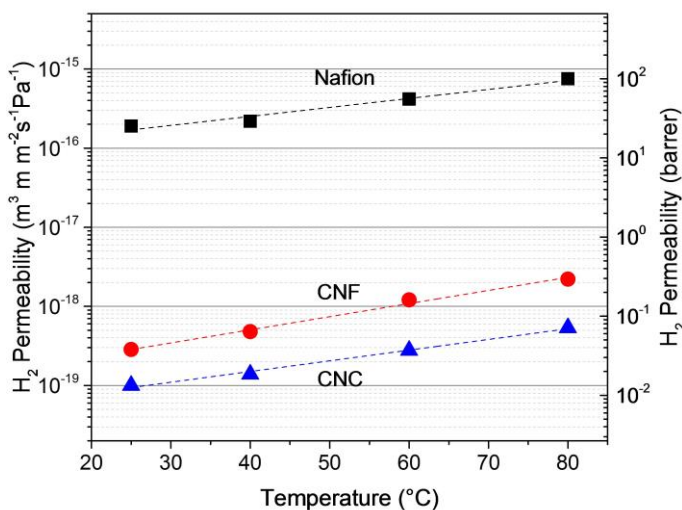


Figure 5.7. Dependence of the hydrogen permeability on temperature for cellulose nanofiber (CNF) and cellulose nanocrystal (CNC) membranes, in comparison to conventional polymer electrolyte membrane, Nafion® 212. Dashed lines are linear fits of the measurement data.

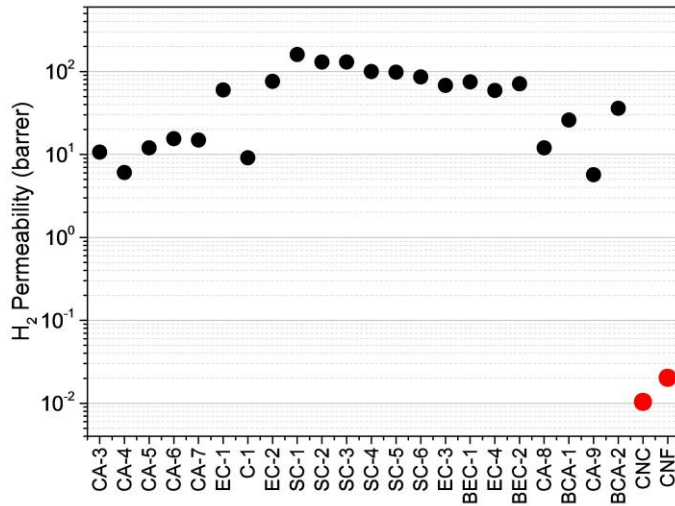


Figure 5.8. Comparison of hydrogen permeability of cellulose nanofiber (CNF) and cellulose nanocrystal (CNC) membranes with literature data for conventional cellulosic membranes (CA = cellulose acetate, EC = ethyl cellulose, SC = silylated derivatives of cellulose, BEC = butylcarbamate of EC, BCA = butylcarbamate of CA).

Table 5.1. Literature data of hydrogen permeability of various conventional cellulose membranes compared to the CNC and CNF nanocellulose membranes used in this study.

| Membrane  | Preparation method                                   | Thickness ( $\mu\text{m}$ ) | H <sub>2</sub> permeability (barrer) | Reference    |
|---|--|-----------------------------|--------------------------------------|--------------|
| Cellulose acetate                                     | CAST, 25% acetone sol.                               | 20                          | 80                                   | Haraya, 1985 |
| Cellulose acetate (DS = 1.75)                         | CAST, 2-methoxyethanol                               | 3000 - 5000                 | 6.05                                 | Puleo, 1989  |
| Cellulose acetate (DS = 2.45)                         | CAST, acetone  | 3000 - 5000                 | 12                                   | Puleo, 1989  |
| Cellulose acetate (DS = 2.84)                         | CAST, methylene chloride                             | 3000 - 5000                 | 15.5                                 | Puleo, 1989  |
| Cellulose acetate                                     | CAST   | 35-100                      | 14.9                                 | Li, 1995     |
| Ethyl cellulose                                       | CAST, 6% chloroform                                  | 40                          | 60                                   | Li, 2001     |
| Cellulose   | CAST, aq. sol.                                       | 18                          | 9.1                                  | Wu, 2002     |
| Ethyl cellulose                                       | CAST 0.5-1% toluene                                  | 40-80                       | 76                                   | Khan, 2006   |
| Silylated cellulose-A                                 | CAST 0.5-1% toluene                                  | 40-80                       | 160                                  | Khan, 2006   |
| Silylated cellulose-B                                 | CAST 0.5-1% toluene                                  | 40-80                       | 130                                  | Khan, 2006   |
| Silylated cellulose-C                                 | CAST 0.5-1% toluene                                  | 40-80                       | 130                                  | Khan, 2006   |
| Silylated cellulose-D                                 | CAST 0.5-1% toluene                                  | 40-80                       | 100                                  | Khan, 2006   |
| Silylated cellulose-E                                 | CAST 0.5-1% toluene                                  | 40-80                       | 98                                   | Khan, 2006   |
| Silylated cellulose-F                                 | CAST 0.5-1% toluene                                  | 40-80                       | 86                                   | Khan, 2006   |
| <b>1</b> Ethyl cellulose, ethoxy content, 49 wt%)     | CAST 0.5-1% chloroform                               | 40-80                       | 68                                   | Khan, 2008   |
| <b>1a</b> <i>t</i> -butylcarbamate of <b>1</b>        | CAST 0.5-1% chloroform                               | 40-80                       | 75                                   | Khan, 2008   |
| <b>2</b> Ethyl cellulose, ethoxy content, 45.6 wt%)   | CAST 0.5-1% chloroform                               | 40-80                       | 59                                   | Khan, 2008   |
| <b>2b</b> <i>t</i> -butylcarbamate of <b>2</b>        | CAST 0.5-1% chloroform                               | 40-80                       | 71                                   | Khan, 2008   |
| <b>3</b> Cellulose acetate, acetyl content, 36.7 wt%) | CAST 0.5-1% chloroform                               | 40-80                       | 12                                   | Khan, 2008   |
| <b>3a</b> <i>t</i> -butylcarbamate of <b>3</b>        | CAST 0.5-1% chloroform                               | 40-80                       | 26                                   | Khan, 2008   |
| <b>4</b> Cellulose acetate, acetyl content, 26.9 wt%) | CAST 0.5-1% chloroform                               | 40-80                       | 5.7                                  | Khan, 2008   |
| <b>4a</b> <i>t</i> -butylcarbamate of <b>4</b>        | CAST 0.5-1% chloroform                               | 40-80                       | 36                                   | Khan, 2008   |
| <b>CNC</b>  | FILTERED aq. sol.                                    | 30                          | 0.01037                              | This work    |
| <b>CNF</b>  | FILTERED then hot-pressed for 20 min (110°, 1.1 MPa) | 32                          | 0.02029                              | This work    |

### 5.3.6 Impedance Spectroscopy

Carboxylic functional groups act as proton donors, and therefore it is interesting to investigate the proton conducting behavior of nanocellulose. *Figure 5.9a* shows the dependence of conductivity on humidity at 30°C. The conductivity of both samples increases with increasing humidity by around 2 to 3 orders of magnitude. This is typical behavior for proton conducting polymers, where water acts as a charge transport medium.<sup>20</sup> *Figure 5.9b* shows Arrhenius plots and conductivity of CNF and CNC membranes at 100% RH. For both membranes the conductivity increases with increasing temperature, by around an order of magnitude. This is also typical behavior in proton conductors. The conductivity of CNF membranes at first increases from 0.01 mS/cm at 30°C to 0.05 mS/cm at 100°C. However above 100°C the conductivity drops to 0.01 mS/cm. This may be due to reduced water uptake at temperatures above boiling point and thus incomplete dissociation of acid groups. The conductivity of the CNC membrane increases continuously from 0.62 mS/cm at 30°C to 4.57 mS/cm at 120°C, without any drop in conductivity at higher temperature. The maximum conductivity of CNC at 120°C is only ~4% the conductivity of Nafion. However it is higher than e.g. values achieved by metal-organic frameworks ( $10^{-7}$  to  $10^{-2}$  S/cm at RT),<sup>21</sup> and other low dimensional proton conductors mentioned in the introduction Chapter 1.7 such as graphene oxide ( $9 \times 10^{-4}$  S/cm at 90 °C) or zirconium phosphate hydrate ( $5 \times 10^{-6}$  to  $6 \times 10^{-3}$  S/cm at RT).

The higher conductivity of CNC compared with CNF is attributed to the acid hydrolysis treatment, which introduces sulfonic acid groups attached via ester bonding, increasing the pH and the number of protons available for conduction. Additionally, the acid hydrolysis process is expected to increase the hydrophilicity of the CNC membrane, improving water retention at high temperature and therefore improving conductivity. The strong hydrogen-bonding network induced by acid hydrolysis is also expected to contribute to the good performance at elevated temperature. Therefore nanocellulose membranes could potentially become alternatives to other high temperature proton conductors such as polybenzimidazole (PBI).

Activation energies for proton transport can be determined from the gradients of Arrhenius plots. The activation energies for proton conduction in CNF and CNC membranes are quite

similar ( $0.21 \pm 0.03$  eV and  $0.24 \pm 0.04$  eV, respectively). This indicates that the same proton conduction mechanism dominates in both cases. The activation energy is slightly higher than that of Nafion ( $E_A = 0.16 \pm 0.02$  eV), in which the Grotthuss mechanism is dominant at high humidity. This difference may be due to the presence of more bulk-like water in the pores of Nafion compared with nanocellulose, leading to a more complete hydrogen-bonding network and enabling faster Grotthuss-like proton transport.<sup>20</sup> This is also supported by the much lower hydrogen permeation in nanocellulose compared with Nafion, indicating lower porosity. Additionally, there may be a nanoconfinement effect in the narrow channels between the microfibrils of nanocellulose, leading to a slight increase in activation energy.<sup>22</sup> Despite the small difference in activation energy, the conduction mechanism in the case of nanocellulose is likely to be dominated by a Grotthuss-like, water mediated mechanism.<sup>23-25</sup> The possible conduction mechanisms are shown schematically in *Figure 5.10*.

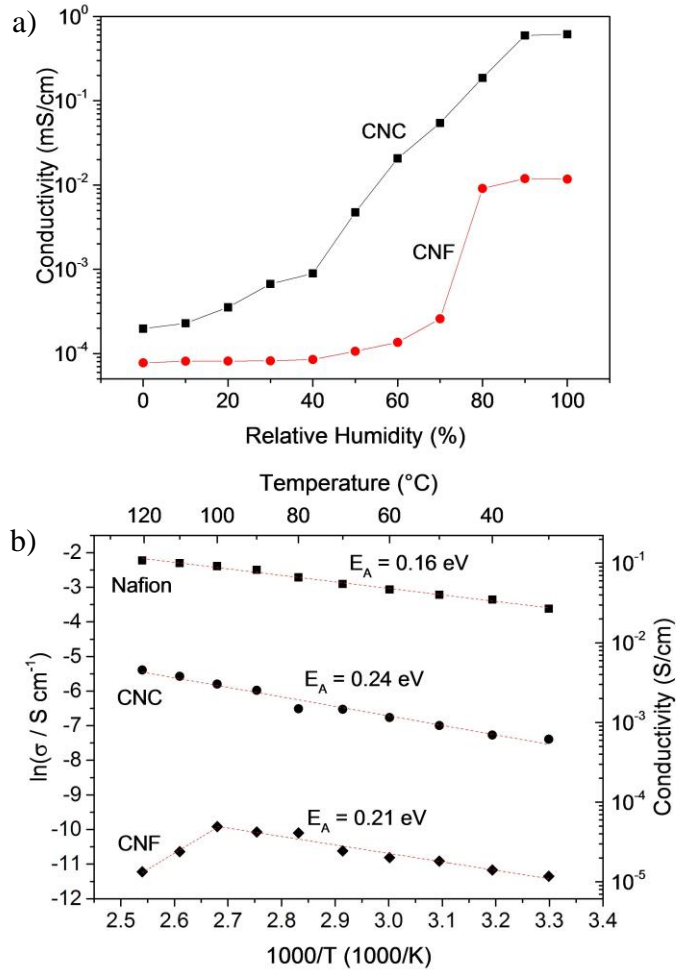


Figure 5.9. a) Dependence of proton conductivity on humidity for cellulose nanofiber (CNF) and cellulose nanocrystal (CNC) membranes at 30°C. b) Arrhenius plot at 100% RH with activation energies and proton conductivity.

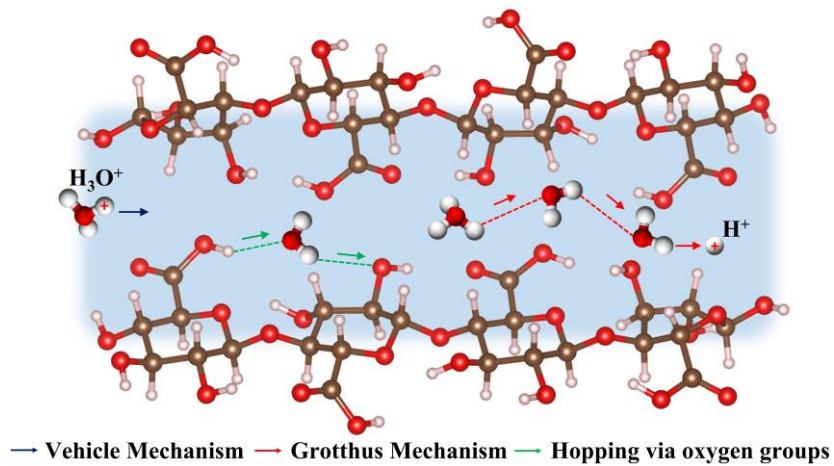


Figure 5.10. Schematic of possible proton conduction mechanisms and pathways in nanocellulose.<sup>26</sup>

## 5.4 Membrane Electrode Assembly Characterization

To date, the operation of a nanocellulose membrane fuel cell (NCFC) utilizing hydrogen gas as fuel has not been reported in the literature to the best of our knowledge. Here, we incorporate vacuum-filtered nanocellulose paper into membrane electrode assemblies (MEAs) in place of Nafion (*Figure 5.11a-b*), and test their performance as fuel cells. The results are shown in *Figure 5.12* (CNF-based NCFC) and *Figure 5.13* (CNC-based NCFC). In the case of CNF (32  $\mu\text{m}$  thickness), the open circuit voltage (OCV) is 0.97 V. This is comparable to Nafion membrane-based fuel cells (0.96 V). This confirms that the nanocellulose electrolyte works effectively in transporting protons, blocking electrons, and that there is very little hydrogen crossover. The OCV drops rapidly by around 70 mV to  $\sim 0.9$  V with increasing current, indicating activation losses comparable to Nafion (in which a  $\sim 60$  mV drop is observed). A maximum power density of  $0.79 \text{ mW/cm}^2$  at a current density of  $1.8 \text{ mA/cm}^2$  was achieved. From the slope of the graph, the internal resistance of the cell was determined to be  $228.1 \Omega \text{ cm}^2$ . This is around three orders of magnitude higher than in a typical Nafion-based PEMFC (e.g.  $100\text{-}200 \text{ m}\Omega \text{ cm}^2$ ).<sup>27</sup> This high resistance is partially due to the low proton conductivity of CNF compared to Nafion, and maybe also higher contact resistance between the membrane and the electrocatalyst layer. This high resistance accounts for the poor fuel cell performance compared with Nafion. In the case of CNC (30  $\mu\text{m}$  thick), the OCV is 0.87 V. This is slightly lower than in the case of CNF, despite the better *ex situ* hydrogen barrier properties. The reduced OCV may be due to pinholes in the membrane as the CNC membranes appear to be more brittle than the CNF membranes and therefore small cracks may form during MEA fabrication and hot-pressing. We are currently investigating this matter further. *In situ* gas permeation measurements will be performed to give more insight into this difference. The polarization curve shows a decrease in cell voltage to 0.75 V at low current densities, corresponding to activation losses. This is followed by a linear ohmic behavior. From the slope of the graph, the internal resistance of the cell is determined to be  $9.5 \Omega \text{ cm}^2$ . This is much lower than the CNF membranes, but still around 100 times higher than for Nafion. The lower resistance in the case of CNC is likely due to the improved proton conductivity, attributed to the sulfonic acid groups. The maximum power density is  $17.2 \text{ mW/cm}^2$  at  $41 \text{ mA/cm}^2$ , which is significantly higher than for CNF, and also attributed to the higher conductivity. The polarization curve shows no sign of mass transport limitation, due

to the relatively low current density. Higher power densities might be achieved by using thinner membranes, and this will be investigated in future research.

Durability measurements were performed directly after polarization curve measurements. The current value used was selected from the polarization curves at 0.5 V cell voltage. The CNF-based NCFC was operated at a constant current of 0.6 mA (*Figure 5.12b*). At the beginning the voltage increased slightly from ~0.50 V up to 0.55 V, probably due to increased humidification of membrane and electrocatalyst during fuel cell operation leading to better conductivity. After about 3 hours, voltage fluctuations occurred and increased in severity. The reason for those fluctuations was the low water level in water bath of the humidifier, leading to condensation of water in the pipes and thus a pressure drop of the gases. After refilling the water bath, the cell voltage showed no sign of fluctuations until after the water level decreased again. After 13 hours the cell voltage was still about 0.54 V, indicating stable operation of the CNF-based NCFC. After the durability measurement, a polarization curve measurement was performed in order to evaluate if the performance of the cell changed during durability measurement. The OCV was unchanged at 0.96 V, however the performance of 0.55 mW/cm<sup>2</sup> at 1.5 mA/cm<sup>2</sup> corresponds to around a 30% drop in performance. From the slope of the polarization curve the ohmic resistance of the cell was determined to be 280.4 Ω cm<sup>2</sup>, 23% higher compared with the resistance before durability measurement. The reason for the increased resistance may be intense swelling of the membrane, or loss of acid groups during operation, resulting in a drop in conductivity.

The CNC-based NCFC was operated with 16 mA constant load current (*Figure 5.13b*). The voltage fluctuates from the beginning of the measurement (by ± 50mV), despite constant water bath levels. Despite this, the voltage remains between 0.4 and 0.5 V. After approximately three hours, the voltage dropped quickly and the measurement was stopped at 0.16 V. Reason for the decrease in cell voltage is likely to be pinhole formation, increasing fuel crossover and leading to failure. The OCV after the durability test dropped to 0.74 V, around 130 mV less than before the measurement. This lends further weight to the hypothesis that pinholes are formed in the membrane leading to fuel crossover. The maximum power density of 7.9 mW/cm<sup>2</sup> at 21.6 mA/cm<sup>2</sup> was significantly decreased (by 56%). From the slope of the polarization curve, the ohmic resistance of the cell was determined to be 17.6 Ω cm<sup>2</sup>, nearly double than measured before the durability test. Again, swelling of membrane might

be responsible for the increase in resistance, as well as loss of acid groups during fuel cell operation.

Visual inspection of the membranes after the measurement revealed cracks and partially thinned regions of the CNC membrane, probably responsible for the OCV drop. The CNF membrane showed no signs of cracking *post operando*. CNCs are highly dispersible in water, and since water is produced at the cathode, membrane thinning or failure is expected to occur. This problem could be solved by e.g. cross-linking cellulose nanocrystals via e.g. esterification or Friedel-Crafts reactions.<sup>28</sup> Also the preparation of composite materials e.g. mixing CNC with CNF, might lead to more stability in wet environment. A straight forward method is assumed to be laminating CNC with a thin layer of Nafion or another proton conductor that prevents leaching of CNC.

Post-operation *ex situ* cross-sections of the MEAs were investigated by SEM (*Figure 5.11c-d*). The gas diffusion layers were detached from the electrocatalyst layer during the cross section preparation, indicating weak interaction with the electrocatalyst layer. However it is observed that little delamination occurs between the electrocatalyst layer and the nanocellulose membrane, indicating a strong interaction and good physical contact.

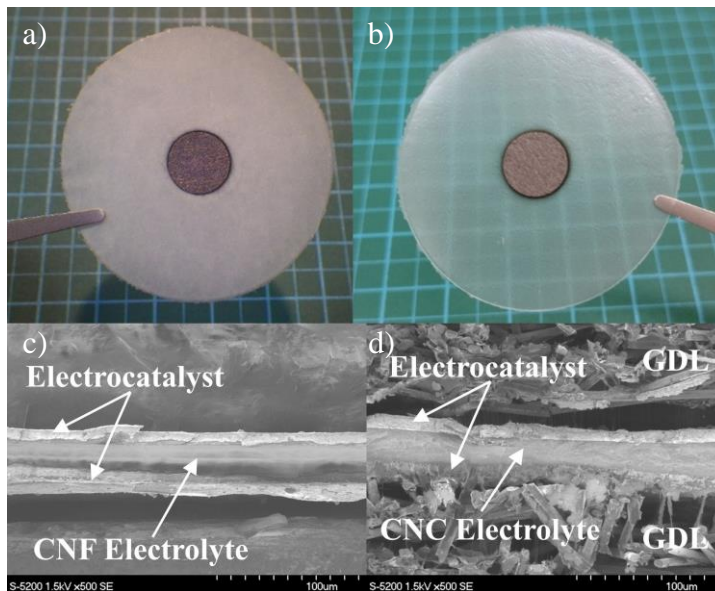


*Figure 5.11. Photographs of MEAs prepared from: a) a cellulose nanofiber (CNF) membrane; and b) a cellulose nanocrystal (CNC) membrane. Post-operation SEM images of cross-sections of CNF (c) and CNC (d) nanocellulose fuel cells (NCFCs).*

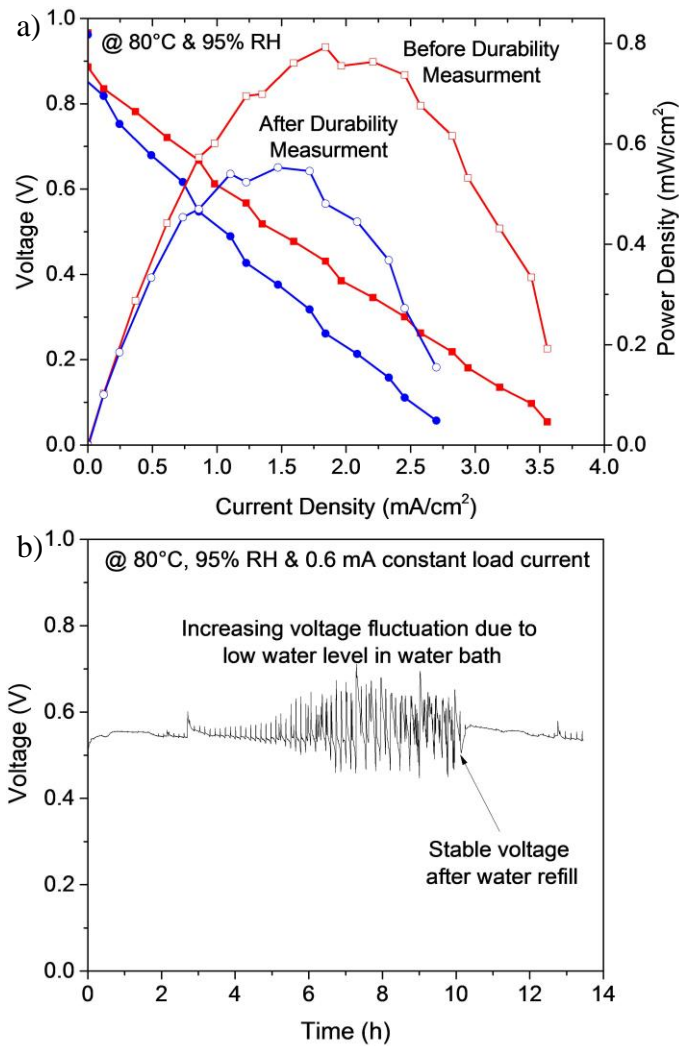


Figure 5.12. a) Polarization curves and power densities of a nanocellulose fuel cell (NCFC) operated at 80°C and 95% RH incorporating a 32  $\mu\text{m}$  thick CNF membrane. b) Cell voltage during durability measurements at constant load current of CNF-based NCFC.

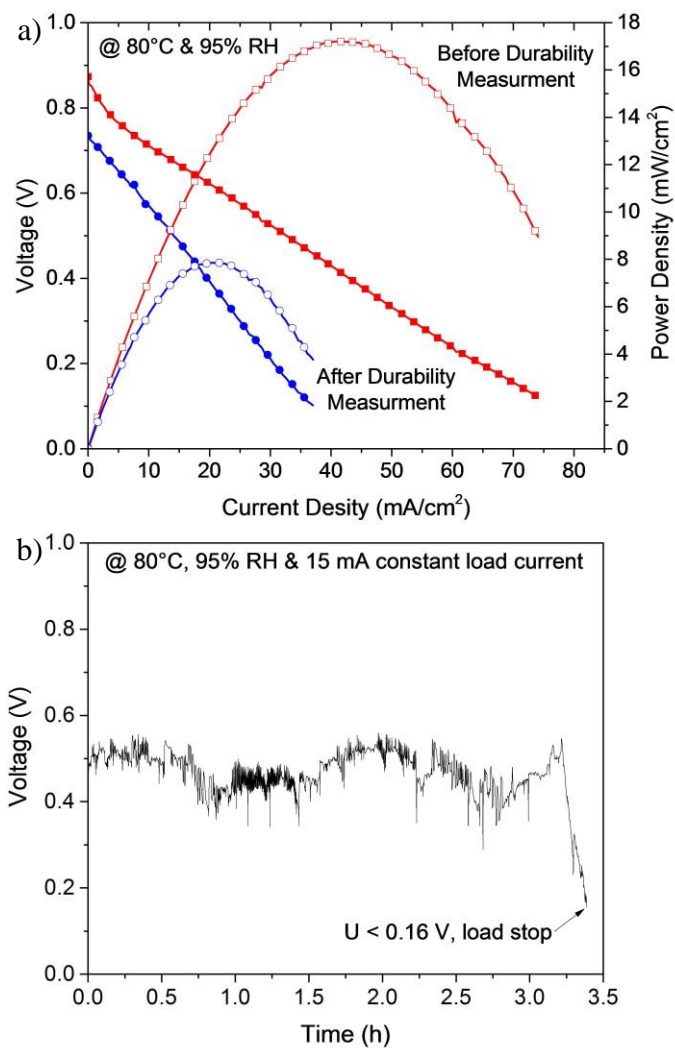


Figure 5.13. a) Polarization curves and power densities of a nanocellulose fuel cell (NCFC) operated at 80°C and 95% RH incorporating a 30  $\mu\text{m}$  thick CNC membrane. b) Cell voltage during durability measurements at constant load current of CNC-based NCFC.

## 5.5 Conclusions

Nanocellulose paper derived from biomass displays proton conductivity that is highly dependent on relative humidity, temperature, and the method of preparation of nanocellulose. Two different types of nanocellulose were compared: cellulose nanofibers (CNFs) and cellulose nanocrystals (CNCs). The fuel cell related properties of nanocellulose are compared with Nafion<sup>®</sup>212 in Table 5.2.

CNF has higher tensile strength (122.8 MPa) and elastic modulus (1494.7 MPa) compared with Nafion (30.7 MPa and 94.9 Mpa, respectively), whereas CNC is very brittle and could not be measured effectively without breaking. CNF had approximately five times higher water uptake than Nafion, which may lead to better water retention for high temperature operation. However, the membrane also swelled to a greater degree than Nafion (6 times), increasing the risk of deterioration under hydration. CNC membranes dissolve when immersed into water due to their high hydrophilicity. Hydrogen permeability through the nanocellulose membranes was around three orders of magnitude lower than in Nafion, with CNCs acting as a slightly better gas barrier than CNFs. This is attributed to the more crystalline nature of CNC, and the tightly packed microstructure. The maximum conductivity of CNF membranes was 0.05 mS/cm at 100°C, and that of CNC paper membranes was 4.6 mS/cm at 120°C (both at 100% relative humidity). This is attributed to a Grotthuss-like water-mediated proton conduction mechanism with an activation energy of around 0.22 eV. The higher conductivity in CNC even at 120°C is attributed to the increased thermal stability and increased acidity of the sulfuric acid groups introduced during acid hydrolysis.

Fuel cells utilizing nanocellulose paper membranes (NCFCs) were fabricated and tested at 80°C and 95% RH using hydrogen fuel. As expected due to the higher conductivity and lower hydrogen gas permeability, fuel cells incorporating CNC displayed better performance (17 mW/cm<sup>2</sup>) than CNF (0.8 mW/cm<sup>2</sup>) due to much lower membrane resistance. The performance of both decreased during durability measurements, probably due to intense swelling and/or thinning of the membrane and loss of proton conducting functional groups. Additionally the high water solubility of CNC seems to promote pinhole formation and thus performance loss by increased crossover. This work shows that nanocellulose paper can be utilized as an ionomer membrane in electrochemical devices such as fuel cells, although

significant optimization is required to compete with more expensive but well-established proton conductors such as Nafion. Especially the high solubility of CNC is an obstacle that has to be overcome for increasing durability of the NCFCs. The raw material cost of nanocellulose as well as the cost per  $\text{m}^2$  membrane are significantly lower than Nafion by several orders of magnitude, indicating that a huge potential for cost reduction is possible by the use of nanocellulose membranes.

This study unveiled several interesting features of nanocellulose, opening up a variety of application possibilities and further research topics. Due to the high gas barrier properties, nanocellulose could be used as low-cost coating material e.g. in hydrogen storage vessels and hydrogen pipelines in order to avoid hydrogen leakage and embrittlement. A layered compound of thin Nafion and CNC layers could result in a membrane with high proton conductivity and improved gas barrier properties, suitable to prepare high power density fuel cells also for elevated temperatures. The OH-groups in nanocellulose offer a variety of possibilities for chemical modification, aiming in particular for an increase in proton conductivity.

Several attempts are planned in order to increase the performance of NCFCs. Due to the extraordinarily high gas barrier properties of nanocellulose, electrode-supported thin-film NCFCs could be fabricated in a similar manner to the printed electrode-supported GOMFCs mentioned in Chapter 3.6, in order to reduce the cell resistance. Furthermore functionalization of nanocellulose with alternative acid groups is planned, e.g. sulfonic or phosphoric acid, in order to increase the proton conductivity and thus fuel cell performance. Preparation of composite materials consisting of CNF and CNC, in order to tailor specific properties such as proton conductivity, water uptake and mechanical strength will be attempted. In order to increase durability of CNC-based NCFCs, lamination of CNC membranes with a thin layer of Nafion ( $\sim 100$  nm) is planned. For a deeper understanding of proton conductivity in nanocellulose it is planned to investigate the proton conductivity of a single nanocellulose fiber by aid of impedance spectroscopy. This result might confirm the assumption of 1D conduction paths within the crystalline part of nanocellulose.

Table 5.2. Comparison of fuel cell membrane related properties of cellulose nanofibers (CNF), cellulose nanocrystals (CNC) and Nafion®212.

| Property   | Nafion®212             | CNF                     | CNC                     |
|--|------------------------|-------------------------|-------------------------|
| Mechanical Strength (MPa)                        | 30.7                   | 122.8                   | -                       |
| Water Uptake (wt%)                               | 25.6                   | 126.2                   | -                       |
| H <sub>2</sub> Permeability at 80°C (barrer)     | 1.01 x 10 <sup>2</sup> | 2.94 x 10 <sup>-1</sup> | 7.13 x 10 <sup>-2</sup> |
| Proton Conductivity $\sigma_{TP}$ (mS/cm):       |                        |                         |                         |
| -At 80°C   | 66.3                   | 0.041                   | 1.49                    |
| -Max.  | 108.3 [120°C]          | 0.05 [100°C]            | 4.57 [120°C]            |
| Proton Conductivity $\sigma_{TP}$ (mS/cm):       | 251.4 [120°C]          | 3.21 [80°C]             | 8.59 [90°C]             |
| Max. Power Density at 80°C (mW/cm <sup>2</sup> ) | 251                    | 0.8                     | 17                      |
| Durability                                       | Good                   | Good                    | Poor                    |
| Raw Material Cost (\$/kg)                        | 24 445                 | 110                     | 551                     |
| Membrane Cost (\$/m <sup>2</sup> )               | 2 445 (50 $\mu$ m)     | 3.32 (30 $\mu$ m)       | 22.29 (30 $\mu$ m)      |

## References

1. Peng, B. L., Dhar, N., Liu, H. L. & Tam, K. C. Chemistry and applications of nanocrystalline cellulose and its derivatives: A nanotechnology perspective. *Can. J. Chem. Eng.* **89**, 1191–1206 (2011).
2. Dufresne, A. Nanocellulose: a new ageless bionanomaterial. *Mater. Today* **16**, 220–227 (2013).
3. Jiang, F., Esker, A. R. & Roman, M. Acid-catalyzed and solvolytic desulfation of H<sub>2</sub>SO<sub>4</sub>-hydrolyzed cellulose nanocrystals. *Langmuir* **26**, 17919–17925 (2010).
4. Moon, R. J., Martini, A., Nairn, J., Simonsen, J. & Youngblood, J. *Cellulose nanomaterials review: structure, properties and nanocomposites*. *Chemical Society Reviews* **40**, (2011).
5. Habibi, Y., Lucia, L. A. & Rojas, O. J. Cellulose Nanocrystals : Chemistry , Self-Assembly , and Applications. *Chem. Rev.* **110**, 3479–3500 (2009).
6. Postek, M. T., Moon, R. J., Rudie, A. W. & Bilodeau, M. A. *Production and Applications of Cellulose Nanomaterials*. (Tappi, 2013).
7. Lin, N. & Dufresne, A. Nanocellulose in biomedicine: Current status and future prospect. *Eur. Polym. J.* **59**, 302–325 (2014).
8. Dong, X. M., Revol, J.-F. & Gray, D. G. Effect of microcrystallite preparation conditions on the formation of colloid crystals of cellulose. *Cellulose* **5**, 19–32 (1998).
9. Barbosa, L. *et al.* A Rapid Method for Quantification of Carboxyl Groups in Cellulose Pulp. *BioResources* **8**, 1043–1054 (2013).
10. Belbekhouche, S. *et al.* Water sorption behavior and gas barrier properties of cellulose whiskers and microfibrils films. *Carbohydr. Polym.* **83**, 1740–1748 (2011).
11. Fukuzumi, H., Fujisawa, S., Saito, T. & Isogai, A. Selective Permeation of Hydrogen Gas Using Cellulose Nanofibril Film. *Biomacromolecules* **14**, 1705–1709 (2013).
12. Lagaron, J. M., Catalá, R. & Gavara, R. Structural characteristics defining high barrier properties in polymeric materials. *Mater. Sci. Technol.* **20**, 1–7 (2004).
13. Siqueira, G., Bras, J. & Dufresne, A. Cellulosic bionanocomposites: A review of preparation, properties and applications. *Polymers (Basel)*. **2**, 728–765 (2010).
14. Nair, S. S., Zhu, J., Deng, Y. & Ragauskas, A. J. High performance green barriers based on nanocellulose. *Sustain. Chem. Process.* **2**, 1–7 (2014).

15. Matteucci, S., Yampolskii, Y., Freeman, B. & Pinnau, I. *Materials Science of Membranes for Gas and Vapor Separation*. (John Wiley & Sons Ltd., 2006).
16. Haraya, K., Obata, K., Hakuta, T. & Yoshitome, H. Permeation of Gases Through a Symmetric Cellulose Acetate Membrane. *J. Chem. Eng. Japan* **19**, 464–466 (1986).
17. Wu, J., Liu, J. & Yang, Q. Gas permeability of novel cellulose membrane. *J. Memb. Sci.* **204**, 185–194 (2002).
18. Walker, G. *Solid-State Hydrogen Storage: Materials and Chemistry*. (Woodhead Publishing, 2008).
19. *Gaseous Hydrogen Embrittlement of Materials in Energy Technologies*. (Woodhead Publishing, 2012).
20. Choi, P., Jalani, N. H. & Datta, R. Thermodynamics and Proton Transport in Nafion - II. Proton Diffusion Mechanisms and Conductivity. *J. Electrochem. Soc.* **152**, 123–130 (2005).
21. Ramaswamy, P., Wong, N. E. & Shimizu, G. K. H. MOFs as proton conductors – challenges and opportunities. *Chem. Soc. Rev.* **43**, 5913–5932 (2014).
22. *Proton conductors: Solids, membranes, and gels—materials and devices*. (Cambridge University Press, 1993). doi:10.1002/adma.19930050923
23. Pandey, K. & Lakshmi, N. Evidence of failure of hopping model of ionic conductivity in phosphomolybdic acid studied by a.c. conductivity measurements. *J. Mater. Sci.* **4**, 1749–1752 (1999).
24. Knauth, P. & Schoonman, J. *Nanocomposites: Ionic Conducting Materials and Structural Spectroscopies*. (Springer, 2008).
25. Paul, D. K., McCreery, R. & Karan, K. Proton Transport Property in Supported Nafion Nanothin Films by Electrochemical Impedance Spectroscopy. *J. Electrochem. Soc.* **161**, F1395–F1402 (2014).
26. Momma, K. & Izumi, F. VESTA 3 for three-dimensional visualization of crystal, volumetric and morphology data. *J. Appl. Crystallogr.* **44**, 1272–1276 (2011).
27. Revankar, S. T. & Majumdar, P. in *Fuel Cells: Principles, Design and Analysis* 748 (CRC Press, 2014).
28. Hou, H., Di Vona, M. L. & Knauth, P. Building bridges: Crosslinking of sulfonated aromatic polymers — A review. *J. Memb. Sci.* **423-424**, 113–127 (2012).

## 6 Conclusions and Future Work

### 6.1 Conclusions

In this work, two different low dimensional ion conducting materials were investigated as novel membrane materials for fuel cells, namely: graphene oxide and nanocellulose.

Fuel cells are the key to a sustainable energy society and the polymer electrolyte membrane fuel cell (PEMFC) is one of the most promising types of fuel cell. For this reason most automobile manufactures use PEMFCs in their fuel cell vehicles. In order to accelerate commercialization, much research is underway to reduce the price by e.g. increasing the power density, operating at higher temperature, and reducing the cost of materials. The search for new membrane materials is an important contribution to this. However despite intensive research on membrane materials over the past 50 years, Nafion (a perfluorinated ionomer membrane and registered trademark of E.I. DuPont de Nemours) is still dominant. Unconventional materials may be needed to compete with Nafion. Nanotechnology has provided novel solutions and performance enhancement in many fields of research due to the interesting and unique properties of materials at the nanoscale ( $< 100$  nm). Therefore nanomaterials are also a promising route to the fabrication of next-generation fuel cell membranes.

In this thesis, the first question to be addressed was whether freestanding and sufficiently flexible membranes could be fabricated from low dimensional ion conductors. Low mechanical stability can impede handling, and high solubility can be problematic during electrocatalyst deposition or fuel operation in high humidity. The second question was whether membranes made from low-dimensional materials satisfy the basic requirements for ion exchange membranes, i.e. sufficient gas barrier; ionic conductivity, and electronic insulation. The final question was whether the novel low dimensional ion conductor membranes can be really applied in fuel cells, and if the material can withstand the harsh fuel cell operating conditions such as high temperature, humidity and pressure. When the low dimensional ion conductors pass all of these requirements, then they can be classified as new fuel cell membrane materials.

In Chapter 3, graphene oxide (GO) was investigated as membrane material. GO membranes were fabricated by simple vacuum-filtration from GO dispersion. Membranes with a thickness of  $> 10 \mu\text{m}$  were self-supporting, flexible and easy to handle without special care. GO membranes had hydrogen permeability three orders of magnitude lower than Nafion, making them ideally suited for application in PEMFCs. Impedance spectroscopy revealed clear humidity- and temperature-dependent conductivity, with  $5.74 \text{ mS/cm}$  at  $80^\circ\text{C}$  and  $0\%$  RH, and  $0.51 \text{ mS/cm}$  at  $90^\circ\text{C}$  and  $100\%$  RH. With the aid of blocking layer measurements, GO was shown to be a mixed electronic-protonic conductor, with transference numbers depending on humidity. Proton conductivity (with activation energies of  $0.05$  to  $0.4 \text{ eV}$ ) was observed at high humidity, indicating a Grotthuss-type proton conduction mechanism. At low relative humidity ( $< 40\%$ ), electronic conductivity dominated. At temperatures  $> 90^\circ\text{C}$  GO was partially reduced (i.e. lost oxygen functional groups), and electronic conduction dominated, indicated by increasing conductivity with decreasing humidity. Cool-down at  $0\%$  RH after measurement at  $120^\circ\text{C}$  showed that GO had transformed to a more or less pure electronic conductor. This finding indicates that PEMFC with GO membranes should be operated at high humidity and low temperature to avoid electronic conduction and short circuiting the cell. Intriguingly, the in-plane conductivity of GO was in the same range as the through-plane conductivity of Nafion, highlighting the anisotropy of low dimensional ionic conductors, and hinting that the conductivity can match that of commercially established ionomers.

GO-based MEAs were fabricated by and integrated into a single cell holder. The resulting graphene oxide membrane fuel cells (GOMFCs) were successfully operated with hydrogen fuel, between  $30$  and  $80^\circ\text{C}$ , at  $95\%$  RH. Higher open circuit voltage (OCV) was recorded compared with Nafion-based PEMFCs, confirming the superior hydrogen barrier properties of GO. For a GOMFC using a  $16 \mu\text{m}$  thick GO membrane the maximum power density was  $\sim 34 \text{ mW/cm}^2$  at  $30^\circ\text{C}$  and  $95\%$  RH. The performance decreased with increasing operation temperature due to reduction of GO, especially in the reducing hydrogen atmosphere on the anode side.

Due to the excellent hydrogen barrier properties, GOMFCs with much thinner membranes were fabricated in order to decrease the area specific resistance by thinning the membrane. Due to the low mechanical stability of very thin GO membranes, these were fabricated using

a novel spray-deposition technique, in effect making an electrode-supported GOMFC. With a membrane thickness of  $\sim 3 \mu\text{m}$  the power density at  $30^\circ\text{C}$  and 95% RH was  $79 \text{ mW/cm}^2$ . This is much higher than for thicker GO membranes. A clear relationship between membrane thickness and GOMFC power density was established, hinting that much higher power densities are achievable, possibly even competing with Nafion. However the electrode-supported GOMFCs also faced the same problem of low durability due to loss of oxygen groups during fuel cell operation. Despite this, these results indicate the possibility of achieving high power densities by spraying or printing of low-dimensional ion conductors to make electrode-supported fuel cells. In conclusion, GO fulfilled the basic requirements of a fuel cell membrane, and was incorporated into operational hydrogen fuel cells. Despite the low durability at present, higher power densities were achieved, especially for very thin, electrode-supported membranes.

In Chapter 4 GO was modified to be used as a novel alkaline anion exchange membrane (AAEM). Pure GO dispersions underwent a cation exchange reaction with KOH, followed by vacuum-filtration to form  $\text{GO}_{\text{KOH}}$  membranes. A change in the microstructure of the  $\text{GO}_{\text{KOH}}$  membranes was confirmed by electron microscopy, and the change in surface chemistry was confirmed by spectroscopic techniques. The gas barrier of  $\text{GO}_{\text{KOH}}$  was even higher than GO. The maximum through-plane conductivity of  $\text{GO}_{\text{KOH}}$  was  $6.1 \text{ mS/cm}$  at  $70^\circ\text{C}$  and 100% relative humidity, which is comparable with commercially available AAEMs. Ion blocking measurements were used to confirm that  $\text{OH}^-$  anions were the dominant charge carrier. Electronic conductivity at lower humidity was only observed at an elevated temperature ( $70^\circ\text{C}$ ). This may be due to the larger interlayer spacing between  $\text{GO}_{\text{KOH}}$  sheets (compared with GO) providing a larger potential barrier to electron hopping. A reverse-Grotthuss type mechanism was inferred from the activation energy. An MEA was prepared using an  $18 \mu\text{m}$  thick  $\text{GO}_{\text{KOH}}$  membrane. The performance of resulting AAEMFC was investigated at  $30^\circ\text{C}$  and 95% RH. The low OCV ( $0.94 \text{ V}$ ) was attributed to some electron conduction. Despite the high  $\text{OH}^-$  anion conductivity, the maximum power density was only  $\sim 1 \text{ mW/cm}^2$  quickly degrading during durability testing. This is mainly attributed to carbonate formation upon exposure of KOH to  $\text{CO}_2$ , decreasing the alkalinity and therefore conductivity of the membrane, as well as forming a barrier to ion conduction between the electrodes and membrane. In conclusion  $\text{GO}_{\text{KOH}}$  fulfills the basic requirements for use in

alkaline fuel cells. It has promising mechanical properties and OH<sup>-</sup> conductivity, but disappointing fuel cell performance. However, this is an important proof-of-concept device, and is the first example of an alkali anion exchange membrane fuel cell based around a pure GO membrane.

In Chapter 5, nanocellulose was explored as a low dimensional proton conductor. Two different types of nanocellulose were investigated: cellulose nanofibers (CNFs), and cellulose nanocrystals (CNCs). CNF and CNC membranes were fabricated by simple vacuum-filtration. CNC membranes dried very quickly, whereas CNF required an additional hot-pressing step to dry sufficiently. CNF paper is highly flexible and mechanically stable, whereas CNC paper is brittle and requires more care during handling. The hydrogen gas permeability of nanocellulose paper was around three orders of magnitude lower than in Nafion. The hydrogen permeability in CNC paper was slightly lower than in CNF paper, probably due to dense packing of cellulose crystals compared with the loose network of cellulose fibers. Impedance spectroscopy revealed a strong dependence of conductivity on temperature and humidity. The maximum through-plane proton conductivity was 0.05 mS/cm for CNF paper, and 3.0 mS/cm for CNC paper at 100°C and 100% RH. At temperature > 100°C the conductivity of CNF paper decreased. However, CNC paper retains its high conductivity even at 120°C (4.6 mS/cm). This result indicates that CNC paper is suitable for application in high temperature PEMFCs (HT-PEMFCs). A Grotthuss-like, water-mediated transport mechanism was inferred from the measured activation energies. MEAs were fabricated from the nanocellulose papers, and nanocellulose fuel cells (NCFCs) were successfully tested at 80°C and 95% RH. The CNF-based NCFC had a power density of 0.8 mW/cm<sup>2</sup>, whilst the CNC-based NCFCs had a power density of 17.2 mW/cm<sup>2</sup>. The higher performance for CNC was attributed to the higher proton conductivity. The CNF-based NCFC displayed lower degradation during durability testing compared with CNC. This was attributed to the higher solubility of CNC compared with CNF, leading to redispersion of the membrane in humid conditions. In conclusion, both nanocellulose papers fulfilled the basic requirements to be used as fuel cell membranes, even at high temperature.

Finally GO and nanocellulose are compared with Nafion, and their fuel cell related properties (for PEMFC application) can be seen in Table 6.1. The tensile strength of CNF (~123 MPa) is around twice that of GO (~55 MPa) and four times that of Nafion (~31 MPa). CNC

membranes are extremely brittle and repeatable measurements could not be performed. GO had the highest water uptake (333 wt%) and lost most of its mechanical stability when immersed in water. This was followed by CNF (126 wt%) and then Nafion (26 wt%). CNC easily dissolves in water due to its high hydrophilicity. The hydrogen gas barrier properties of GO and nanocellulose are comparable, and both materials display around three orders of magnitude lower hydrogen permeability compared with Nafion. Nanocellulose showed higher temperature stability than GO and CNC showed the highest through-plane proton conductivity of the investigated low dimensional ionic conductors. With 4.6 mS/cm at 120°C, the conductivity of CNCs is roughly 4 to 5% the conductivity of Nafion. GO on the other hand showed a very high in-plane conductivity due to the fast proton transport in the low dimensional conduction pathway (mono- or multilayer of water), approaching the values of the through-plane conductivity of Nafion. The power density was higher in GO-based PEMFCs, due to the relatively thin GO membranes used. The use of thinner nanocellulose membranes could also dramatically increase the power density of NCFCs and this will be the subject of future work. CNF showed highest durability of the investigated low dimensional ionic conductors, whereas CNC-based NCFCs lost their performance quickly. The durability of GO is strongly affected by partial reduction (loss of oxygen containing functional groups), whereas CNC high hydrophilicity seems to be responsible for quick performance loss due to thinning of the membrane by water produced during fuel cell operation. The achieved power densities are still lower than for Nafion-based PEMFCs, however the electrode-supported cell design could be suitable to further reduce the membrane resistance and therefore increase the power density. As the cost of the investigated membranes is much lower than Nafion, and less material is required for e.g. electrode-supported MEA fabrication, there is potential for significant cost reduction for devices using these materials. Based on these results, we conclude that nanocellulose, especially CNC, seems to be the most promising material studied here for membranes in next-generation fuel cells.

The results in this work showed that low dimensional ionic conductors can be successfully applied as fuel cell membranes in PEMFCs and also AAEMFCs and unveiled some interesting findings. The extraordinarily high gas barriers for these materials are very promising for fuel cell applications. Despite the lower conductivity compared to Nafion, reasonably high power densities could be achieved by fabricating electrode-supported MEAs

with thin membranes. Additionally this novel fabrication method is a step forward towards fully printable fuel cells and will help to automate fuel cell fabrication, thus accelerating fuel cell commercialization. In-plane proton conductivity of GO is approximately two orders of magnitude higher than the through-plane conductivity, with values approaching the through-plane conductivity of Nafion. The in-plane proton conduction of GO occurs in along low-dimensional conducting pathway (i.e. mono- or multilayer water) as well as along the surface. This feature, together with the mixed ionic-electronic conductivity of GO makes it an interesting material for applications that require surface/grain boundary conductivity, such as for the oxygen reduction reaction in electrocatalyst layers. The low cost of nanocellulose and its high gas barrier properties make it to an interesting low-cost coating material for e.g. hydrogen storage vessels and hydrogen pipelines in order to avoid hydrogen leakage and embrittlement. Proton conductivity in pure nanocellulose and its application as a fuel cell membrane has been reported here for the first time. This finding might lead to increased scientific interest in the application of nanocellulose in electrochemistry.

*Table 6.1. Fuel cell related properties of Nafion, graphene oxide, cellulose nanofibers (CNF) and cellulose nanocrystals (CNC).*

| <b>Property</b>                              | <b>Nafion®212</b>      | <b>GO</b>               | <b>CNF</b>              | <b>CNC</b>              |
|--|------------------------|-------------------------|-------------------------|-------------------------|
| Mechanical Strength (MPa)                    | 30.7                   | 54.5                    | 122                     | -                       |
| Water Uptake (wt%)                           | 25.6                   | 333                     | 126                     | -                       |
| H <sub>2</sub> Permeability at 80°C (barrer) | 1.01 x 10 <sup>2</sup> | 9.50 x 10 <sup>-2</sup> | 2.94 x 10 <sup>-1</sup> | 7.13 x 10 <sup>-2</sup> |
| Proton Conductivity $\sigma_{TP}$ (mS/cm):   |                        |                         |                         |                         |
| -At 80°C                                     | 66.3                   | 0.41                    | 0.041                   | 1.49                    |
| -Max.  | 108.3 [120°C]          | 0.51 [90°C]             | 0.05 [100°C]            | 4.57 [120°C]            |
| Proton Conductivity $\sigma_{TP}$ (mS/cm):   | 251.4 [120°C]          | 51.5 [70°C]             | 3.21 [80°C]             | 8.59 [90°C]             |
| Max. Power Density (mW/cm <sup>2</sup> )     | 251 [80°C]             | 79 [30°C]               | 0.8 [80°C]              | 17 [80°C]               |
| Durability                                   | Good                   | Low                     | Good                    | Low                     |
| Raw Material Cost (\$/kg)                    | 24 445                 | 200 000                 | 110                     | 551                     |
| Membrane Cost (\$/m <sup>2</sup> )           | 2 445 (50 $\mu$ m)     | 880 (3 $\mu$ m)         | 3.32 (30 $\mu$ m)       | 22.29 (30 $\mu$ m)      |

## 6.2 Future Work

In this work GO and nanocellulose were successfully tested as fuel cell membranes in PEMFCs and AAEMFCs. However further improvements are necessary in order to increase fuel cell power density and durability.

The main mode of performance loss in GOMFCs was loss of oxygen functional groups in the reducing hydrogen atmosphere. One method to prevent this will be to laminate GO with very thin Nafion layers (e.g. < 100 nm), preventing direct contact between GO and hydrogen. Another problem is that GO can redisperse in water, possibly leading to membrane thinning and pinhole formation during fuel cell operation. In order to solve this issue, GO sheets will be immobilized by cross-linking, e.g. by utilizing  $Al^{3+}$  ions, or by covalent bonding with polymers. In order to increase the conductivity of GO, surface functionalization with more acidic functional groups will be performed, such as sulfonic acid. The most promising aspect of this work was the fabrication of electrode-supported fuel cells with extremely thin membranes. Therefore this will be continued with other proton conducting materials such as Nafion and nanocellulose. A major problem with the electrode-supported work was the low OCV. Therefore we plan to investigate the reason for this in more detail, for example by looking for cracks or pinholes via laser microscopy and scanning electron. After this we will optimize the fabrication process to increase the OCV.

For AAEMFCs the electrocatalyst layer was deemed to be one of the limiting factors in fuel cell performance, and therefore the ionomer-electrocatalyst ratio in this layer will be optimized. As  $CO_2$  poisoning is the major reason for the low performance and durability, it is then planned to fabricate the membranes and MEAs in a glove box under nitrogen atmosphere, to prevent  $CO_2$  exposure. AAEMFCs will be then be operated with purified air or pure oxygen. Finally we will apply non-precious catalysts in the electrocatalyst layers.

Since CNF paper was more stable than CNC paper but CNC paper had higher proton conductivity we will fabricate composited membranes to take advantage of the different properties of each material. We will attempt to increase the proton conductivity by chemical modification of nanocellulose e.g. with sulfonic acid groups. The solubility will be decreased by lamination and/or crosslinking, in order to prevent membrane thinning and pinhole formation. As nanocellulose exhibited excellent hydrogen gas barrier properties, it is planned

to fabricate electrode-supported NCFCs with very thin membranes ( $< 5 \mu\text{m}$ ). Combining composited materials with acid functionalization, thin membranes, lamination, crosslinking and high operation temperatures is expected to result in much higher fuel cell power densities, as well as higher durability.

As in-plane conductivity of nanocellulose has not been investigated at a wide temperature and humidity range yet, it is planned to conduct a systematic study of in-plane conductivity by aid of impedance spectroscopy. The obtained knowledge will provide a better understanding of proton conduction anisotropy in low dimensional proton conductors. The proton conductivity of a single cellulose nanofiber/nanocrystal will be also investigated using conductive environmental scanning probe microscopy.